Investigation of new nanofluids based on molten salts and their corrosion mechanisms for thermal energy storage applications

Udayashankar Nithiyanantham

A dissertation presented for the Doctoral degree in Physics with an "International Doctor" mention

Leioa, September 2019

INVESTIGATION OF NEW NANOFLUIDS BASED ON MOLTEN SALTS AND THEIR CORROSION MECHANISMS FOR THERMAL ENERGY STORAGE APPLICATIONS

By

Udayashankar Nithiyanantham

Directed by

Dr. Abdessamad Faik

Prof. Josu Mirena Igartua Aldamiz

A dissertation presented for the Doctoral degree in Physics with an "International Doctor" mention

Leioa, September 2019

Acknowledgements

Abstract

Thermal energy storage (TES) is considered as a vital component for concentrated solar power (CSP) technology, which leads to cost-effective dispatchable electricity production. The commercial TES technology in CSP plants is based on a two-tank solution of molten nitrate salts. The binary inorganic salt which consists of a mixture of 60 wt% of $NaNO_3$ and 40 wt% of KNO_3, so-called "Solar salt", is used due to its suitable operating temperature range, high density, low vapor pressure, and relatively high heat capacity. While, its poor thermal conductivity is considered as the main drawback that requires a complicated heat exchanger design for a better heat transfer efficiency during the charge and discharge processes. Thus, it contributes to the increment of the levelized cost of electricity (LCOE) in CSP plants. However, for further reduction of the CSP costs, the efficiency of the whole system can be improved by enhancing the thermophysical properties of the molten salt as the specific heat capacity and thermal conductivity.

Recently, the development of nanofluids based on molten salt with anomalous enhancements of those properties was identified as a promising approach. Even some enhancements were already reported in the literature, a big discrepancy of the results was observed due to several factors such as the enhancement mechanisms are still unknown, the complexity of the nanofluid preparation method, the determination of those properties, the initial state of the nanoparticles dispersion and its evolution with time.

In this work, we present an optimized simple dry method for the preparation of nanofluids to obtain a homogeneous dispersion of nanoparticles within the molten salt. In addition, to reveal the mechanisms of thermophysical properties and improve the dispersion stability, different type, shape, size and composition of the

nanoparticles were used. For that purpose, monodispersed SiO_2 and $SiO_2@Al_2O_3$ core-shell nanoparticles were developed for the first time to prepare the molten salt-based nanofluids with improved stability compared to the commercial nanoparticles based nanofluids.

Finally, the effect of adding nanoparticles in the molten salt on its corrosivity with the tank material is still needed to be explored. In the present work, we discovered new corrosion mechanisms related to the addition of the nanoparticles in the molten salts. In addition, a simple graphitization method was proposed as an anticorrosion method for molten binary nitrate salt with carbon steel.

Resumen

El almacenamiento de energía térmica (TES, por sus siglas en inglés) se considera un componente vital para las centrales termosolares de concentración (CSP, por sus siglas en inglés), ya que permite una producción de electricidad gestionable y rentable. La tecnología TES comercial en plantas de CSP se basa en una solución de dos tanques de sales de nitrato fundidas. Dicha sal inorgánica binaria, consistente en una mezcla de 60% en peso de $NaNO_3$ y 40% en peso de KNO_3, llamada "sal solar" se usa debido a su adecuado rango de temperatura de operación, alta densidad energética, baja presión de vapor y relativamente alta capacidad calorífica. Por otro lado, su mala conductividad térmica se considera su principal desventaja, ya que requiere un diseño complicado del intercambiador de calor para posibilitar una rápida transferencia de calor durante los procesos de carga y descarga. Por lo tanto, contribuye al incremento del coste de electricidad nivelado (LCOE, por sus siglas en inglés) en las plantas de CSP. En ese sentido, para una mayor reducción de los costes de CSP, la eficiencia de todo el sistema se puede mejorar al aumentar las propiedades termofísicas de la sal fundida, como la capacidad térmica específica y la conductividad térmica.

Recientemente se identificó como un enfoque prometedor el desarrollo de nanofluidos con base de sal fundida, debido a las mejoras anómalas de propiedades termofísicas que muestran. A pesar de que algunas de esas mejoras se han publicado en la literatura, se ha observado una gran discrepancia entre los resultados mostrados. Dicha discrepancia es debida a diversos factores, como la falta de confirmación de los mecanismos físicos que producen la mejora, la complejidad del método de preparación de nanofluidos, la determinación de esas propiedades, el estado inicial de La dispersión de las nanopartículas y su evolución con el tiempo.

En este trabajo presentamos un método simple y optimizado para la preparación en seco de nanofluidos con una dispersión homogénea de nanopartículas dentro de la sal fundida. Además, para revelar los mecanismos de mejora de las propiedades termofísicas y aumentar la estabilidad de la dispersión, se utilizaron diferentes tipos de nanopartículas con diferentes tamaños, composiciones y formas. Para ese propósito, se desarrollaron por primera vez nanopartículas mono dispersas de SiO_2 y de "core-shell" de $SiO_2@Al_2O_3$ para la obtención de nanofluidos basados en sales fundidas con una estabilidad mejorada en comparación con los nanofluidos basados en nanopartículas comerciales.

Finalmente, también es necesario analizar el efecto que produce la adición de nanopartículas en la corrosividad de la sal fundida sobre los distintos materiales del tanque. En el presente trabajo, se descubren nuevos mecanismos de corrosión relacionados con la adición de las nanopartículas en las sales fundidas. Además, se propone un método simple de grafitización como método anticorrosión para la sal fundida de nitrato binario con acero al carbono.

Table of Contents

Abbreviations and Symbols

Abbreviations

AISI	American Iron and steel institute
BET	Brunauer-Emmett-Teller
Cc	Concentration
CO_2	Carbon dioxide
CS	Carbon steel
CSP	Concentrated solar power
DSC	Differential scanning calorimetry
EDX	Energy-dispersive X-ray spectroscopy
enhanc.	enhancement
FIB	Focused ion beam
FTIR	Fourier transform infrared spectroscopy
HTF	Heat transfer fluid
incr.	incremets
LCOE	Levelized cost of electricity
LFA	Laser flash analysis
LFR	Linear Fresnel reflectors
LHS	Latent heat storage
LP	Liquid phase
MWCNTs	Multi-walled carbon nanotubes
nm	Nanometer
NPs	Nanoparticles
NRs	Nanorods
PCMs	Phase change materials

PDC	Parabolic dish collectors
PTC	Parabolic trough collectors
PV	Photovoltaic
Q_{salt}	Quantity of salt
Ref	Reference
RT	Room temperature
SEM	Scanning electron microscope
SHS	Sensible heat storage
SP	Solid phase
SPT	Solar power tower
SS	Stainless steel
SWCNTs	Single-walled carbon nanotubes
TcES	Thermochemical energy storage
TEM	Transmission electron microscope
TES	Thermal energy storage
TG-DTA	Thermogravimetry and differential thermal analysis
UV	Ultraviolet
V_{tank}	Volume of the tank
XRD	X-ray diffraction
XPS	X-ray photoelectron spectroscopy

Symbols

C_p	Specific heat capacity	J/K.g
λ	Thermal conductivity	W/m.K
T	Temperature	ºC
α	Thermal diffusivity	mm^2/s
η	Viscosity	Pa.S
ZP	Zeta potential	mV
ΔH	Enthalpy	J/g

List of Figures

List of Tables

Chapter 1. Introduction

1.1. Scope of the thesis

The main aim of this work is to develop stable molten salt nanofluids with enhanced thermophysical properties for thermal energy storage application at concentrated solar power plants. Also, the lifetime of the storage system components is one of the critical parameters to be considered for the further industrial application of the developed nanofluids in CSP plants. So, the compatibility test between the storage materials and storage tank was also targeted in the present work aiming to understand the effect and the corrosion mechanisms when nanoparticles are added to the base molten salt.

So far, the molten salt-based nanofluids are prepared by using classical wet methods. However, the classical wet method was widely used but it has several drawbacks such as the long processing time and difficulty to scale it up for commercial applications. In this work, we developed a new simple physical shaking method for the nanofluids preparation which presents several advantages such as the shorter processing time and the possibility of scale up into industrial applications. In the second step, the reported works in literature have investigated the molten salt nanofluids by using commercial nanoparticles such as Al_2O_3 and SiO_2 nanoparticles, which prevents the systematic investigation of the nanoparticles shape and size effects on not only the enhancement of the thermophysical properties but also, on the dispersion stability of the nanofluid. The present work introduced the development of advanced nanoparticles like SiO_2 with different sizes and $SiO_2@Al_2O_3$ core-shell nanostructures aiming not only to maximize the thermophysical properties enhancement; but also, to shed light on the understating the effect of long-term stability of the nanofluids. The stabilization of the nanofluids will help to understand the discrepancy of the results reported in the literature by different authors for the

same system. Furthermore, the most research results reported in literature focus only in the enhancement of specific heat capacity, in this regard, the present work will investigate the effect of adding nanoparticles on the enhancement of thermal conductivity. Special attention was also made to investigate the viscosity and stability of the system developed within this thesis work aiming to understand the effect of the size, shape, composition (between Al_2O_3 and SiO_2) and agglomeration of nanoparticles on the possible undesirable increase of the viscosity and stability of the system. Finally, the compatibility between the molten salt nanofluids and carbon steel under different corrosion test conditions was carried out to understand the mechanisms responsible for the change of the corrosion rate compared to the base fluid. In addition, to mitigate the corrosion effect a new graphitization method was introduced in this work as a protective layer.

The present thesis work is structured in five main parts, as follows:

In Chapter 1: A general overview on renewable energies and thermal energy storage was presented together with the state-of-the-art of the development of molten salt nanofluid highlighting many aspects such as the preparation method, the enhancement of the thermophysical properties, the effect of adding nanoparticles on the viscosity and the effect on the corrosion behaviour of the nanofluids.

In Chapter 2: This chapter begins with the preparation methods of different sizes of SiO_2 and different composition of $SiO_2@Al_2O_3$ core-shell nanoparticles. The commonly used wet preparations methods of nanofluids are compared with the newly developed dry method. The optimization of the preparation of nanofluids and their characterization will be highlighted aiming to the dispersion stability of nanofluid with time. Furthermore, the compatibility of the developed nanofluids is studied by carbon steel, in this regard, the experimental methods for corrosion protocol, the sample preparation for cross-section analysis by SEM and FIB techniques is elaborated in this chapter. In addition, the detailed description of the instruments is used for the structural and thermophysical characterization of the prepared materials such as nanoparticles and nanofluids were shown in this section. Especially, sample preparation and measurement conditions of the thermophysical properties included more in detail due to the difficulties of the techniques.

In Part 1: This part is divided into three main chapters where commercial and synthesized nanoparticles were used for the preparation of nanofluids based on

eutectic nitrate salt ($NaNO_3$:KNO_3 51:49 wt%) as a base fluid. The commercial Al_2O_3 and SiO_2 nanoparticles and new synthesized monodispersed SiO_2 and $SiO_2@Al_2O_3$ core-shell nanoparticles were used aiming to investigate the size, shape and composition effects not only on the enhancement of the thermophysical properties but also on the dispersion stability of the nanofluids. Initially, the utilized nanoparticles were characterized by several techniques to know the structural and morphological properties by using XRD, FTIR, SEM, BET, TEM, etc. Then the detailed thermophysical properties such as specific heat capacity, thermal diffusivity/conductivity, enthalpy, viscosity, thermal and visual stability of the nanofluids were studied by using different techniques such as DSC, LFA, Rheometer, STA, Dilatometer and visual stability test at high temperature.

In Part 2: This part is divided into three main chapters where the compatibility test of nanofluids with storage tank materials was presented. The main aim is to investigate the effects of nanoparticles addition on the corrosivity of the molten salts. On the first hand, the effect of adding commercial Al_2O_3, SiO_2 and TiO_2 nanoparticles was studied. On the second hand, the use of a simple graphitization process of the carbon surface to protect it against the corrosivity of the molten salt was highlighted. For that purpose, systematic corrosion experiments were carried out at two temperatures of 310ºC and 390ºC under air atmosphere by using the exposure times of 250h, 500h, 1000h and 1500h. To shed some light on the corrosion mechanisms and quantify corrosion rates a combination of advanced material characterization techniques as Focused Ion Beam, SEM, EDX, XPS depth profiling, XRD and TGA were applied.

In Conclusions: The main results are summarized demonstrating the main advantages and drawbacks of the nanofluids developed in this thesis work.

1.2. Background

Energy is an essential need for a human being and having a major impact on economic developments. Each year, additional energy is required to meet the increase of the population, improvement of technology and worldwide industrialization. The global energy demand was increased by 2.1% in 2017 compared with 0.9% on average over the previous five years [1]. The thermodynamic first law of conservation of energy states that the energy can be neither created nor destroyed in an isolated system but it can be transferred from one form to another form. As a result, considering universal as an isolated system, the entire object in the modern world is functioned by relying on this principle; i.e. the transformation of one form of energy into another form (e.g. heat into electricity). So far, the generation of a major part of electricity depends on the non-renewable energy sources of fossil fuels (coal, oil, and natural gases) and the minor parts are belonging to nuclear energy and renewable energy sources of biomass, geothermal, solar, wave and wind energies (Figure 1).
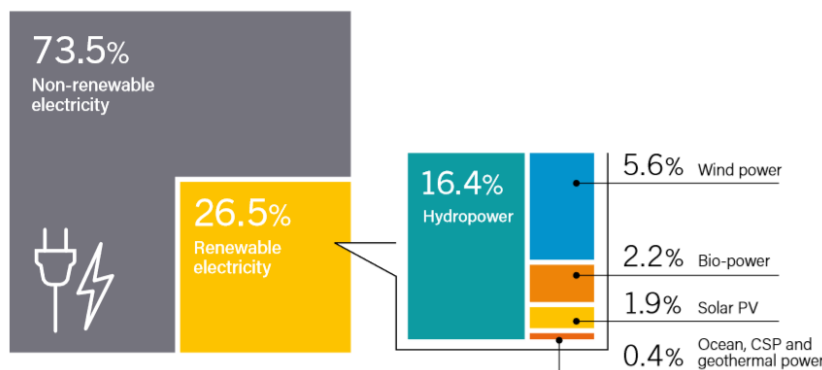
Figure 1.1. Estimated global electricity production from renewable energies, (End-2017) [2].

Fossil fuel energies are the essential energy sources for the past decades and it is inexpensive to extract, stable energy sources, easy to store and it can be easily transferred from one place to another place [3]. While burning the fossil fuel, it releases gases (Figure 2) of nitrous oxide (N_2O), methane (CH_4), carbon dioxide (CO_2) and a trace of fluorinated gases (RF-gases) into the air, which causes air pollution and it has many negative effects on the environment [3]. Among the different gases, CO_2 plays a major role in the greenhouse effects, by absorbing and transmitting the thermal radiation, which is responsible for global warming effects [4].
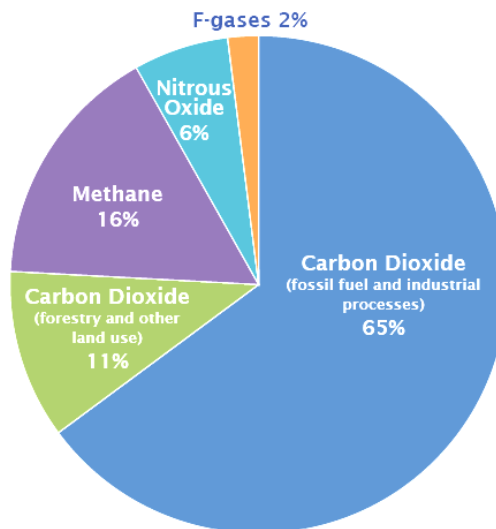
Figure 1.2. Global greenhouse gas emission by gases based on 2010 data [5].

Increasing the global energy demand and awareness of environmental effect lead to looking for alternative energy sources. Accordingly, renewable energy sources are the ones that are able to fulfill the energy requirements without contributing to climate change or global warming effects. The third law of thermodynamics state that the entropy of an isolated system will be constant if the temperature is absolute zero value. Again, if we consider universal is an isolated system by reducing greenhouse gases the temperature of the system will be reduced, which will result in the regulation of the climate changes. As an alternative to fossil fuels, different types of renewable and sustainable energy technologies are globally used to generate electricity such as geothermal, biomass, hydropower, wind and solar power. In the last years, the renewable energy showed rapid growth compared to non-renewable sources that will result in the production of 25% of global energy demands in the close future [1]. Figure 1.3 shows the expected growing trend of the world net electricity production from different types of renewable energy sources where a very promising scenario is expected for solar energy power.
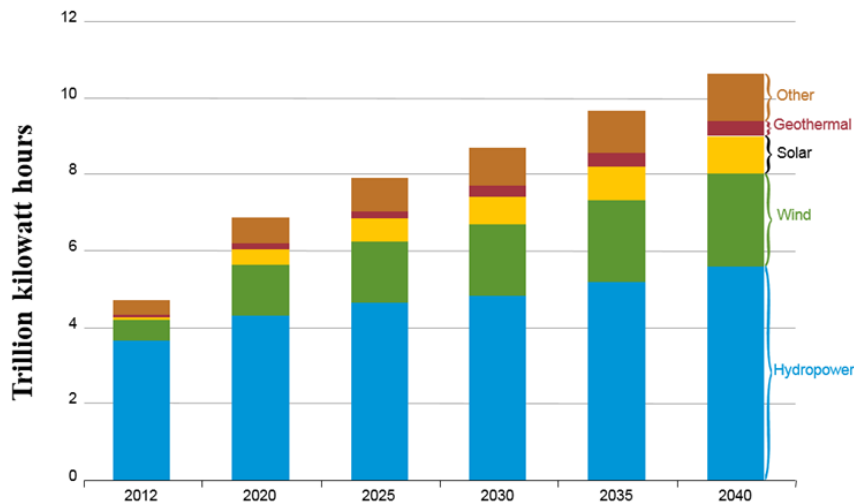
Figure 1.3. Projection of world net electricity from different types of renewable energy sources from 2012-2040 [6].

Within this scenario, renewable energy-based solar power showed a fast-growing trend of 8.3% per year [6]. Solar power is used to produce electrical energy by the direct or indirect process via solar radiation. Solar power is reliable, abundant in nature, sustainable and clean energy, which is utilized for producing a different form of energy by a different mechanism. The prediction says that the annual potential of solar energy is around 1575 EJ, which is much higher than the world primary energy required per year (573 EJ) [7]. Among the solar energy technologies, the direct photovoltaic (PV) conversion system and indirect concentrated solar power (CSP) technology are the most commercially used ones for the production of electricity.

1.3. Photovoltaic (PV) system

Photovoltaic systems are working based on the conversion of light (photon) into electricity by using semiconducting materials via the photovoltaic effect (Figure 1.4). The photovoltaic effect is discovered by Alexandre-Edmond Becquerel in 1839 and which is used in the solar cell to produce electricity. In the photovoltaic conversions process, most of the visible to Ultraviolet (UV) regions were used to produce the electricity via a light absorbing material. The silicon technology is the dominant one of PV solar cells where combinations of multi-crystalline silicon and monocrystalline silicon materials have been optimized to improve the efficiency but also to reduce production costs, hence make it more feasible for various applications. In this type of solar cell technology, n-type and p-type silicon semiconductors are

joined together called p-n junction, which creates the internal electric field [8]. The p-type silicon donates the electron and receives hole, while n-type silicon accepts the electron. When the solar radiation incident on the cell, the photon excites some of the atoms in the semiconducting materials and which creates the electron-hole pairs. Simultaneously, due to the internal electric field, the pairs tend to separate, results in an electron move to the negative electrode and hole move towards the positive electrode. Finally, the electric current extract from the circuit and supply to the grid [9]. The big advantages of the photovoltaic devices are the little required maintenance and lower costs; while their biggest limitation is the non-dispatchability of their produced electricity which requires a high extra cost for the incorporation of energy storage devices.
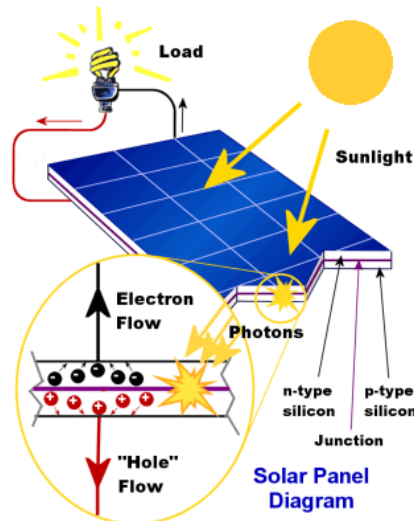
Figure 1.4. Photovoltaic conversion process [10].

1.4. Concentrated solar power (CSP) technology

The CSP technology is functioned by concentrating a large area of the sunlight at a specific point by using heliostats (mirrors) which help to achieve high temperature working fluids. Then this high temperature of the fluid is used to produce electricity through it continues thermal cyclic process. The CSP has a major advantage of dispatchability to produce the electricity compared to all other renewable energy technologies. Also, the CSP technology compared to PV has the possibility to store the intermittence solar radiation that later to be used to produce stable output power [11]. The CSP systems are classified according to the position of the receiver whether it is fixed or mobile, tracking system, the shape of the mirror and operating temperature of the system [12].

The different types of CSP technology are: i) Parabolic trough collectors (PTC), ii) Linear Fresnel reflectors (LFR), iii) Solar power tower (SPT) and iv) Parabolic dish collectors (PDC). The position of the receiver is fixed in power tower and linear Fresnel systems but which is movable in the parabolic trough and parabolic dish systems. The Parabolic trough collectors and Linear Fresnel reflectors are called a line focusing system because the mirrors are focusing the solar radiation along one axis. Solar power tower and parabolic dish collectors are called a point focus system, where the mirror focuses the solar radiation along two axes [13]. The point focusing system is achieving higher efficiency compared to line focusing system. The parabolic trough and tower power plant systems count with different advantages such as the cost-effective, wide operational experience and maturity of the technology [14].

1.4.1. Parabolic trough collectors (PTC)

In the parabolic trough collectors, solar radiation is concentrated by a parabolic curve trough-shaped reflector, which directs the sunlight towards absorber pipe (tube) positioned in the focal line of the parabola (Figure 1.5). The heat transfer fluid (HTF) flows through the pipe and temperature is raised up to 400°C. The maximum working temperature of the current system is limited by the decomposition temperature of the HTF involved in the process, i.e. thermal oil. The reflecting mirror and absorbing tubes are oriented towards the north to south direction to ensure the maximum absorbance of sun radiation. In parabolic trough system, a group of parallelly connected reflecting mirrors are called as a solar field and absorbing tubes are called as a heat collector. Then the heat transfer fluid is transferred through the central receiver tubes to increase the temperature of power block working fluid, i.e. steam, to rotate the turbine to produce the electricity.
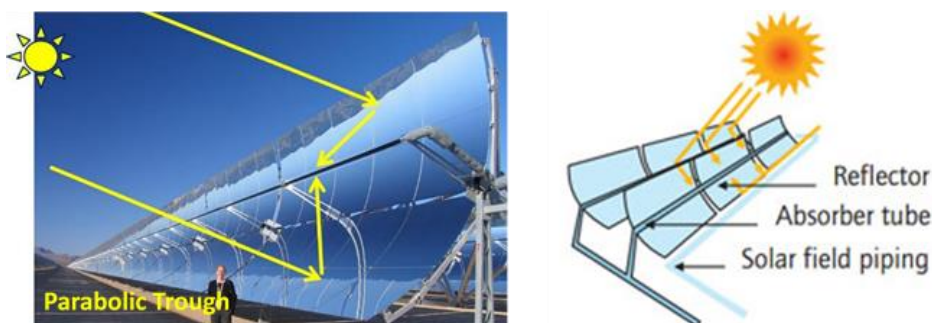
Figure 1.5. Parabolic trough collectors system [15, 16].

1.4.2. Solar power tower (SPT)

Solar power tower or central receiver system consists of the combination of many large sun tracking and reflecting mirrors are called heliostats (Figure 1.6). In heliostats, the flat mirrors are used to track the sun at two axes. The heliostat use to concentrates the solar power and reflects towards the central receiver, which is placed on the top of a fixed tower. The HTF increases its temperature, by circulating through the central receiver, up to its decomposition temperature of 565°C, i.e. the decomposition temperature of molten Solar salt used in most cases. The SPT system is able to increase the size of the solar field to achieve higher temperatures that help to increase the thermodynamic efficiency of the system [17].
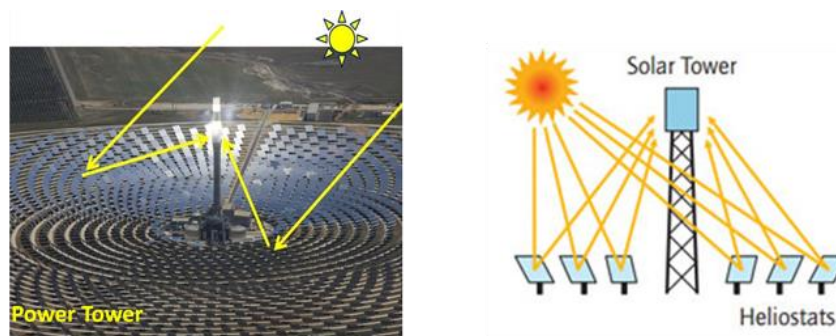
Figure 1.6. Solar power tower system [15, 16].

1.4.3. Linear Fresnel reflectors (LFR):

In the linear Fresnel reflector, a large number of flat or slightly curve shaped mirrors are used to reflect the solar radiation along the pipe, which is fixed above the parallel collectors (Figure 1.7). Linear Fresnel reflector system is operating at a lower temperature compared to other systems where the maximum temperature is around 300°C. The difference of LFR from the PTC system is the mirrors because it rotates individually while focusing the solar radiation at the top of the fixed absorbed collector. The mirrors are aligned towards the north-south orientation to gain maximum annual power collection efficiency. The main advantage of LFR is the flexible mirror and it is separately fixed below the absorber tube, so this simple design was reducing the investment cost. This system has the facility of direct steam production, so it eliminates the need for heat transfer fluids and heat exchanger. LFS has lower efficiency compared to PTC and SPT due to the solar radiation loss in the absorber tube. This solar radiation loss is due to the focal line distorted by astigmatism, where, secondary mirrors are necessary to refocus the increase the system efficiency [18]. The main limitation of the LFR system is the high cost of its

storage system to store the steam, which is produced in the solar field, or to transfer the heat to other storage media.
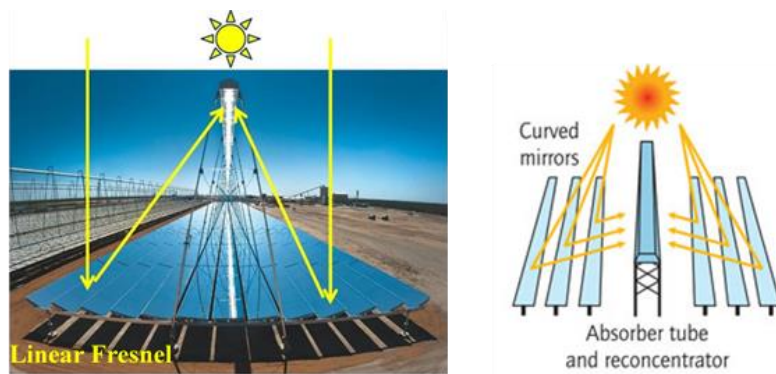
Figure 1.7. Linear Fresnel reflector [15, 16].

1.4.4. Parabolic dish collectors (PDC)

Parabolic dish collectors (PDC) system consists of a parabolic-dish shaped mirror that reflects the solar radiation at a focal point where the receivers are located (Figure 1.8). PDC has the highest optical concentration, which provides the highest optical and thermal efficiency of the system. Parabolic dish collectors are operating in the temperature range between 120-1500°C, which is higher than all other CSP technologies. The absorbed heat is directly used by a heat engine which is mounted on the receiver [19]. The PDC is moving in two-axis to track the sun in order to achieve maximum efficiency. Potentially, the PDS system has the highest efficiency compared to all other CSP techniques and Sandia National energy lab demonstrated the 31.5% efficiency of solar energy to grid conversion [18]. The parabolic dish collecting system is high cost and the thermal energy storage (TES) system has low feasibility for the commercial application. The Stirling and Brayton cycle engines are currently used for power conversion in the PDC system [19].
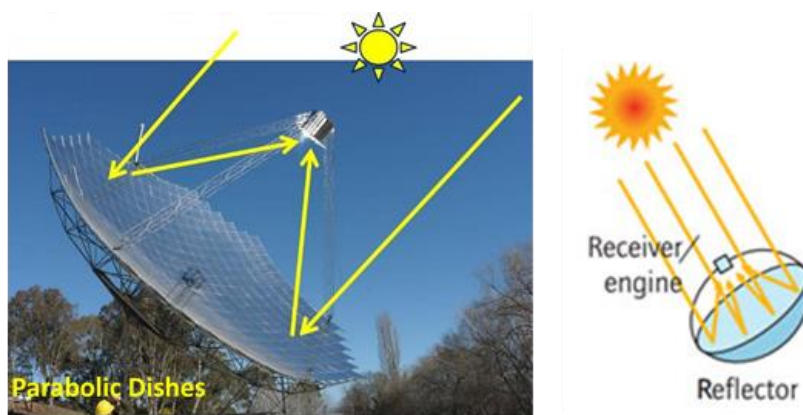
Figure 1.8. Parabolic dish collectors [15, 16].

1.5. Thermal energy storage (TES)

As explained above, one of the main advantages of CSP technology is its cost-effective energy storage concept, unlike wind or PV technologies, based on direct heat storage in the thermal energy storage (TES) system. In TES process, the heat energy is transferred to the storage medium which can be used later to produce the electricity. TES system is economically feasible and easy to scale up to large storage systems. TES system reduces the mismatch between the demand and energy supply, balance the fluctuation of the temperature and increases the efficiency of the CSP plants. The TES system is also used in some industries to store the industrial waste heat that nowadays in most cases it is simply dissipated to the environment, which is dramatically increasing the global warming effect. So, the TES system provides environmental and economic benefits by saving the industrial waste heat to be used in the same industrial process that helps to reduce the combustion of fossil fuels and the electricity demand.

In general, TES can be based on thermochemical energy storage (TcES) by reversible chemical reaction, latent heat storage (LHS) using phase change materials and sensible heat storage (SHS) using solid or liquid materials [13].

1.5.1. Thermochemical heat storage (TcES)

Thermochemical energy storage stores the energy by means of reversible reactions where the heat is stored during the endothermic reaction and is released during the reverse reaction, i.e. exothermic reaction [20]. The heat energy stored/released is directly proportional to the mass of the reactive material and reaction enthalpy according to the following equation (eq. 1):

$$Q = m \cdot \Delta H_{reaction} \qquad \text{(eq. 1)}$$

Where, m is the mass of the storage material (kg) and $\Delta H_{reaction}$ is the reaction enthalpy (kJ. Kg^{-1}).

The energy storage density in thermochemical energy storage is higher than in sensible heat and latent heat storages. In addition, the TcES has the advantage of a long storage period due to the possibility of storing the reactant material at room temperature [21]. Despite that, due to the complexity of the thermochemical storage system, the development of this technology is still at the laboratory scale.

1.5.2. Latent heat storage (LHS)

In the Latent heat storage process, heat energy is stored during the phase change of storage materials at a constant temperature. The energy stored/produced by LHS is directly proportional to phase change enthalpy of the storage material, where a larger amount of heat can be stored compared to the sensible heat storage process. Therefore, the heat energy is stored during the increase of the temperature and dissipated during the decrease of the temperature. The amount of the stored heat is directly proportional to the mass and enthalpy of the phase transformation according to the following equation (eq. 2):

$$\mathbf{Q = m \cdot \Delta H}_{latent} \qquad \text{(eq. 2)}$$

Where, m is the mass of the storage material (kg) and ΔH_{latent} is enthalpy of phase transformation (kJ. Kg^{-1})

The phase change materials (PCMs) are classified as organic, inorganic and metallic, where the organic PCMs adapted for low-temperature application but are considered relatively expensive and flammable; while the inorganic and metallic PCMs have large latent heat and commonly used for high-temperature applications [20]. The phase change temperature of the latent heat storage material is denoted in the decreasing orders: solid-solid > solid-liquid > liquid-gas phase change. In general, the solid-solid phase change has very low latent heat and the liquid-gas phase change has the highest latent heat but a huge volume change during the phase transformation which makes difficult to develop at commercial application [7]. The most commonly used phase change process for energy storage is solid-liquid phase transformation due to the combination of its good latent heat and the feasibility for its development for commercial systems.

1.5.3. Sensible heat storage (SHS)

The sensible heat storage system is the most mature technology for thermal energy storage applications due to their easy heat transfer and storage principle. Accordingly, the SHS system stores the heat energy while increasing the temperature and release the heat energy by decreasing the temperature. The amount of the stored heat is directly proportional to the mass, heat capacity and working temperature of the storage materials, according to the following equation (eq. 3):

$$\mathbf{Q = m \cdot C_p \cdot \Delta T} \qquad \text{(eq. 3)}$$

Where, m is the mass (kg), C_p is the specific heat capacity (kJ kg^{-1} K^{-1}) and ΔT is the working temperature range during the charging and discharging processes of storage material.

The materials have been used for SHS purpose must have high specific heat capacity, which leads to increase the overall efficiency and reduces the size of the storage tank and thus results in the reduction of the total investment cost. The sensible heat storage materials can be in solid form such as ceramic materials or in liquid form such as molten salt. Nowadays, the molten salt-based TES system is more matured in terms of commercial technology and it is installed in all commercial CSP plants with the storage system. The advantages for the use of molten salt material in a two-tank configuration are the high thermodynamic efficiency, low thermal losses, low vapor pressure, non-flammability behaviour and plays a major aspect in the economic and environmentally friendly approach.

The most commonly studied molten salts for TES purpose are Solar salt, ($NaNO_3$-KNO_3 with 60:40 wt.%), Hitec ($NaNO_3$-KNO_3-$NaNO_2$ with 7:53:40 wt.%) and HitecXL ($NaNO_3$-KNO_3-$Ca(NO_3)_2$ with 7:45:48 wt.%). The melting temperatures of the Solar salt, Hitec and HitecXL are 223°C, 142°C and 120°C, respectively [22]. Since Hitec and HitecXL have low melting points, but they also have lower decomposition temperatures compared to Solar salt. The decomposition temperatures of Hitec, HitecXL and Solar salt are 454°C, 500°C and 565°C, respectively [12]. However, among the studied salts, the binary nitrate salt ($NaNO_3$-KNO_3) counts with the operating temperature range and thermodynamic properties that are most suitable for the current CSP technology.

Solar salt is broadly studied by different researches and used in commercial CSP plants. The melting temperatures of $NaNO_3$ and KNO_3 are 307°C and 334°C, respectively; while their binary eutectic mixture ($NaNO_3$-KNO_3 with 51:49 wt.%) has a lower melting temperature of 222°C [7]. For the commercial purpose, 60 wt.% of $NaNO_3$ and 40 wt.% of KNO_3 was used to reduce the cost of the energy storage material due to the lower price of $NaNO_3$ compared to KNO_3.

As it is mentioned above, the storage material plays an important role because its energy storage capacity/density and thermal conductivity determine the storage material amount and the energy transfer efficiency thus result are important to define the storage tank size and heat exchanger design. However, for further reduction of the CSP costs, the efficiency of the whole system can be improved by the

enhancement of the thermophysical properties of the storage material such as the specific heat capacity, thermal conductivity and operating temperature range.

In the last years, the enhancement of thermophysical properties of the molten has been targeted by the scientific community by adding a minor concentration of nanoparticles to the base salt commonly known as nanofluid. This approach was firstly proposed by Maxwell in 1873 to increase the thermophysical properties of aqueous fluids. In 1902, Maxwell proposed the enhancement of the thermal conductivity of aqueous fluids by dispersing solid particles having micro or millimeter size. Two different shaped TiO_2 (spherical and rod shape) nanoparticles were dispersed in DI water to investigate their effects of changing concentration from 0.5 to 5 volume fraction (vol.%) on the thermal conductivity. From the analysis, 5 vol.% of TiO_2 suspended in DI water shows an enhancement of thermal conductivity by 30% for TiO_2 spheres (15 nm) and 33% for TiO_2 nanorods (10 nm * 40 nm) [23]. Furthermore, nanofluids based on DI water, ethylene glycol and oil with different types of nanoparticles have been developed and the clear enhancements of the thermal conductivity were observed [24]. Also, the colloidal dispersion stability of those nanofluids has been improved by using some nanoparticles surfactant stabilizers that can be operated at low operating temperature range (below 150ºC). It is already reported that the thermal conductivity of ionic liquid was increased by the addition of different types of nanoparticles such as Al_2O_3, Au, CuO, Fe_2O_3, stacked graphene nanofiber, MWCNTs, SWCNTs, SiO_2, ZnO [25, 26]. Since the molten inorganic salts have a higher operating temperature range (above 150ºC), it is a very challenging task to prepare well-dispersed molten salt-based nanofluids.

1.6. Molten salt based nanofluids

1.6.1. Preparation of molten salt-based nanofluids.

The preparation method has a major influence to get homogeneously dispersed nanofluids with the maximum enhancement of the thermophysical properties and reproducible results. However, different preparation methods have been used in literature such as the most common two-step wet method, in-situ formation, ball mill method and high-temperature dispersion method.

1.6.1.1. Two-step wet methods

The nanofluids are commonly prepared through a two-step wet method. The most common preparation protocol is shown in Figure 1.9 and it consists of the following steps:

1. Initially, 1 wt% of nanoparticles was added in the DI water and sonicated for at least 60 minutes to break the agglomeration of the nanoparticles.

2. Then, dissolving the 99 wt% of molten salt into the above dispersed nanoparticles solution and sonicated again for at least 60 minutes. Different levels of sonication energy were used to optimize the homogeneity of the nanofluids.

3. After sonication, different evaporation speeds were tested aiming to investigate the quick and slow evaporation steps on the final state of the dispersion of nanoparticles within the nanofluid.
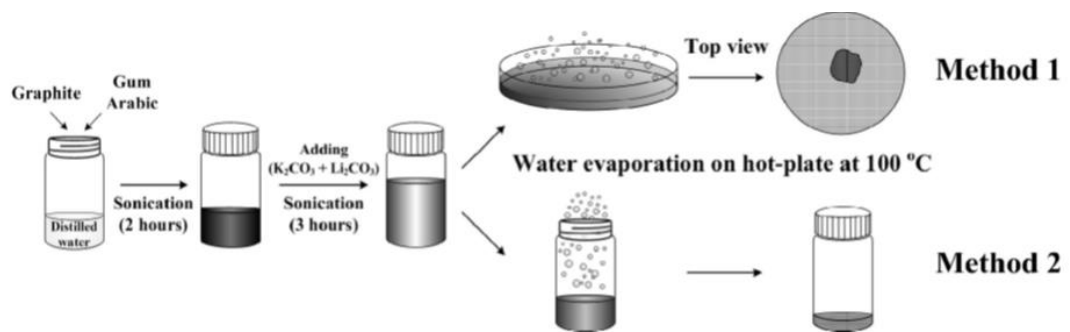
Figure 1.9. Schematic diagram for the preparation of molten salt-based nanofluid by wet methods [27].

1.6.1.2. In-situ method for nanofluid preparation

In the *in-situ* preparation method, the nanoparticles precursor was directly seeded inside the molten salt, instead of dispersing them by the wet method, aiming to avoid the initial agglomeration state of the nanoparticles. As an example, titanium (IV) oxysulphate (TiOSO$_4$) precursor has been used to obtain TiO$_2$ and Solar slat based nanofluid as shown in Figure 1.10 [28]. The appropriate amount of TiOSO$_4$ precursor and molten salt were added together, then grinded for 15 minutes in a pestle and mortar. Once it is well grinded, the mixture was transferred into the alumina crucible and kept at 450°C for 30 minutes.
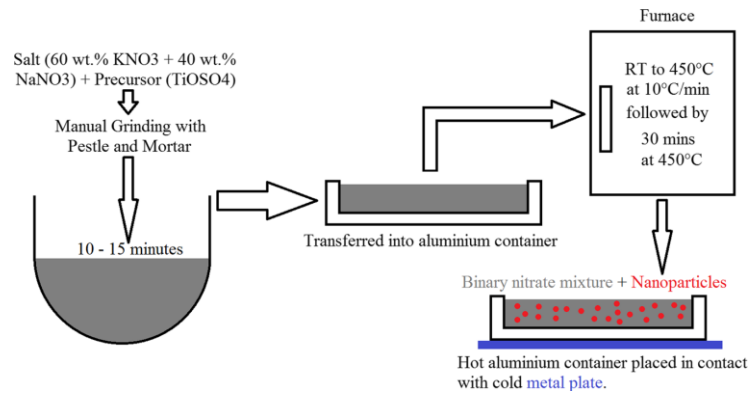
Figure 1.10. *In-situ* method for the preparation of molten salt-based nanofluids [28].

1.6.1.3. Physical Ball-Mill dry method

The present method is simple compared to the wet method and has several advantages such as shorter preparation time and one-step process, which help to reduce the risk for the agglomeration of nanoparticles [29]. Initially, the nanoparticles are dispersed within the salt by means of ball milling using stainless steel balls to break the agglomeration of nanoparticles (Figure 1.11). In this method, several factors need to be optimized like the size of the balls, amount the materials and time of physical shaking to obtain a homogeneous dispersion. Unfortunately, under the conditions used in that work, the final goal was not achieved where nanoparticles agglomerates and pure salt zones were distinguished by SEM and EDX analyses. Also, the authors concluded that the stainless steel balls may affect the size and shape of the added nanoparticles.
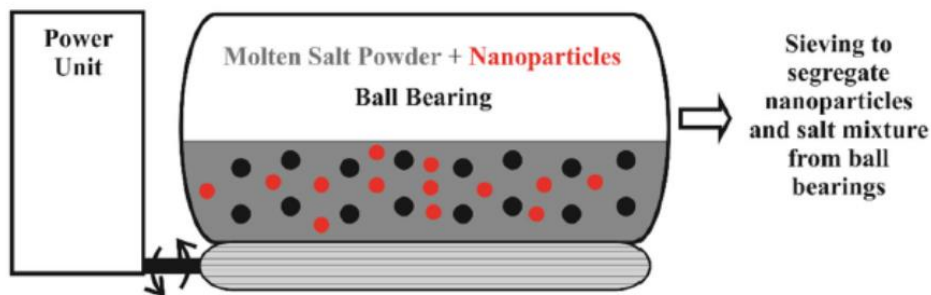
Figure 1.11. Physical Ball-Mill method for nanofluid preparation [28].

1.6.1.4. High-temperature twin-screw micro-compounder method

The twin-screw micro-compounder method follows a new protocol to prepare the nanofluid by direct dispersion of nanoparticles into the molten salt at high temperature (300°C) [30]. This new component consists of the twin-screw extruder with the addition of the recirculating channel (Figure 1.12). The recirculating

channels were used to recycle the nanofluids during the mixing phase, which improves the dispersion of nanoparticles in the base fluids. The twin screws are used to well mixing of nanoparticle in the base fluids at 300ºC.
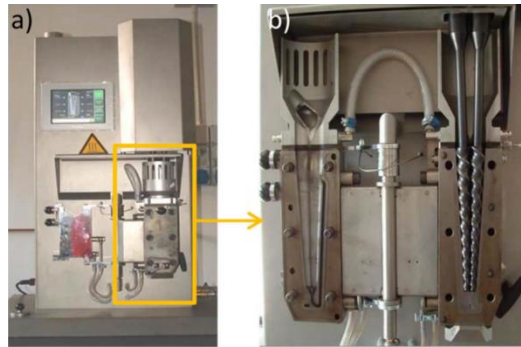
Figure 1.12. a) Twin-screw micro-compounder and b) Incorporated recirculating channel and twin screws [30].

1.6.1.5. High-temperature probe sonication method

Initially, the salts were melted in the furnace and nanoparticles are separately dispersed in acetone using ultrasonication for 30 minutes. Then this dispersed nanoparticle solution was injected into molten salt and acetone was evaporated ~ 30 seconds by left the nanoparticles in the molten salt. After that, the nanoparticles added molten salts were sonicated for 5 minutes by probe sonication while it is in the molten state. Figure 1.13 shows the home-made furnace equipped with an ultrasonicate probe for the dispersion process of the nanoparticles at high temperature [31].
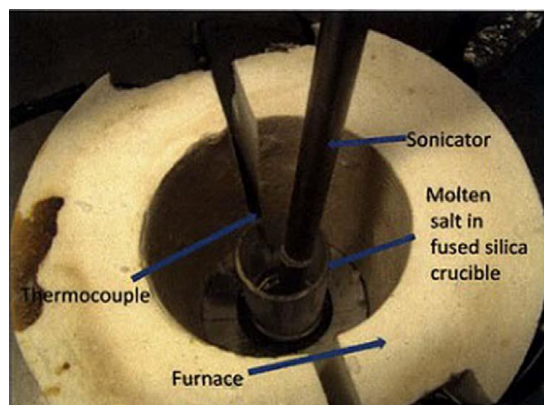
Figure 1.13. Home-made ultrasonicate furnace for the nanofluid preparation [31].

1.6.2. Thermophysical properties of molten salt-based nanofluids

1.6.2.1. Specific heat capacity of molten salt-based nanofluids

The primary aim of the development of molten slat nanofluids is to increase the specific heat capacity aiming to decrease the amount of storage material needed

to store a given amount of energy and consequently to reduce the size of the storage tank. Accordingly, the C_p enhancement of the molten salt nanofluid was studied enormously, but the reported results in literature show a big discrepancy including their theoretical predictions due to the mechanisms of the enhancement are still unknown yet. The most commonly proposed mechanism for the enhancement of C_p for molten salt (ionic liquid) is the interaction between the salt and nanoparticles which is proportional to the specific surface area of the nanoparticles. However, since the results of the theoretical prediction of ionic liquid-based nanofluids were not correlated with the experimental results, therefore several new mechanisms have been proposed in [32, 33] as the following:

Specific heat capacity of the nanoparticles From the theoretical prediction, the specific heat capacity of nanoparticles increases while decreasing the size of nanoparticles due to the high surface area, so the nanoparticles having high C_p compared to their bulk material. In the case of NPs, the atom placed in the surface of the NPs is less confined, so the low frequency with high amplitude of surface atoms leads to the high surface energy of the NPs [32].
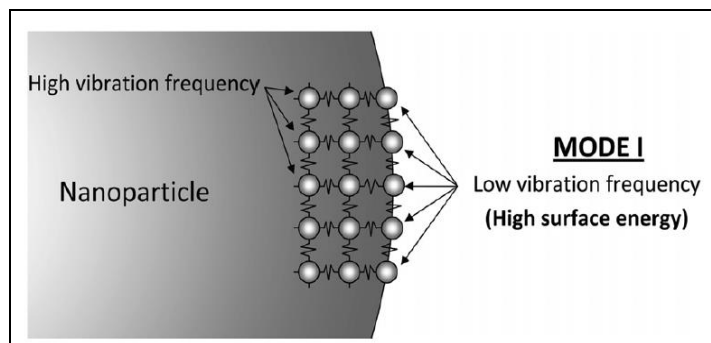
Figure 1.14. Specific heat capacity model-I

Solid-fluid interaction energy High surface area of the nanomaterial extremely increase the interfacial thermal resistance between the nanoparticles and its surrounding molten salt, but this effect is negligible in macroscale level. High interfacial thermal resistance (call it as Kapitza resistance) help to store the additional heat energy due to the interaction of vibration energy between the nanoparticle atoms and their interfacial molecules, simultaneously C_p of the nanofluids was increased [32].
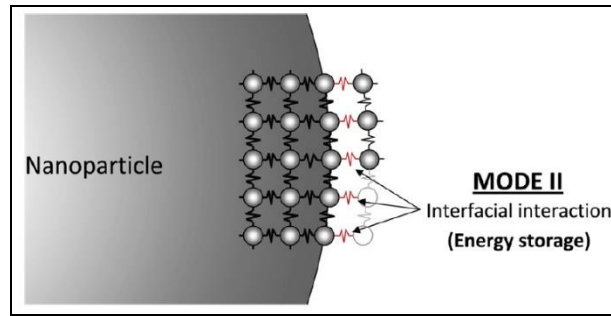
Figure 1.15. Specific heat capacity model-II

Semi-solid layer formation by layering effect Liquid molecules of molten salts adhering the surface of nanoparticles and forming the 'semi-solid' liquid layer. This thickness of the molten salts adhering layer is depending on the surface energy of the nanoparticle. Finally, this semi-solid layer formation has high thermal properties compared to their bulk liquid of molten salt which leads to an increase in the C_p of nanofluids [32].
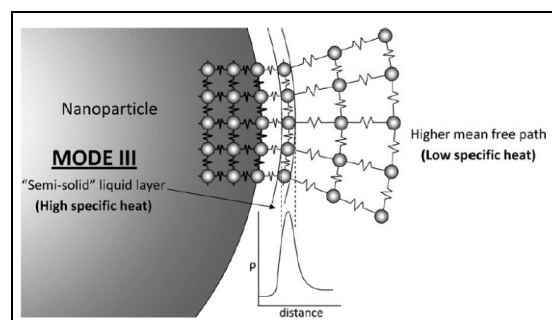
Figure 1.16. Specific heat capacity model-III

The ionic exchange capacity of nanoadsorbents The present mechanism is based on the ionic exchange capacity between the nitrate salts (Na, K, and Li nitrates) with metal oxides (alumina and silica) which are studied by using FTIR spectroscopy techniques. The ionic exchange capacity of the nanoadsorbents and specific heat capacity of the molten salt-based nanofluid is depending on the surface area of the nanoparticles and interaction between the salt and nanoparticles. While increasing the concentrations of the nanoparticles, the active sites were reduced due to the agglomeration of nanoparticles. The nanoparticles have a lower size with higher surface area provides higher ionic exchange capacity. The protonation by HCl is increasing the ionic exchange capacity due to the additional exchangeable H^+ on the surface of the nanoparticles. From the results, they observed that the adsorption of the nitrate anions on the surface of the nanoparticles which lead to increasing the specific heat capacity of the nanoparticles and this increase is depending on the effect

of the ionic exchange process. The interfacial structure of ordered ion provides the interaction between the salt and nanoparticles, which helps to functionalize the nanoparticles and simultaneously enhance the specific heat capacity of the nanofluids [33].
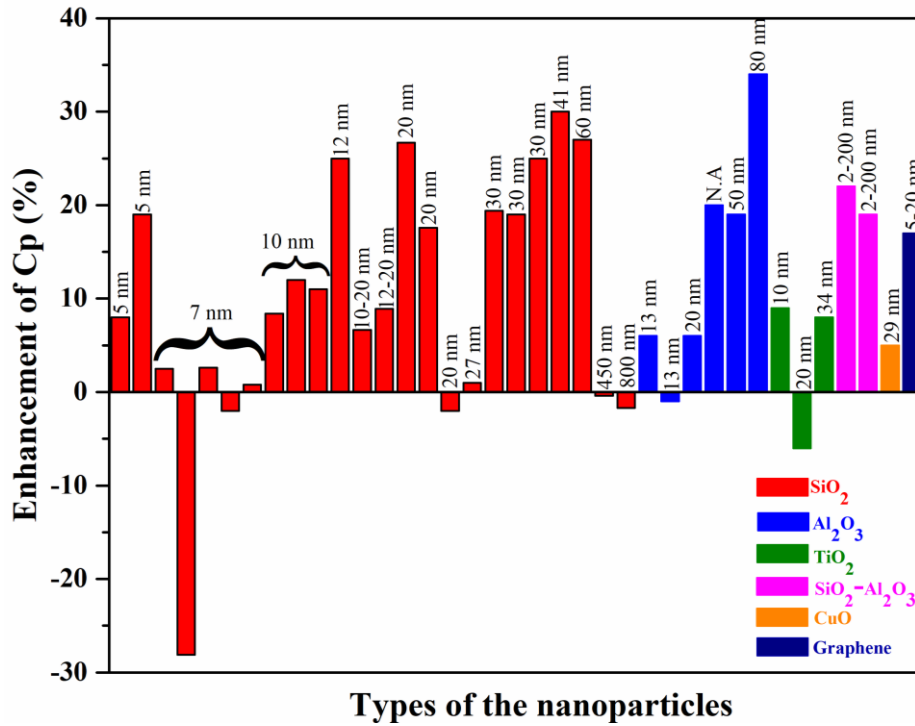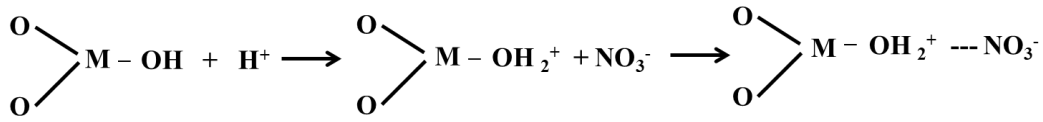
Figure 1.17. C_p of the solar salt with 1 wt% NPs (SiO$_2$, Al$_2$O$_3$, TiO$_2$, Al$_2$O$_3$- SiO$_2$, CuO and graphene) [29, 36-47]

Table 1.1. Specific heat capacity of Solar salt based nanofluids.

NPs	Size (nm)	Cc. (wt%)	T(ºC)	C_p enhanc. (%)	Ref.
Al$_2$O$_3$	13	0.9, 2.7, 4.6 vol%	320	-3, -8, -13	[34]
	90	0.9, 2.7, 4.6 vol%	320	-1 -6, -8	[34]
	40	0.78	350	30	[35]
	n.a.*	1	350	20	[36]
	50	1	SP, LP*	11, 19	[37]
	13	0.5, 1, 1.5	SP	-5, 20, -3	[38]
	13	0.5, 1, 1.5	LP	-8, 6, -3	[38]

	20	0.5, 1, 1.5, 2	LP	2, 6, 7, 8	[39]
	80	1	LP	34	[40]
	13	1	SP, LP	22, -1	[41]
SiO$_2$	7	0.5, 1, 1.5	SP	-16, 15, 2	[38]
	7	0.5, 1, 1.5	LP	-19, 0.8, -1	[38]
	NA	1	350	19	[36]
	10	1	SP, LP	11, 11	[37]
	10	2	SP, LP	18, 23	[37]
	40	1	LP	30	[40]
	7	1	SP, LP	30, -2	[41]
	20	1	250-350	18	[42]
	10-20	0.5, 1	30-50	-2, -0.5	[43]
	10-20	0.5, 1	300-500	5, 7	[43]
	5, 10, 30, 60	1	LP	8, 12, 19, 27	[44]
	12	0.5, 1, 1.5, 2	250-420	3, 25, 2, 4	[45]
	10, 20, 30	1	260-400	8, 27, 19	[46]
TiO$_2$	10	1	SP, LP	8, 9	[37]
	10	2	SP, LP	18, 24	[37]
	20	0.5, 1, 1.5	SP	-14, -6, -11	[38]
	20	0.5, 1, 1.5	LP	-16, -6, -12	[38]
	34	0.1, 0.5, 1, 1.5	440	10, 9, 8, 2	[29]
SiO$_2$-Al$_2$O$_3$	2-200	0.5, 1, 1.5	SP	-2, 58, 35	[38]
	2-200	0.5, 1, 1.5	LP	-7, 22, 1	[38]
	2-200	1	SP, LP	52, 19	[41]
CuO	29	0.1, 0.5, 1, 1.5	440	2, 5, 5, 5	[29]
Graphene	5-20 nm x 10-20 µm	0.1, 0.5, 1, 1.5, 2, 2.5	250-450	-16, 18, 1	[47]

*n.a., SP and LP stand for not available, solid phase and liquid phase, respectively.

1.6.2.2. Thermal conductivity of the molten salt nanofluids

The increase of the thermal conductivity of the molten salt will result in simplification of the heat exchanger designs and consequently will give a positive effect on the investment costs of the CSP plants. In literature, the enhancement of heat capacity has attracted the attention of the scientific community; while very few works were investigated the effect of adding nanoparticles on the thermal conductivity of molten salt nanofluids. Table 1.2 summarized the observed changes in the thermal conductivity of molten salt nanofluids by adding different types of nanoparticles, where negative and positive effects were obtained. The mechanism responsible for the enhancement of the effective thermal conductivity is the localized convention of the nanoparticle by the effect of Brownian motion. Maxwell-Garnett conduction model says that the convection caused by the Brownian motion of the nanoparticle decreases while increasing the particle size [48]. According to the model, the NPs have high convection when are lighter or having a lower size, which is observed in the water, ethylene glycol and oil-based nanofluids regardless of the thermal conductivity of the nanoparticles [48]. In addition, some deviation in the thermal conductivity values may be due to the percolation network structure formation by the nanoparticles due to their agglomeration. However, the discrepancy of the reported results may be due to the partial agglomeration of the nanoparticles (percolation network); while, the negative effect may be obtained due to the settle down of the nanoparticles (interfacial resistance effect).

Table 1.2. Thermal conductivity of Solar salt based nanofluids.

NPs	Size (nm)	Cc. (wt%)	T($^{\circ}$C)	λ enhanc. (%)	Ref.
Al$_2$O$_3$	40-60	1	300-500	20 to 25	[49]
	n.a.*	0.09, 0.17, 0.30	150	-25,-13, -28	[37]
	n.a.*	0.53, 0.78, 1.19	150	-25,-15, -25	[37]
	L=50 nm, D=10	0.5, 1, 1.5	396	20, 34, 67	[50]
SiO$_2$	7	0.5, 1, 1.5	396	-18, 45, 16	[50]
MWCNTs	L= 3-15 µm D=12-15 nm	0.3, 0.4	300	293, 90	[51]
MgO	1-2 µm	10 vol.	250-400	39	[52]
Fe$_2$O$_3$	20-40	0.5	450	60	[53]

*n.a, L and D stand for not available, length and diameter, respectively.

1.6.2.3. The viscosity of the molten salt-based nanofluids

The rheological properties of the molten salt-based nanofluid are very important parameter together with the heat capacity and thermal conductivity to determine the final efficiency of the TES system because increasing the viscosity will increase the pumping power. Furthermore, the viscosity of the nanofluid has an impact on the convective heat transfer coefficient which must also be considered. The viscosity of the water-based nanofluid is extensively investigated, while the viscosity of molten salt-based nanofluids has attracted less attention which may due to the complexity to determine this property at high temperature. The viscosity of the nanofluids depends on several factors such as temperature, the volume fraction of NPs, agglomeration of the NPs, shape of the NPs, size of the NPs, type of the base fluids and stability of the nanofluids. Mainly the agglomerations of the nanoparticles increase the viscosity enormously. Commonly the molten salt-based nanofluids show the Newtonian behaviour by means of constant viscosity with an increase of shear rates. The following Table 1.3 show overview of the viscosity results of the molten salt-based nanofluids that are obtained from the literature. Similar to specific heat and thermal conductivity results, different effects have been obtained varying from small decrease (-34%) to a big increase of viscosity (1130%) depend on the nature, shape, size, agglomeration and concentration of nanoparticles.

Table 1.3. Viscosity of Solar salt based nanofluids

NPs	Size (nm)	Cc. (wt%)	T(ºC)	η incr (%)	Ref.
Al$_2$O$_3$	(L=50, D=10)	1.5	300-400	-15, 0.63	[54]
	40-80	1, 2	250-500	-9, 68	[55]
SiO$_2$	10-20	0.5, 1	250-500	2.4 to 106, 101 to 189	[43]
	7	1.5	300-400	3.5, 22	[54]
Graphene	n.a.	2	250-500	3 to 248	[55]
CuO	29	0.1	250-500	5 to 18%	[56]

*n.a. stands for not available

1.7. Corrosion effect of the molten salt-based nanofluids

Molten salts have several advantages like high operating temperature, efficiency and even commercialized for different industrial applications. Although, it

is highly corrosive in nature, which reduces the lifetime of storage system components. There are several works that have been investigated the corrosion effect of the molten salts; while, only a few works studied the corrosivity of molten salt nanofluids and their corrosion inhibition mechanisms. The corrosion is defined as physical-chemical interaction between the surface of the container material and its environment, which affects the real properties of the container material by means of introducing impurities and modifying its superficial composition. The corrosion effect of the aqueous alumina nanofluids was studied with copper, alumina and stainless steel (SS) materials, among them copper shows the highest corrosion while stainless steel shows lower corrosion effects in the environmental condition [57]. The electrochemical study shows the prevention of carbon steel (CS) from the corrosion influence by functionalized with multi-walled carbon nanotubes (MWCNT) [58]. The corrosion and erosion study was based on the low carbon steel were performed in seawater by using nano-size and micro-size alumina materials. This report was also indicating that the presence of the Al_2O_3 particle acts as a corrosion inhibitor for a certain time period, but after a particular time, the corrosion-erosion was higher in the presences of Al_2O_3 particles compared to the base fluids [59]. The corrosion behaviour of Incoloy 800 H and stainless steel AISI 310 was performed in 34.42 wt% NaCl – 55.47 wt% KCl in a nitrogen atmosphere at 700°C and from the study Incoloy 800 H show ~2500 μm/yr while stainless steel AISI 310 show 4500 μm/yr [60]. So take into account of all these parameters, the corrosion behaviour was already studied with different kinds of storage materials like stainless steel 316L which contains Fe-Cr, Incoloy 800HT has Ni–Fe, Inconel based Ni-Cr and CS has the major composition Fe-C [61]. Based on the alloy composition, the corrosive resistances withstand even at high temperature and the heat energy can be able to store at high temperature to maximize the efficiency of the system. For example, the inorganic salt reacts with the metal iron (Fe) and it converts the Fe into different oxidation states of iron like Fe^{2+} and Fe^{3+}. Generally, the presence of chlorine in the salt as an impurity leads to provoking the corrosion reaction [62]. The molten nitrate salts were studied at 600ºC in contact with stainless steel 316 and stainless steel 347H, the results show the descaling of metal oxide layer (corrosion layer) where 4.4 μm was observed for SS316 and ~ 4.8 μm for SS347H after 3000 hours of post corrosion study [63]. A. S. Dorcheh et al. demonstrated the corrosion effect on the low-chromium ferritic-martensitic X20CrMoV11-1 steel (X20 steel) and stainless

steel 316 (SS316) at 600ºC using Solar salt [64]. They observed maximum corrosion layer of ~18 µm for SS316 and ~1600 µm for X20 steel after 1000 hours and the higher corrosion behaviour of X20 steel is due to the lower Cr content and which could not be able to protect the surface during the corrosion immersion test [64]. The corrosion properties of stainless steel (SS) 304 and stainless steel 316 were studied at 570ºC for 7000 hours by using binary nitrate salts and they observed corrosion rates of 6 and 15 µm/year for SS 304 and SS 316, respectively [65]. The same author also studied the corrosion effect of CS A36 at 316ºC for 7000 hours in binary nitrate salt and they observed a corrosion rate of around 1-4 µm/year [65].

Recent research shows the dynamic and static corrosion immersion test using Solar salt at 500ºC in contact with the CS A516 during 100 hours, the authors observed the formation of the oxide layer of ~ 23.3 µm for the static test and ~ 31 µm for the dynamic corrosion test [66]. Cortes et al. investigated the corrosion effect of Hitec salt in direct contact with the CS and low-Cr alloy steels at 390ºC during 2000 hours. From the analysis, they obtained a thickness of the oxide layer of ~ 2.66 µm for CS, ~ 6.05 µm for low-Cr alloy steel T22 (Cr= 2.25 wt%) and ~ 7.05 µm for low-Cr alloy steel T11 (Cr= 1.2 wt%) [67]. The authors also confirmed that the increase in the Cr content in the CS helps to decrease the corrosion rate due to its corrosion resistive nature [67].

The corrosion evolution of HitecXL salt was also studied with the immersion of the CS and SS up to 1500 hours. The thickness of the oxide layer was obtained for CS, SS 316 and SS 304 after 1500 hours of static test corrosion tests are 20 µm, 16 µm and ~ 13 µm, respectively [68]. The complete corrosion inhibition from the inorganic salt is still far from the present research investigation, but different types of coating and passive layer formations show a reduction of the corrosion rate. Alumina and silica oxides are proved that they have the ability to form a passive layer against further increases in the oxidation layer [69]. Inorganic metal oxide of CeO_2 nanoparticles combined with sol-gel coating techniques was used as a corrosion inhibitor and show the formation of the protective layer [70]. The aluminium substrate coated with hybrid inorganic sol-gel (SiO_x/ZrO_x) solution is used as a corrosion protective layer. In particular, the porous nanoparticles filled with corrosion inhibitors materials, which will release the inhibitor materials near to the defected surface and finally it produced the self-healing corrosion inhibition layer [71].

The sol-gel coating ZrO_2 -3%mol Y_2O_3 was coated by spin coating on the P91 steel. Then this sample was tested for corrosion study in Solar salt at 500ºC for 1000 hours. From that, the authors observed that the ZrO_2-Y_2O_3 is not only reducing the corrosion rate, but it also helps to reduce the environmental impact [72]. The potentiodynamic polarization measurements and electrochemical impedance spectroscopy show that the silica-based hybrid coating with cerium salt can form the corrosion protection layer in the surface of the CS. This study also indicated that the increase the thickness of the coating layer provides the additional corrosion resistance due to the higher concentration of the nanoparticles in the surface, which produce the barrier effect [73].

However, all the published reports have been investigated several systems under different corrosion test conditions such as atmosphere, temperature, dynamic mode, static modes and different exposure time. Mainly, all the above corrosion studies were performed by using molten salt without the addition of the nanoparticles in the base fluids. Most recently, our group investigated the corrosion effect of HitecXL based nanofluids on CS at 310ºC and the results showed the increase of corrosion layer is due to the presence of nanoparticles. The increase of the corrosion effect was observed 3 times higher in the Al_2O_3 based nanofluids and ~ 2 times for SiO_2 based nanofluids compared to the pure HitecXL salt [74]. In addition, we investigated the corrosion inhibition mechanism by developing simple graphite coating method in CS to prevent its corrosion by HitecXL at temperatures up to 500ºC [75]. Recently, the Al_2O_3 and SiO_2 based nanofluids were studied by using two different grades (different in impurities) of Solar salt [76] and the corrosion test is conducted by using SS 347 at 565ºC up to 1000 hours. The authors found that the addition of SiO_2 nanoparticles into Solar salt reduces the corrosion rate. The addition of Al_2O_3 nanoparticles into the Solar salt results in the formation of the needle-like structure with alumina which additionally acts as a corrosion protective layer. Finally, from the results they observed that when a high purity of base fluid is used, the corrosion rate obtained for Solar salt, Al_2O_3 based nanofluid and SiO_2 based nanofluid are 0.021 mm/year, 0.007 mm/year and 0.022 mm/year, respectively. Also, they found that when a low purity base fluid of Solar salt is used, the corrosion rate obtained for Solar salt, Al_2O_3 based nanofluid and SiO_2 based nanofluid are 0.027 mm/year, 0.019 mm/year and 0.024 mm/year [76]. This higher corrosion rate obtained for the low purity of the base fluid is due to the presence of a higher

concentration of Cl in the salt, which increases the corrosion rate. Taken into consideration all the investigated systems, still, there is a lack of information to understand the effect of adding nanoparticles on the corrosivity of the nanofluids and the mechanisms responsible for these changes of the corrosion rates.

Chapter 2. Materials and Characterizations

2.1. Materials

2.1.1. Synthesis of nanoparticles

2.1.1.1. Synthesis of the SiO$_2$ nanoparticles

Three types of SiO$_2$ nanoparticles with average sizes of 27 nm, 450 nm and 800 nm have been used for the preparation of the nanofluids. The SiO$_2$ 27 nm was received from Sigma-Aldrich and the other two (SiO$_2$ 450 nm and 800 nm) were prepared in this work. The Stöber method [77] was used for the synthesis of the SiO$_2$ nanoparticles with particle sizes of 450 nm and 800 nm.

Initially, silica precursor of tetraethyl orthosilicate (Si(OC$_2$H$_5$)$_4$) (concentration ~ 0.4 M, the equivalent mass of 3.332 g) was added into 40 ml ethanol. Then this solution mixture was stirred for 15 minutes at room temperature to obtain a homogeneous solution. After 15 minutes of stirring, a quantity of 6 ml of ammonium hydroxide (NH$_4$OH) was added dropwise. The final solution has pH ~ 8 that was kept under magnetic stirring at room temperature for 2 hours. In order to obtain silica nanoparticles with higher size than the previous material, the same synthesis procedure was carried out with a pH = 9 by means of increase to 8 ml of ammonium hydroxide (NH$_4$OH). Finally, SiO$_2$ nanoparticles were collected using centrifugation at 8000 rpm and cleaned by ethanol for 3 times. The collected powder was initially dried in an oven at 80°C and further calcined in the furnace at 600°C. The schematic presentations of the synthesis process of SiO$_2$ nanoparticles (SiO$_2$-NPs) were shown in Figure 2.1. The final nanoparticles were labelled by SiO$_2$-X, where X refers to particles size.
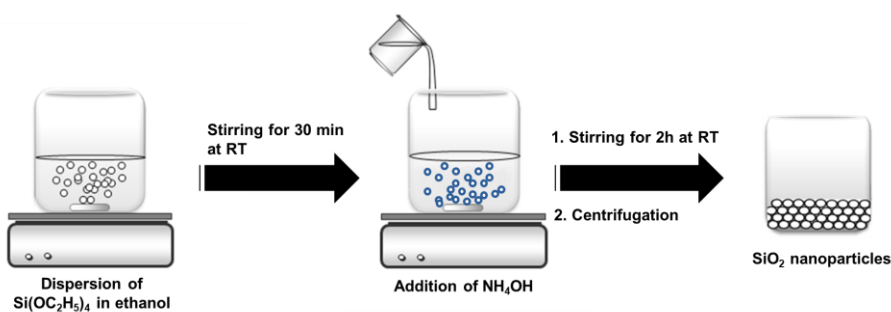
Figure 2.1. Scheme of the preparation process for SiO$_2$ nanoparticles.

2.1.1.2. Synthesis of the SiO$_2$@Al$_2$O$_3$ core-shell nanoparticles

The chains like an aggregation of SiO$_2$@Al$_2$O$_3$ core-shell nanomaterials were synthesized via wet chemical route as it is shown in Figure 2.2. The Al$_2$O$_3$ nanoparticles having a size of ~ 12 nm, purchased from Sigma Aldrich, were used in the preparation as inner core material. To prepare the outer shell, tetraethyl orthosilicate (Si (OC$_2$H$_5$)$_4$) 1.666 g (~ 0.2 M) was added in 40 ml of ethanol and stirred for 15 minutes at room temperature. The mixture of the 40 ml of ethanol with 4 ml of ammonium hydroxide (NH$_4$OH) was prepared, and then this mixture was added dropwise into the previous solution mixture and continued stirring for 30 minutes. Subsequently, 10 ml Si precursor was added to the dispersed Al$_2$O$_3$ nanoparticles solution that previously prepared by dispersion of 500 mg in 40 ml of ethanol by means of ultra-sonication for 30 minutes. The reaction takes place between the interaction of Si-OH and Al$_2$O$_3$ nanoparticles. Finally, the synthesized materials were collected using centrifugation followed by calcination at 600ºC with a heating rate of 5ºC/min and kept in isotherm condition for 4 hours at 600ºC. The thickness of the outer layer of the SiO$_2$ was increased by increasing the volume of Si precursor, i.e. 10 ml, 20 ml and 35 ml, which is confirmed by TEM analysis. The final materials were mentioned as SiO$_2$@Al$_2$O$_3$-X, i.e. SiO$_2$@Al$_2$O$_3$-10, SiO$_2$@Al$_2$O$_3$-20 and SiO$_2$@Al$_2$O$_3$-35, where X = the volume of Si precursor in ml.
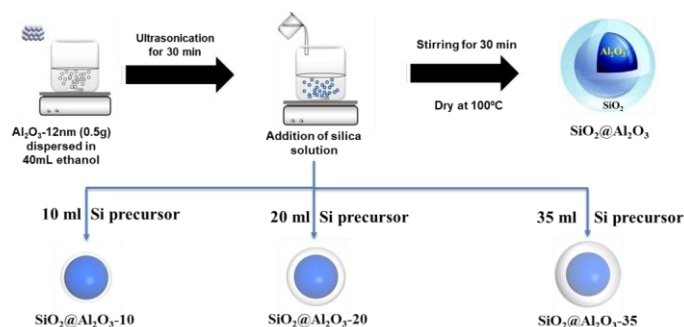
Figure 2.2. Schematic representation for the synthesis of SiO$_2$@Al$_2$O$_3$ core-shell nanomaterials.

2.1.2. Preparation of the nanofluids

2.1.2.1. Classical wet method

The molten salt-based nanofluids are most commonly prepared by the wet preparation method. A simple scheme of the steps followed to prepare molten salt-based nanofluids was shown in Figure 2.3. As a first step, the inorganic salts (i.e. eutectic binary salt composed by 51 wt% $NaNO_3$ and 49 wt% KNO_3) were dissolved in distilled water. Then, once the salts are completely dissolved the corresponding amount of nanoparticles (most commonly 1 wt%) was added to the solution under ultra-sonication process during 30 minutes aiming to obtain a homogeneous solution (well dispersion of the nanoparticles). Finally, the solution was dried in the sand bath at 80°C to remove water and then, the obtained powder is again subjected to drying process at 120°C during 12 hours for the complete removal of water. The final product is a dry mixture of salts and nanoparticles that being saved in a glove box for its further investigation.
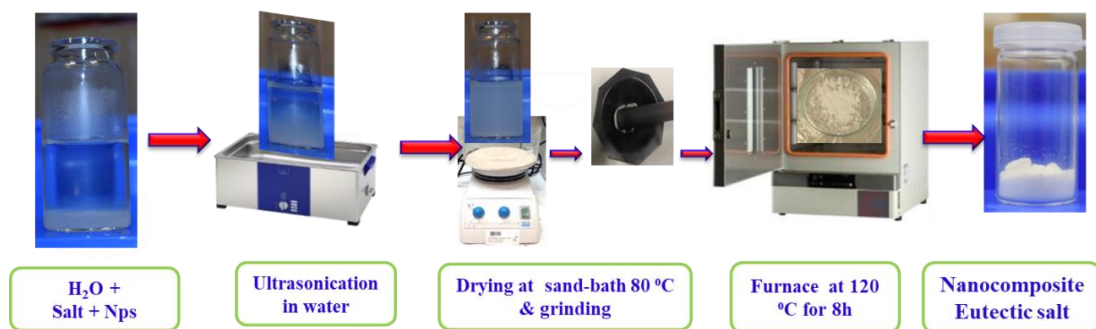
Figure 2.3. Schematic representation for the preparation molten salt-based nanofluids by the classical wet method.

It should be mentioned here that this method is the most followed in the literature to prepare molten salt-based nanofluids, although several drawbacks have already been identified for its use for practical applications such as:

I) The agglomeration nanoparticles trend when the distilled water is used as dispersed media.

II) The difficulty to control the dispersion of the nanoparticles during the slow drying step in the sand bath.

III) A long processing time and multi-step processes to obtain the molten salt-based nanofluids.

IV) The complexity of process scaling up for industrial applications that require a large amount of nanofluid (thousands of tons).

2.1.2.2. Advanced dry method

Taking into consideration the limitations of the classical wet method mentioned above, a new simple method for the preparation of nanofluids was proposed in this work. The first aim of this method is to avoid the trend of the agglomeration of the nanoparticles when they are added to distilled water and during the drying process. As the main challenge for a dry method is the identification of process able to disperse well the nanoparticles within the salt without affecting the size and shape of nanoparticles nor the chemical composition of the salt. In literature, a ball milling method was proposed where stainless steel balls were used in the process, in which the authors identified the possibility of changing the size and shape of nanoparticles during the physical shaking process.

However, in the present work, a simple dry method consisting of physical mixing of the salts and nanomaterials without using balls is proposed for the first time. Firstly, the eutectic salt mixture was prepared by pre-dried $NaNO_3$ and KNO_3 in the weight ratio of 51:49 and melted at 360°C for 6 hours. Once the molten salt was cooled down to room temperature, it was ground to obtain a solid powder of the eutectic salt in order to guarantee that the homogeneity of the mixture is maintained under the subsequent shaking process. This melting step was used in this work to guarantee the correct stoichiometry of the samples that will be used for the characterization of the nanofluid, and it will not be necessary for the industrial application. Then, the nanomaterials (1wt.%) were added to the corresponding amount of the eutectic salt and the mixture was introduced into an aluminium bottle. As it was indicated above, the introduction of stainless steel balls in the preparation process may have some side effects; however, in the present preparation method, no balls were used. Instead, it is expected that the relatively large particles of the salt break the agglomeration of the nanoparticles. The aluminium bottle was fixed inside the physical milling instrument (Prep 8000-series High-Energy Shaker Mill) and mixed for different shaking times where 15 min was identified as the optimum time for good dispersion of the nanoparticles. The speed of the shaking process was approximately 1080 cycles per minute.

The physical shaking method proposed in this work has several advantages compared to the previously used methods for molten salts-based nanofluids preparation. In particular, apart from the homogeneous dispersion of the nanoparticles in the eutectic salt, this method has a short preparation time, it is simple to scale up and does not require the use of water, which may be responsible for the partial formation of nanoparticles agglomerates and the introduction of new impurities into the system. Figure 2.4 summarizes the steps followed for the preparation of nanofluids by the dry method.
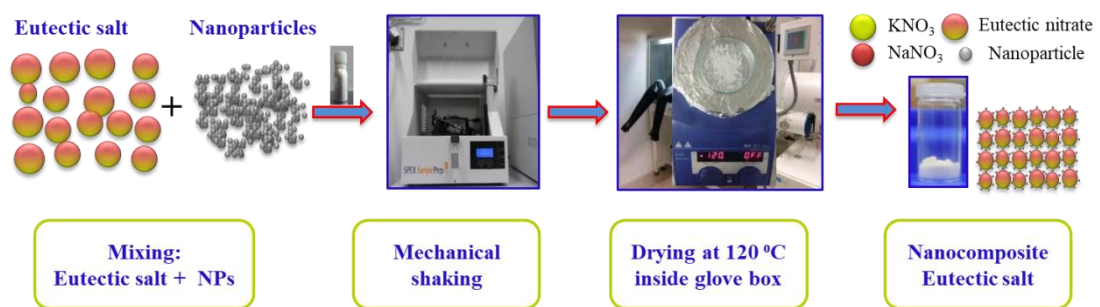
Figure 2.4. Schematic representation for the preparation molten salt-based nanofluids by the advanced dry method.

The validity of the dry method was confirmed by SEM and EDX analyses. As an example, Figure 2.5 shows the SEM images and their corresponding EDX compositional maps obtained for the nanofluids based on eutectic salt and Al_2O_3 nanoparticles prepared by wet and dry methods. As it can be observed, in the case of wet method homogeneous distributions of the K and Na elements were obtained, while a non-homogeneous distribution of Al elements was detected. However, these results revealed that with this wet method it is difficult to maintain the dispersion of the nanoparticles during the drying process due to their tendency to settle down or agglomeration.

In the case of dry method, the result confirms that homogeneous distributions of Na, K and Al elements were achieved. Accordingly, the physical milling method is considered as an advanced method for obtaining a homogeneous dispersion of the nanoparticles with a very simple process and shorter processing time.
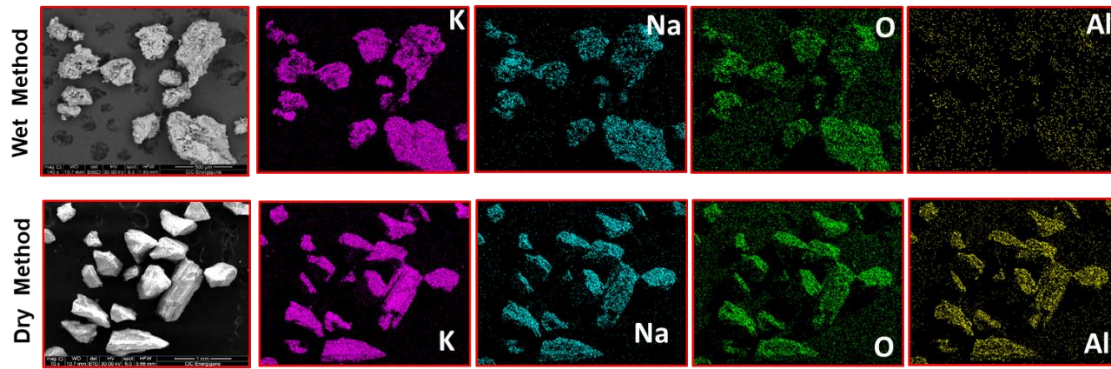
Figure 2.5. SEM images and their corresponding EDX compositional maps for Al_2O_3 based nanofluids prepared by wet and dry methods.

2.1.3. Stability of the nanofluids

The enhancement of the thermophysical properties mainly depends on the dispersion stability of the nanofluids. In this sense, the discrepancy of the thermophysical results reported in the literature for the same system may be explained by the initial dispersion state of the nanofluid and its evolution with time, i.e. during the characterization process. However, in the present work, special attention was given to this point aiming to correlate the thermophysical properties of the nanofluid to its real dispersion state at the moment of the measurements. In this regard, a visual stability test was conducted in the furnace at molten state for several time periods. As examples, Figure 2.6 demonstrated the visual stability tests conducted for Al_2O_3 and SiO_2 based nanofluids in comparison with the eutectic salt. For the visual stability, the test tubes were used to conduct the experiment under a static mode in the furnace at molten state for 24 hours time period.

In the case of Al_2O_3 based nanofluid, in each image in Figure 2.6a the tubes from right to left denote the eutectic salt (Eutectic), Al_2O_3-NPs based nanofluids (Al_2O_3-NPs) and Al_2O_3-NRs based nanofluid (Al_2O_3-NRs). It was observed that the nanoparticles started to settle down at the bottom of the tube immediately after the melting process. But it was also detected that a part of nanoparticles is still homogeneously dispersed in the base fluid after 1 hour, which might have an influence on the enhancement of the thermophysical properties. The stability of the nanofluids was explained by two different mechanisms according to their driven force between an ionic liquid to a solid interface. One is an ionic liquid-based steric force and another one is ionic liquid-based solvation force [78]. The steric force is due to the strong interaction between the ions and particle surface, which prevents

the aggregation of the nanoparticles. The solvation force is also helping to stabilize the nanoparticles against the Van der Waals force in the ionic liquids [78]. Even after one day, we can see some nanoparticle in the eutectic fluids apart from the sedimentation part. Furthermore, this sedimentation of the nanoparticles may occur due to the density difference between the nanoparticles and molten eutectic salt.

In the case of SiO_2 based nanofluids, Figure 2.6b shows the visual stability test performed in the furnace at $400°C$ for SiO_2-27, SiO_2-450 and SiO_2-800 based nanofluids. The results demonstrate that the SiO_2-27 nanoparticles were floating on the top of the molten salt while in the case of the SiO_2-450 and SiO_2-800 the dispersion of the nanoparticles was relatively maintained even after 24 hours. The synthesized SiO_2 nanoparticles in this work show a positive effect on the stability of the nanofluids with time, which may provide guidance on the development of stable nanofluids.
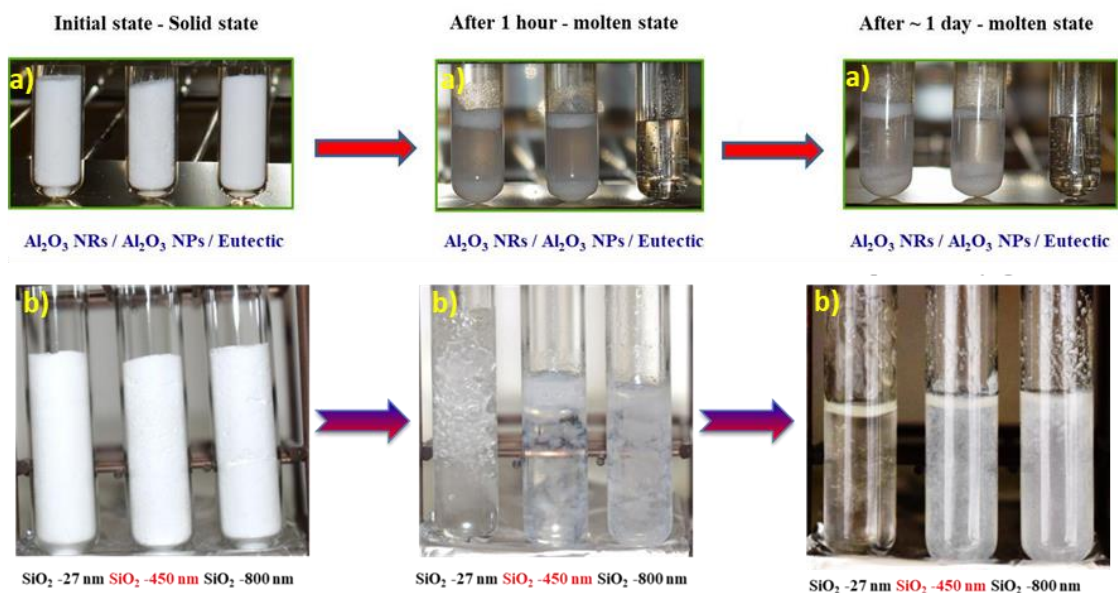
Figure 2.6. Visual stability tests conducted at molten state for the Al_2O_3 and SiO_2 based nanofluids in comparison with eutectic salt.

2.2. Corrosion test protocol

Basically, molten salts have corrosion nature; especially at high temperature the corrosion effect is pronounced. However, the compatibility study between storage container materials and molten salt is essential in the aspects of safety and increasing the lifetime of storage system components as well the stability of the salt. In this study, carbon steel A516.Gr70 with the following chemical composition in weight percentage was used: 98.68% Fe, 0.97% Mn, 0.31% C and 0.04% P.

For the corrosion tests, pieces of CS A516 Gr70 having a size of around $3 \times 12 \times 14$ mm were used. These pieces were cleaned with ultra-sonication for 15 minutes using acetone followed by ethanol and finally with DI water. It is worth to mention here that the samples were used under the conditions close to practical applications without applying any polishing or other external treatment of the CS surface, which may enormously affect the evolution of the corrosion rate. In particular, polishing the CS surface will remove the oxide layer and carbon-rich layer which present in the surface and it not comparable with the real applications.

The mass of the CS was controlled before and after the corrosion tests. The corrosion tests were conducted in alumina crucible by immersing CS pieces in 5 g of eutectic salt or nanofluids. The corrosion tests were conducted under air at 390ºC for periods of 250, 500, 1000 and 1500 hours under static immersion condition. Figure 2.7 demonstrated a simplified scheme of the protocol followed in the corrosion tests. After the corrosion tests, the samples were carefully washed with hot water. In order to check the effect of the presence of microbubbles in the nanofluid, the corrosion tests were also performed at 310ºC following the same protocol and experimental conditions.

Figure 2.7. A scheme of the corrosion test protocol.

A specific sample preparation method for the SEM cross-section analysis to study the corrosion effect of the eutectic salt and nanofluids immersed carbon steel samples were followed. After the corrosion test, the samples were immersed in the rubber which is prepared by mixing of Aka-Resin (1 ml) and Aka-Cure catalyst (0.1 ml), then this resin was kept overnight for the solidification process. Finally, the resin holder with the sample was cut in half or polished ~ 2 mm to observe the corrosion cross-section layer. This special resin holder was avoiding the exfoliation of the corrosion layer from the CS and which gives more accuracy about the

corrosion thickness layer of the sample. Figure 2.8 demonstrated a scheme of the specific preparation method to obtain a cross-section of the tested carbon steel.
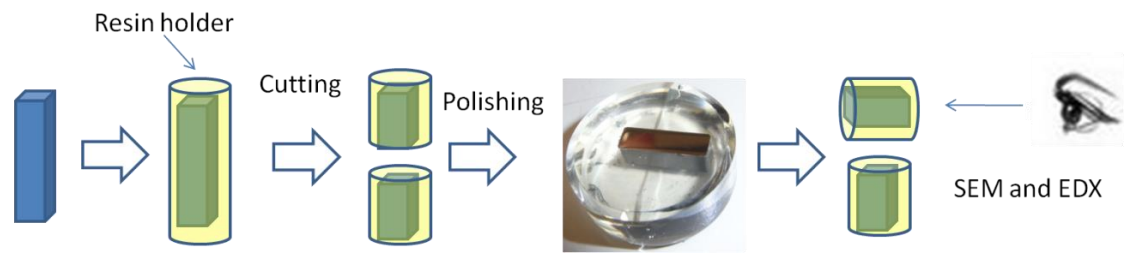
Figure 2.8. Sample preparation method for SEM cross-section analysis.

FEI Helios NanoLab 450S DualBeam – Focused ion beam (FIB) with FEG SEM was used to record micrographs of the surfaces of carbon steel samples after the corrosion tests. Also, the FIB technique was deployed to observe a cross-sectional view of the corrosion layer. Figure 2.9 shows the steps of the cross-section preparation procedure. First, Pt protective layer (~ 1 micron) was deposited above the spot of interest on the carbon steel surface (Figure 2.9a) via electron beam (3 keV) stimulated decomposition of a Pt-containing gaseous precursor (Figure 2.9b). Next, a staircase-shaped cavity was excavated using a focused Ga ion beam (30 keV, 9.6 nA) (Figure 2.9c). The dimensions of this cavity were around 15 μm wide, 30 μm long and 20 μm deep at the cross-sectional plane. Finally, polishing of the cross-section surface was performed by low-current (30 keV, 100 pA) focused Ga ion beam followed by 52° tilt of the sample for the cross-section analysis (Figure 2.9d). Using a low-voltage (3 keV) and low-current polishing combined with Pt protective layer, allowed to preserve the corrosion layer in its initial form and to gain the details of its topology usually inaccessible when mechanical polishing is applied.
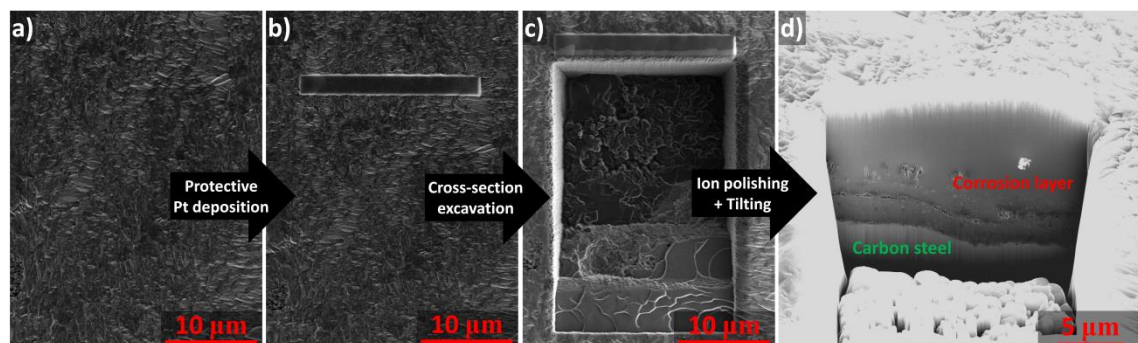
Figure 2.9 The main steps of cross-section view preparation using FIB technique: a) carbon steel; b) Pt protective layer of ~500 nm deposited on carbon steel; c) staircase-shaped cavity excavated using focused Ga ion beam; d) 52° tilted view of the cross-section.

2.3. Characterizations

2.3.1. Structural characterizations

2.3.1.1. X-ray diffraction (XRD)

XRD is the most commonly used tool to identify the crystalline phase and unit cell dimension of the crystalline materials. In 1912, Max Von Laue has discovered the phenomena about the XRD, accordingly, the X-ray diffraction was related to the constructive interference of the monochromatic X-ray and crystalline sample. The XRD is functioned with initial generation of X-ray by cathode ray tube, then monochromatic radiation is attained by the filter, followed by collimated is used to concentrate and finally, the X-rays are directed towards the sample. The interaction of X-ray with sample produces the diffraction peak if it is obeying the Braggs law ($n\lambda = 2d \sin\theta$). Then the detector records the X-ray and process to the signals to a count rate. From the Braggs law, n is an integer, λ is the wavelength of the X-ray, θ is the incident angle of the X-ray and d is the spacing between the atom layers. Copper is widely used as a source of target materials and the radiation of the CuKα source is 1.5418 Å.

The XRD measurement of the samples was done by using Bruker D8 Advance X-ray diffractometer, which is equipped with a LYNXEYE detector using CuKα1 radiation ($\lambda = 1.5418$ Å). The samples are measured in the 2θ range between 10 to 90° with a scanning rate of 2°/min. After the measurements, the obtained data were analysed using EVA software to know the phase compositions and structures of the materials.

2.3.1.2. Fourier transform infrared spectroscopy (FTIR)

FTIR technique helps to identify the molecule structure of a wide range of the solid, liquid and gases by absorption or emission of the infrared spectrum. While the interaction of infrared into the sample molecules, it will absorb the radiation with a specific wavelength and it changes the dipole moment of the sample molecules. Simultaneously, the vibration energy level of sample molecules transfers from ground state to excited state. Then, the frequency of the absorption peak is identified by the energy gap and the number of absorption peaks is depends on the number of vibrational freedom of the molecules. The infrared portion of electromagnetic spectrum in the region of 12800-10 cm^{-1} is classified into different regions: near-infrared is 12800-4000 cm^{-1} mid-infrared is 4000-200 cm^{-1} and far-infrared

1000-50 cm^{-1}. The most commonly used infrared region is 4000-200 cm^{-1} because the absorption radiations of most of the inorganic and organic compounds are lying in this region. The mid-infrared is used to analyse the fundamental vibration associated with their rotational-vibrational structure of the molecules. In the FTIR spectra, the absorption band between 1450 to 600 cm^{-1} is difficult to identify, because it follows a unique pattern and it's called fingerprint region. Similarly, the absorption band corresponds to the region from 1450 to 600 cm^{-1} is usually observed due to the stretching vibration of diatomic molecules.

The interferometer having the components of IR source, beam splitter, moving mirror, stationary mirror and detector. The IR source passes towards the beam splitter (interferometer) and ideally, 50% of light refracted towards the fixed mirror and 50% of light is transmitted to the moving mirror. Then the lights reflected from the two mirrors return to the beam splitter and from that, some of the lights are passed through the sample and finally reached to the detector. The sample absorbs the light according to their chemical properties.

In the present work, the samples were analysed using Perkin Elmer FTIR Spectrum 400 DTGS spectrophotometer under an argon atmosphere at room temperature by directly placing the powder sample on the sample holder.

2.3.1.3. Zeta potential (ZP) analysis

Zeta potential measurement is used to identify the surface functionality and dispersion stability of the particles in solution. The zeta potential analysis helps to study the magnitude of the electrostatic/charge attraction or repulsion between the particles. The zeta potential is necessary for the surface of the materials, which is in direct contact with the liquid because the functional group of the material reacts with the surrounding medium.

The zeta potential analysis of aqueous dispersed SiO_2 nanoparticles was measured using Malvern zetasizer (nano series) at room temperature. For the ZP measurement, the refractive index of 1.460 and absorption of 0.000 was used as input values for the aqueous dispersed SiO_2 nanoparticles. Similarly, the refractive index of 1.760 and absorption of 0.100 was used for Al_2O_3 nanoparticles.

2.3.1.4. Brunauer-Emmett-Teller (BET) Analysis

BET technique is used to determine the specific surface area and pore size distribution of the materials. Nitrogen is commonly used as absorbed gas for BET

analysis. The specific surface area of the materials is calculated by physical adsorption of the gas molecules on the solid surface and the adsorbed gas related to the monomolecular layer on the surface. Physical absorption is relatively weak forces (Van der Waals forces) between the adsorbate gas molecules and material surface.

BET analysis was carried out in an automated gas adsorption analyser model Micromeritics ASAP 2460. Nitrogen sorption isotherms of the nanoparticles were measured after outgassing of the samples at 250ºC under vacuum for 6 hours.

2.3.1.5. *Raman spectroscopy*

Raman spectroscopy helps to identify the vibration, rotational and other low frequencies in the system. The Raman effect is mainly correlated to the polarizability of the electron in the molecules. While photon interacts with matter, absorption or scattering will occur and this scattering is classified into elastic and inelastic scattering. The elastic process is called Rayleigh scattering and inelastic scattering is called Raman scattering. The electric field component of the scattered photon will interrupt the electron clouds and exit the system to the virtual state. In the Raman scattering, system exchanges energy with photons and decays the vibrational energy below or above the initial state. The frequency shift is the difference between the incident and scattered photon which is called a Raman shift. Depends on the gain or loss in the vibrational energy, the Raman shift occurs up or downshift of the scattered photon frequency compared to the incident photon. The shift in energy gives information about the vibrational modes of the system.

The Raman spectra of the materials were collected at room temperature by using Renishaw spectrometer (Nanonics Multiview) having an excitation wavelength of 532 nm with an Ar ion laser.

2.3.1.6. *Scanning electron microscope (SEM)*

The SEM helps to obtain the image of the sample by scanning on the sample surface with a focused electron beam. The interacted electrons with the surface give the various signals that show the information about morphology, topography and composition of the materials. The entire electron column present in the vacuum helps to prevent the contamination and external noise or disturbance, which increases the resolution of the image.

In the SEM module, an electron beam is thermionically emitted from the cathode of tungsten filament, which is fitted in the electron gun. Then the electron

beams are focused by condenser lenses with a spot size between 0.4 to 5 nm in diameter. Concurrently, the electron beam passes through the scanning coil or deflector plates in the electron column and lens deflect the beam in x and y directions. Finally, the deflected electron scans the surface in rectangular area and produces the images. Tungsten filament is commonly used thermionic electron gun and other types of lanthanum hexaboride (LaB_6) were also used. The electron beam has the voltage range between 0.2 keV to 40 keV.

The nonconductive specimen is usually coated by conducting materials to avoid the charging of the sample surface by the electron beam. While the electron interacts with the specimen it produces the secondary electron, backscattered electron and characteristic X-rays. When the electron beam interacts with the sample, it penetrates few microns which depend on the accelerating voltage and density of the samples. The maximum resolution of the SEM image mainly depends on the electron spot size and volume of the electron beam interaction with the sample. SEM can achieve the resolution of below 1 nm, but typically it can provide the image with high resolution of 1-20 nm. The energy exchange between sample and electron beam reflects the high energy electrons by elastic scattering, while inelastic scattering emits the secondary electrons. The secondary electrons are providing the high-resolution image compared to the backscattered electrons. However, backscattered electron gives the different contrast pattern depends on the composition of the multiphase in their topographic images. The diffracted backscattered electron provides the information about crystal structure and orientation of the minerals while characteristic X-rays are used for elemental analysis.

Energy-dispersive X-ray spectroscopy (EDX) is used to identify the chemical composition of the materials with their quantitative abundance and elemental composition mapping in a wider range. The chemical composition is identified by the emission of X-ray, which produced while the interaction of electron beams with the specimen (sample). While the electron beam is bombarded on the specimen, the electrons are emitted from atoms comprising the sample. Then the corresponding electron vacancies of holes are filled by an electron from the higher energy state. During this transition from a higher energy shell to lower energy shell, the energy difference can be released as X-ray.

In order to determine the size and shape of the nanoparticles and to investigate their dispersion within the nanofluids Quanta 200 FEG scanning electron microscope (SEM) equipped with energy-dispersive X-ray spectroscopy (EDX) was used. Also, these techniques were used to analyse the elemental composition and mapping of the surface and cross-section of the carbon steel for the corrosion study. For an optimum image generation, the SEM microscope was operated in high vacuum mode at accelerating voltages of 30 kV. The images were collected by using the backscattered electron detector (BSED).

2.3.1.7. Transmission electron microscope (TEM)

In TEM, a high energy beam of electron transfer through a thin sample and the interaction between the sample and electron produces the image. TEM can also be used to identify the crystal structure and chemical composition of the materials. TEM is working by the basic principle of an optical microscope, but in TEM electron is used rather than light. The commonly used emission source in TEM is tungsten filament or lanthanum hexaboride (LaB_6). The high voltage of 100 keV to 300 keV is applied to emission source for thermionic or field electron emission purpose. The magnification of TEM is approximately 100X to more than 1000,000X.

Initially, the electron gun has produced the beam of electron and condenser lens is used to focus the beam to object. The image producing system consists of the objective lens, movable sample stage, intermediate and projector lens, which helps to focus the electron beam through the sample. Finally, highly magnified images were produced in a fluorescence screen or charge coupled device (CCD) camera.

The prepared nanomaterials were characterized by transmission electron microscopy (TEM), model FEI Tecnai F20 electron microscope, which is operating at 200 kV. The preparation of the samples was carried out by sonication of the solid particle in the ethanol and small droplet of the sample was transferred onto a holey carbon film fixed on a 3 mm copper grid (200 mesh).

2.3.1.8. Density measurement

The helium pycnometer is used to measure the density of the sample by displacing the volume of gas by a known mass of the materials. The skeletal density of cylindrical pellet of eutectic salt was measured at room temperature by using helium pycnometer AccuPyc II 1340 from Micromeritics. For the accuracy of the

results, 10 consecutive measurements were measured and an average value was considered as a final density.

2.3.1.9. X-ray photoelectron spectroscopy (XPS)

The XPS technique is a useful tool to measure the elemental composition, chemical state, electronic state and empirical formula of the materials. XPS is functioned by the irradiation of X-ray beam on the solid surface and concurrently measuring the kinetic energy of the electron obtained from a surface depth of 1-10 nm. By measuring the kinetic energy of the emitted electron, the properties like binding energy of the electron, elemental properties and chemical state of the materials can be defined. The position and intensity of the peak are used to define the electronic state and quantitative information about the materials.

The XPS study was performed in an ultra-high vacuum system using hemispherical electron analyser PHOIBOS 150 (SPECS). The twin Al/Mg anode X-ray source X-ray XR50 (SPECS) is operated at 12 keV with 100 W power. The XPS spectrums were obtained by the fixed analyser transmission mode with pass energies of 20 eV and 90 eV for detecting high-resolution elemental spectra line and survey spectrum. Finally, the obtained XPS data were fitted using CasaXPS data processing software. The XPS depth profiling was performed by using sputter gun IQ12 (SPECS) operated in scanning mode with an argon ion beam with the kinetic energy of 5 keV. The sputtering rate was nearly 1-3 nm min^{-1}.

2.3.2 Thermophysical analysis

2.3.2.1. Differential scanning calorimetry (DSC)

Accurate specific heat capacity (Cp) of the most common materials was measured by differential scanning calorimetry (DSC) technique. The DSC technique also provides information about the endothermic (heat absorption) and exothermic (heat release) properties of the materials during the physical transition process, thermodynamic process and reaction kinetics.

In a heat flux DSC cell, the sample and reference pans are placed in the thermoelectric sensor which is surrounded by the furnace. During the increase/decrease of temperature, the differential heat flow of the sample and reference is measured according to the following equation (eq. 1),

$$q = -\frac{\Delta T}{R_r} + \Delta T_0 \left(\frac{R_r - R_s}{R_r R_s}\right) + (C_r - C_s)\frac{dT_s}{dt} - C_r \frac{d\Delta T}{dt} \qquad \text{(eq. 1)}$$

Where, $\varDelta T$ is the difference between the sample (T_s) and reference (T_r) temperatures, $\varDelta T_0$ is the difference between the sensor (T_0) and sample (T_S) temperatures, T_0 is the control temperature, R_r is the reference sensor thermal resistance, R_s is the sample sensor thermal resistance, C_r is the reference sensor heat capacity and C_s is the sample sensor heat capacity.

The specific heat capacity and enthalpy of the nanofluids were measured by using the Thermal Analysis DSC 2500 model in the temperature range of 50-350°C with a heating/cooling rate of 10 °C/min. Aluminium hermetic pans were used for the reference as well as for the sample crucibles which are hermetically closed in an argon atmosphere. Between 32 mg to 38 mg of the sample mass used to obtain the proper contact between the sample and bottom surface of the crucible. Before each measurement, the sapphire was measured to validate the uncertainty of the measurement and an error of less than 2% was obtained.

2.3.2.2. Laser flash apparatus (LFA) technique

Thermal diffusivity is the measure of how fast the heat can propagate through the materials or medium. In 1960, Parker et al. introduced the laser flash apparatus (LFA) techniques that can provide information about the thermal diffusivity (α). The measurement is done by heating of the front side of the materials with a high-intensity laser pulse and changes in the temperature related to the backside of the sample were measured by an infrared camera. In ideal adiabatic condition, the thermal diffusivity is defined as $\alpha = 0.1388.\ l/t_{50}$. Where l is the thickness of the sample and t_{50} is the time to the half maximum (S).

The thermal diffusivity of the nanofluids was measured in solid and liquid states by means of a Laser Flash Apparatus (Netzsch LFA 457 model). In the case of solid state, a square sample with 10 mm length and thickness of around 2 mm was used. In the case of the liquid state, the sample was prepared by melting the salt in a home-made stainless steel holder with micro-rough surfaces in order to solve the problem of measurements inaccuracy related to the wetting phenomena caused by the molten inorganic salt. In the case of solid state, a graphite film prime was added over the top and bottom surfaces of the sample which is aiming to minimize the experimental error. In the case of the liquid state, a graphite coating over the top and bottom surfaces of the holder was applied. Finally, the thermal conductivity was

calculated by using $\lambda = \alpha(T) \cdot \rho(T) \cdot Cp(T)$. Where, α is thermal diffusivity, ρ is density and C_p is specific heat capacity of the sample.

2.3.2.3. Thermogravimetry analysis (TGA)

The thermogravimetric analysis (TGA) is a technique that used to control the mass variation of a sample while the temperature of the measuring chamber is increased/decreased at a controlled rate under the controlled flow of gas. During the measurement different gases can be used as a purging medium such as air, nitrogen and argon. This technique is useful for investigation of thermal stability of nanofluids and the pristine salts by controlling the mass change with temperature under the same experiment conditions such as the atmospheric gas, gas flow and heating rate. For this purpose, a thermal analyzer NETZSCH STA 449 F3 Jupiter instrument was used where sample and reference crucibles were placed in a symmetrical position in the furnace. The measurements were performed under air and argon atmospheres from room temperature to 700°C with a heating rate of 10 °C/min.

2.3.2.4. Rheometer

A rheometer is used to measure the deformation and flow properties of the liquid under an applied force. Different geometries are used such as parallel plates, concentric cylinders or cone and plate depend on the fluid's characteristics. The sample is placed inside the geometry where torque is applied on the upper plate (applied shear stress) to determine the shear strain. The viscosity is defined as the ratio between the shear stress and shear rate as described in the following equation (eq. 2).

$$\text{Viscosity} = \frac{Stress}{Shear\ rate} \qquad\qquad (\text{eq. 2})$$

Discovery Series Hybrid Rheometer-1 (DHR) model from the thermal analysis (TA) was used to measure the viscosity of the prepared nanofluids and pristine salts. The viscosity measurement was studied by using 25 mm parallel plate geometry by using around 1 gram of the sample in the form of a pellet. The distance between geometry was fixed to an optimum gap of 1 mm. The measurements are performed under a static temperature of 250, 300, 350 and 400°C in an argon atmosphere with the velocity of 10 rad/s for 20 minutes.

2.3.2.5. Contact angle measurement

The KRUSS HT-2 Contact Angle (CA) instrument is used to study the wettability or contact angle of the molten salt-based nanofluids (MSBNFs) on a carbon steel substrate. The CA measurements are performed under an air atmosphere, with a ramp of 2 °C/min until 400°C. At least three measurements are conducted for each sample to assure confidence and the presented values are the average of the three best measurements. For reproducibility of the measurement, a standardized sample preparation method was used.

Initially, the 100 mg of the sample was placed in the 4 mm diameter die then compressed at 120 MPa for 3 minutes. To correlate the wettability behaviour of the nanofluids with the corrosion phenomena, the substrate (CS) used in the corrosion test is also used for the CA measurement. The roughness of the substrate plays a crucial role on the CA, so the roughness of the CS (20 mm x 20 mm x 2 mm) was measured by using EPS interferometer before and after the measurements. The roughness is S = 0.43 ±0.2 µm.

2.3.2.6. Dilatometry

The dilatometer is used to characterize the dimensional change (expansion/shrinkage) with the function of temperature. The expansion coefficient of the material is calculated by the following equation (eq. 3):

$$\alpha = \frac{1}{L_0} \cdot \frac{\Delta L}{\Delta T} \qquad \text{(eq. 3)}$$

Accordingly, α is the linear expansion coefficient, L_0 is the initial length of the sample, ΔL is the change in the length and ΔT is the change in the temperature. For a dilatometry analysis, the material was placed inside the special sample holder which is located in the furnace. The length of the sample is changed when it is subjected to temperature and concurrently linear variable displacement transducer core is moved. Then, the displacement record is directly proportional to the output signal. The linear thermal expansion (dL/L_0) of the nanofluids and pristine salts was studied in solid-state using dilatometer by Netzsch Model 402C in the temperature range of 30–200°C at a heating rate of 10°C/min in the nitrogen atmosphere. The dilatometer contains the alumina sample holder with a push rod. The cylindrical shape of the sample was prepared by melting the binary mixture and produced by a

replica method with a size of 2.5 cm length and 1 cm of diameter. Before the measurement, the calibration was done by using alumina standard with a length of 15 mm and a diameter of 6 mm. Finally, the thermal expansion coefficient was calculated by a change in the length compared to the initial length of the sample over the temperature range.

Part 1. Development of Molten Salt-Based Nanofluids

Part 1. General Introduction

Molten salt based nanofluids were investigated for high-temperature TES purpose aiming to increase the thermocyclic efficiency of the system. In literature, the commercial binary nitrate mixture of $NaNO_3:KNO_3$ (60:40 wt%) was used as the base fluid for the development of the nanofluids. In this study, as the specific mechanisms for the anomalous enhancements are still unclear, we used eutectic nitrate salt, i.e. $NaNO_3:KNO_3$ (51:49 wt%), having a single melting/crystallization temperature, because the non-eutectic mixture has multiple melting/crystallization, which might distort the interaction between the nanoparticle and salts. In addition, the non-eutectic salt may lead to its segregation during the melting and solidification processes which are not the case on an industrial scale, since the salt is used all the time in a molten state. For the preparation of the molten salt-based nanofluids, in addition of the Al_2O_3 and SiO_2 commercial nanoparticles commonly studied in the literature, the new synthesized monodispersed SiO_2 and $SiO_2@Al_2O_3$ core-shell nanoparticles were used aiming to improve the dispersion stability and thermophysical properties of the nanofluids. Initially, the shape effect on the thermophysical properties was studied by using two different shapes of Al_2O_3 nanomaterials, i.e. nanospheres and nanorods. Simultaneously, the size effect on the thermophysical properties was studied by using different sizes of SiO_2 nanoparticles having the size of 27 nm, 450 nm and 800 nm. Finally, the effect of composite

nanoparticles was studied by using hybrid $SiO_2@Al_2O_3$ core-shell nanoparticles by changing the ratio between the inner and shell diameters.

Initially, the utilized nanoparticles were characterized by several techniques to know the structural and morphological properties by using XRD, FTIR, SEM, BET, TEM, etc. The molten salt-based nanofluids were prepared by the new physical milling process and the milling time was optimized to get homogeneous dispersion of the nanoparticles in the eutectic salt. Then the detailed thermophysical properties such as specific heat capacity, thermal diffusivity/conductivity, enthalpy, viscosity, thermal and visual stability of the nanofluids were studied. For the thermophysical properties, the accuracy of the measurements was ensured by optimizing several parameters responsible for the discrepancy of the results presented in the literature. Furthermore, the effect of adding nanoparticles on the nanofluid viscosity was highlighted. Finally, the thermal and dispersion stabilities of the nanofluids have been studied at high temperature.

Chapter 3. Nanoparticles Shape Effect

Two types of Al_2O_3 nanoparticles, i.e. nanorods (NR) and nanospheres (NS), have been used to investigate the shape effect on the enhancement of the most relevant properties of the molten salt currently used in CSP power plants. Initially, the structural characterization of the two different shapes of Al_2O_3 nanoparticles was studied using XRD, FTIR, TEM, BET, etc. Then, the nanoparticles were used to prepare the molten salt-based nanofluids by simple dry method in order to study the thermophysical properties. A good dispersion of 1 wt.% Al_2O_3 nanomaterials in the base eutectic salt, i.e. 51wt.% $NaNO_3$ – 49 wt.% KNO_3 was achieved by a shaking time of 15 minutes. Their stability and thermophysical properties have been studied by means of TGA, DSC, LFA, Rheometry and Dilatometry. The Al_2O_3-NPs based nanofluid (Al_2O_3-NPs-nanofluid) and Al_2O_3-NRs based nanofluid (Al_2O_3-NRs-nanofluid) show enhancements of the specific heat capacity (C_p) in the liquid phase of 3% and 6%, respectively. The thermal conductivity analysis demonstrates enhancements of 12 % and 20% in solid states and 16% and 12% in the liquid phase for Al_2O_3-NPs-nanofluid and Al_2O_3-NRs-nanofluid, respectively. The viscosity increments of 25% and 37% were observed for Al_2O_3-NPs-nanofluid and Al_2O_3-NRs-nanofluid, respectively.

3.1. Structural analysis

Two types of Al_2O_3 nanoparticles with a size of 13 nm and 50 nm, received from Sigma Aldrich, were used for the preparation of the nanofluids. As it was mentioned above, a big discrepancy was obtained for the published results by different groups when the same type and size of the nanoparticles were reported.

However, in this work, we decided to characterize the as-received commercial nanoparticles aiming, on the first hand, to understand the discrepancy of the reported results; and, on the second hand, to understand the mechanisms responsible for the enhancements in the thermophysical properties of the investigated nanofluids.

The analysis of the size and shape of the two types of the Al_2O_3 nanomaterials was carried out by TEM analysis. Figure 3.1a shows the TEM images and their corresponding histograms for Al_2O_3 (13 nm) and Al_2O_3 (50nm) nanoparticles. In the case of Al_2O_3 (13 nm) nanoparticles, a spherical shape with an average size of 12 ± 2 nm was observed. In the case of Al_2O_3 (50 nm), a nanorod shape was observed instead of a spherical form as it can be clearly seen in Figure 3.1b. The histograms of the nanorods demonstrated that the average diameter is 5 ± 1 nm and a length of 40 ± 10 nm. However, the shape of the nanoparticles may differ among the suppliers of nanoparticles with the same type and size and may be the source of the discrepancy of the reported results in the literature. Hereafter, we will refer to Al_2O_3 (13 nm) and Al_2O_3 (50nm) as Al_2O_3-NPs and Al_2O_3-NRs, respectively.
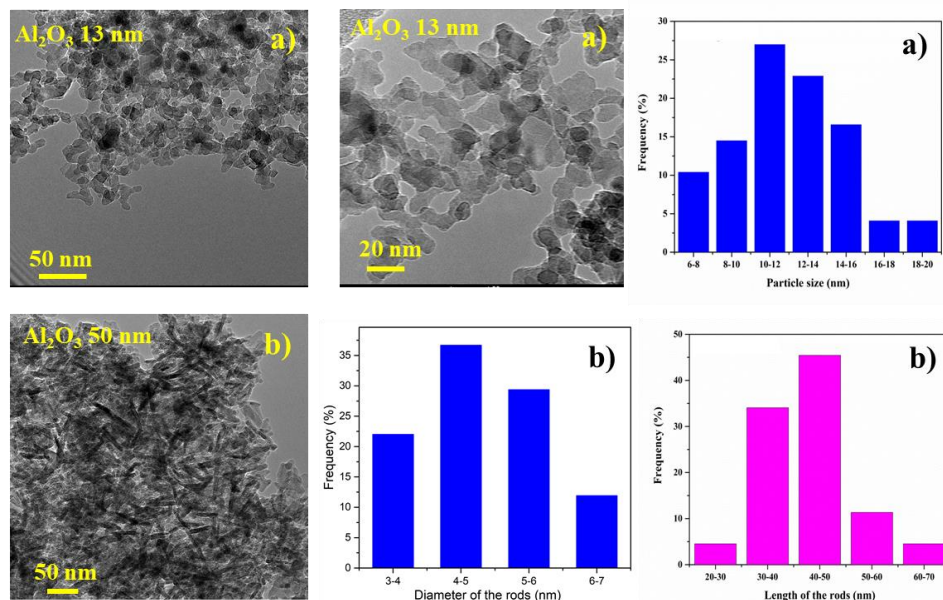
Figure 3.1. TEM images of the two different morphologies and their corresponding histograms for Al_2O_3 nanomaterials, a) Al_2O_3-13 nm and b) Al_2O_3-50 nm.

The specific surface area of Al_2O_3-NPs and Al_2O_3-NRs was evaluated using the nitrogen physisorption analysis shown in Figure 3.2. The BET surface area results are in agreement with TEM/EDX results because both materials adopt a

spherical form: the smaller particle size should lead to a higher specific surface. The specific surface area of Al_2O_3-NPs and Al_2O_3-NRs was evaluated using the Brunauere-Emmett-Teller (BET) method over the P/P_0 range from 0 to 1 in the X-axis. Figure 3.2 shows the adsorption/desorption curves obtained for Al_2O_3-NPs and Al_2O_3-NRs. From the N_2 physisorption analysis, the measurement shows the type II isotherm and flat region in the middle indicating a monolayer formation. In the higher relative pressure, the adsorption and desorption show high adsorbed quantity which is due to the filling of the interparticle space. The adsorption and desorption isotherms confirm the non-porous nature of the investigated nanomaterials. From the measurement, we obtained the BET specific surface area for Al_2O_3-NPs and Al_2O_3-NRs are 93 m^2/g and 124 m^2/g, respectively.
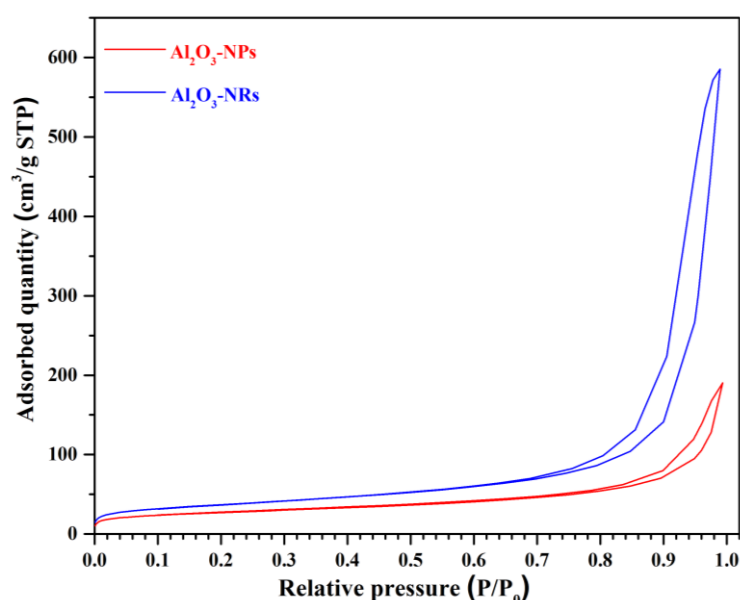
Figure 3.2. BET absorption and desorption curves of the Al_2O_3-NPs (red line) and Al_2O_3-NRs (blue line).

In order to identify more parameters that may be responsible for the observed discrepancy of the reported results, XRD patterns were collected and analysed for the Al_2O_3-NPs and Al_2O_3-NRs, as-received and after being treated at 600°C for 6 h, and the results are presented in Figure 3.3. The Al_2O_3-NPs shows the presence of the cubic structure (γ-Al_2O_3) with the space group Fd-3m (COD # 1101168); while, Al_2O_3-NRs shows the presence of both structures α-Al_2O_3 and γ-Al_2O_3. The α-Al_2O_3 phase is a hexagonal structure with the space group R -3 c (COD # 9008081). The presence of sharp and broad diffraction peaks in the α-Al_2O_3 diffraction pattern indicates the preferred orientation due to its form as nanorods [79]. The α-Al_2O_3 or

corundum phase of the alumina is considered as more thermodynamically stable materials [80]. However, the presence of γ-Al$_2$O$_3$ may be due to the fast cooling process of these materials during the fabrication process. In order to check the stability of the γ-Al$_2$O$_3$ in Al$_2$O$_3$-NPs and Al$_2$O$_3$-NRs, the materials were calcined at 600°C (the maximum temperature of the application) for 6 h with a heating/cooling ramp of 5 °C/min. After the calcination, we did not observe any significant changes in neither case, which indicates that the γ-Al$_2$O$_3$ phase is stable up to the maximum temperature of the application (600ºC). The presence of the α-Al$_2$O$_3$ and γ-Al$_2$O$_3$ in the nanoparticles is related to the fabrication processes that can differ from one supplier to another, which may affect the enhancement of the thermophysical properties and may be responsible for the discrepancy of the reported results in the literature.
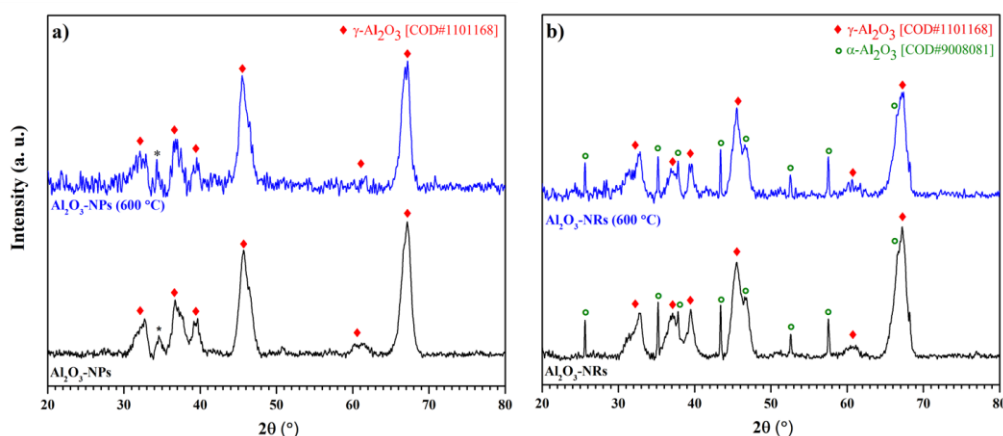
Figure 3.3. XRD diffractograms of as-received and calcined at 600ºC (6 hours): a) Al$_2$O$_3$-NPs and b) Al$_2$O$_3$-NRs. The (*) correspond to unidentified phase.

3.2. Preparation and analysis of nanofluids

A simple dry method consisting of physical mixing of the salts and nanomaterials is proposed for the first time in the present work. Firstly, the eutectic salt mixture was prepared by pre-dried NaNO$_3$ and KNO$_3$ in the weight ratio of 51:49 and melted at 360 °C for 6 hours. Once the molten salt was cooled down to room temperature, it was ground to obtain a solid powder of the eutectic salt in order to guarantee that the homogeneity of the mixture is maintained under the subsequent shaking process. Then, the Al$_2$O$_3$ nanomaterials (1wt.%) were added to the corresponding amount of the eutectic salt and the mixture was introduced into an aluminum bottle. As it was indicated above, the introduction of stainless steel balls in

the preparation process may have some side effects; however, in the present preparation method, no balls were used. Instead, it is expected that the relatively large particles of the salt break the agglomeration of the nanoparticles. The aluminum bottle was fixed inside the physical milling instrument (Prep 8000-series High-Energy Shaker Mill) and mixed for a shaking time of 15 min. This shaking time was previously optimized in a systematic study to investigate the effect of the shaking time on the dispersion state and the results will be presented and discussed in a separated research article. The dispersion state of the prepared nanofluids was analysed by SEM and EDX techniques. Figure 3.4 shows the SEM and EDX mapping images for pure eutectic salt, Al_2O_3-NPs-nanofluid and Al_2O_3-NRs-nanofluid. In this figure, it can be clearly seen that the homogeneity of the salt mixture and the good dispersion of the nanoparticles within the salt were achieved, with no evidence of nanoparticles agglomerates.

The physical shaking method proposed in this work has several advantages compared to the previously used methods for molten salts based nanofluids preparation. In particular, apart from the homogeneous dispersion of the nanoparticles in the eutectic salt, this method has a short preparation time, it is simple to scale up and does not require the use of water, which may be responsible for the partial formation of nanoparticles agglomerates and the introduction of new impurities into the system.
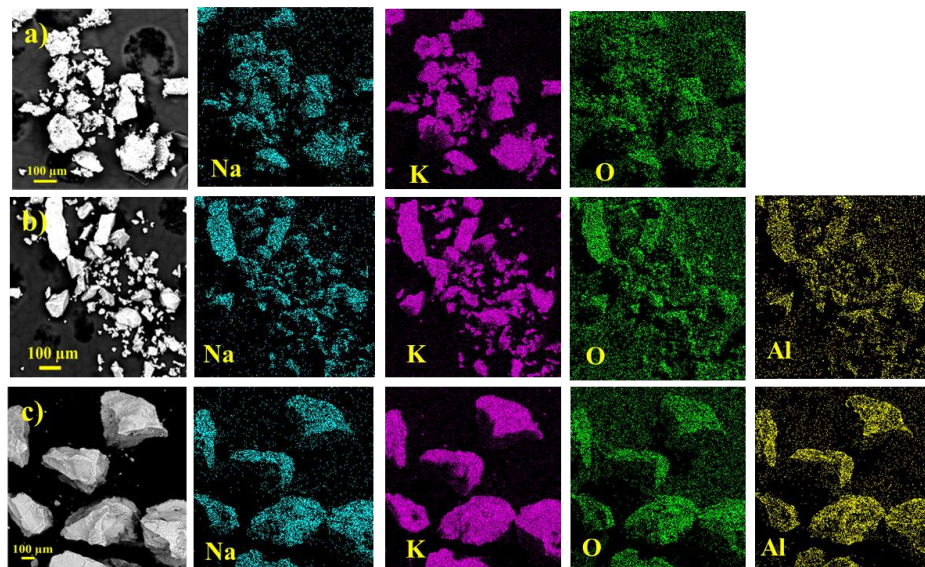
Figure 3.4. SEM images and their corresponding EDX compositional maps for: a) Eutectic salt, b) Al_2O_3-NPs-nanofluid and c) Al_2O_3-NRs-nanofluid.

The FTIR spectra of the eutectic salt, nanomaterials and nanofluids were measured at room temperature in transmission mode in the range of 4000–400 cm^{-1}. The stretching and bending vibration modes were determined, aiming to use this information to detect any structural changes of these nanoparticles and inorganic salts during the preparation processes. Figure 3.5 shows the room temperature FTIR spectra of Al_2O_3-NPs, Al_2O_3-NRs, eutectic salt, Al_2O_3-NPs-nanofluid and Al_2O_3-NRs-nanofluid before and after the melting process. In the case of Al_2O_3-NPs, the bands around 510 cm^{-1} and 741 cm^{-1} were ascribed to the Al-O-Al bending mode and stretching vibration of Al-O bond in the γ-Al_2O_3 phase, respectively [81]. In the case of Al_2O_3-NRs, it is clear that the presence of both α-Al_2O_3 and γ-Al_2O_3 crystalline material due to the shift of the stretching and bending wavelengths and the band's form. The strong absorption broad bands were also assigned to the Al-O-Al bending mode and Al-O stretching vibration mode in the γ-Al_2O_3 phase. The present of α-Al_2O_3 is indicated by the presence of sharp hump over the broad peak in the region of 513 cm^{-1} and 728 cm^{-1} as indicated by red circles in the corresponding spectrum. The FTIR spectrum of the eutectic salt and eutectic salt with Al_2O_3 nanomaterials, obtained before and after the melting process, are also shown in the same Figure 3.5. In the case of the eutectic salt, we observed a small hump and band at around 725 cm^{-1} and 832 cm^{-1} for asymmetric in-plan bending modes and bending mode of the N-O bond. The broad peak obtained at around 1340 cm^{-1} corresponds to N-O asymmetric stretching modes. Two other weak bands are observed at around 1781 cm^{-1} and 2428 cm^{-1}, which correspond to the stretching modes of nitrate ions [82]. In addition, similar spectra were observed for Al_2O_3-NPs-nanofluid and Al_2O_3-NRs-nanofluid before and after the melting process. The FTIR results indicate, on the first hand, no degradation or modification of the involved eutectic salt during the shaking process; and, on the second hand, no specific interaction between the nanoparticles and eutectic salt during the preparation processes. Taking into consideration these results, we can validate this new dry method as a proper method for obtaining nanofluids without any degradation and modification of the base salt.
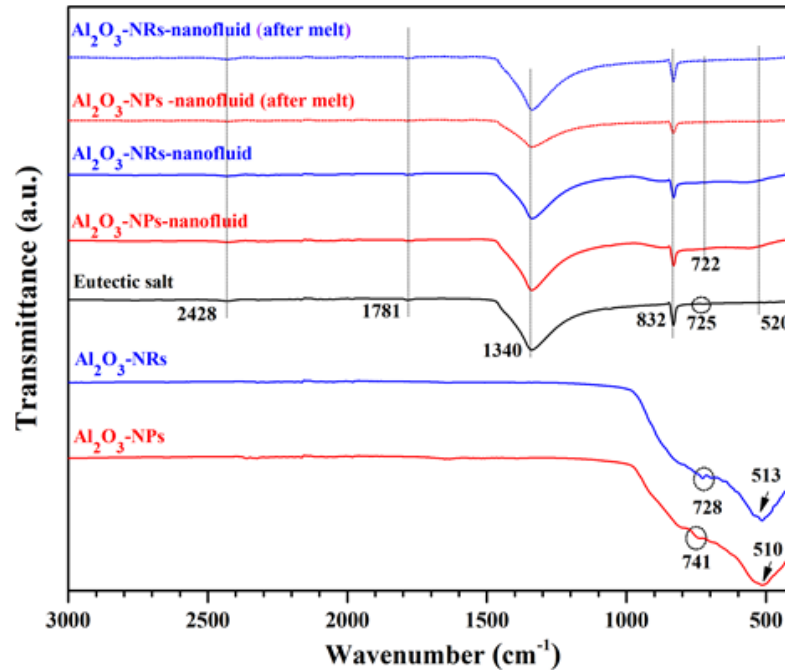
Figure 3.5. FTIR spectra of the nanomaterials, eutectic salt and nanofluids before and after melting process.

3.3. Thermophysical characterizations

3.3.1. Specific heat capacity analysis

Figure 3.6 shows the obtained specific heat capacity (C_p) curves for Al_2O_3–NPs, Al_2O_3–NRs, eutectic salt, Al_2O_3–NPs-nanofluid and Al_2O_3–NRs-nanofluid, in the solid and liquid states, in the temperature range of 120ºC – 340ºC. The Al_2O_3 nanoparticles count with lower C_p values compared to that of the eutectic salt, where values of 0.814 J/K·g and 0.871 J/K·g at 310ºC were obtained for Al_2O_3–NPs, Al_2O_3–NRs, respectively. These values are different from the value (0.835 J/K·g) reported at 310°C for the Al_2O_3 nanomaterials having a size range of 40-50 nm [83], but the differences are not significant. These differences are due to the crystallinity of the material, i.e. the concentrations of the α-Al_2O_3, γ-Al_2O_3 phases and amorphous part. The eutectic salt shows a C_p value of 1.45 J/K·g at 310ºC, as can be seen in Figure 3.6, which is in agreement with the most reported values in the literature [37]. Therefore, according to a simple mixing theory, the calculated specific heat capacity for nanofluids (dotted curves) shows slightly lower values than the pure eutectic salt due to the lower C_p of the Al_2O_3 nanomaterial compared to that of eutectic salt, as can be clearly seen in the inset Figure 3.6b. On the contrary, the experimental results show higher values of C_p for the nanofluids than for the eutectic salts, both in the

solid and liquid states. The C_p values obtained for the Al_2O_3–NPs-nanofluid and Al_2O_3–NRs-nanofluid at 310ºC were 1.5 J/K·g and 1.54 J/K·g, with average anomalous enhancements of 3% and 6%, respectively. The enhancement of the specific heat capacity due to the addition of nanoparticles may be explained through different hypotheses, among them; first, the formation of a compact solid salt layer on the surface of the nanoparticles and the interfacial thermal resistance arising at the solid-liquid interface, which acts as additional thermal capacity [32, 84]. In our case, we observed that the Al_2O_3-NRs-nanofluid has a higher specific heat capacity compared to that of the Al_2O_3-NPs-nanofluid which may be due to the higher surface area Al_2O_3-NRs (124 m^2/g) compared to that of Al_2O_3-NPs (93 m^2/g), i.e. more compact solid salt layer formation and higher interfacial thermal resistance. These results are in good agreement with the conclusion of the theoretical study presented in [85].
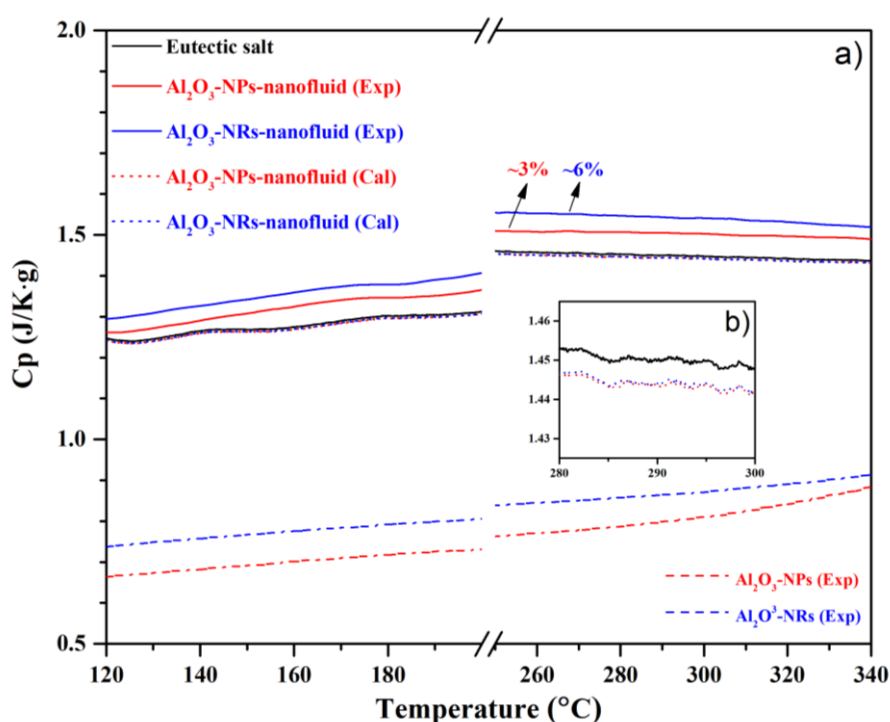
Figure 3.6. Specific heat capacity for Al_2O_3–NPs, Al_2O_3–NRs, eutectic salt, Al_2O_3–NPs-nanofluid and Al_2O_3–NRs-nanofluid.

3.3.2. Enthalpy measurements

Enthalpy and melting temperature of the eutectic salt and Al_2O_3 based nanofluids were simultaneously measured by the DSC technique and the results are shown in Figure 3.7. As it can be seen in the inset of Figure 3.7b, the doping of the

eutectic salt by Al_2O_3 induces slight changes in the form of the heat flow curves during the solid-liquid phase transformation. The melting and solidification enthalpies, as well as the melting and solidification temperatures, are reported in Table 3.1, in order to evaluate their variation in the presence of the nanoparticles. It is interesting to mention here that the addition of the Al_2O_3 nanomaterials into the eutectic salt leads to a decrease by around 1ºC of the melting point as well as the crystallization temperature of the nanofluids compared to eutectic salt. Similar results were already observed with doping of Solar salt by 1wt.% of Al_2O_3, TiO_2, SiO_2, where, the onset melting temperature was decreased by less than 1% compared to the base salt [38]. The author also showed that the dispersion of 1wt.% of SiO_2-Al_2O_3 in the Solar salt leads to a reduction of the onset melting temperature by 10°C [38]. These decreases on the melting point and solidification temperatures may be due to the nano-sized confinement of the salt in the interparticle space, and/or the pronounced heat transfer behaviour of the nanomaterials.

On the other hand, the melting and solidification enthalpies obtained for the nanofluids were lower than that of the base eutectic salt, which is due to the presence of 1wt.% of oxide material, i.e. nanoparticles, that were not contributing to the enthalpy. This result is in good agreement with the one reported in [22]. On the contrary, an anomalous enhancement of the enthalpy by more than 15% was reported for nanofluids based on Solar salt and 1wt.% of Al_2O_3, SiO_2 and Al_2O_3-SiO_2 [38]. It is important to note that in the last work, as mentioned above, the enthalpy enhancement was accompanied by an important decrease of the melting temperature of the same nanofluids, which may be due to the partial decomposition of the nitrate salts to nitrite salts during the preparation process.

Table 3.1. Melting and solidification enthalpies and temperatures of the eutectic salt, Al_2O_3-NPs-nanofluid and Al_2O_3-NRs-nanofluid.

Fluid	$\Delta H_{heating}$ (J/g)	T_m (°C)	$\Delta H_{cooling}$ (J/g)	T_{sol} (°C)
Eutectic salt	104	222	103	223
Al_2O_3-NPs-nanofluids	103	222	102	223
Al_2O_3-NRs-nanofluids	103	222	103	223
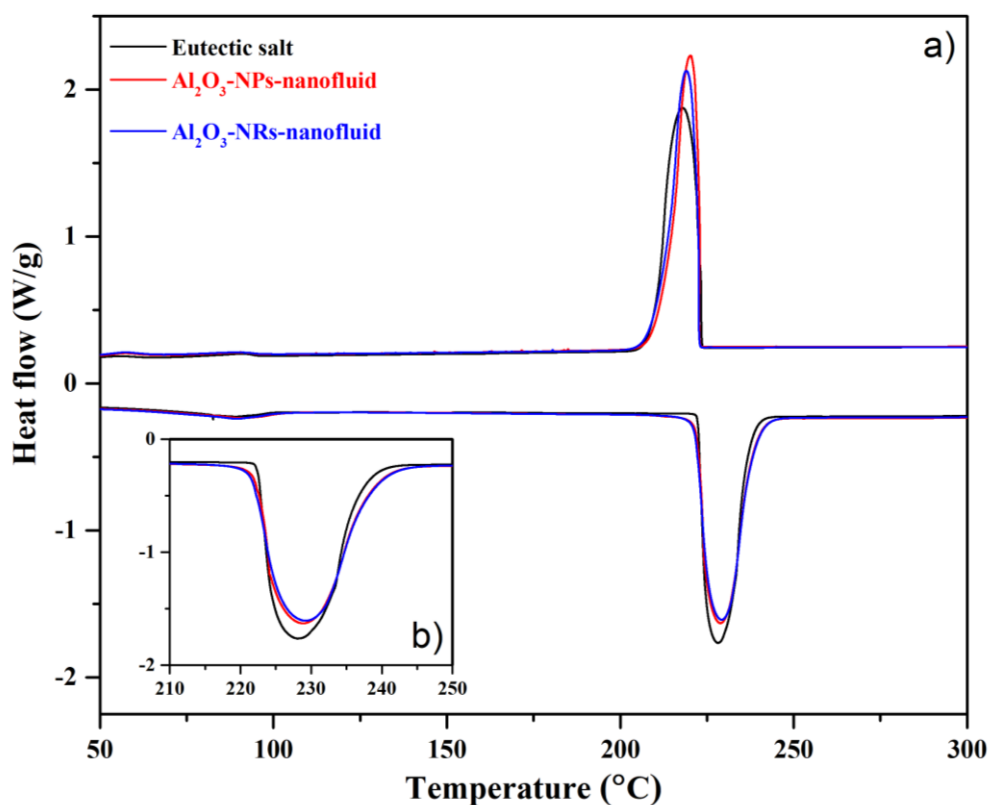
Figure 3.7. DSC measurements for eutectic salt, Al_2O_3-NPs-nanofluid and Al_2O_3-NRs-nanofluid.

3.3.3. Thermal conductivity analysis

Thermal diffusivity/conductivity of the eutectic salt and nanofluids were measured in the solid state as well in the molten state and the results are presented in Figures 4.10 a and b. The thermal conductivity was determined indirectly as follows $\lambda (T) = \alpha(T) \cdot \rho(T) \cdot Cp(T)$, as described in the experimental section. In the solid state, the density of the eutectic salt was measured at room temperature and its evolution with temperature was calculated (Figure 3.10), by using the thermal expansion of a salt pellet obtained from dilatometry as described below. In the liquid state, the density of the nanofluids was considered similar to that of the eutectic salt which was obtained from [86, 87]. The measurements were carried out in the temperature range from 50ºC to 200ºC covering the solid state and from 250ºC to 400ºC covering the liquid state. The thermal diffusivity and thermal conductivity for the eutectic salt, Al_2O_3-NPs-nanofluid and Al_2O_3-NRs-nanofluid are shown in Figure 3.8.

In the solid state, thermal conductivity enhancements of around 20% and 12% were observed for Al_2O_3-NRs-nanofluid and Al_2O_3-NPs-nanofluid, respectively. These enhancements are generally due to the contribution of the higher

heat transfer characteristic of the nanoparticles, i.e. high nanoparticle thermal conductivity of 2.5 W/m·K as considered in [88]. The highest enhancement was obtained for Al_2O_3-NRs-nanofluid, that might be due to the larger size of Al_2O_3-NRs compared to Al_2O_3-NPs and to the higher heat transfer behaviour through a preferred orientation along a particular direction [89]. Furthermore, while increasing the temperature the thermal conductivity of all three samples decreased, caused by the decrease of their thermal diffusivity and density, typical for inorganic salts.

In the liquid state, an opposite trend was obtained where a positive temperature dependence of the thermal conductivity, for all the samples, was observed that may due to the molten salt convection. Furthermore, at 270ºC the same thermal conductivity enhancement of 11% was observed for Al_2O_3-NPs-nanofluid and Al_2O_3-NRs-nanofluid. This enhancement may be due to two factors: the first one is related to the secondary nanostructure formation, which is proportional to the specific surface area of the nanoparticles and the second factor is linked to the Brownian motion of the nanoparticles inside the base fluids, affected by the nanoparticles size and shape [34, 90]. The maximum enhancements obtained at 400°C are 16 % and 12% for Al_2O_3-NPs-nanofluid and Al_2O_3-NRs-nanofluid, respectively. It can be seen that while increasing temperature the nanoparticles based nanofluid shows higher enhancement than nanorods based fluid because the second factor (Brownian motion) becomes dominant. In other words, the heat transfer due to the Brownian motion, by means of smaller spherical nanoparticles, is more efficient compared to larger nanorods, due to their shape and size. These results are in agreement with the conclusions reported in [90, 91].
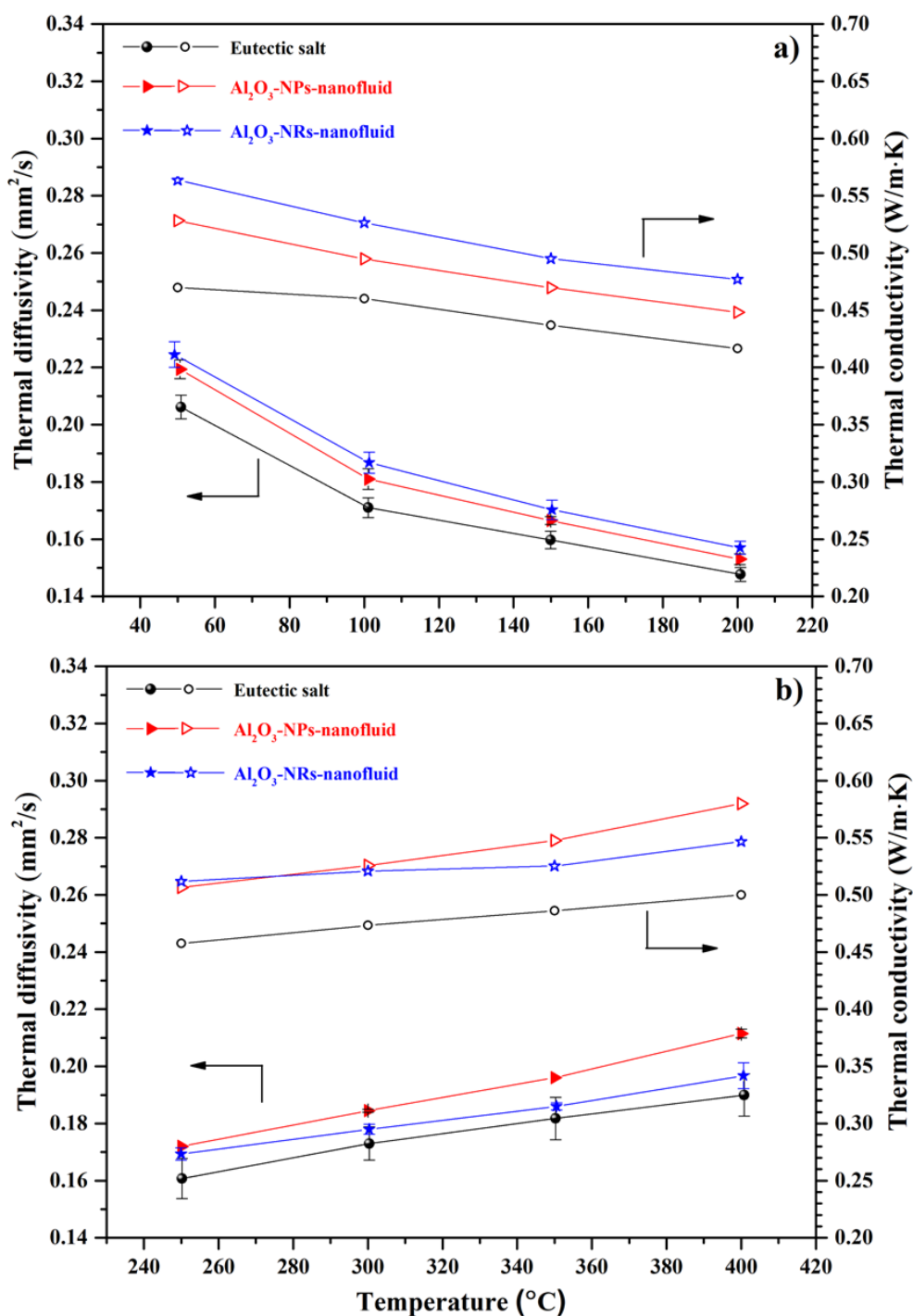
Figure 3.8. Thermal diffusivity (closed symbols) and conductivity (open symbols) of the eutectic salt, Al$_2$O$_3$-NPs-nanofluid and Al$_2$O$_3$-NRs-nanofluid in the solid state (a) and in a liquid state (b).

Thermal evolution of eutectic slat density

The density of the cylindrical pellet of eutectic salt was measured at room temperature by using helium pycnometer. The measurements were performed for 10 times and an average value of 2.1736 g/cm³ was obtained. The evolution of the

density of the eutectic salt was calculated by means of room temperature density and the thermal expansion according to the following equation.

Figure 3.9 shows the linear thermal expansion (dL/L_0) obtained by dilatometer for the eutectic salt pellet in the temperature range from 30°C to 200°C. From the graph, we can distinguish two linear thermal expansion coefficients of $1.66 \cdot 10^{-5}$ K^{-1} and $6.38 \cdot 10^{-5}$ K^{-1} for the temperature ranges of 30°C – 90°C and 90°C – 200°C, respectively. This behaviour is due to the solid-solid phase transition of KNO_3 salt as explained in [92].

Figure 4.10 shows the calculated evolution of density with temperature from the density at room temperature and thermal expansion curve using the following formula:

$$\rho(T) = \frac{\rho_{RT}}{\left(1 + \frac{dL}{L_0}\right)^3}$$

Where, ρ (T) is the variation of density with temperature, ρ_{RT} is density at room temperature and dL/L_o is the linear thermal expansion.
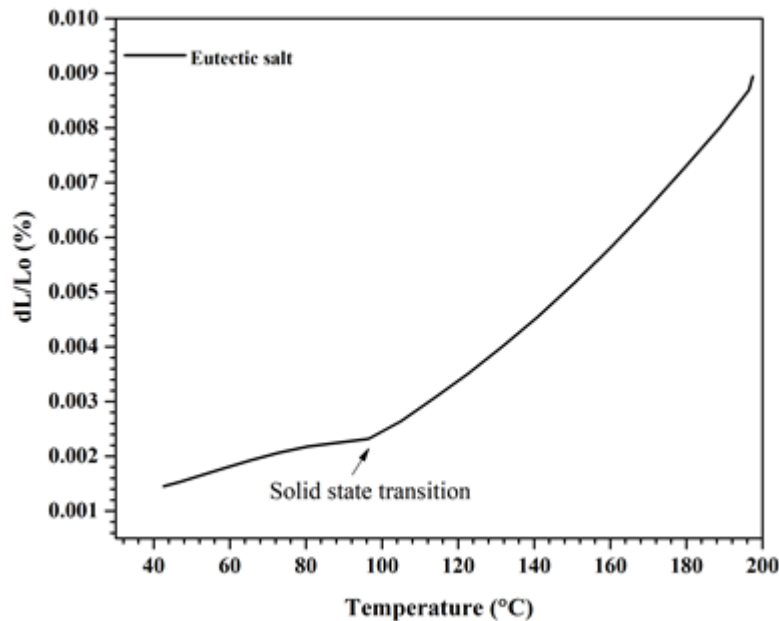
Figure 3.9. Dilatometry measurement of the eutectic salt.
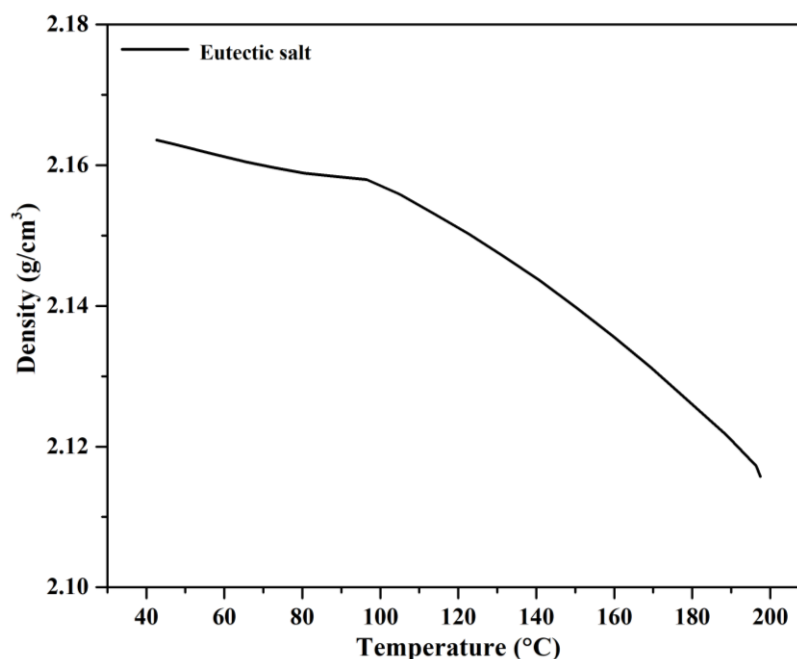
Figure 3.10. Calculated density of eutectic salt as a function of temperature.

3.3.4. Viscosity analysis

The viscosity of the base fluid and nanofluids was measured at 250, 300, 350 and 400°C – Figure 3.11 The suspension of 1 wt.% of Al_2O_3 nanoparticles in the base fluid results in a viscosity increase. The viscosity decreases with temperature for all the samples due to the weakening of the intermolecular attractions [93]. The Al_2O_3-NRs-nanofluid has higher viscosity compared to that of the Al_2O_3-NPs-nanofluid due to the high hydrodynamic resistance of the Al_2O_3 nanorods. In addition, we observed a decrease in the viscosity while increasing the temperature, but in comparison with the eutectic salt, the increment of viscosity was high at the highest temperature. The Al_2O_3-NPs-nanofluid and Al_2O_3-NRs-nanofluid show, respectively, increments of 5% and 12% at 250°C and 25% and 37% at 400°C compared to the eutectic salt. This trend may be due to a partial agglomeration of the Al_2O_3 nanomaterial at high temperatures. The viscosity of nanofluids based on molten salt was studied in [94], where it was reported an increment of 61% at 250°C when 1 wt.% of fiber-shaped Al_2O_3 nanoparticles with a length of 50 nm and a diameter of 10 nm were added to Solar salt. The concentration, nature, shape and size of the nanoparticles used in the experiment are similar in the present work. Therefore, the higher viscosity increment of 61% may be due to the agglomeration of

the nanoparticles caused by the use of Alumisol 10 A, a water-based nanofluid, as a source of nanoparticles. The absence of more viscosity experimental values for similar nanofluids in literature obstructs further comparisons.

The increase of the viscosity is not beneficial for this kind of nanofluids since an increase of the pumping power will be necessary, so minimizing the effect on the viscosity is considered an important parameter for the industrial implementation of these materials. Therefore, in the present work, it was demonstrated that the elongated structure of the nanorods with higher hydrodynamic resistance results in higher viscosity compared to that of the spherical nanoparticles.
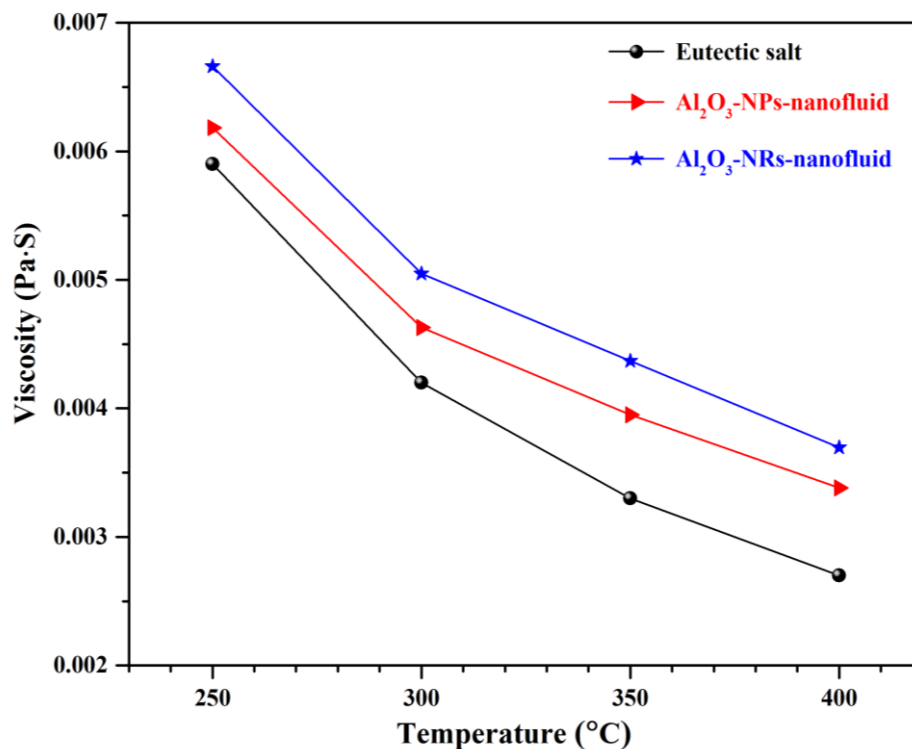
Figure 3.11. Rheological analysis of the eutectic salt, Al_2O_3-NPs-nanofluid and Al_2O_3-NRs-nanofluid.

3.3.5. Thermal stability analysis

TGA analysis of the eutectic salt, Al_2O_3-NPs-nanofluid and Al_2O_3-NRs-nanofluid with a heating rate of 10 °C/min under argon atmosphere was conducted. Figure 3.12 shows the TGA decomposition curves obtained for the samples in the temperature range from 100ºC to 700ºC. Generally, the decomposition point depends on several parameters such as the impurity of the salt, heating rate, atmospheric condition and crucible materials. However, in the present work, we tried to fix

similar parameters for the three investigated materials aiming for obtaining comparative results.

From the TGA results, we observe a similar decomposition behaviour for nanofluids compared to the eutectic slat, with no major mass loss or change in the decomposition temperature observed. In all the cases, we observed around 1% of mass loss at 638°C, which generally indicates the stability of eutectic salt was not affected by the addition of the nanomaterials. These results confirm that, on the first hand, the nanoparticles did not affect the stability of the base salt, and, on the second hand, the dry method used in the present work did not introduce any kind of contamination by new impurities to the salt.
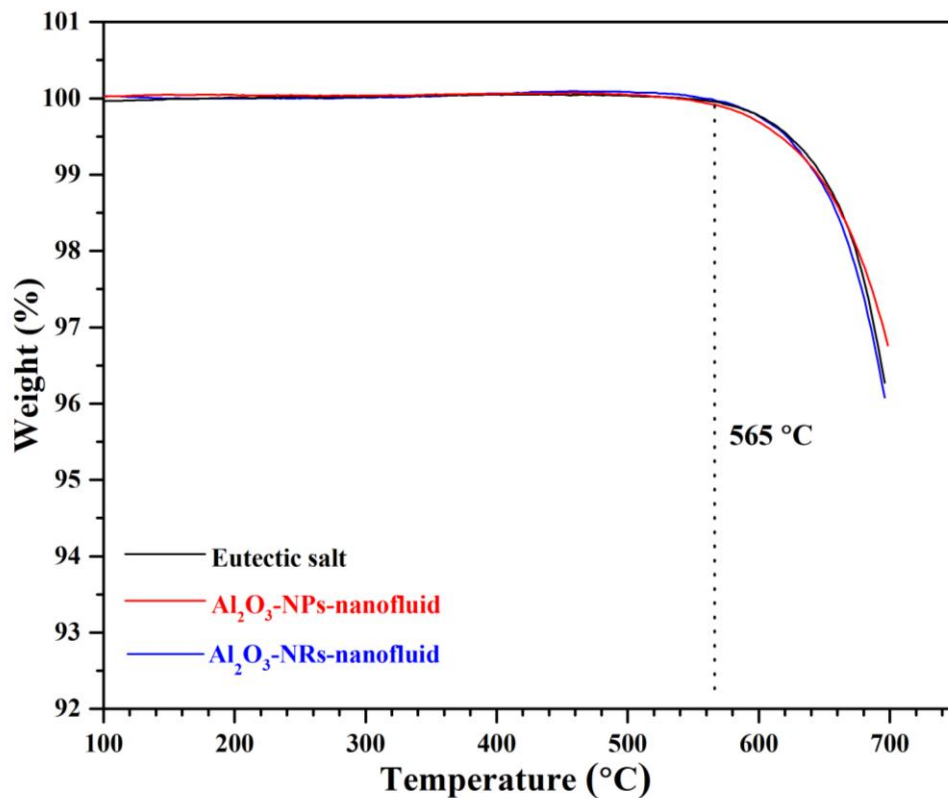
Figure 3.12. TGA decomposition curves of the eutectic salt, Al_2O_3-NPs-nanofluid and Al_2O_3-NRs-nanofluid.

3.4. Economical evaluation

The main motivation of the scientific community for developing nanofluids with enhanced thermophysical properties is lowering the investments costs at CSP plants and thus reducing the levelized cost of electricity (LCOE) produced by this renewable technology making it more competitive. Taking that into consideration, it

is very important to highlight the economic benefits of using the results obtained in the present work. First, a new simple method has been demonstrated as an efficient method for nanofluid preparation. This dry preparation method has several advantages compared to a wet method such as a good dispersion of nanoparticles, short preparation time and the possibility of on-site preparation. This allows obtaining nanofluids at industrial scale with a reasonable cost compared to the wet method.

Second, both nanofluids show significant enhancements of heat capacity by 3% and 6% that will lead to a reduction of the quantity of the required storage media to store the same amount of energy and by, consequence, the volume of the storage tanks can be reduced. In order to highlight this benefit, a simplified calculation, due to the fact that rigorous evaluation is quite complicated, was made taking Noor III CSP Tower plant at Ouarzazate, Morocco, as an example. In this particular case, 37.500 tons of Solar salt is used inside tanks with a volume of 14.243 m^3 for each one [95]. Table 3.2 shows the energy densities calculated for Solar salt, Al_2O_3-NPs-nanofluids and Al_2O_3-NRs-nanofluids, by using equation (1), where E is energy density, C_p is the average specific heat capacity of the fluids in the particular operating temperature and T1 and T2 are the initial and final working temperature of the fluids (380ºC – 565ºC):

$$E = \int_{T1}^{T2} Cp \, dT \qquad (1)$$

Therefore, the quantity of the fluid and the volume of each tank were calculated based on the energy density obtained for each and the results are presented in Table 3.2. As can be seen, the quantity of the storage material required in the case of Al_2O_3-NPs-nanofluids and Al_2O_3-NRs-nanofluids are respectively 36.193 tons and 35.092 tons which correspond to a reduction of 1.307 tons and 2.408 tons in comparison to the case of Solar salt. For the tank volume, a reduction of each tank volume by 492 m^3 and 915 m^3 were respectively obtained for Al_2O_3-NPs-nanofluids and Al_2O_3-NRs-nanofluids compared to Solar salt case.

Finally, the enhancement of the thermal conductivity obtained for Al_2O_3-NPs-nanofluids and Al_2O_3-NRs-nanofluids will increase the heat transfer efficiency from the storage fluid to water for steam production that is used to turn the steam turbine. Thus, this will lead to a considerable simplification of the heat exchanger configuration and will result in further costs reduction.

Table 3.2. Average values of heat capacity and thermal conductivity, the calculated energy density, quantity of salt and tank volume for Solar salt, Al_2O_3-NPs-nanofluids and Al_2O_3-NRs-nanofluids.

CSP plant	Material	Average C_p (kJ/kg*K) in 380-565°C	Average λ (W/m·K) in 380-565°C	Energy density (kJ/kg)	Q_{salt} (tons)	V_{tank} (m^3)
NOOR III	Solar salt	1.5	0.5	277	37500	14243
	Al_2O_3-NPs-nanofluid	1.55	0.6	287	36193	13746
	Al_2O_3-NRs-nanofluid	1.6	0.55	296	35092	13328

Chapter 4. Nanoparticles Size Effect

Despite the big effort made in the literature to obtain molten salts based nanofluids with enhanced thermophysical properties, their stability remains an open issue. In this regard, the present chapter aims to investigate the nanoparticles size effect on the enhancements of the heat capacity, thermal conductivity and viscosity of the molten salt, where special attention was made to understand the dispersion stability behaviour of the investigated nanofluid. For that purpose, the effect of SiO_2 nanoparticles size was systematically studied. Three types of SiO_2 nanoparticles with average sizes of 27 nm, 450 nm and 800 nm, the first one received from Sigma-Aldrich and the other two prepared in this work, have been used for the preparation of the nanofluids. By means of in situ high-temperature observations and zeta potential experiments, it was demonstrated that larger nanoparticles lead to better stability of a molten salt based nanofluid, despite the lower enhancement of thermophysical properties. The obtained results define a clear pathway for the development of molten salts based nanofluids, where a compromise between stability and thermophysical properties enhancement may be tuned by nanoparticle size.

4.1. Structural analysis

The SiO_2 nanoparticles were analysed by SEM and TEM techniques to identify the size, shape and initial agglomeration state of their particles. Figure 4.1 shows the TEM micrograph of the commercial SiO_2 nanoparticles and SEM micrographs of both synthesized SiO_2 nanoparticles obtained at 600°C with their size distribution histograms. The commercial SiO_2 nanoparticles show interconnected spherical particles shapes with an average size of each particle of 27 ± 1 nm.

Whereas, the synthesized SiO$_2$ nanoparticles show a spherical shape with monodispersed nature. The nanoparticles synthesized at pH ~ 8 have an average size of 450 ± 40 nm while increasing the pH of the solution from 8 to 9 the average size of SiO$_2$ was increased to 800 ± 30 nm. All different sizes of SiO$_2$ nanoparticles were calcined at 600°C and the calcination process did not exhibit any change of size and morphology, which indicates the stability of nanoparticles at high temperature. For simplification, the SiO$_2$ nanoparticles with the average size of 27 ± 1 nm, 450 ± 40 nm 800 ± 30 nm are referred in the text as SiO$_2$-27, SiO$_2$-450 and SiO$_2$-800, respectively.
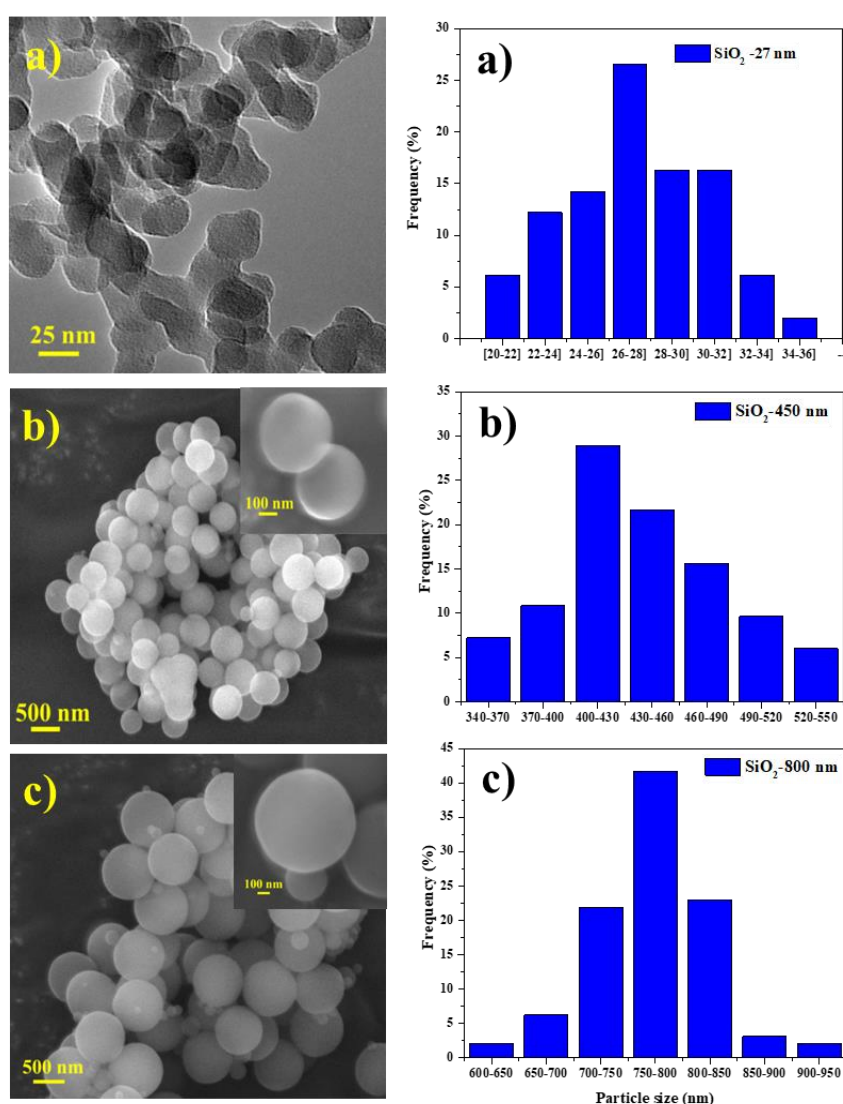
Figure 4.1. (a) TEM micrograph and its size histogram of the commercial SiO$_2$ nanoparticles and (b,c) SEM micrographs and their size histograms of the synthesized SiO$_2$ nanoparticles after calcination at 600°C.

The XRD analyses of SiO_2-27, SiO_2-450 and SiO_2-800 after calcination at 600°C are shown in Figure 4.2. From the obtained diffractograms, it is clear that the three different sizes of SiO_2 nanoparticles show the typical amorphous nature of the SiO_2 materials. The amorphous nature was confirmed by the broad diffraction peaks appeared at around 22°, as well as no other observable sharp peaks in the pattern [96].
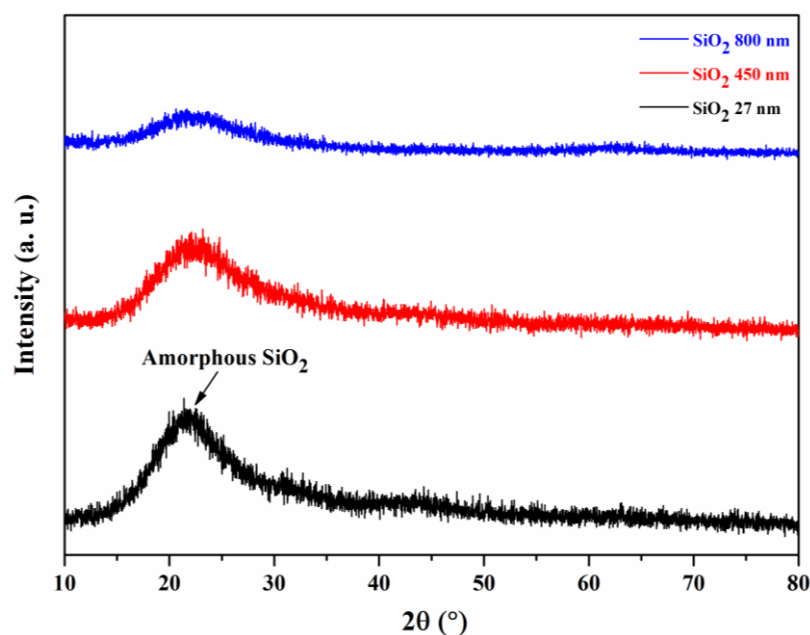
Figure 4.2. X-ray diffraction (XRD) patterns collected at room temperature for SiO_2-27, SiO_2-450 and SiO_2-800 nanoparticles calcined at 600°C.

FTIR analysis was carried out to know the vibration modes of the SiO_2-27, SiO_2-450 and SiO_2-800 which is obtained before and after the calcination at 600°C. The obtained FTIR spectra at room temperature are shown in Figure 4.3. The peaks at 1220 cm^{-1} and 1070 cm^{-1} denote the asymmetric stretching vibration modes of Si-O-Si bond. The peak observed at 947 cm^{-1} for synthesized SiO_2-450 and SiO_2-800 is due to asymmetric bending and stretching vibration modes of Si-OH and which is not appearing in the samples calcined at 600°C [97]. The symmetric vibration of Si-O bond was observed at 812 cm^{-1} and bending vibration of Si-O-Si bond was obtained at 458 cm^{-1} [98]. The FTIR results confirm the obtaining of pure silica oxide materials.
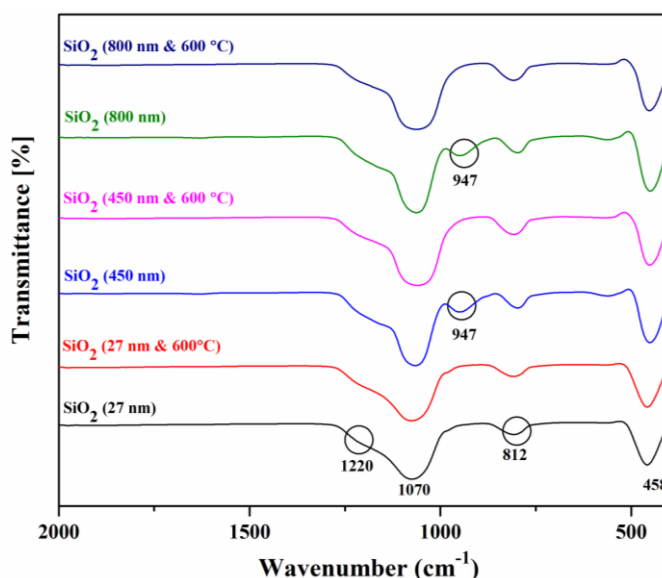
Figure 4.3. FTIR spectra of the three different sizes of SiO_2 nanoparticles showed before and after calcination at 600°C.

For understating the effect on the thermophysical properties, the surface area of the nanoparticles is having major contributions. Therefore, the surface area of the three SiO_2 nanoparticles was analysed by N_2 physisorption technique and their corresponding isotherms were shown in Figure 4.4. The surface areas of 148 m^2/g, 12.6 m^2/g and 5.6 m^2/g were observed for SiO_2-27, SiO_2-450 and SiO_2-800 nanoparticles, respectively. In general, the specific surface area is inversely proportional to the size of the particles, which is the same case observed in this work. But the higher surface area of SiO_2-27 compared to SiO_2-450 and SiO_2-800 ones are associated to artificial interparticle pores of the interconnected particles (Figure 4.1a) differently to synthesized ones, which are monodispersed (Figures 4.1 and 4.13c).
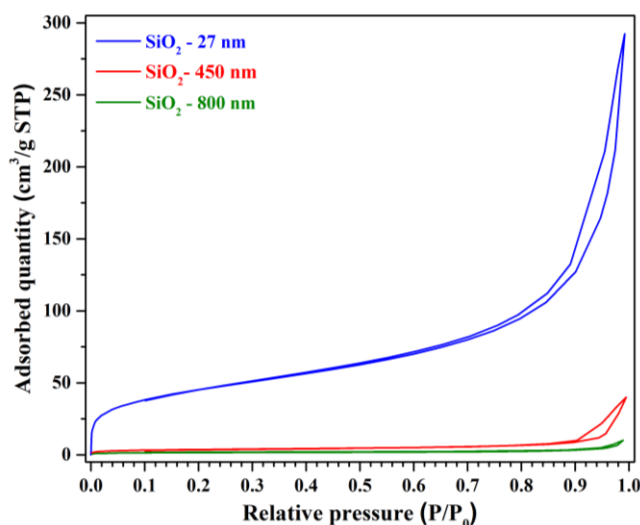
Figure 4.4. Adsorption/desorption Brunauer –Emmett-Teller (BET) isotherms of the SiO_2-27 and B) SiO_2-450 and SiO_2-800 nanoparticles.

4.2. Preparation of SiO₂ based molten salt nanofluids and analysis

The dispersion of the SiO_2 nanoparticles in the molten salt was studied with the help of SEM-EDX mapping as shown in Figure 4.5. The homogeneous dispersion of nanoparticles in the molten salt was optimized by studying the dispersion time of high-energy physical milling from 5 to 30 min, the corresponding SEM micrographs are shown in Figure 4.5. The dispersion of nanoparticles in the nanofluids has a major contribution for obtaining not only the maximum enhancement of thermophysical properties but also the stable performance with time. While non-homogeneous dispersion produces sedimentation of the nanoparticle and final results will affect the thermophysical properties of the nanofluids which give aberrant values and may be the response of the discrepancy of the results were reported in the literature [99].

In the present study, the nanofluids prepared between 5 and 10 minutes show a non-homogeneous dispersion of the SiO_2 nanoparticles into molten salt. Nevertheless, once we increased the time of physical milling to 15 min the SiO_2 nanoparticles become more homogeneously dispersed into the molten salt, which is evidenced by SEM image and EDX mapping. Furthermore, while the dispersion time increased to 30 min the nanoparticles tend to agglomerate. The optimum well-dispersed SiO_2 based nanofluids were obtained at the physical milling time of 15 min. This method has an advantage of shorter preparation time, no need for additional temperature treatment to evaporate water and it can be easily scaled up to industrial levels.
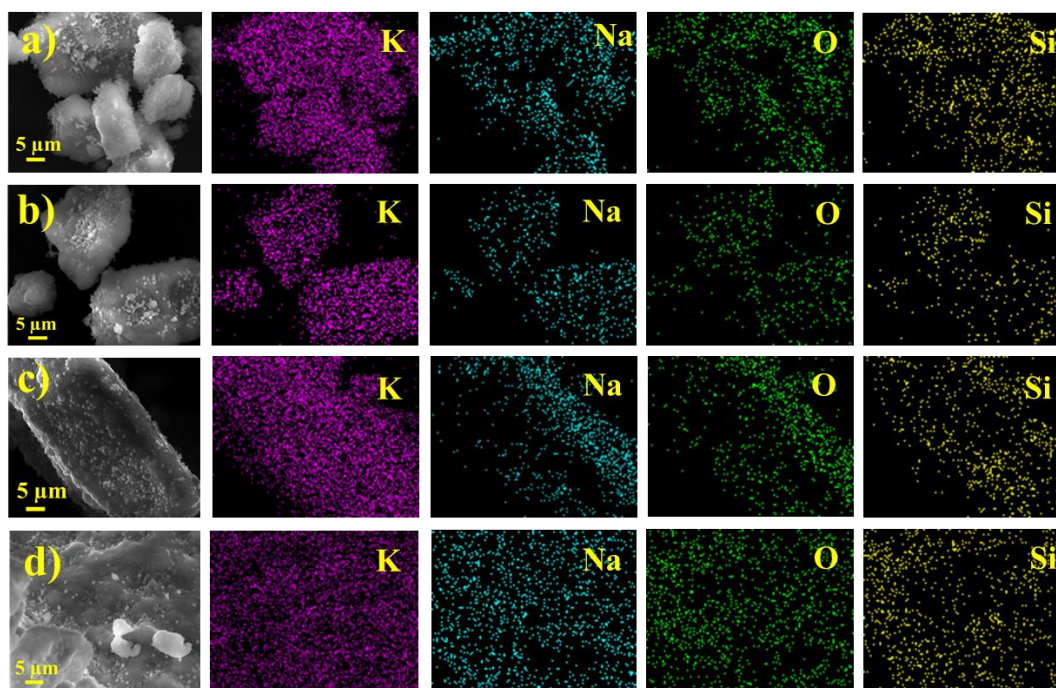
Figure 4.5. SEM micrographs and their corresponding EDX mapping for SiO₂-800 based nanofluids after a) 5 min, b) 10 min, c) 15 min and d) 30 min of physical dispersion.

4.3. Thermophysical characterizations

The specific heat capacity measurements of SiO₂-27, SiO₂-450 and SiO₂-800 nanofluids are summarized in Figure 4.6. The SiO₂-27 based nanofluid shows around 1% of C_p enhancement compared to the base fluid. The high surface area of the nanoparticles which is come from the narrow inter-particles space leads to increase the thermal resistance between the molecules of eutectic salt and nanoparticles, this state will increase the interfacial interaction between the nanoparticles and molten salt helping to enhance the C_p value [32, 53]. Nanofluids prepared with SiO₂-450 and SiO₂-800 show a decrease of C_p -0.4% and -1.7%, which may be due to the related lower surface areas. The effect on the C_p value by addition of nanoparticles in the molten salt can be due to several reasons like Van der Waals force, the attractive force between the nanoparticles, sedimentation of the nanoparticles, the surface area of nanoparticles, nanoparticles dispersion and surface charge between the nanoparticles [53]. In the molten salt nanofluids, the electrostatic interaction between different salt mixtures and nanoparticles is different and simultaneously the nanoparticle tends to separate. After separation of the nanoparticles, the salt compounds crystallize on the surface of the nanomaterials as nanostructured materials. So depends on the size and surface area of the added nanoparticles, this

nanostructure will form and accordingly the smaller size of the nanostructure will give better enhancement compared to their bulk materials [100]. The larger size of the synthesized SiO_2 nanoparticles was not helping to enhance C_p of SiO_2-450 and SiO_2-800 based nanofluids.
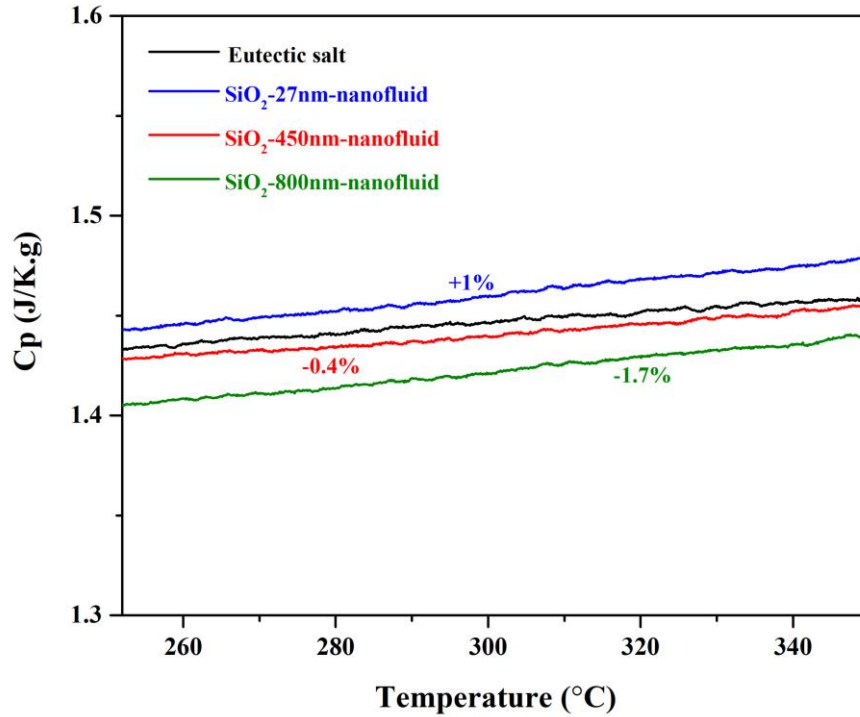
Figure 4.6. Specific heat capacity of eutectic salt and eutectic salt + 1wt% of three different SiO_2 nanoparticles.
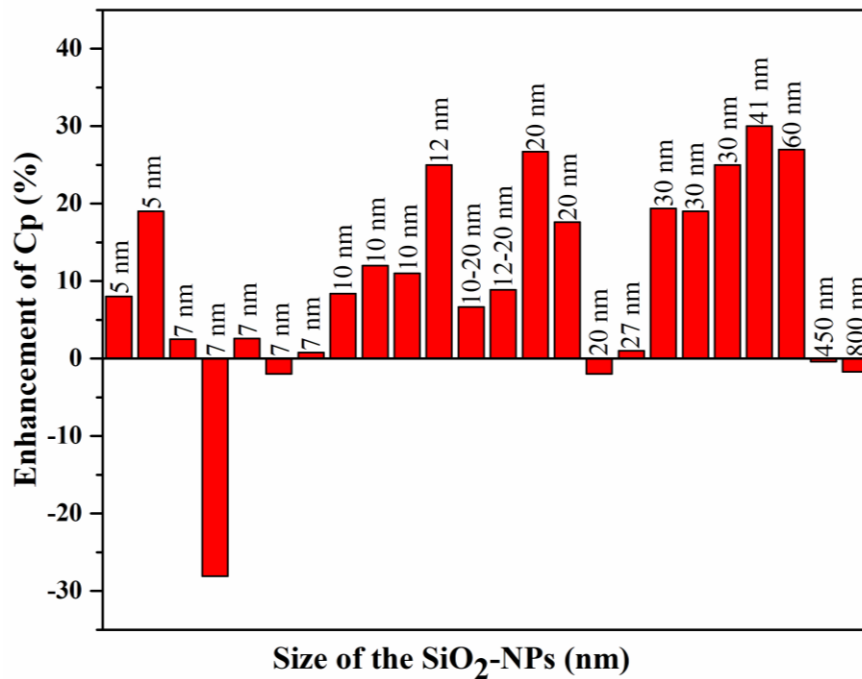
Figure 4.7. Specific heat capacity modification of binary nitrate salt + 1 wt % SiO_2-NPs in the liquid state [36-38,40-46].

From the overall literature overview (Figure 4.7), it is clear that the positive and negative values were observed from the different works, which may be due to the preparation method, size and most importantly stability of the nanofluids. The highest enhancement of 30% was observed for binary nitrate salt + 1 wt % SiO_2-NPs (41 nm) [101] and the negative effect of -28.1% were observed for binary nitrate salt + 1 wt % SiO_2-NPs (7 nm) [30].

The thermal diffusivities/conductivities of the eutectic nitrate salt and three different molten salt-based nanofluids are shown in Figure 4.8. The three SiO_2 based nanofluids show decrement of thermal diffusivity/conductivity compared to their base fluids. The maximum decrement of thermal diffusivity is -18% and thermal conductivity is ~ -17% for SiO_2-800 nanofluids at 400°C. The increment in the thermal conductivity of the nanofluids depends on the properties of the nanomaterials like chemical nature, stability, concentration and surface area, etc. [53]. From the present study, we found that the spherical monodispersed nanoparticles reduce the thermal conductivity. The Brownian motion of particles and natural convection occurs during the phase change has a major influence on the thermal conductivity of the nanofluids [53].
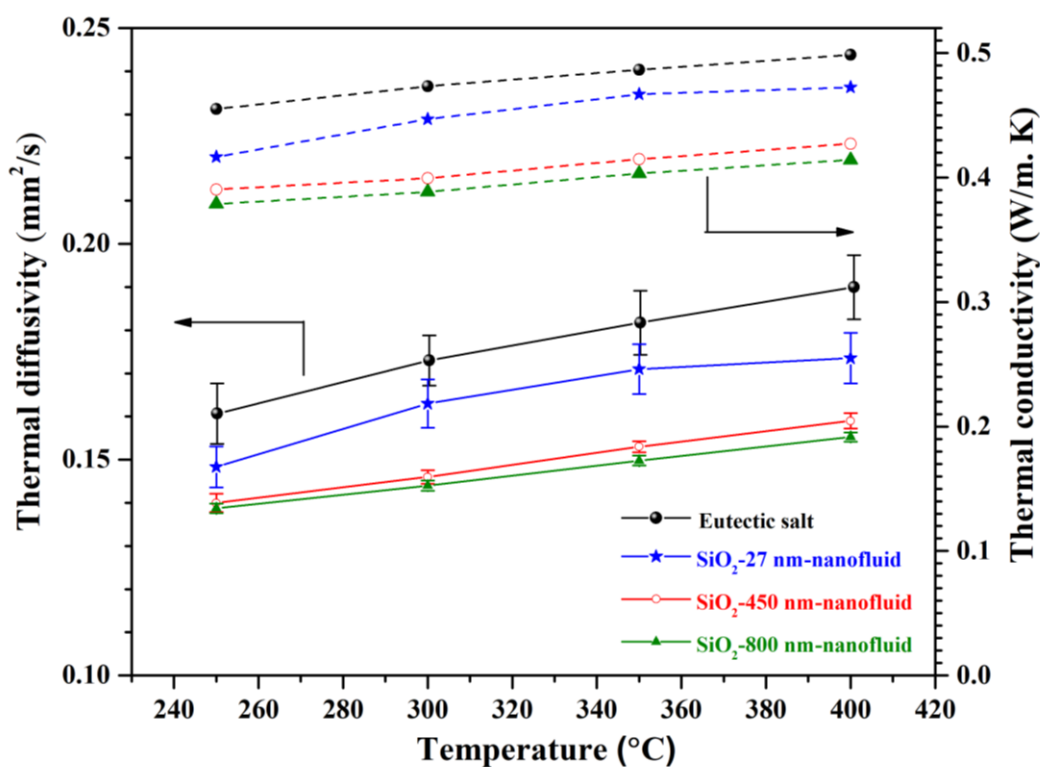
Figure 4.8. Shows the thermal diffusivity and thermal conductivity measurement of eutectic salt, SiO_2-27, SiO_2-450 and SiO_2-800 nanofluids in the temperature range 250-400°C.

Thermophysical properties are deviating due to the stability nanofluids. Regarding the thermal conductivity measurement, very few works were presented, especially for the binary nitrates salt with nanoparticles. From the available report, Belén et al. show the 45 % increment of thermal conductivity by addition of the solar salt with 1 wt% SiO_2 nanoparticles (7 nm) [50].

The viscosity of the nanofluids has a considerable effect on the several thermophysical properties such as the convective heat transfer, pumping power and pressure drop in laminar flow, etc. In general, the viscosity of the base fluids increases while adding the nanoparticle which is due to the particle volume friction and the effect on the internal shear stress in the fluids [102]. The present work investigated the viscosity of three SiO_2 based nanofluids compared to the pure eutectic salt. The obtained results exhibit an increment of viscosity, which depends on the size of added SiO_2 nanoparticles as shown in Figure 4.9. Accordingly, the SiO_2-27 nanofluid shows the highest increment of viscosity by 238% while SiO_2-450 and SiO_2-800 nanofluids show respectively 32% and 27% at 250°C compared to the pure eutectic salt. Similarly, at a higher temperature, around 400°C the nanofluid contains SiO_2-27 shows an increment of 404%, SiO_2-450 and SiO_2-800 show around 48% compared to the pure eutectic salt. The nanofluids SiO_2-450 and SiO_2-800 show lower viscosity compared to SiO_2-27 is due to the lower inter-molecular attraction between the base fluids and nanoparticles as a result of the lower surface area of the synthesize SiO_2-450 and SiO_2-800 nanoparticles [103].

The SiO_2-27 nanofluids show an increase of viscosity ~ 5 times higher compared to the eutectic salt at 400°C, which is due to higher agglomeration of nanoparticles. A similar conclusion was obtained for ethanol (density 0.798 g/cm^3) based nanofluids with SiO_2 nanoparticles having a size of 35 nm, 94 nm and 190 nm and the results demonstrate that the nanoparticle having a larger size (190 nm) in the base fluid possess the lower viscosity [104]. The smaller particle size has a more compressed layer than larger particle due to higher surface area and smaller size has more volumetric concentration [105]. While decreasing the particles size at constant volume fraction, the inter-particle distance is decreasing which favours the Van der Waals attractive force, resulting in the agglomeration and higher viscosity of the nanofluids and the phenomenon was clearly observed in the present study [106].

However, monodispersed and spherical shaped synthesized SiO_2 nanoparticles show lower viscosity due to the presence of individual nanoparticles,

even in the melting state, compared to the one of commercially purchased SiO_2-27.
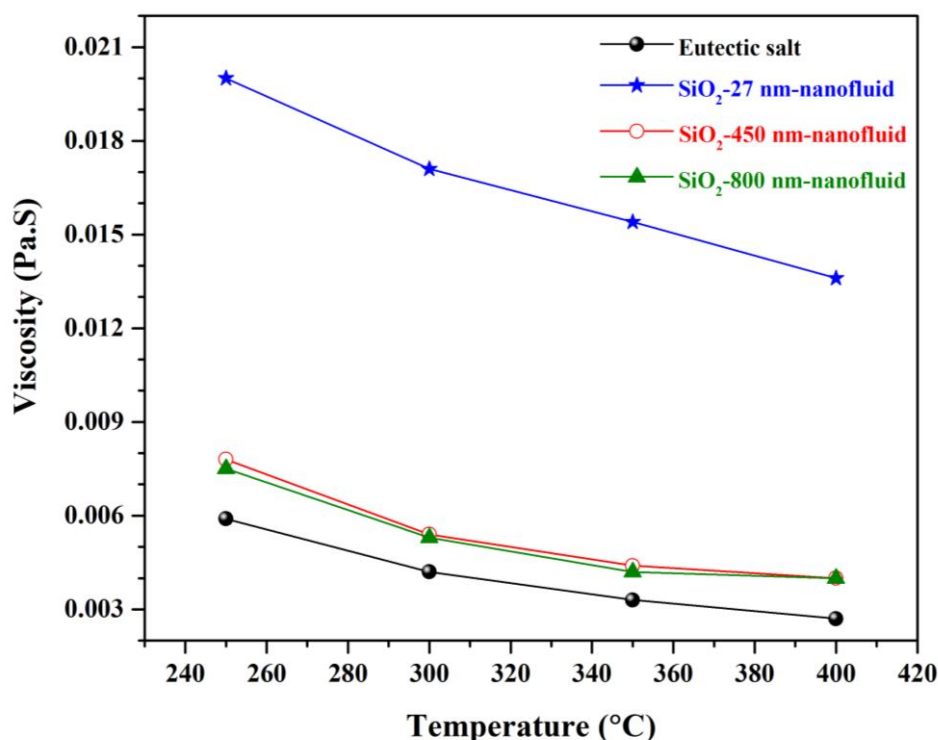
Figure 4.9. Rheometer analysis of the eutectic salt, SiO_2-27, SiO_2-450 and SiO_2-800 nanofluids.

Finally, the Surface charge of the nanoparticles is the most fundamental properties to know about the tendency of the colloidal stability of nanofluids. The stability of the nanofluid depends on the zeta potential value of the nanoparticles, accordingly if the value is $\pm$ 0-10 mV then it is highly unstable, $\pm$ 10-20 mV is relatively stable, $\pm$ 20-30 mV is moderately stable and $> \pm$ 30 mV is highly stable [107]. The measured zeta potential value for the aqueous based SiO_2-27, SiO_2-450 and SiO_2-800 is -28 mV, -36 mV and -36 mV, respectively. The synthesized SiO_2 nanoparticles have the tendency for high dispersion stability inside the nanofluids.

Figure 4.10 shows the stability test performed at the static mode in the furnace at 400°C for SiO_2-27, SiO_2-450 and SiO_2-800 based nanofluids. After re-dispersion by mechanical agitation, the results demonstrate that the SiO_2-27 nanoparticles were floating on the top of the molten nanofluid while in the case of the SiO_2-450 and SiO_2-800 maintained dispersed even after 24 hours.

In summary, the synthesized SiO_2 nanoparticles have shown a negative impact on the enhancement of the heat capacity and thermal conductivity; while a positive effect was obtained for the viscosity and dispersion stability with time. This result provides guidance on the development of stable nanofluids with enhanced

thermophysical properties through optimizing the combination between the size of the nanoparticles and the zeta potential value.
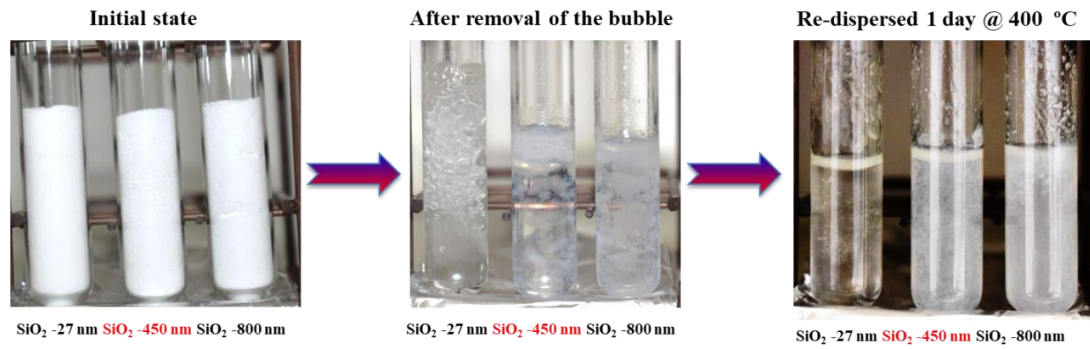
Figure 4.10 Visual stability of the molten salt-based SiO_2 nanofluids.

Chapter 5. Nanoparticles Composition Effect

Up to now, different types of monotype nanoparticles, especially Al_2O_3 and SiO_2 nanoparticles have been used for the preparation of molten salt-based nanofluids. Thus, the present chapter aims to investigate the effect of adding $SiO_2@Al_2O_3$ core-shell nanoparticles, which possess different chemical nature and gravitation effect in the base fluids, on the dispersion stability and thermophysical properties of the nanofluids. Therefore, the Al_2O_3-12 nm nanoparticles were used as a core and the thickness of the SiO_2 outer shell was controlled by changing the concentration of silica precursor. The formation of $SiO_2@Al_2O_3$ core-shell was confirmed by FTIR, TEM, SEM, EDX analyses. The new $SiO_2@Al_2O_3$ core-shell nanoparticles will help to obtain the stable nanofluids based on the inorganic molten salts. However, $SiO_2@Al_2O_3$-10, $SiO_2@Al_2O_3$-20 and $SiO_2@Al_2O_3$-35 core-shell nanoparticles with an inner diameter, i.e. Al_2O_3, of 12 nm and shell diameter, i.e. SiO_2, of around 1 nm, 2 nm and 5 nm were obtained, respectively. The effects of the new $SiO_2@Al_2O_3$ core-shell nanoparticles on the thermophysical properties of the base fluid ($NaNO_3$-KNO_3 with 51-49 wt%) were studied by laser flash analysis (LFA) and rheometry techniques. Changes of the thermophysical properties and viscosity of the nanofluids were observed depending on the thickness of the outer shell size of SiO_2 in the nanomaterials.

5.1. Characterization of the core-shell nanoparticles

Figure 5.1 shows the room temperature XRD diffractogram of $SiO_2@Al_2O_3$-10, $SiO_2@Al_2O_3$-20 and $SiO_2@Al_2O_3$-35 core-shell nanoparticles after being calcined at 600ºC. From the XRD analyses, the three different types of $SiO_2@Al_2O_3$

core-shell nanomaterials show as main phase Al_2O_3 with the cubic structure (γ-Al_2O_3) having a space group of F d -3 m. In addition, the presence of a small broad peak at around 22º was found which corresponds to the amorphous SiO_2 [108]. The pre-eminence of the Al_2O_3 peaks was observed due to very thin layer formation of SiO_2 on the top of Al_2O_3 nanomaterials. The amorphous nature of SiO_2 was found in all the $SiO_2@Al_2O_3$ core-shell nanomaterials.
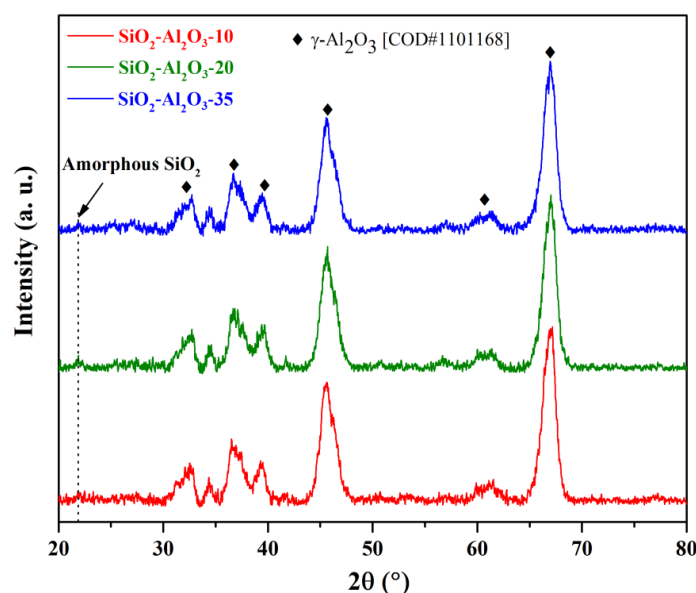
Figure 5.1. X-ray diffraction (XRD) diffractograms of three $SiO_2@Al_2O_3$ core-shell nanoparticles calcined at 600°C.

The FTIR spectra of SiO_2, Al_2O_3, $SiO_2@Al_2O_3$-10, $SiO_2@Al_2O_3$-20 and $SiO_2@Al_2O_3$-35 nanoparticles are shown in Figure 5.2a. In case of SiO_2, the band observed at 459 cm^{-1} corresponds to Si-O-Si bending modes, 807 cm^{-1} is due to stretching vibration modes of Si-O-Si bond and at 1074 and 1220 cm^{-1} due to Si-O-Si asymmetric stretching modes [109]. In the case of Al_2O_3, the band at 511 cm^{-1} is assigned to the Al-O-Al bending mode, the one at 745 cm^{-1} to the Al-O stretching vibration mode and the band from 900 to 400 cm^{-1} is assigned for the vibrations of Al-O bond for Al octahedral [110, 111].

In the case of $SiO_2@Al_2O_3$ core-shell nanoparticles, compared to the individual Al_2O_3 and SiO_2 nanoparticles, we observed the appearance of new bands and the shift of the band positions corresponding to the wavenumbers of 811, 753, 730, 699, 657, 542 and 520 cm^{-1}. The appearance of new bands and the band shift were evidencing the formation of $SiO_2@Al_2O_3$ core-shell nanoparticles, which is also confirmed by SEM, TEM and EDX analyses. The presence of the SiO_2 characteristic bands is clearly observed in the region 1240-970 cm^{-1} as can be seen in

Figure 5.2b, thus, confirm the formation of the $SiO_2@Al_2O_3$ core-shell nanoparticles [108]. On the other hand, while increasing the concentration of Si precursor, the intensity of the bands is increased due to the increasing of outer SiO_2 shell thickness.
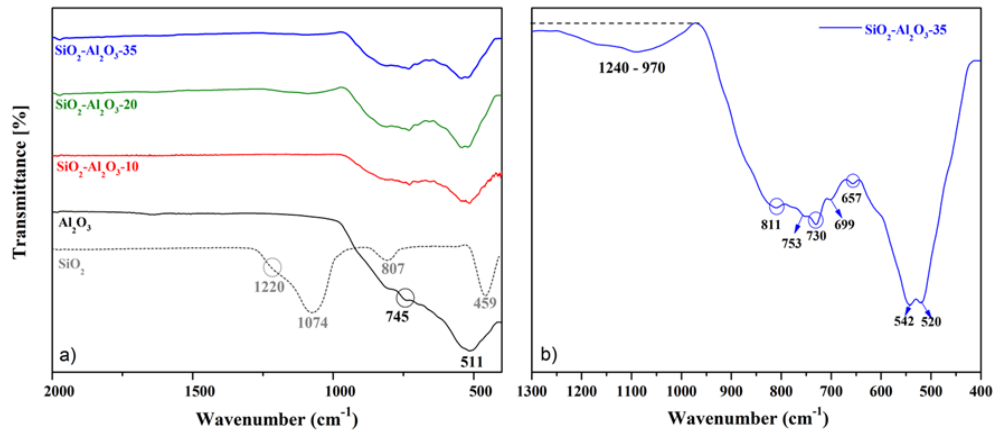
Figure 5.2. a) FTIR spectra of SiO_2, Al_2O_3 and $SiO_2@Al_2O_3$-10, $SiO_2@Al_2O_3$-20 and $SiO_2@Al_2O_3$-35 core-shell nanoparticles. b) enlarged view of $SiO_2@Al_2O_3$-35 spectra.

Figure 5.3 shows the SEM micrographs and their EDX with mapping analyses obtained for $SiO_2@Al_2O_3$-10, $SiO_2@Al_2O_3$-20 and $SiO_2@Al_2O_3$-35 core-shell nanoparticles. The homogeneity of synthesized core-shell nanomaterials was confirmed by EDX with a good distribution of Si and Al nanomaterials. The carbon peak present in the EDX spectrum is due to the adhesive carbon tape, which is used during the SEM sample preparation. In addition, the distribution of the Si and Al were confirmed from mapping as well. As it is expected, the weight and atomic concentrations of Si element increased while increasing the thickness of the outer shell.
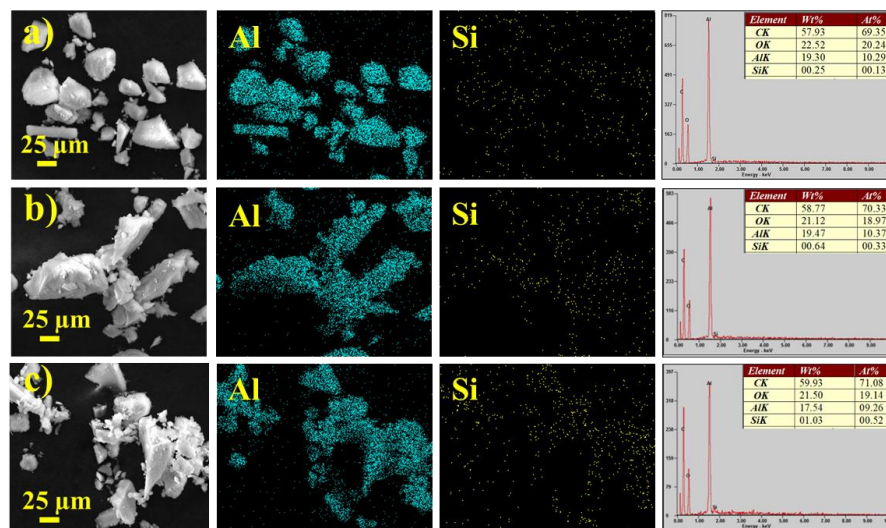
Figure 5.3. SEM micrographs and their corresponding EDX mapping and analyses of a) $SiO_2@Al_2O_3$-10, b) $SiO_2@Al_2O_3$-20 and c) $SiO_2@Al_2O_3$-35 core-shell nanoparticles.

Figure 5.4 shows the TEM micrographs of chain-like aggregation of SiO$_2$@Al$_2$O$_3$-10, SiO$_2$@Al$_2$O$_3$-20 and SiO$_2$@Al$_2$O$_3$-35 core-shell nanoparticles. From the TEM image, it is clear that the different thicknesses of the SiO$_2$ layer observed depend on the concentration of Si precursor. The SiO$_2$@Al$_2$O$_3$-10 nanoparticles show a particle size of 12 ± 2 nm, however, for the lowest concentration of Si precursor, the coating layer of SiO$_2$ is not clearly visible by TEM. Nevertheless, the presence of Si was observed by SEM-EDX with mapping analysis. While increasing the concentration of the Si precursor, the coating of the SiO$_2$ on the top of Al$_2$O$_3$ was clearly visible from the TEM image and forms a well-connected chain-like aggregation structure. For the sample of SiO$_2$@Al$_2$O$_3$-20 we observed a particle size of 14 ± 2 nm with an outer shell thickness of around 2 nm. Similarly, the size of SiO$_2$@Al$_2$O$_3$-35 is 17 ± 2 nm with an outer shell thickness of around 5 nm.
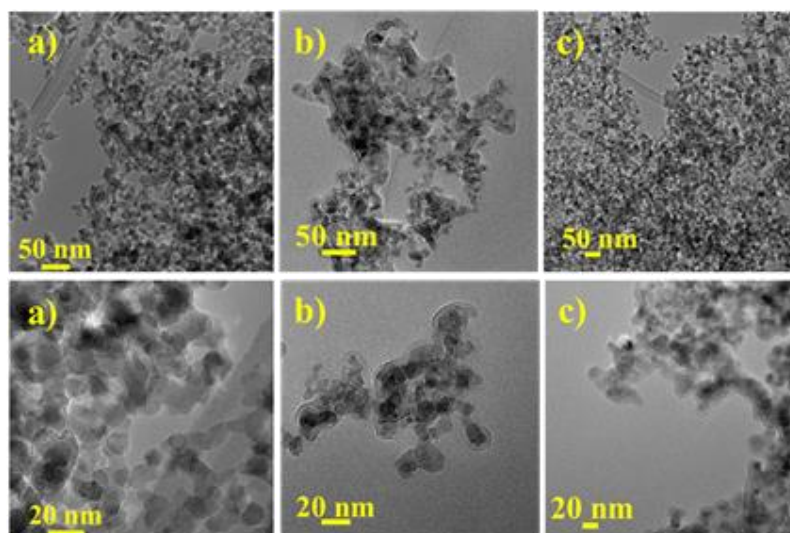
Figure 5.4. TEM micrographs with small and large magnifications of a) SiO$_2$@Al$_2$O$_3$-10, b) SiO$_2$@Al$_2$O$_3$-20 and c) SiO$_2$@Al$_2$O$_3$-35 core-shell nanoparticles.

5.2. Thermophysical properties of the nanofluids

The specific heat capacity, thermal conductivity, and viscosity are the key characteristics properties of the nanofluids, which are used in TES applications. According to Shin et al., the C$_p$ enhancement depends on different factors such as high surface energy or surface area of nanoparticles, semi-solid layer formation over the nanoparticles by molten salt and solid fluids interaction [112]. The C$_p$ enhancement was also explained by Zhang et al. by lamellar network structure via the creation of different thicknesses of high-density salt phase on the surface of the nanoparticles [99]. Recently, Mondragón et al. reported this enhancement to be

related to the ionic exchange properties between nanoparticles and molten salt [33]. So, the specific heat capacity of the molten salt-based nanofluids depends on the different parameters such as the preparation method of nanofluids, structure and size formed between nanoparticle and base fluids. There are several works demonstrating the influence of nanoparticle type on the specific heat capacity[99, 113, 114]. In the present work, a detailed investigation of the thermal conductivity and viscosity of $SiO_2@Al_2O_3$ core-shell molten nitrate salt based nanofluid was carried out.

Figure 5.5 shows the thermal diffusivity values obtained for the nanofluids based on $SiO_2@Al_2O_3$-10, $SiO_2@Al_2O_3$-20 and $SiO_2@Al_2O_3$-35 core-shell nanoparticles in the temperature range of 250-400ºC. Different results were obtained depending on the thickness of the outer shell of $SiO_2@Al_2O_3$ nanoparticles. A positive effect was observed for $SiO_2@Al_2O_3$-35, whereas, a negative effect was obtained for $SiO_2@Al_2O_3$-10 and $SiO_2@Al_2O_3$-20 core-shell based nanofluids. Thermal diffusivity of $SiO_2@Al_2O_3$-10 nanofluid shows a -8 to -4% decrease, $SiO_2@Al_2O_3$-20 nanofluid varies from 0 to -2% and $SiO_2@Al_2O_3$-35 nanofluid show an increase of 7 to 14% compared to the base fluid. Thermal conductivity (Figure 5.6) was calculated by using thermal diffusivity, density and specific heat capacity values of the corresponding $SiO_2@Al_2O_3$ nanofluids. Accordingly, $SiO_2@Al_2O_3$-10 nanofluid shows lower values by -6 to -2%, $SiO_2@Al_2O_3$-20 nanofluid shows different values ranging from 3 to -1% and $SiO_2@Al_2O_3$-35 nanofluid shows an increase of 11 to 19% in the temperature range of 250-400ºC.
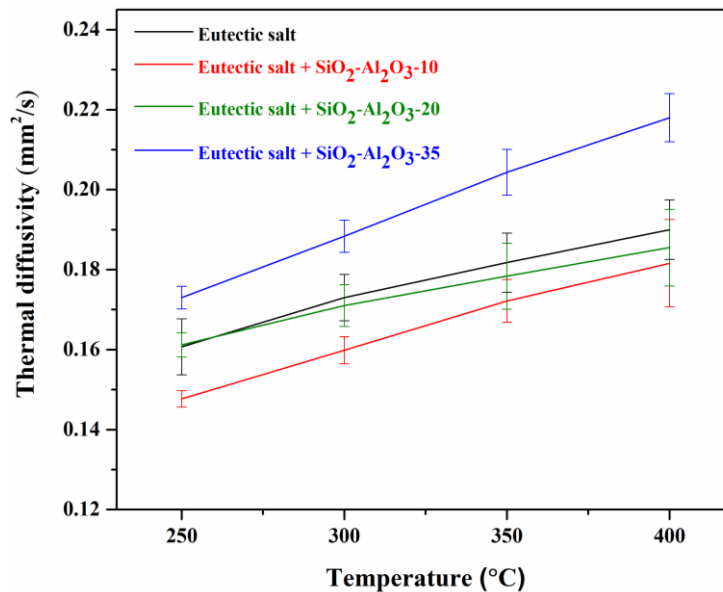
Figure 5.5. Thermal diffusivity of eutectic salt and eutectic salt + 1 wt% of $SiO_2@Al_2O_3$ core-shell nanoparticles.

Generally, different mechanisms were proposed for the enhancement of the thermal conductivity of nanofluids like Brownian motion of the nanoparticles, interfacial layer between the nanoparticles and base fluids, clustering effects of the nanoparticles and the intrinsic heat transport properties of the nanoparticles [11, 115]. In our case, a maximum enhancement of the thermal conductivity of 19% was observed for $SiO_2@Al_2O_3$-35 nanofluid, while zero or negative enhancements were observed for $SiO_2@Al_2O_3$-10 and $SiO_2@Al_2O_3$-20 nanofluids. This observation confirms that the well-connected chain-like aggregation between the SiO_2 and Al_2O_3 nanomaterials plays an important role in the enhancement of the thermal conductivity. Increasing the concentration of Si precursor helps to form a well-connected network structure, in this case for $SiO_2@Al_2O_3$-35 core-shell nanoparticles. Since this interconnected chain-like aggregation provides a preferential heat direction path which helps to increase the thermal conductivity of the nanofluids [100]. While lacking interconnection between the SiO_2 and Al_2O_3 nanomaterials due to the low concentration of Si precursor in the case of $SiO_2@Al_2O_3$-10 and $SiO_2@Al_2O_3$-20 core-shell nanoparticles may lead to a lower or negative effect on thermal diffusivity.
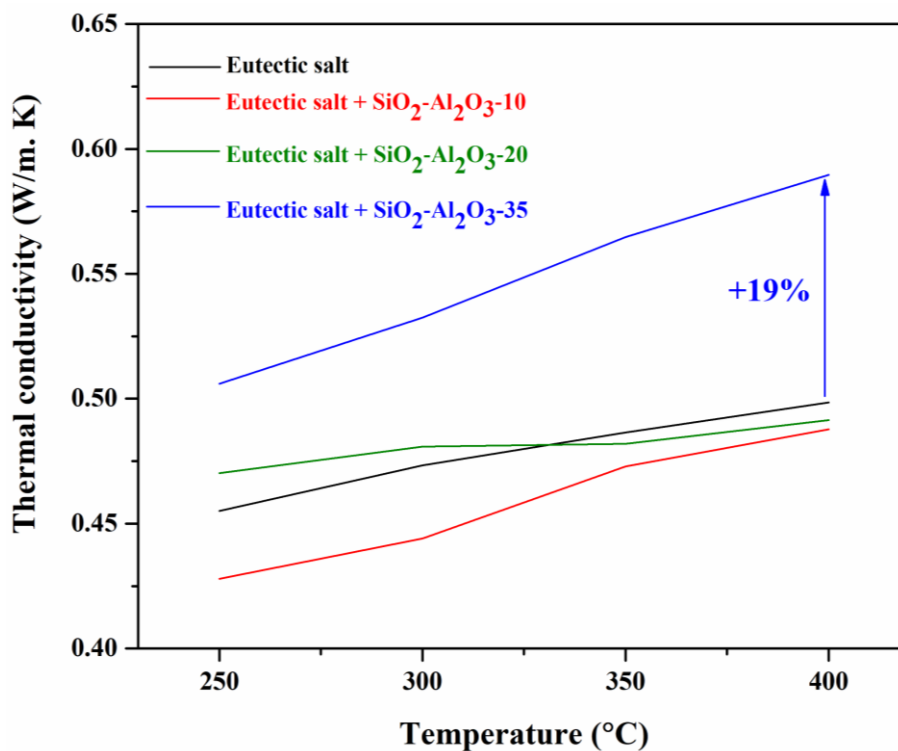
Figure 5.6. Thermal conductivity of eutectic salt and eutectic salt + 1 wt% of $SiO_2@Al_2O_3$ core-shell nanoparticles.

A huge effort from the scientific community was focused on the investigation of the enhancements of C_p and thermal conductivity, but only a few works show the effects of viscosity by the addition of nanoparticles in the molten salt [55, 94]. It is well known that the addition of nanoparticles in the molten salt increases the viscosity, which is simultaneously affecting the heat transfer properties due to the modification of the Reynolds number affecting the pumping power and pressure drop in the laminar flow [94, 102]. Apart from that, a big increase of such property value may limit further deployment of these nanofluids. Figure 5.7 shows the viscosity values obtained for the nanofluids based on $SiO_2@Al_2O_3$-10, $SiO_2@Al_2O_3$-20 and $SiO_2@Al_2O_3$-35 core-shell nanomaterials in the temperature range of 250-400ºC. The increment of the viscosity was observed for the $SiO_2@Al_2O_3$-10 nanofluids ranges from 16 to 25%, $SiO_2@Al_2O_3$-20 nanofluids range from 16 to 30% and $SiO_2@Al_2O_3$-35 nanofluids range from 25 to 34% compared to the base fluids. In general, at the higher temperature, the viscosity of the nanofluids decreased due to the weakening of the intermolecular attraction between the base fluid and nanoparticles, which is in agreement with the results published in [102]. This investigation shows that an elongated structure of nanoparticles provokes higher viscosity increase compared to a spherical one and that the viscosity of nanofluids decreased by increasing the sizes of the nanoparticles, which means lower specific surface area [102, 116]. In our case, the well-interconnected chain-like structure has high elongation, which explains that the $SiO_2@Al_2O_3$-35 nanofluid counts with higher viscosity compared to $SiO_2@Al_2O_3$-10 and $SiO_2@Al_2O_3$-20 core-shell nanoparticle based nanofluids.
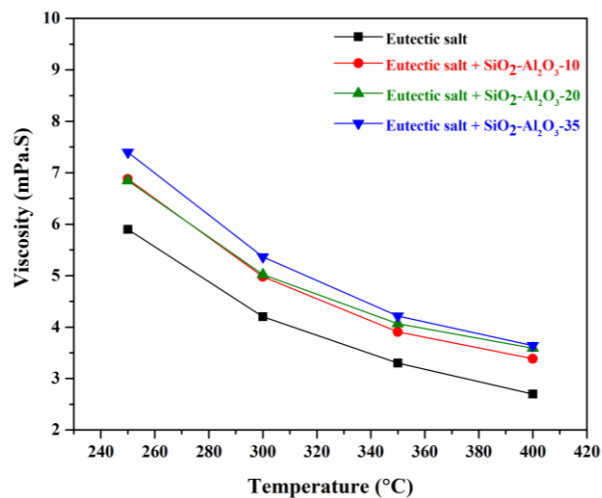
Figure 5.7. Viscosity of nanofluids based on eutectic salt and 1 wt% $SiO_2@Al_2O_3$ core-shell nanoparticles.

Part 1. General Conclusion

The molten salt-based nanofluids were introduced to enhance the thermophysical properties of the eutectic salt. In this work, an optimized simple dry method for obtaining nanofluids by physical shaking results in good dispersion of the nanomaterials within the base fluid, i.e. molten salt. To improve the dispersion stability of the nanofluid which is the responsible for the discrepancy of the reported results in the literature, different type, size, composition and shape of nanoparticles were used to prepare the nanofluids.

In the case of nanoparticles shape effect, two nanofluids based on Al_2O_3 nanospheres (Al_2O_3-NPs) and Al_2O_3 nanorods (Al_2O_3-NRs) were investigated. The Al_2O_3-NPs-nanofluid and Al_2O_3-NRs-nanorods show enhancements of their specific heat capacity and thermal conductivity, but as expected, an increase of their viscosity was observed. The different enhancements were attributed to the contributions of the size, shape and specific surface area of the involved nanoparticles

- In the solid state, the Al_2O_3-NRs-nanofluid has the highest enhancement of the thermal conductivity of 20% and the lowest enhancement of thermal conductivity of 12% was observed for Al_2O_3-NPs-nanofluid.

- In the liquid state, the highest enhancement of the specific heat capacity of 6% was observed for Al_2O_3-NPs-nanofluid, while for Al_2O_3-NPs-nanofluid it is 3%, which correlates to the specific surface area of the nanoparticles. Accordingly, Al_2O_3-nanorods shows higher specific heat capacity compared to the Al_2O_3-nanoparticles via its high surface area, which provides high interfacial resistance or interaction and it helps to store the additional energy.

- In the case of the thermal conductivity, similar enhancements of around 11% were observed for both nanofluids below 270ºC. A higher enhancement of 16% for Al_2O_3-NPs-nanofluid was obtained as compared to 12% for Al_2O_3-NRs-nanofluid above 350ºC, due to the predominant contribution of the nanoparticles Brownian motion, which is more pronounced for Al_2O_3-NPs with smaller size and spherical shape.

- For the viscosity, the lowest increment of 5% was observed for Al_2O_3-NPs-nanofluid compared to 12% for Al_2O_3-NPs-nanofluid at 250°C, which was attributed to the difference in the hydrodynamic resistances of the investigated nanoparticles.

In summary, the Al_2O_3-NPs-nanofluid and Al_2O_3-NRs-nanofluid present different behaviours in liquid and solid states. The Al_2O_3-NRs-nanofluid presents the best enhancements of the specific heat capacity and thermal conductivity in the solid state, while in a liquid state, the Al_2O_3-NPs-nanofluid presents the highest thermal conductivity enhancement and the lowest increment of viscosity.

In the case of nanoparticles size effect, three nanofluids based SiO_2 nanoparticles with three different sizes of 27 nm, 450 nm and 800 nm were studied. The obtained results can be summarized as follows:

- Nanofluids based on 450 nm and 800 nm silica nanoparticles demonstrate superior stability, as compared to nanofluids based on 27 nm nanoparticles, which was confirmed by visual observations and zeta potential experiments.

- Nanofluids based on 450 nm and 800 nm silica nanoparticles demonstrate only 48% viscosity enhancement, contrary to nanofluids based on 27 nm nanoparticles for which viscosity increased 5 times at 400ºC, as compared to a nanoparticle-free molten salt.

- Nanofluids based on 450 nm and 800 nm silica nanoparticles show no enhancement of heat capacity or thermal conductivity, suggesting that a compromise between nanofluid stability and thermophysical properties is governed the nanoparticle size.

- The synthesized monodispersed nanoparticles were homogeneously dispersed in the molten salt, which is beneficial for understanding the correlation between the theoretical and experimental results.

The obtained results provide a methodological route for the development of stable nanofluids with enhanced thermophysical properties by optimizing the size and zeta potential value of the nanoparticles. From the size effect of SiO_2 nanoparticles, the smaller size with a high surface area of the nanomaterials based nanofluids shows the higher enhancement of the thermophysical properties and the higher negative impact on the viscosity; while increasing the size of the nanoparticles shows no enhancements of thermophysical properties and lower impact on the viscosity.

In the case of nanoparticle composition effect, three nanofluids based on synthesized $SiO_2@Al_2O_3$ core-shell with different thicknesses of the SiO_2 shell were investigated.

- The synthesized $SiO_2@Al_2O_3$ core-shell nanoparticles show the enhancement of thermophysical properties of nanofluids, depending on the thickness of the SiO_2 layer on the top of Al_2O_3 nanoparticles. From the accomplished analyses, we observed enhancements of thermal conductivity of ~19% for the nanofluids based on $SiO_2@Al_2O_3$-35 core-shell nanoparticles. Such observation can be explained by the formation of a chain like aggregation of $SiO_2@Al_2O_3$-35 core-shell nanoparticles, promoting the heat transfer in the nanofluid. A similar phenomenon may be responsible for the observed increment of 25 to 34% in the viscosity of this nanofluid.

- In general, the shape, size and composition of the nanoparticles need to be optimized in order to obtain a good compromise between the long-term dispersion stability of the nanofluids and the optimal increase of their thermophysical properties. It is worth to mention here that the surface area of the nanoparticles is playing a crucial factor for enhancing the thermophysical properties mainly specific heat capacity and thermal conductivity.

- On the contrary, the high surface area of the nanoparticles playing a negative role in the increment of the viscosity of the investigated nanofluid. Therefore, nanoparticles with big particle sizes and higher specific surface area,

nanoporous materials, may lead to better enhancement of the thermophysical properties with limited impact on the viscosity.

Part 2. Nanofluid Compatibility with Tank Material

Part 2. General Introduction

Currently, the considerable scientific effort is focused on the development of new molten salt-based nanofluids as storage materials with enhanced thermophysical properties. The corrosion mechanism between the molten salt and storage materials is clear and several works are shown in the literature. However, the effect of adding nanoparticles in the molten salt is still needed to be explored because it will profoundly detrimental for the implementation of nanofluids on an industrial scale. The present part of the thesis investigated the effects of nanoparticles addition on the corrosivity of the molten salts. On the first hand, the effect of adding the commercial Al_2O_3, SiO_2 and TiO_2 nanoparticles were studied. On the second hand, the use of a simple graphitization process of the carbon surface to protect it again the corrosivity of the molten salt was highlighted. For that purpose, systematic corrosion experiments were carried out by using different time intervals like 250h, 500h, 1000h and 1500h. The experiments were conducted under an air atmosphere at two temperatures of 310°C and 390°C. To shed some light on the corrosion mechanisms and quantify corrosion rates a combination of advanced material characterization techniques like SEM, EDX, XPS depth profiling, FIB, XRD and TGA were applied.

However, by using nanofluids based on a eutectic mixture of $NaNO_3$-KNO_3 (51 wt%-49 wt%) we demonstrated that nanoparticles doping has complex effects on the corrosion rates of carbon steel. In particular, if the negative effect of

microbubbles of air trapped between the nanoparticles is not predominant, one can obtain reduced corrosion rates due to the incorporation of the nanoparticles into the oxidation layer. In this sense, we have studied that addition of 1wt% of nanoparticles to molten binary nitrate salt to reduce the corrosion rate of carbon steel tested at 390°C by a factor of 3 and had a stabilizing effect on the corrosion scale. The anticorrosion effect of nano-additive was attributed to the formation of the iron-nanoparticle mixed oxides on the carbon steel surface. In view of presented results, the use of molten salts based nanofluids in the CSP pertains not only to enhance thermophysical properties, but also to improve compatibility with construction materials. On the other hand, the graphitization anticorrosion method for carbon steel in contact with molten binary nitrate salt demonstrated a similar effect. It has been demonstrated that the surface spray-coating by graphite reduces the corrosion rate at least by a factor of 6 and stabilizes the corrosion scale by iron carbide crystals at temperatures of 390°C.

In general, the obtained results are important both for expanding the very limited knowledge on the corrosion aspects of molten salts based nanofluids, as well as for the comprehensive evaluation of the feasibility of such nanofluids for TES applications.

Chapter 6. Effect of Al$_2$O$_3$ and SiO$_2$ Nanoparticles

The main motivation for the present chapter is to fulfill the gap between the pronounced interests in molten salts based nanofluids and limited information regarding their corrosivity. Here we focus on Al$_2$O$_3$ and SiO$_2$ nanoparticles dispersed in binary eutectic nitrate salt (NaNO$_3$-KNO$_3$ with 51:49 wt.%) and their effect on the corrosion of carbon steel A516 Gr70, which is widely used construction material for TES units. It was possible to separate two different corrosion aspects of molten salts based nanofluids, namely a positive effect of the incorporation of stable oxides into the corrosion layer and a negative effect of microbubbles formation. In this regard, reduced corrosion rates for molten salts based nanofluids were obtained as compared to the base fluids (molten salts without nanoparticles), when the negative effect of microbubbles was minimized. This decrease is mainly due to the incorporation of nanoparticles into the corrosion layer. It was identified that in order to take benefit of this positive effect, special attention must be taken during the melting process of the nanofluid in order to minimize the negative effect of microbubbles inside the storage tank at concentrated solar power plants.

6.1. Corrosion test protocol

For the corrosion tests, pieces of CS A516 Gr70 having a size of around 3 × 12 × 14 mm were immersed in 5 g of each fluid, namely of eutectic salt and Al$_2$O$_3$ and SiO$_2$ based nanofluids. The corrosion tests were conducted under static immersion condition in an air atmosphere at 390ºC for periods of 250, 500, 1000 and

1500 hours. In order to check the effect of the microbubbles, the corrosion tests were also performed at 310ºC following the same protocol and conditions. The details of the corrosion protocol were mentioned in chapter 2.

6.2. Carbon steel analysis

Examples of SEM cross-sections of carbon steels after corrosion tests with eutectic salt, as well as after the tests with Al_2O_3 and SiO_2 based nanofluids are presented in Figure 6.1, where well-defined corrosion layers are evident for all the samples.
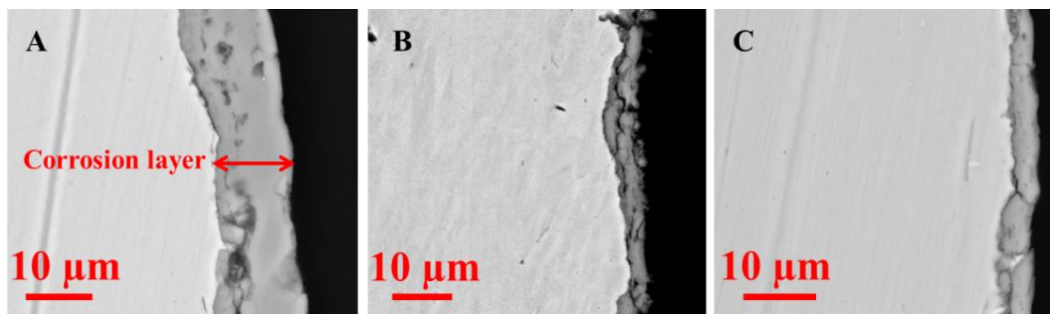
Figure 6.1. SEM cross-section images of the carbon steel after 1500 hours of corrosion tests at 390ºC with A) Eutectic salt, B) Al_2O_3 based nanofluid and C) SiO_2 based nanofluid.

A careful statistical evaluation of the corrosion layer thickness from the cross-section images clearly reveals that Al_2O_3 based nanofluid and SiO_2 based nanofluid have lower corrosion thicknesses as compared to the pure eutectic salt - Figure 6.2A. In particular, the obtained oxide layer after 1500 hours immersion tests for the eutectic salt is ~ 15.8 $\pm$ 2.5 µm, for Al_2O_3 nanofluid, it is ~ 6.4 $\pm$ 0.8 µm and for SiO_2 nanofluid, it is ~ 5.7 $\pm$ 1.6 µm. Such results correspond to the following corrosion rates: ~ 92 µm/year, ~ 37 µm/year and ~ 33 µm/year for the eutectic salt, Al_2O_3 nanofluid and SiO_2 nanofluid, respectively. Expectedly, the thickness of the corrosion layer was increased with time for all the samples as can be seen in Figure 6.2A. In addition, the maximum corrosion penetration depth was also analysed for each sample and is presented in Figure 6.2B. The highest penetration depth was observed for pure salt, while lower values were obtained for the nanofluids, following the same trend as the average corrosion layer thickness.
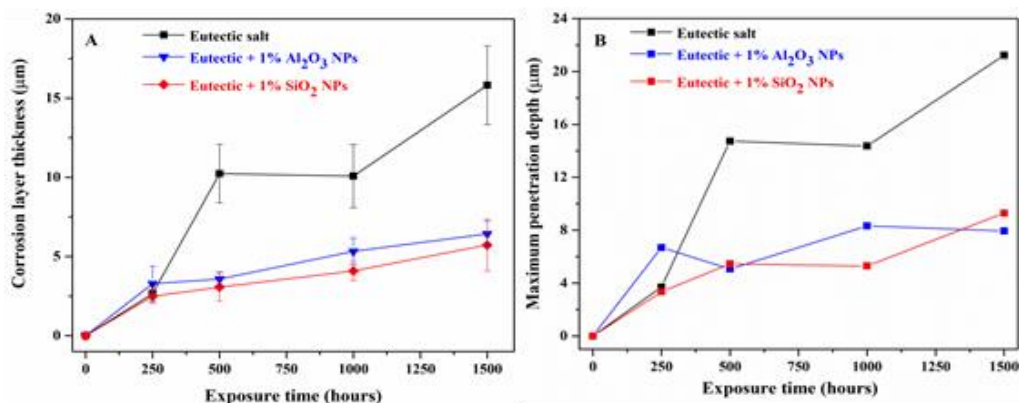
Figure 6.2. (A) Evolution of the corrosion layer thickness at 390°C and (B) maximum corrosion penetration depth for carbon steel during the immersion corrosion tests with pure eutectic salt and Al_2O_3 and SiO_2 based nanofluids.

Remarkably, the presence of nanoparticles also modified the corrosion rate evolution (Figure 6.2A). While pure eutectic salt demonstrates close to a linear increase of corrosion layer with time, nanofluids demonstrate close to parabolic dependence, where corrosion rates significantly decrease for exposure times higher than 250 hours.

From the cross-section analysis, it is evident that the corrosion layer after the tests with nanofluids exhibits more cracks as compared to the pure salt case - Figure 6.1. This may be explained by the phase composition of the corrosion layer - Figure 6.3. In the case of nanofluids, the corrosion layer is formed by two different oxides, namely, magnetite (Fe_3O_4) and hematite (Fe_2O_3). Whereas, in the case of pure salt, it shows only a single oxidation phase of maghemite (Fe_2O_3). The presence of two different types of oxide phases in the corrosion layer might be responsible for the formation of cracks [65]. It is important to note that Fe_2O_3, being the higher oxidation state of iron as compared to Fe_3O_4, additionally signifies a higher corrosion rate for pure eutectic salt compared to the nanofluids. From Figure 6.3 one can see that the peaks of the iron phase are more pronounced for the case of nanofluids. In general, the observable peaks of iron for all the samples are due to the fact that the penetration depth of the X-ray beam exceeds the corrosion layer thickness. In this sense, more pronounced peaks of pure iron phase in case of nanofluids confirm the lower thickness of the corrosion layer as compared to the pure salt case. In particular, for the case of Al_2O_3 and SiO_2 based nanofluids the corrosion layer thickness is around 5 µm (Figures 6.1 and 6.2), so the X-ray beam penetrates the corrosion layer and largely reaches the pure iron phase. While in case of pure molten salts, the

corrosion layer is around 15 µm, so the X-ray beam hardly reaches the pure iron phase. This explains why for the case of nanofluids the intensity of iron peaks is much higher compared to pure salt.
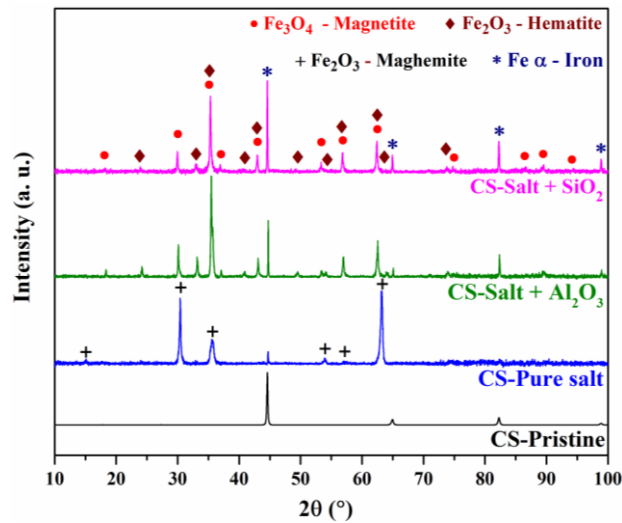
Figure 6.3. XRD patterns of CS before and after 1500h corrosion test at 390ºC. Pristine CS (black color), after corrosion test with eutectic salt (blue color), after corrosion test with Al_2O_3 nanofluid (green color) and after corrosion test with SiO_2 nanofluid (pink color).

The corrosion tests were conducted by using eutectic salt, Al_2O_3 and SiO_2 based nanofluids for time periods of 250, 500, 1000 and 1500 hours at 310°C. XRD patterns of carbon steel (CS) after these tests are shown in Figure 6.4 and are compared with pristine carbon steel. From the XRD analysis, it is evident that the hematite (Fe_2O_3) and magnetite (Fe_3O_4) phases are formed for all the samples after corrosion tests.
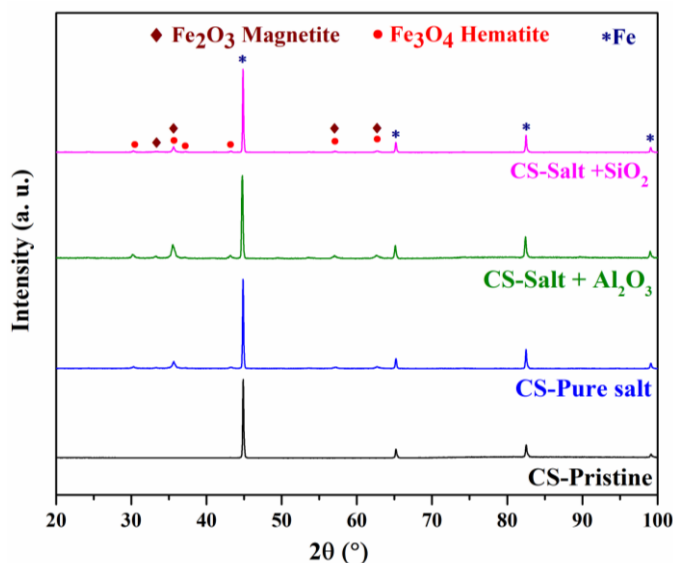
Figure 6.4. XRD patterns of CS before and after 1500 hours of corrosion tests at 310ºC. Pristine CS (black color), Eutectic salt immersed CS (blue color), Al_2O_3 based nanofluids immersed CS (green color) and SiO_2 based nanofluids immersed CS (pink color).

The mass gain analysis for all the samples is in agreement with the SEM observations. The mass gain evaluation graph from the initial state to 1500 hours is shown in Figure 6.5 and the mass gain over the different time periods was calculated using the following equation:

$$\frac{\Delta m}{S_0} = \frac{m_i - m_f}{S_0}, \qquad (1)$$

where, Δm indicates the changes in the mass of the specimen, S_0 is the initial area of the specimen, m_i is the initial mass of the specimen and m_f is the final mass of the specimen at different time intervals [117].
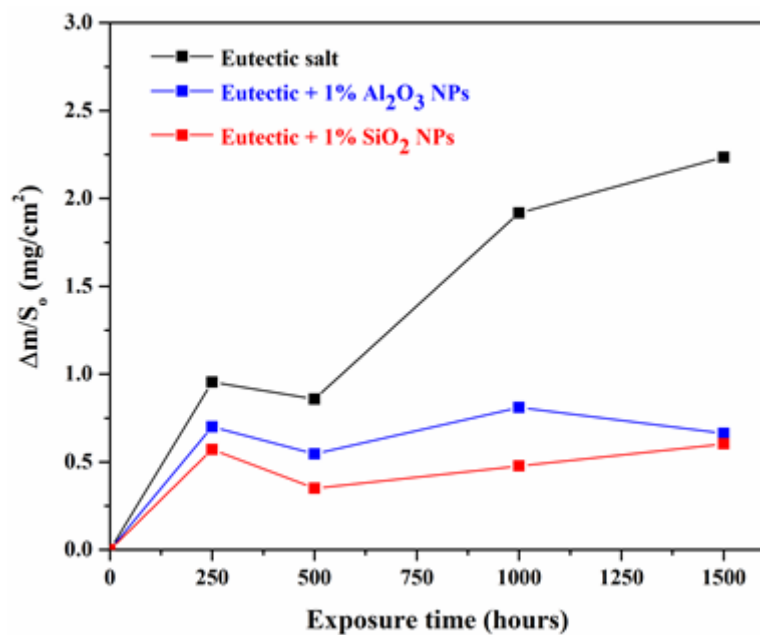
Figure 6.5. Gravimetric analysis of the carbon steel after corrosion tests with eutectic salt, Al_2O_3 and SiO_2 based nanofluids at 390ºC.

Pure eutectic salt resulted in higher mass gain as compared to Al_2O_3 and SiO_2 based nanofluids, which corroborates the higher oxidation in the case of eutectic salt. The obtained mass gain after 1500 hours corrosion test with eutectic salt is ~ 2.2 mg/cm^2, after Al_2O_3 based nanofluids it is ~ 0.7 mg/cm^2 and after SiO_2 based nanofluids, it is 0.6 mg/cm^2 respectively. The same behaviour was found for the Al_2O_3 based nanofluids with a mass gain after 1500 hours lower than the one at 1000 hours. The dynamics of oxidation is also in agreement with the SEM and XRD analyses.

The dynamics of oxidation is also evident from the XRD analysis - Figures 6.3 and 6.4. The observed decrease of corrosivity for the nanofluids can be due to the

incorporation of stable nanoparticles into the corrosion layer and hence its stabilization. For example, it has been reported that the formation of a uniform thin layer of alumina on the surface of the alloy before exposure to the molten chloride salt reduces the corrosion rate [118]. With this regard, the pronounced growth of the corrosion layer before 250 hours may be due to the rapid formation of the initial oxide. While after the formation of a thickness of around 2.5 μm and the incorporation of Al_2O_3 and SiO_2 nanoparticles into the oxide layer the corrosion rate decreases. This phenomenon is clearly noticeable from the Figure 6.2A, where for 250 hours the thickness of the corrosion layer is similar in all the cases, including the eutectic salt; however, starting from 500 hours, the corrosion rate of the eutectic salt is higher compared to nanofluids. Both Al_2O_3 and SiO_2 nanofluids show a similar thickness of the oxidation layer in the whole time range.
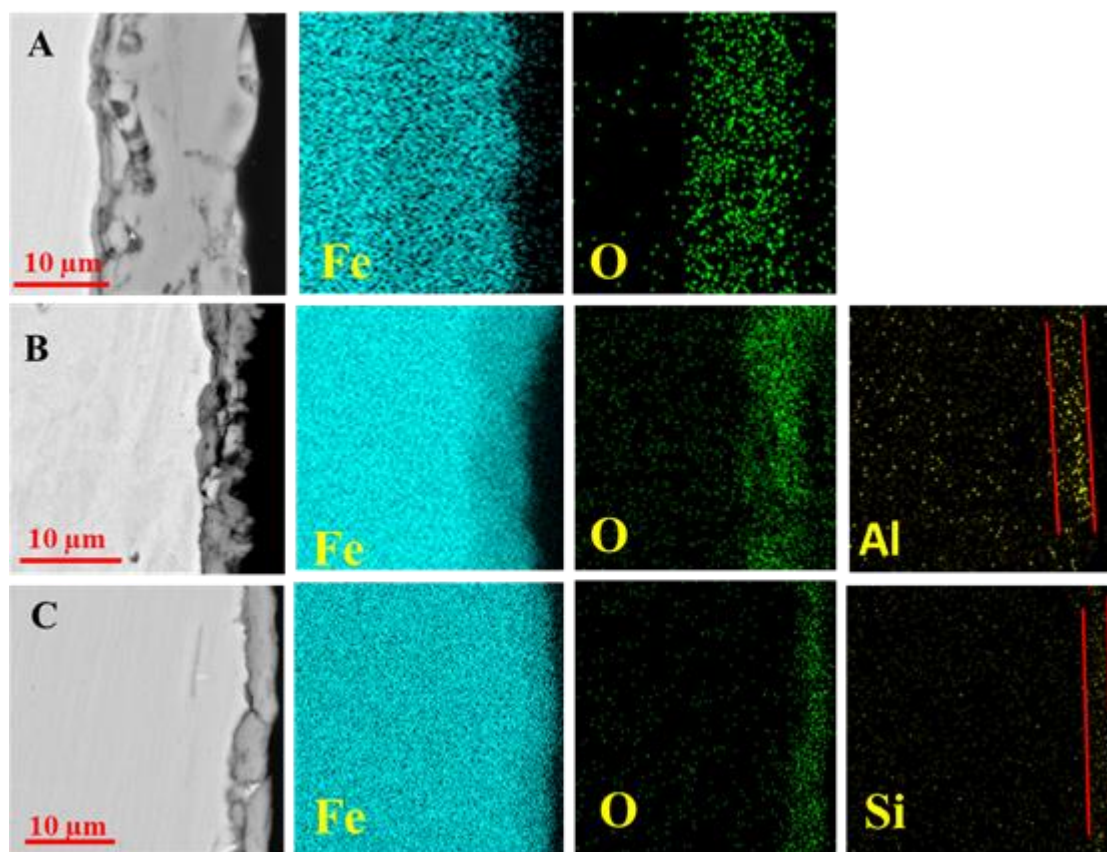
Figure 6.6. SEM images and their corresponding EDX mapping for cross-sections of carbon steel after 1500 hours corrosion test at 390ºC with A) Eutectic salt, B) Al_2O_3 based nanofluid and C) SiO_2 based nanofluid.

The maximum penetration depth of the corrosion was also identified from the SEM cross-section analysis as can be seen in Figure 6.2B. Such localized corrosion is important from a practical point of view, as it is responsible for construction

material failure. After 1500 hours the maximum penetration depth of the corrosion layer for the eutectic salt is ~ 21 µm, for Al_2O_3 nanofluid it is ~ 8 µm and for SiO_2 nanofluid it is ~ 9 µm. The reduced maximum penetration depth for nanofluids may also be due to the incorporation of nanoparticles into the corrosion layer. In order to explore such a hypothesis, the EDX-analysis was performed for all the samples - Figure 6.6.

From the EDX-mapping, it is clear that after the immersion tests with carbon steel and eutectic salt, the corrosion layer is formed by iron oxide (only iron and oxygen are detected in the layer), and after the tests with nanofluids additionally the elements of nanoparticles (Al or Si) are detected in the corrosion layer. Particularly, high concentration of Al was clearly observed in Al_2O_3 based nanofluid case (Figure 6.6B) and a high concentration of Si was detected for SiO_2 nanofluid case (Figure 6.6C), which is marked with red lines. The incorporation of the Al and Si elements in the oxide has a relatively similar thickness. This passive layer formation by the nanoparticle may act as a corrosion inhibitor, which reduces the thickness of the oxide layer as compared to eutectic salt due to physical or chemical incorporation of nanoparticles.

One should note that the chemical incorporation of alumina nanoparticles is likely to reduce the corrosion rates. For example, it was demonstrated that high Al content in stainless steel alloys reduces the corrosion rates due to protective alumina layer formation [119–121]. In this work, we found reduced corrosion rates for both alumina and silica-based nanofluids. This allows presuming similar protection mechanism for both nanoparticles. However, the mechanism behind the effect of Si is yet to be demonstrated. On the other hand, possible physical incorporation of the nanoparticles into the corrosion scale needs further investigation, as while the short-term effect may be positive due to reduced diffusion of molten salt, in long-term run physical phenomena like erosion and spallation may take place.

The incorporation of nanoparticles into the corrosion layer reduces the concentration of nanoparticles in the salt and therefore affects the thermophysical properties of the nanofluid. Under the conditions of the corrosion tests performed in this work, the amount of incorporated nanoparticles is very low. In particular, no noticeable difference in Al/Si concentration was detected by EDX analysis for the salts after the corrosion tests as compared to as-prepared salts. Nevertheless, for the

real application, such incorporation should be taken into account and additional nanoparticles need to be added to the salt to compensate for the loss.

The phases containing Al or Si expectedly were not detected by means of XRD (Figure 6.3) due to the very low concentration of nanoparticles in the salt.
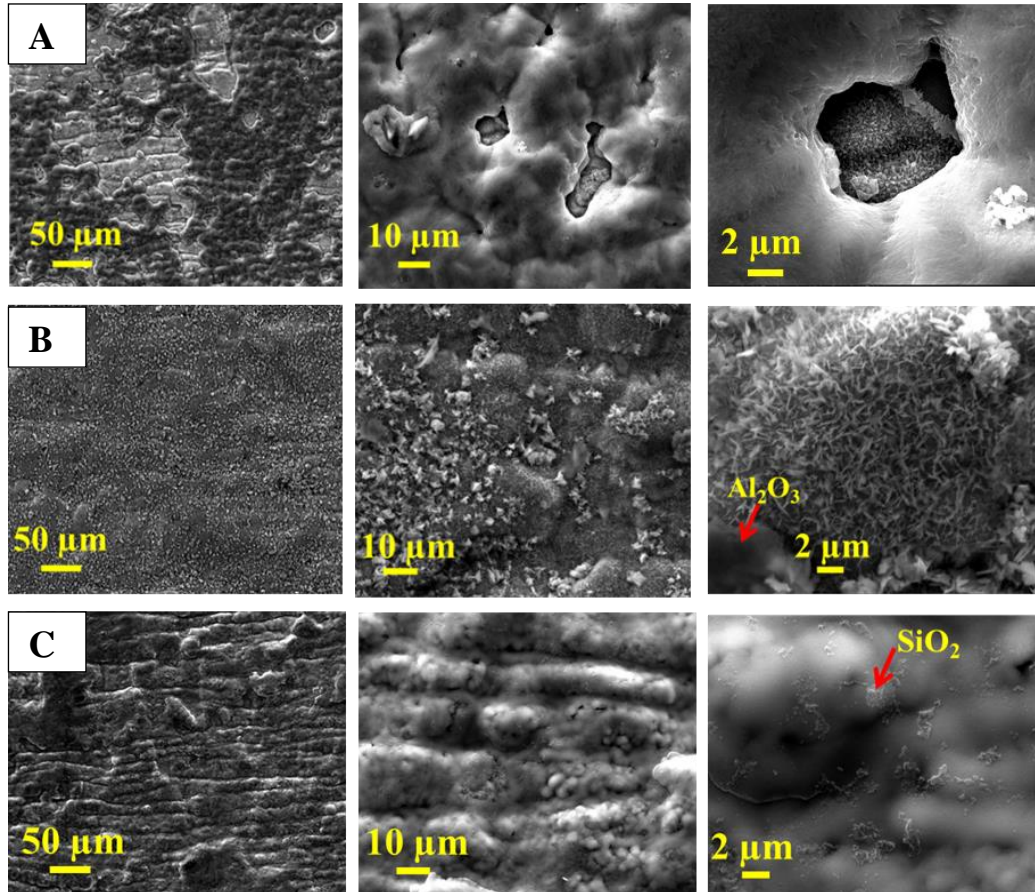
Figure 6.7. SEM images for the surface of the carbon steel after 1500 hours corrosion test at 390ºC with A) Eutectic salt, B) Al_2O_3 based nanofluid and C) SiO_2 based nanofluids.

The SEM analysis of surfaces of carbon steel after the corrosion tests further supports the positive effect of nanoparticles - Figure 6.7. The surface of CS after the corrosion test with eutectic has more defects compared to nanofluids cases. In particular, the surface is not homogeneously oxidized and large spots of 50-100 µm with a higher degree of oxidation (according to oxygen content – Figure 6.8B) are present all over the surface (Figure 6.7A). The higher magnification of such defects in Figure 6.7 demonstrates significantly higher corrosion penetration, which results not only in higher corrosion rates as will be shown below but also in higher values of corrosion layer standard deviation (Figure 6.11). On the contrary, the surfaces of carbon steel after corrosion tests with nanofluids are homogeneously oxidized and

the defects mentioned above were not detected (Figure 6.7B and 6.7C). The inclusions of corresponding nanoparticles were also detected (Figure 6.7B and 6.7C).

The elemental composition for the surfaces of the CS before and after 1500 hours corrosion tests is shown in Figure 6.8. The pristine CS has two different types of roughness with similar Fe composition as it can be observed in Figure 6.8A. After 1500 hours corrosion test with the eutectic salt, the oxidation of the surface and non-homogeneous incorporation of Mg can be detected – Figure 6.8B. While after 1500 hours of corrosion tests with nanofluids the Mg was not detected, instead the elements of Al and Si were found for Al_2O_3 and SiO_2 based nanofluids cases respectively. Mg is a typical impurity in the nitrate salts, which were used for the preparation of the eutectic salt. More commonly, Mg interacts with magnetite (Fe_3O_4) and forms a stable compound of Magnesium ferrite ($MgFe_2O_4$) phase [117]. Competitive incorporation of Mg and elements of corresponding nanoparticles signifies the chemical interaction of the nanoparticles with the corrosion layer, rather than just physical incorporation. In our previous work, we discussed this effect in terms of different electronegativity of Mg, Al and Si elements [122].
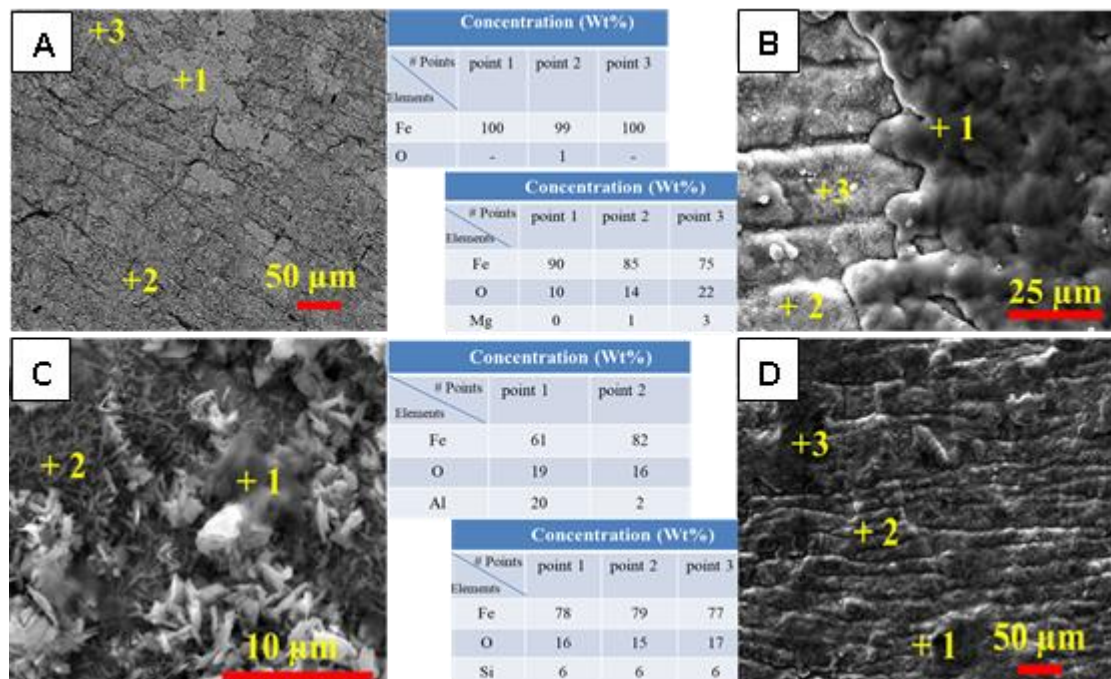
Figure 6.8. SEM and EDX analyses of the surface of a) pristine carbon steel; and carbon steels after 1500 hours corrosion tests at 390°C with b) Eutectic salt; c) Al_2O_3 based nanofluid, and d) SiO_2 based nanofluids.

The reduced corrosion rates of nanofluids as compared to pure eutectic are in strong contradiction with our previously reported results for HitecXL salt based

nanofluids [68, 122], where we identified two major factors affecting the corrosion of carbon steel by molten HitecXL with nanoparticles: 1) incorporation of nanoparticles into the corrosion layer and 2) formation of microbubbles, which remain in the salt for a long time ($\sim$ 4 days at 310°C in that case) increasing the oxidation rates [122]. Particularly, one can clearly see the formation of agglomerates after the nanofluid preparation (Figure 6.13). Such agglomerates result in an inter-particles pores, which contains air. After melting the salt, this air tends to be released in the form of bubbles.
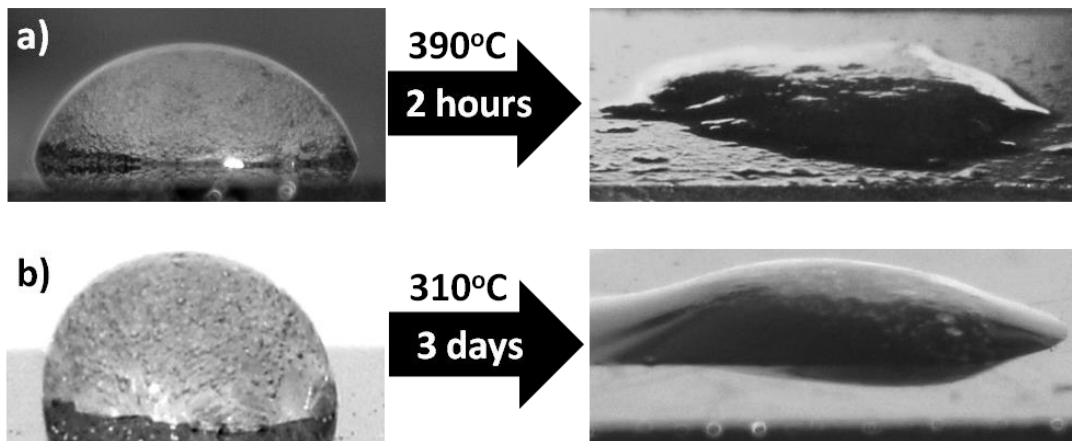
Figure 6.9. Air microbubbles evolution in molten Al_2O_3 nanofluid at a) 390ºC and b) 310ºC.

In the present work, due to the different composition of the salt and the higher temperature of corrosion tests the microbubbles were removed from the molten salts after a shorter time period (several hours) after melting, while for HitecXL salt it was more than 4 days [122]. Therefore, the comparison of previously obtained result [122], and present results allow separating these two major aspects of nanofluids. In particular, one can suggest that incorporation of nanoparticles into the corrosion layer reduces the corrosion rates by stabilizing the oxidation scale, while the pronounced the formation of the microbubbles favours the corrosion due to increased amount of oxygen in the system. In order to check the air microbubbles evolution in the case of eutectic salt, we performed two experiments using Al_2O_3 based nanofluid at 310ºC and 390ºC and the results are demonstrated in Figure 6.9. At 390ºC, it takes only $\sim$ 2 hours for microbubbles of air to escape completely from the molten salt, but at 310ºC even after 3 days, some microbubbles are still visible. In order to confirm the effect of air bubbles on the corrosion rates, we performed immersion corrosion experiments with eutectic salt and Al_2O_3 and SiO_2 based nanofluids at 310ºC.

Remarkably, at 310ºC the corrosion layer is larger for nanofluids compared to pure salt, which is evident from the statistical cross-section analysis (see Figure 6.10 for the example), which is in agreement with the previous work performed for HitecXL based nanofluids [122].
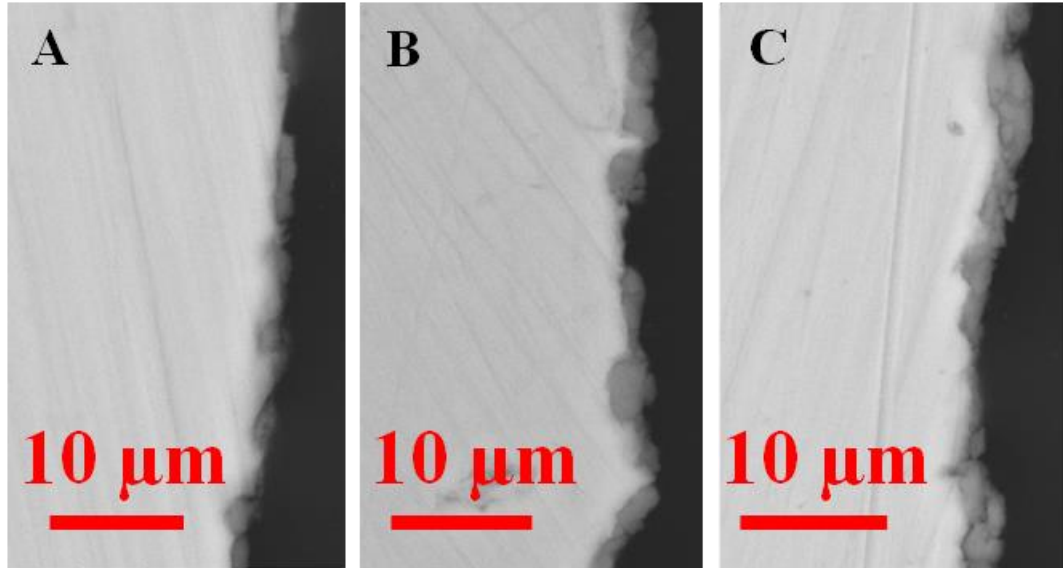
Figure 6.10. Cross-sections of carbon steel after 1500 hours of corrosion tests at 310ºC with A) Eutectic salt, B) Al_2O_3 based nanofluid and C) SiO_2 based nanofluids.

The results of the corrosion tests at 310ºC experiments are compared with the results of corrosion tests performed at 390ºC in Figure 6.11. It is notable that at 310ºC the presence of nanoparticles in the molten salts increases the corrosion rate about twice compared to pure eutectic. This is in strong contrast to the results obtained at 390ºC, where the presence of nanoparticles results in lower corrosion rates (Figure 6.2). Such observations are in favour of the hypothesis that the negative effect of air microbubbles is prevailing at 310ºC, while it becomes secondary at 390ºC due to their fast evaporation. On the other hand, incorporation of nanoparticles decreases the corrosion rates and is observed independently on temperature.
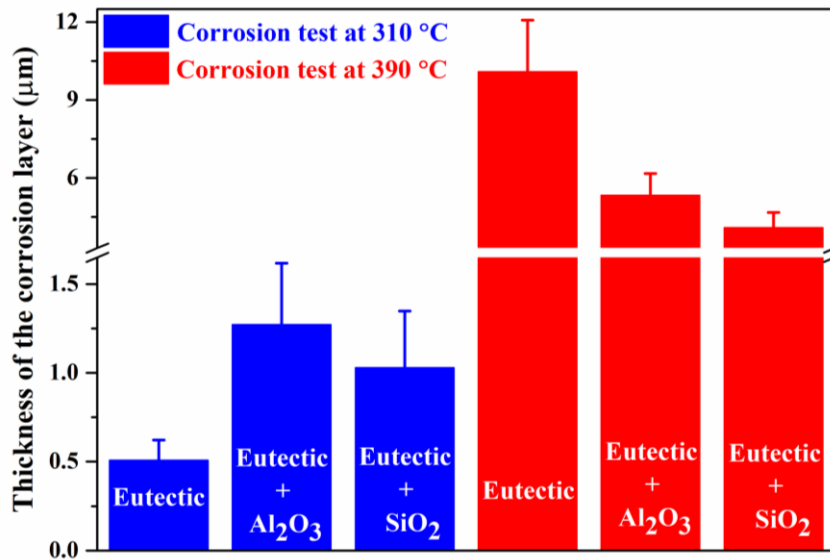
Figure 6.11. Corrosion layer thickness for carbon steel after 1000 hours immersion tests at 310ºC and 390ºC with pure eutectic salt and Al_2O_3 and SiO_2 based nanofluids.

6.3. Molten salt and molten salt-based nanofluids analysis

Molten salts and molten salts based nanofluids were examined before and after the corrosion tests in order to check for any degradation phenomena. FTIR spectra of pure eutectic salt, Al_2O_3 and SiO_2 based nanofluids were analysed after corrosion and no modifications were found, which is shown figure 6.12. In the FTIR spectra of SiO_2 nanomaterials, the peaks observed at 464 cm^{-1} and 1070 cm^{-1} correspond to bending and asymmetric stretching vibration modes of Si-O-Si bonds, whereas, the peak at 812 cm^{-1} corresponds to the symmetric vibration of Si-O bond [123]. In Al_2O_3 nanomaterials, the strong absorption bands observed near to 726 cm^{-1} and 516 cm^{-1} can be assigned to Al-O stretching mode and Al-O-Al bending mode of γ-Al_2O_3 [81]. In the pure eutectic salt, the peaks were observed at 721 cm^{-1} for asymmetric in-plan bending modes, 828 cm^{-1} due to O-N-O bending mode and 1334 cm^{-1} due to NO_3 stretching mode [82]. The small peaks near to 1774 cm^{-1} and 2434 cm^{-1} describe the stretching modes of nitrate ions [82]. The addition of the nanoparticles into the salt did not result in the formation of new interaction (no new peaks at the FTIR spectra) between nanomaterials and eutectic salt. Such a result suggests the absence of pronounced interaction of molten salts and nanoparticles.
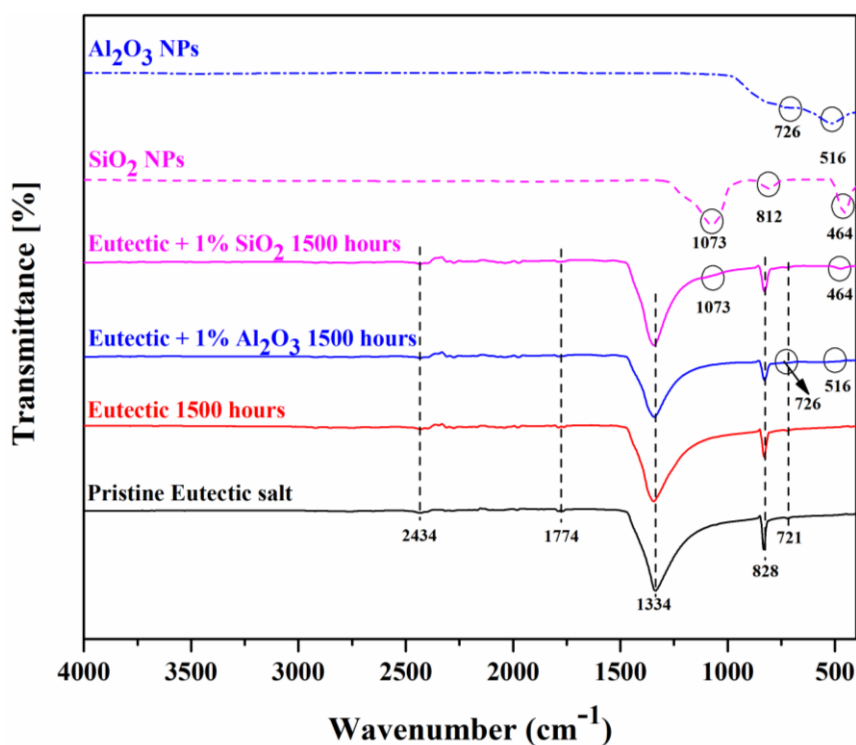
Figure 6.12. FTIR spectra of pristine Al_2O_3 NPs, SiO_2 NPs and eutectic salt; and tested eutectic salt, Al_2O_3 based nanofluids and SiO_2 based nanofluids after 1500 hours corrosion test.

The observed peaks for eutectic salt and nanomaterials remained in the same positions without changing their wavenumber region. The pristine Al_2O_3 and SiO_2 based nanofluids show prominent metal oxide bonds for Al_2O_3 and SiO_2 nanomaterials combined with eutectic salt. After 1500 hours of corrosion reaction, we did not find any new peaks, which confirmed that there is no additional impurity present in the fluids, and no decomposition reaction occurred, such as the conversion of NO_3 to NO_2, in the tested nanofluids.

The dispersion of the nanoparticles before and after the corrosion tests were verified by SEM technique. The as-prepared nanofluids demonstrate the good distribution of the nanoparticles with agglomerates of no more than ~200 nm (Figure 6.13a). After the corrosion tests, much larger agglomerates of around 2 µm were formed (Figure 6.13b). Such agglomerates were observed all over the salt after the corrosion test. The obtained results suggest that even though due to agglomeration during the corrosion test the local concentration of nanoparticles may be different from the initial 1 wt%, the surface of carbon steel is constantly exposed to SiO_2 / Al_2O_3 permitting chemical and physical interaction. It, however, should be noted that agglomeration reduces the concentration of the nanoparticle elements available for a

chemical reaction. Therefore, pronounced agglomeration can mitigate the anticorrosion effect of nanoparticles in molten salts and should be avoided.
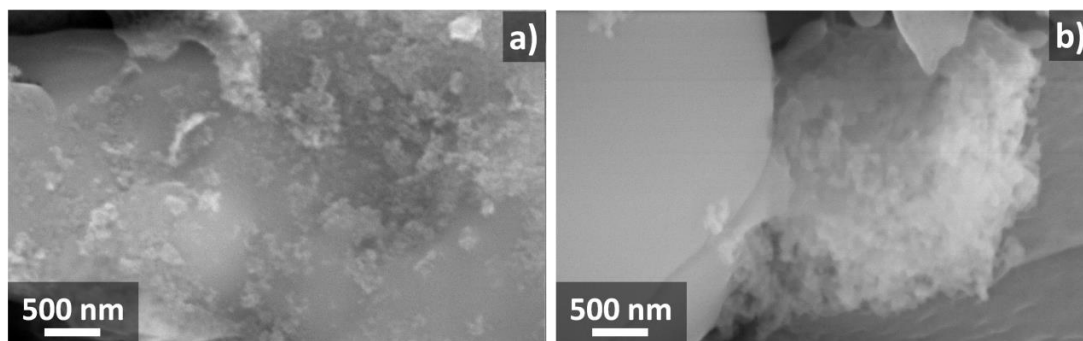
Figure 6.13. SEM images of Eutectic + SiO_2 salt a) before and b) after 1500h corrosion test at 390°C.

It is important to note that some settling of nanoparticles is likely to occur in a real system, which can affect the corrosion of the surfaces where the particles settle. Therefore, systematic study of the effect of nanoparticles settling on the corrosion (or potentially erosion) should also be performed.

6.4. Enthalpy and melting temperature

The enthalpy of eutectic salt, Al_2O_3 and SiO_2 based nanofluids were studied after 1500 hours corrosion test and the results are shown in Figure 6.14. In general, the reported results in literature show that the enthalpy of the molten salt slightly decreases or increases depends on the concentration and types of the nanoparticles used [29]. For example, 1% CuO nanoparticles doped molten salt was decreasing the enthalpy, while 1% TiO_2 nanoparticles doped molten salt was increasing the enthalpy as compared to the base salt [29]. In our present study, we observed small changes in the enthalpy of eutectic salt by the addition of the Al_2O_3 and SiO_2 nanoparticles - Table 6.1. These changes might be due to size and agglomeration of the nanoparticle inside salt, which will alter or affect the properties of the base fluids [29]. Similarly, we observed minor modifications in onset melting temperature for Al_2O_3 and SiO_2 based nanofluids in comparison with base eutectic salt due to the addition of nanoparticles. The change in the melting temperature by the addition of the nanoparticles may be due to the confinement of the salt in the pores (inter-particle) generated by the agglomeration of the nanoparticle [29]. The values for the melting and solidification temperatures and the enthalpy during melting and solidification processes obtained for the eutectic salt, Al_2O_3 and SiO_2 based nanofluids after 1500

hours corrosion tests are presented in Table 6.1. It is noteworthy to mention here that the obtained deviations are within the experimental error of the DSC equipment, which confirms that the addition of the Al_2O_3 and SiO_2 nanomaterials did not affect significantly the melting and enthalpy of the investigated eutectic salt.
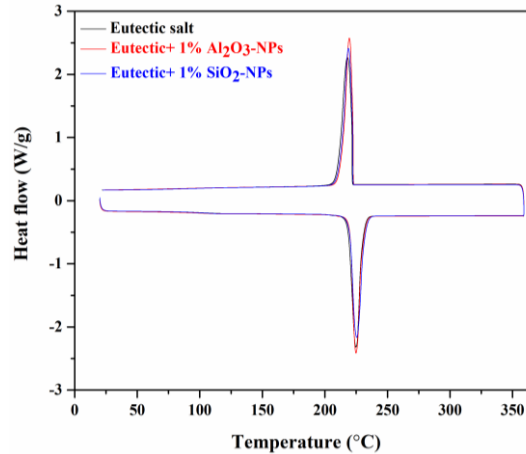
Figure 6.14. DSC analysis of eutectic salt, Al_2O_3 based nanofluid and SiO_2 based nanofluid after 1500 hours corrosion test.

Table 6.1. Enthalpy, melting temperature and crystallization temperature of the eutectic salt, Al_2O_3 and SiO_2 based nanofluids for after 1500 hours corrosion test.

Fluid	ΔH_m (J/g)	T_m (°C)	ΔH_{sol} (J/g)	T_{sol} (°C)
Eutectic	105	218	103	222
Eutectic + Al_2O_3 NPs	104	220	103	222
Eutectic + SiO_2 NPs	103	220	103	222

6.5. Thermogravimetric analysis (TGA)

Thermogravimetric analysis of the eutectic salt, Al_2O_3 and SiO_2 base nanofluids were carried out after 1500 hours corrosion tests to observe the stability of post-tested molten salts and the results are plotted in Figure 6.15. The samples were analysed with pre-correction using alumina sample holder as a reference crucible to get the accuracy of the measurements. To know the decomposition point, the tests were conducted in air atmospheres from RT to 700ºC with a heating ramp of

10ºC/min. From the analysis, we observed a more stable performance of the three different molten salts until 565°C.
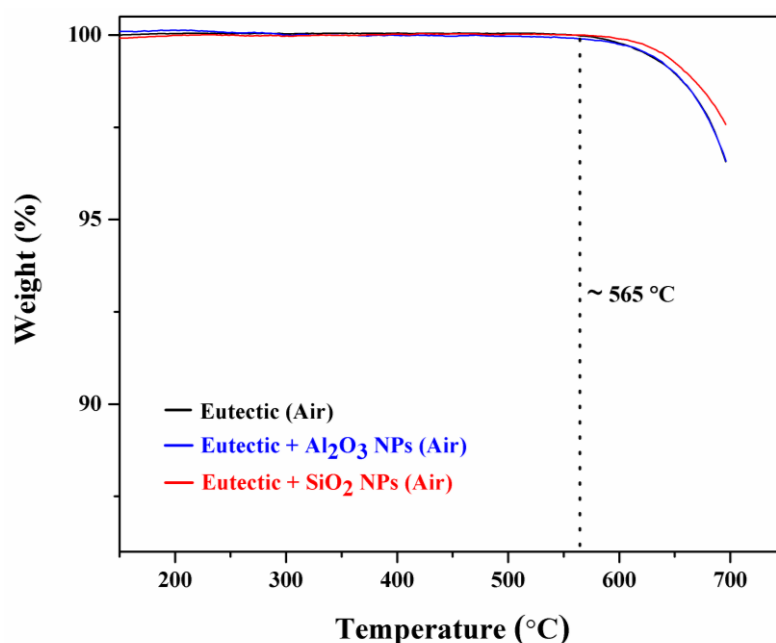
Figure 6.15. Thermogravimetric analysis of eutectic salt and Al_2O_3 and SiO_2 based nanofluids after 1500 hours corrosion test.

Similarly, no modifications were observed for melting temperature and enthalpy after the corrosion tests (Figure 6.14 and Table 6.1). Additionally, we did not observe any major change in the decomposition point for all the samples after the corrosion tests compared to as prepared ones - Figure 6.15. Such results indicate the absence of a chemical reaction between nanoparticles and the salt. This is important in terms of chemical stability of the nanofluid. Additionally, it indicates that the addition of nanoparticles is unlikely to modify the electrochemical potential of the salt, which is an important parameter for the corrosion process. Finally, the TGA analysis confirmed that the addition of nanoparticles did not produce major change on the thermal stability of the molten salt.

Chapter 7. Effect of TiO₂ Nanoparticles

The aim of this work is to define the dominant phenomena affecting the corrosivity of molten salts based nanofluids. For this purpose, a set of advanced techniques was applied to carbon steel tested with molten binary nitrate salt doped with titania nanoparticles. The corrosion rates were found to decrease considerably when nanoparticles were added, which was confirmed by three independent techniques (mass gain, cross-section analysis and XPS depth profiling). It was identified that the formation of mixed iron-titanium oxide is responsible for the stabilization of the corrosion layer and reduced corrosion rates.

7.1. Corrosion test protocol

For the corrosion tests, pieces of CS A516 Gr70 having a size of around $3 \times 12 \times 14$ mm were used. The corrosion tests were conducted in alumina crucible by immersing CS pieces in 5 grams of eutectic salt or TiO₂ based nanofluid. The corrosion tests were conducted under static immersion condition in an air atmosphere at 390ºC for periods of 250, 500, 1000 and 1500 hours.

7.2. Nanoparticles analysis

SEM imaging of titania nanoparticles (Fig. 5.15, insert) has confirmed the average size of 21 nm specified by the supplier. Raman spectroscopy is the technique of choice for titania polymorphs characterization. Fig. 5.15 shows a Raman spectrum from the titania nanoparticles. The main peaks centered at 148 cm $^{-1}$, ~400 cm $^{-1}$, ~520 cm $^{-1}$ and ~640 cm $^{-1}$ are close to the peaks positions in anatase, thus

concluding that the titania nanoparticles used in this study are mainly anatase polymorph.
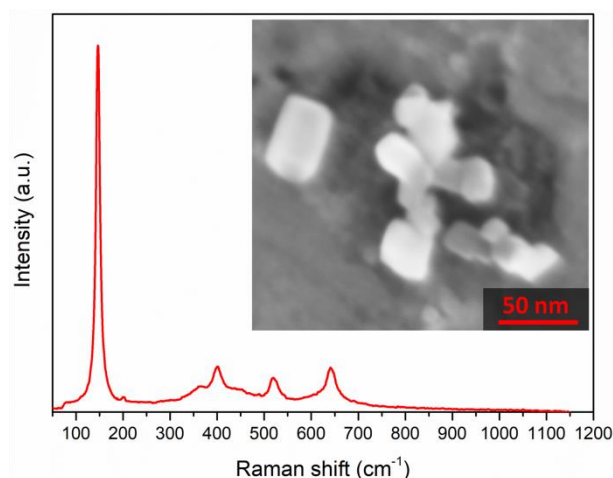
Figure 7.1. Raman spectrum of TiO_2 –nanoparticles. Insert: SEM micrograph

7.3. Carbon steel analysis

A pronounced separation of the corrosion layer (peel off) in the case of a pure nitrate salt is clearly seen (Figure 7.2a), while homogeneous corrosion appears when titania nanoparticles were added (Figure 7.2b). The high-magnification micrographs reveal the difference in the corrosion layer morphology (Figures 7.2c and 7.2d versus Figures 7.2e and 7.2f). Specifically, one can see that the nanoparticles are merging with the typical flakes of iron oxide (Figure 7.2f) - the nanoparticles no longer possess the well-defined crystal shape as compared to the pristine nanoparticles (Figure 7.1, insert). Such observation is in favour of the chemical reaction between the nanoparticles and the corrosion layer. Another argument to support the idea about possible chemical reactions between titania and salt comes from the EDX analysis. Tables in Figure 7.1 list elemental concentrations for the corresponded surfaces. In case of nanoparticles-free nitrate salt apart from iron and oxygen, magnesium was detected. Magnesium is a common impurity in nitrate salts and is often detected in the corrosion layers [68,75,122,124,125]. On the other hand, for the nitrate salt doped with titania nanoparticles titanium was detected instead of magnesium, which indicates the predominance of the titania - iron reaction over the magnesium-iron reaction. Titanium was found all over the surface of the carbon steel. In some places, titanium forms large agglomerates ~5 µm in size, as it is evidenced in Figure 7.3.

Element	O	Mg	Fe
At%	23.9	0.9	75.2

Element	O	Ti	Fe
At%	42.3	2.5	55.2
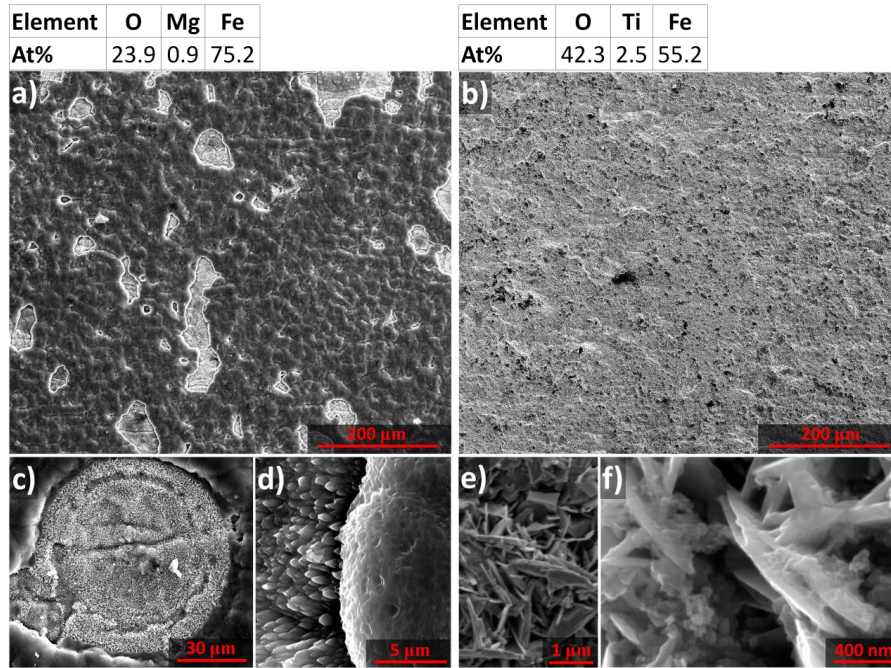
Figure 7.2. SEM micrographs of the surface of CS after 1500h corrosion test at 390ºC with nanoparticles-free nitrate salt (a, c, d) and nitrate salt doped with 1wt% of TiO_2 (b, e, f).
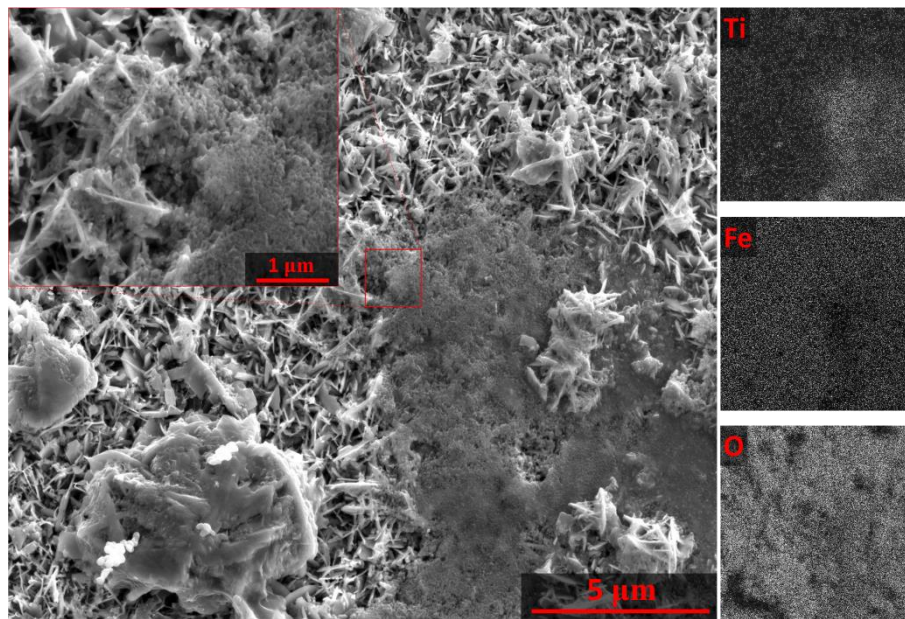
Figure 7.3. SEM micrographs and EDX-mapping of the surface of CS after 1500h corrosion test at 390ºC with nitrate salt doped with 1wt% of TiO_2.

XPS spectra shown in Figure 7.4 confirm the above mentioned observations, namely, the presence of titanium and the absence of magnesium in the corrosion layer of carbon steel for the case of nitrate salt doped with titania nanoparticles (green line in Figure 7.4) while presence of magnesium was detected in the case of nanoparticle-free nitrate salt (red line in Figure 7.4).
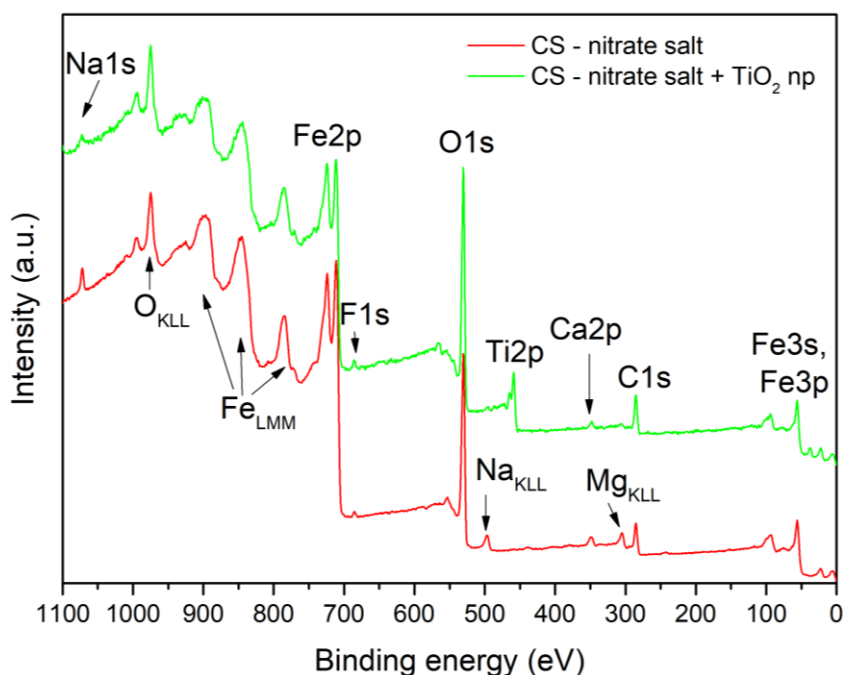
Figure 7.4. XPS spectra of the surfaces of carbon steel (CS) after the 1500h corrosion tests with nitrate salt and nitrate salt doped with TiO_2 nanoparticles (np).

XRD diffractograms presented in Figure 7.5 reveal evolution of the chemical phase composition of carbon steel after the corrosion tests with nanoparticle-free nitrate salt and with the salt doped with titania nanoparticles. In particular, the surface of carbon steel after 1500h corrosion tests with nanoparticles-free nitrate salt contains two phases, namely, iron (Fe) and hematite (Fe_2O_3). On the other hand, the corrosion products after the tests with nitrate salt doped with titania are formed by magnetite (Fe_3O_4), which is a lower degree of oxidation compared to hematite, and iron-titanium mixed oxide ($Fe_{1.7}Ti_{0.3}O_3$). The former phase suggests that upon oxidation of carbon steel in molten nitrate salt some Fe^{3+} iron atoms are substituted by titanium in hematite phase. Formation of such mixed oxide can be an explanation of the stabilization effect, which prevents corrosion layer from peeling off (Figure 7.2). Quantitative XPS analysis of the carbon steel surface elemental composition after corrosion tests (Table 7.1) gives Ti:Fe ratio ~ 0.20 which is in accord with the XRD derived result: Ti:Fe=0.18.
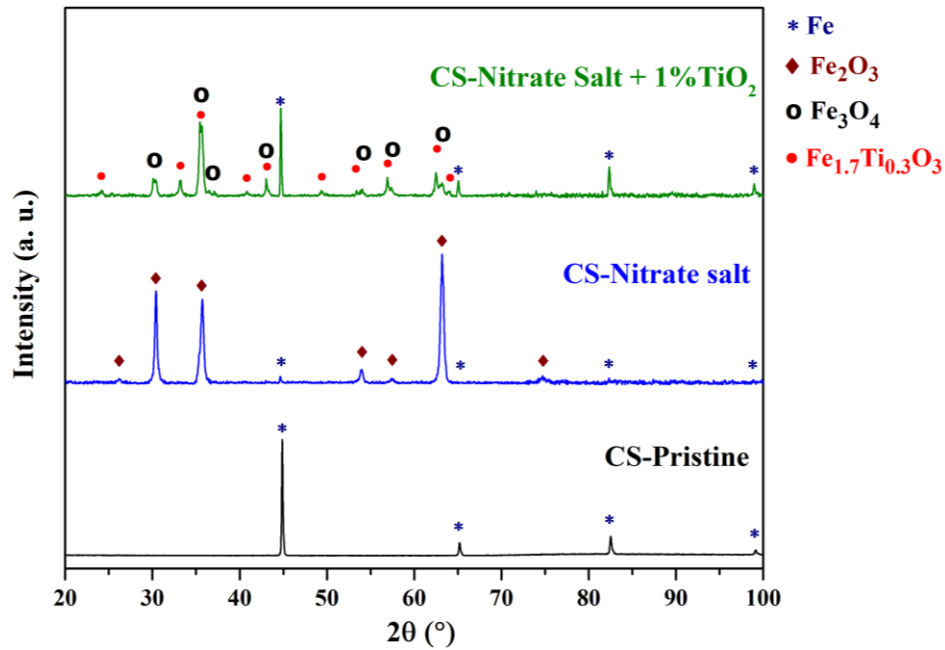
Figure 7.5. XRD diffractograms of carbon steel before and after 1500h corrosion tests at 390ºC with nitrate salt and nitrate salt doped with nanoparticles.

Table 7.1. Quantitative XPS analysis (at%) of carbon steel after 1500h corrosion tests at 390ºC with nitrate salt (CS) and nitrate salt doped with nanoparticles (CS + TiO_2)

	Ti2p	Fe2p	O1s	C1s	Mg
CS + TiO_2	5	26	47	22	-
CS	-	32	66	1	1

In order to quantify the effect of iron-titanium mixed oxide formation in the corrosion layer, the rate of oxidation was determined using three independent techniques. First, the mass gain evolution was examined, which was found to be more than twice lower for nitrate salt doped with nanoparticles than that for the nanoparticles-free salt after 1500h corrosion tests – Figure 7.6a. Next, a similar trend was observed for the corrosion layer evolution (Figure 7.6b), which was determined from the statistical examination of the cross-sections of carbon steel (Figure 7.7 as an example). Finally, the obtained results were confirmed by the XPS depth profiling technique, which revealed the enhanced thickness of the oxidation layer for nanoparticles-free nitrate salt compared to the salt doped with titania nanoparticles – Figure 7.8. Combined results of three techniques described above showed reduction by a factor of ~3 of the corrosion rate after 1500h corrosion tests for the salt doped with nanoparticles.
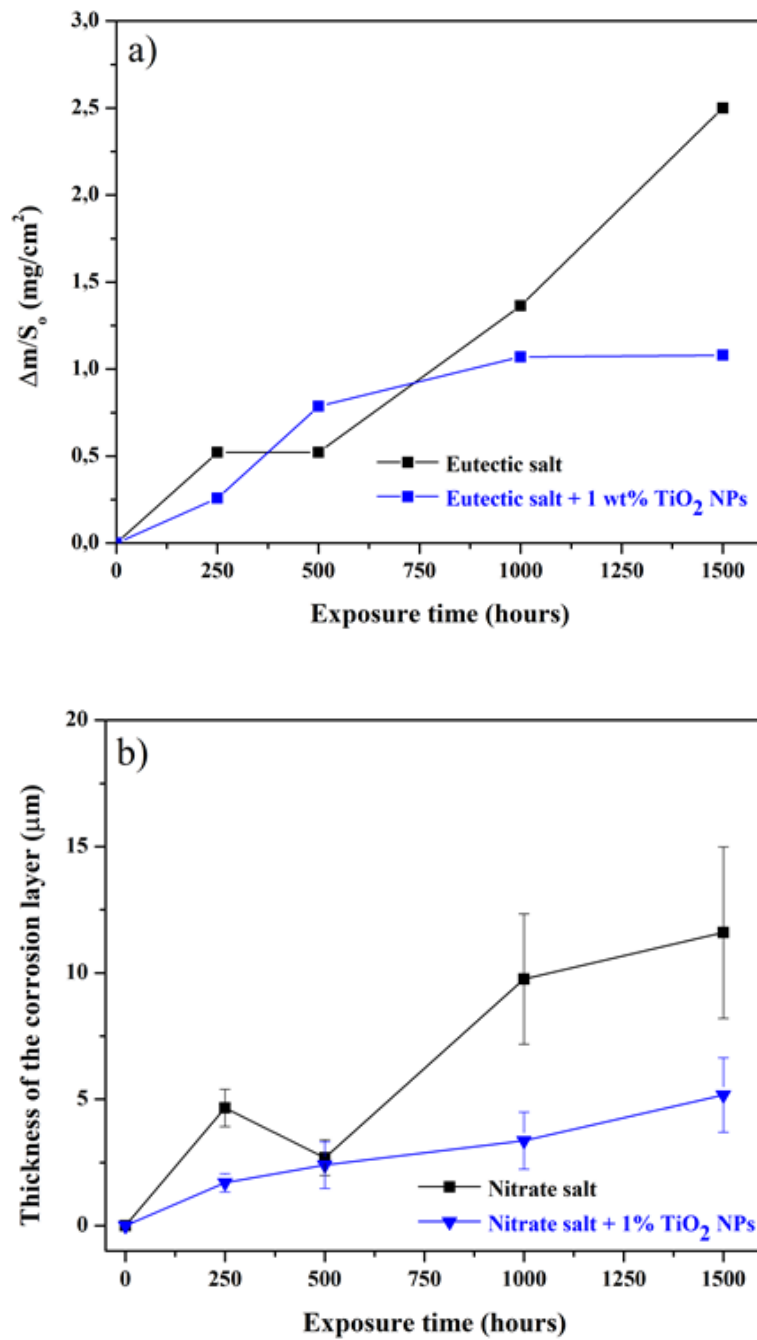
Figure 7.6. a) mass gain and b) corrosion layer thickness for carbon steel tested with molten nitrate salt and nitrate salt doped with TiO_2 nanoparticles at 390ºC.
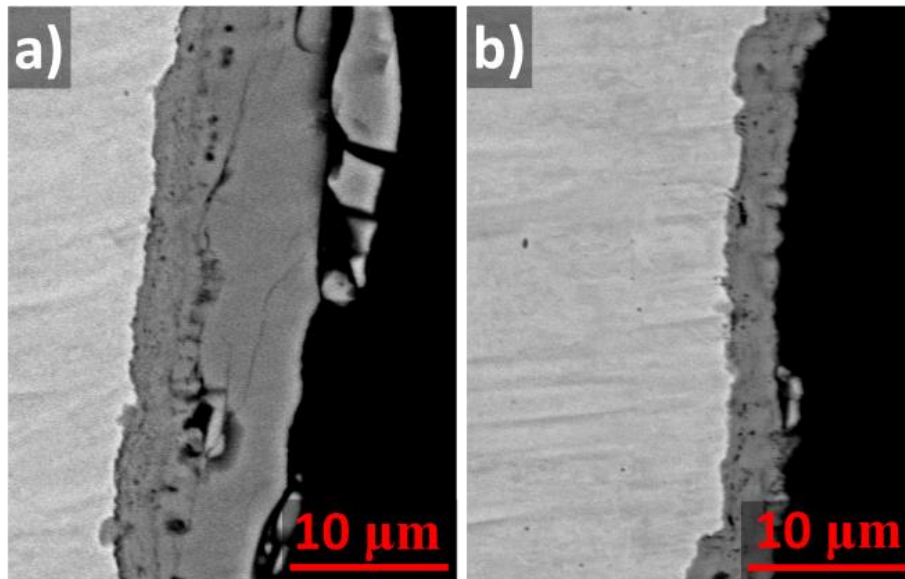
Figure 7.7. Cross-section of carbon steel after 1500h corrosion test at 390ºC with a) nitrate salt and b) nitrate salt doped with nanoparticles.

Additional important observation can be extracted from XPS depth profiling experiments. In the case of nanoparticles-free nitrate salt magnesium incorporation into the corrosion layer of carbon steel can be tracked all along with the oxide layer (Figure 7.8a, green line). This suggests that Mg forms a mixed oxide with iron upon oxidation in molten nitrate salt. We were not able to determine the Mg-containing phase by means of XRD due to its very low content as can be seen the EDX (Figure 7.2a) and from the XPS (Figures 7.4 and 7.8a) data. On the contrary, the titanium-containing phase ($Fe_{1.7}Ti_{0.3}O_3$) was found to be located mostly in the topmost surface of the corrosion layer (Figure 7.8b). In particular, the concentration of Ti drops exponentially after sputtering away ~1 µm of material and continue to decrease with depth in the corrosion scale. Such observation allows suggesting that after the formation of the mixed iron-titanium oxide further oxidation of carbon steel takes place by the diffusion of oxygen through the $Fe_{1.7}Ti_{0.3}O_3$ phase. Such diffusion is apparently slower as compared to the diffusion through the mixed iron-magnesium oxide, which results in the lower corrosion rates in the case of nitrate salt doped with nanoparticles compared to nanoparticles-free salt.
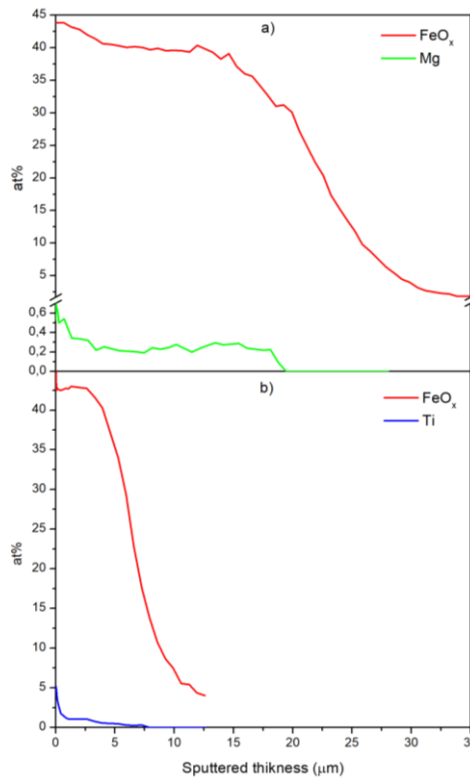
Figure 7.8. XPS depth profiling for carbon steel after 1500h corrosion test at 390ºC with a) nitrate salt and b) nitrate salt doped with titania nanoparticles. Red lines present a depth profile of the iron oxide component (FeOx) of the Fe2p XPS spectral line. FeOx component intensity represents the contribution from several oxidation states of iron excluding metallic iron.

Based on the XPS depth profiling and XRD analysis presented above, while taking into account EDX mapping, one can schematically represent the corrosion scale of carbon steel after the corrosion tests with nanoparticles-free molten nitrate salt and nitrate salt doped with titania nanoparticles (Figure 7.9).
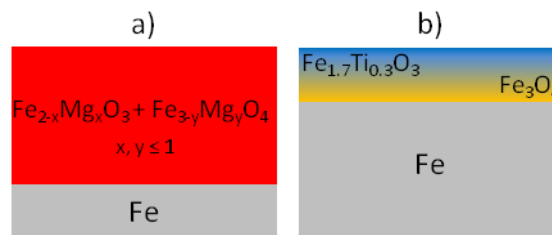
Figure 7.9. Schematic representation of corrosion layer of carbon steel after corrosion test at 390ºC with molten a) nitrate salt and b) nitrate salt doped with titania nanoparticles based on XPS depth profiling and XRD analysis.

Finally, the focused ion beam technique was used to obtain textural properties of the corrosion layers' cross-section. Due to low-voltage ion polishing, the cross-section of the corrosion scale reveals the textural features (like cracks, voids, etc), which are typically lost during the mechanical polishing applied in conventional

cross-section preparation. Figure 7.10 clearly shows that corrosion layer of the carbon steel after the corrosion tests with molten nitrate salt poses more cracks (Figure 7.10a) as compared to the case of molten salt doped with titania nanoparticles (Figure 7.10b).
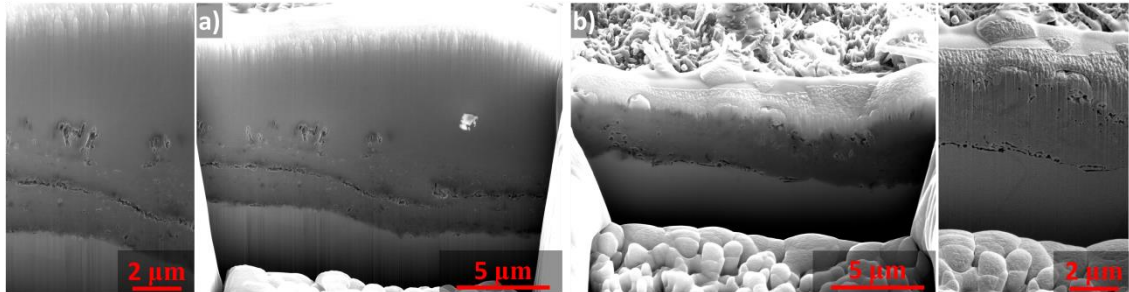
Figure 7.10. Cross-section view of carbon steel after 1500h corrosion test at 390ºC with a) nitrate salt and b) nitrate salt doped with titania nanoparticles. Obtained with focused ion beam technique.

All the described above observations provide strong evidence of the anticorrosion effect of titania nanoparticles doping into the molten nitrate salt. This effect we assign to the formation of mixed iron-titanium oxides. It is known from the literature that the doping by other nanoparticles like silica [37, 76, 122, 126] or alumina [76,122] also results in their incorporation into the corrosion layer. In particular, the incorporation of Al_2O_3 [6] and SiO_2 [37, 126] nanoparticles was reported to decrease the corrosivity of molten salt. While in other work SiO_2 nanoparticles incorporation had a negligible effect on the corrosion, rates [6]. In the case when corrosion tests were performed at lower temperature (310ºC) micro-bubbling of the nanofluids were found to be a dominating effect which led to increased corrosion rates, even though, the incorporation of Al_2O_3 and SiO_2 nanoparticles was also reported [3]. In this work, we have found that the mechanism of titania nanoparticles incorporation involves formation of mixed oxide with iron. Such results may also shed some light on the possible mechanism of SiO_2 and Al_2O_3 nanoparticles doping. In particular, in work [6] iron-silicon mixed oxide was reported as a corrosion product after corrosion test of Solar salt with SS 347. However, this Fe_2SiO_4 phase did not have a predominant role for the corrosion rates and the overall corrosivity of the salt did not change despite of nanoparticles doping [6].

7.4. Nanofluid analysis

It is generally known that the nanoparticles doping can change the wetting properties of a fluid [127], which pertains to corrosion phenomena. With this regard,

high-temperature contact angle measurements were performed for molten salts and salt doped with nanoparticles. It was found that in the investigated temperature range, nanoparticles doping did not change the wetting properties of molten nitrate salt (Figure 7.11). Therefore, obtained reduction of corrosivity can be attributed to the mixed oxide formation, rather than to the wetting properties of the nanofluid.
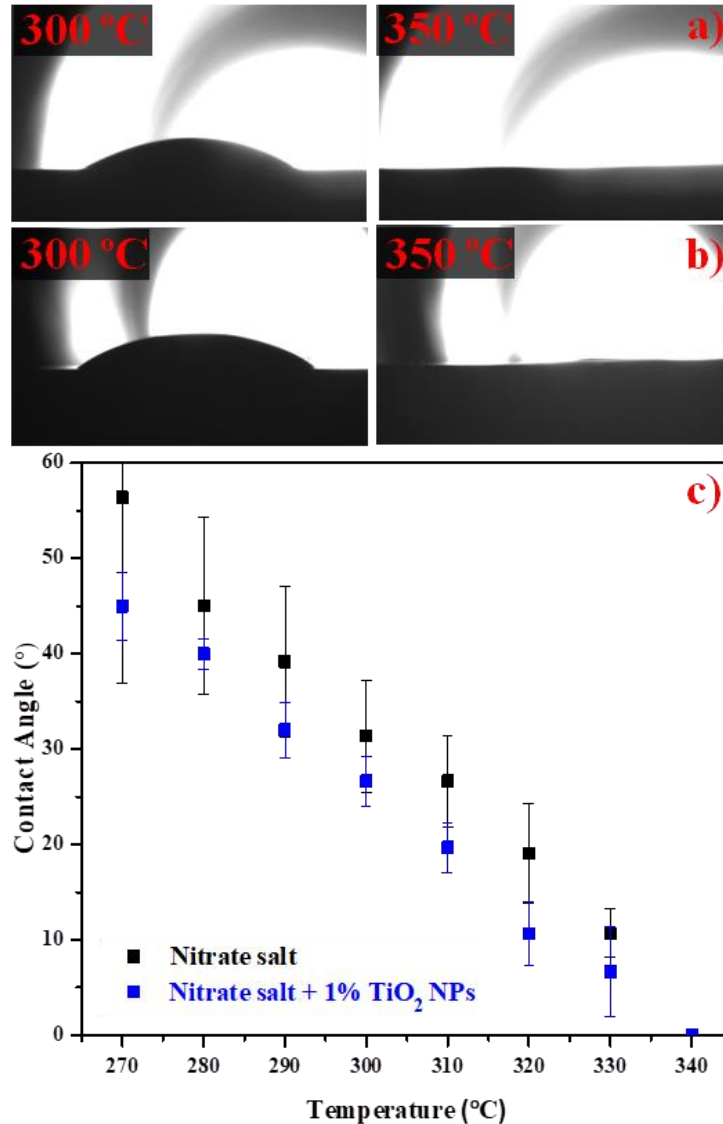
Figure 7.11. Contact angles of a) molten nitrate salt, b) molten nitrate salt + TiO_2 NPs and c) their temperature dependence.

It should be noted that both salts and nanoparticles were examined in terms of possible degradation after the corrosion tests by XRD (Figure 7.12) and no evidence of such modifications were detected. It was also verified that nanoparticles doping does not affect the decomposition temperature (and hence the operational temperature range) of the salt (Figure 7.13)
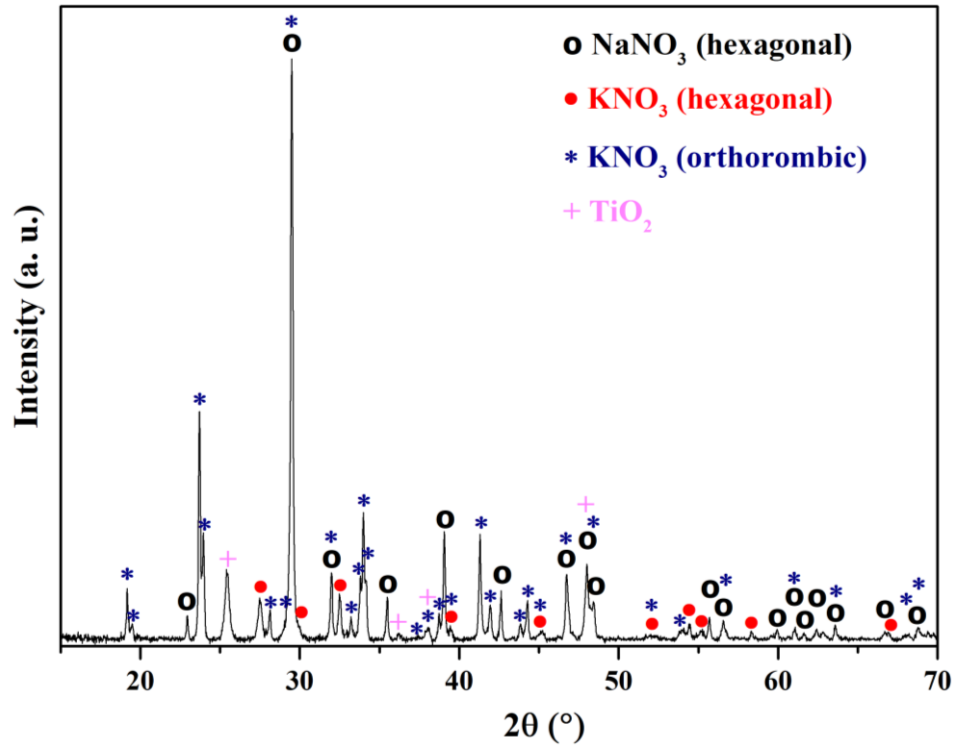
Figure 7.12. XRD pattern of binary nitrate salt doped with 1wt% TiO$_2$ nanoparticles after 1500h corrosion test with carbon steel at 390ºC.
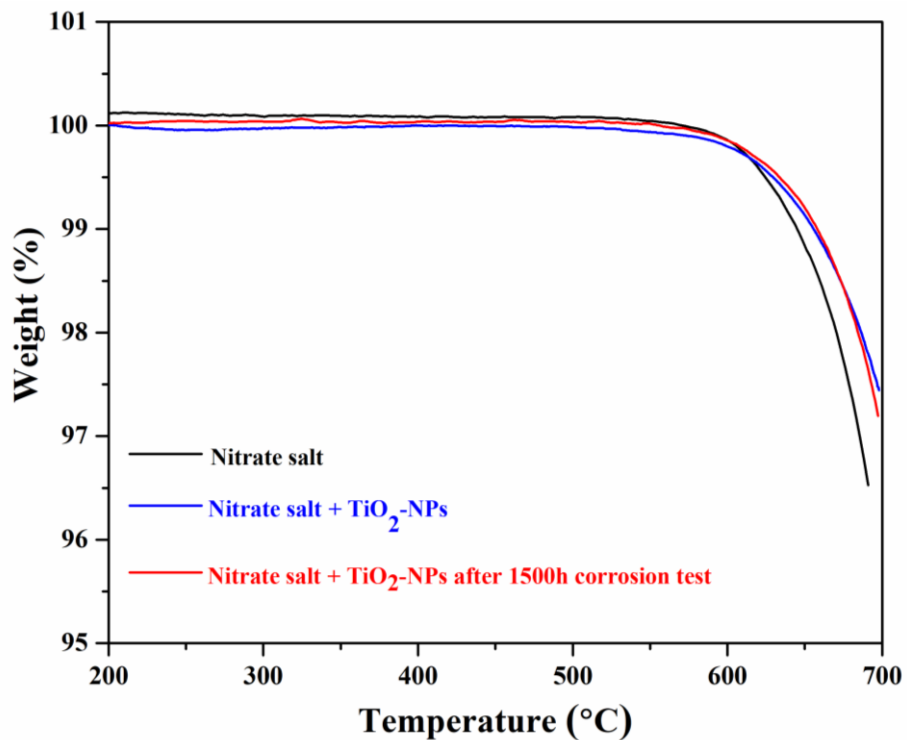
Figure 7.13. Thermogravimetric curves of as prepared nitrate salt, nitrate salt + 1wt% TiO$_2$ nanoparticles and nitrate salt + 1wt% TiO$_2$ nanoparticles after 1500h corrosion test at 390ºC.

Chapter 8. Graphitization as an Efficient Inhibitor Method

The aim of this chapter is to test the graphitization method as a corrosion inhibitor for carbon steel by molten binary nitrate salt ($NaNO_3$-KNO_3), improving its durability and operational temperature range, particularly for the TES applications at CSP plants. This method was demonstrated to be effective in reducing corrosion rates, stabilizing the corrosion scale and preventing its separation. It has been demonstrated that the surface spray-coating by graphite of carbon steel reduces the corrosion rate at least by a factor of 6 and stabilizes the corrosion scale by iron carbide crystals at temperatures of 390ºC.

8.1. Results and discussions

Figure 8.1 shows surface morphology of carbon steel after 1500h corrosion tests at 390ºC. It is clear that the binary nitrate salt severely corrodes the carbon steel, which involves pronounced separation of the corrosion scale, localized corrosion and cracking (Figure 8.1a). In contrast, the graphitized carbon steel demonstrated significantly less corroded surface after the test - Figure 8.1b. Even though, graphitization did not result in a completely homogeneous surface after the corrosion test as some localized separation of the corrosion scale was evident. The depth of such spots is considerably lower (Figure 8.1b), as compared to that of the non-graphitized steel sample (Figure 8.1a). A high-magnification image of the FIB made cross-section reveals that the corrosion scale of the non-graphitized carbon steel possesses more cracks as compared to the graphitized carbon steel – Figure 8.2. The

comparison of EDX analysis revealed the important difference in the chemical composition of the surfaces of non-graphitized (Figure 8.1a) and graphitized (Figure 8.1b) carbon steels: the graphitized samples do not have Mg (a common impurity in nitrate salts) incorporated in the corrosion scale. This suggests that the reaction between graphite and carbon steel is competitive to the reaction of Mg with carbon steel. This may explain the difference in the textural appearance of the surfaces of graphitized and non-graphitized carbon steels at high magnification − Figures 8.1a and 8.1b. However, due to a very low concentration of the graphite in the system (around 0.08 wt%), it is difficult to distinguish any carbon containing phase at the surface of graphitized carbon steel. In order to understand the mechanism and type of the involved chemical reactions, additional experiments for graphitized carbon steel with nitrate salt containing 2wt% of graphite were conducted. It was verified by the thermogravimetric method that the nitrate salt containing graphite is stable at the temperature of corrosion tests − Figure 8.3. One can see that such experiments resulted in a homogeneous surface of carbon steel without localized corrosion (Figure 8.1c), which suggests that the amount of deposited graphite during the graphitization can be optimized to reach even better corrosion resistance as compared to the results shown in Figure 8.1b. One can also clearly see the formation of cubic crystals inside the corrosion scale (Figure 8.1c, inset), which have a stabilizing effect. XRD examination (see below) showed that the crystals are iron carbide.

Element	O	Mg	Fe
At%	30.0	2.9	67.1

Element	O	Fe
At%	20.6	79.4

Element	O	C	Fe
At%	18.6	0.9	80.5
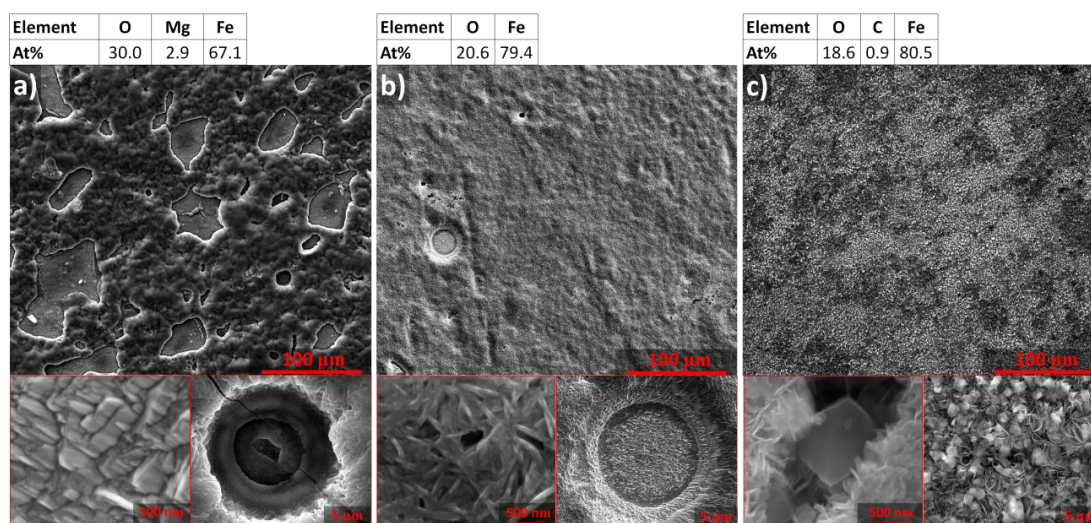
Figure 8.1. SEM micrographs and EDX analysis of the carbon steel surface after 1500 hours of corrosion tests at 390ºC. a) carbon steel + nitrate salt; b) graphitized carbon steel + nitrate salt; c) graphitized carbon steel + nitrate salt + 2%wt graphite.
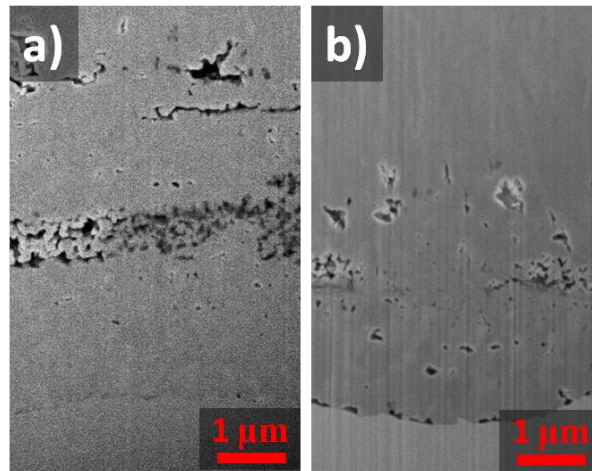
Figure 8.2. FIB/SEM cross-section analysis of carbon steel after 1500h corrosion tests at 390ºC. a) carbon steel + nitrate salt; b) graphitized carbon steel + nitrate salt.
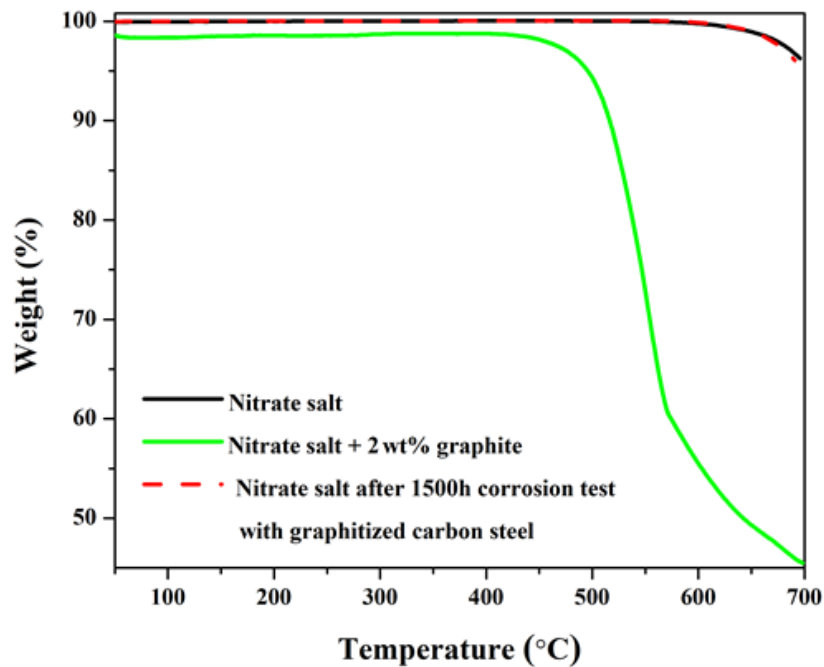
Figure 8.3. Thermogravimetric test for binary nitrate salt and binary nitrate salt + 2wt% graphite

The representative images of the cross-sections are demonstrated in Figure 8.4. Results of cross-sectional examination of the studied samples are summarized in Table 8.1. The data revealed reduced corrosion rates in the case of graphitized carbon steel and a further decrease of corrosion rate of the graphitized carbon steel when 2wt% of graphite was added into the salt. The obtained values were additionally verified with the cross-section measurements using the FIB technique.

Table 8.1. Corrosion layer thickness (L) of carbon steel (CS) after 1500h corrosion test at 390ºC.

Sample	Max L (µm)	Average L (µm)	Standard deviation (µm)	Corrosion rate (mm/year)
CS + nitrate salt	21.99	18.71	2.93	0.109
Graphitized CS + nitrate salt	15.17	11.36	1.97	0.066
Graphitized CS + nitrate salt + 2wt% Graphite	4.74	3.12	0.59	0.018
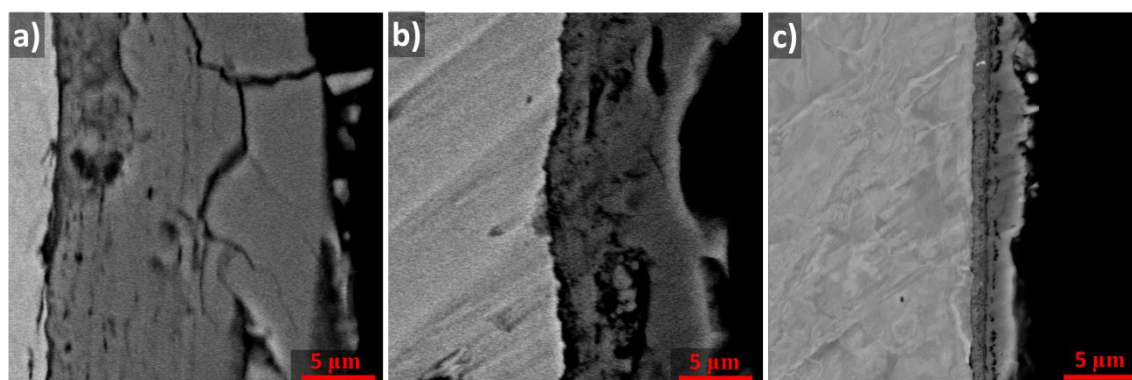
Figure 8.4. SEM micrographs of the cross-sections of carbon steel after 1500h corrosion tests at 390ºC. a) carbon steel + nitrate salt; b) graphitized carbon steel + nitrate salt; c) graphitized carbon steel + nitrate salt + 2%wt graphite.
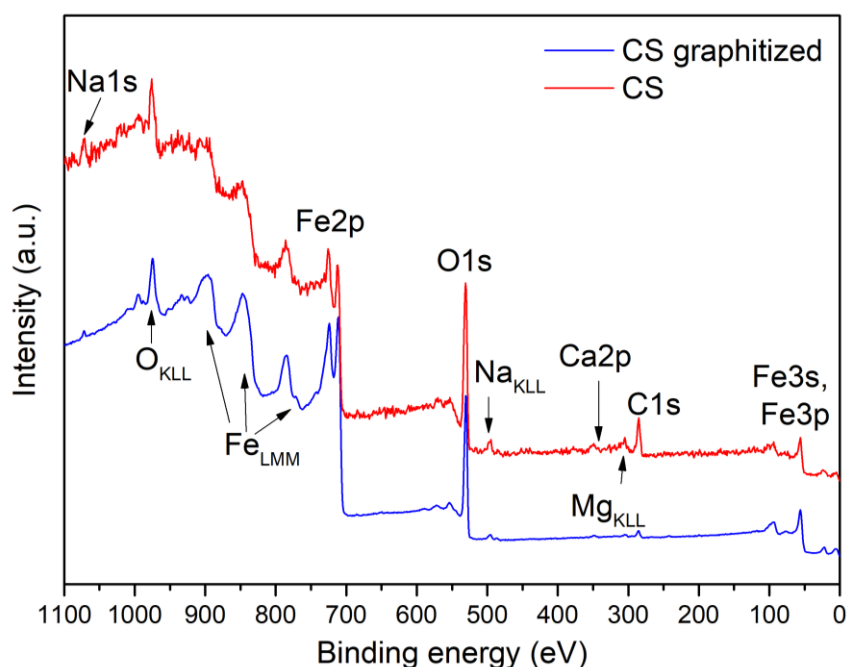
Figure 8.5. XPS survey spectra for carbon steel (CS) and graphitized CS after 1500h corrosion tests at 390ºC. The surfaces were cleaned before acquiring the XPS spectra by Ar ion clusters.

In order to gain further insights into the corrosion mechanism and verify the obtained corrosion rates, XPS depth profiling was applied to the graphitized and non-graphitized samples of carbon steel. Comparative analysis of XPS surveys spectra shown in Figure 8.5 confirms the presence of Mg in the non-graphitized carbon steel after the corrosion test, as well as its absence in the graphitized sample. Due to higher surface sensitivity (below 1nm thickness, detection limit ~0.1 at%) of XPS, low traces of Na and Ca were detected in the corrosion scale. The Ca and Na originate from the salt´s impurities. Those two elements were only detected on the surface of the samples and their peaks disappeared after removal of ~ 100 nm of the scale by means of ion-sputtering. On the contrary, the Mg was found to be present in the corrosion scale of non-graphitized carbon steel up to the depth of 20 μm – Figure 8.6b. The XPS depth profiling confirmed the reduced corrosion scale thickness of the graphitized carbon steel (Figure 8.6a) as compared to the non-graphitized sample (Figure 8.6b).

XRD analysis is in accordance with the SEM and XPS data (Figure 8.7). In particular, it was found that corrosion scale of non-graphitized carbon steel (Figure 8.7a) is formed not only by iron oxide hematite (Fe_2O_3) but also by the Mg-containing phase – magnesioferrite (Fe_2MgO_4). In the case of graphitized carbon steel (Figure 8.7b) the corrosion scale is formed by two iron oxides, namely hematite (Fe_2O_3) and magnetite (Fe_3O_4). Any other phase, which may be responsible for the corrosion rates reduction and stabilization of the scale was not identified, probably due to the low initial concentration of graphite in the system and consequently the low amount of this phase. In the case when 2wt% of graphite was added to the salt the surface of graphitized carbon steel is covered by the scale of hematite (Fe_2O_3), magnetite (Fe_3O_4) and iron carbide (Fe_5C_2), also known as Hägg carbide. The crystals in the former phase were evidenced by SEM (Figure 8.7c).

It was verified by means of thermogravimetric analysis that the decomposition temperature of the salt after the corrosion test with the graphitized carbon steel was not modified (Figure 8.3). The melting temperature and the enthalpy of phase transitions were also found to be similar to pristine nitrate salt. This suggests that all the sprayed graphite has reacted with the carbon steel and the properties of the nitrate salt, including its maximum operational temperature, were not affected.

From the described above observations (SEM, XPS) one can clearly see that graphitization reduces the corrosion rates of carbon steel in contact with molten

nitrate salt at 390°C. The reduced corrosion rates (Table 8.1) are due to the formation of iron carbide phase (XRD, SEM), which stabilizes the corrosion scale and prevents its separation during the corrosion test. The sufficient amount of carbon (graphite) in the system is crucial for the formation of the stabilizing phase of iron carbide. In particular, significantly reduced corrosion rates of carbon steel in the case of 2wt% of graphite were added into the salt, suggest that the amount of graphite sprayed over the surface of the carbon steel can be further optimized to reach even better protection quality. It is evident that the reaction of iron with graphite is competitive to the reaction of iron with Mg (SEM-EDX, XPS, XRD), which may also affect corrosion rates and will be the subject of further work.
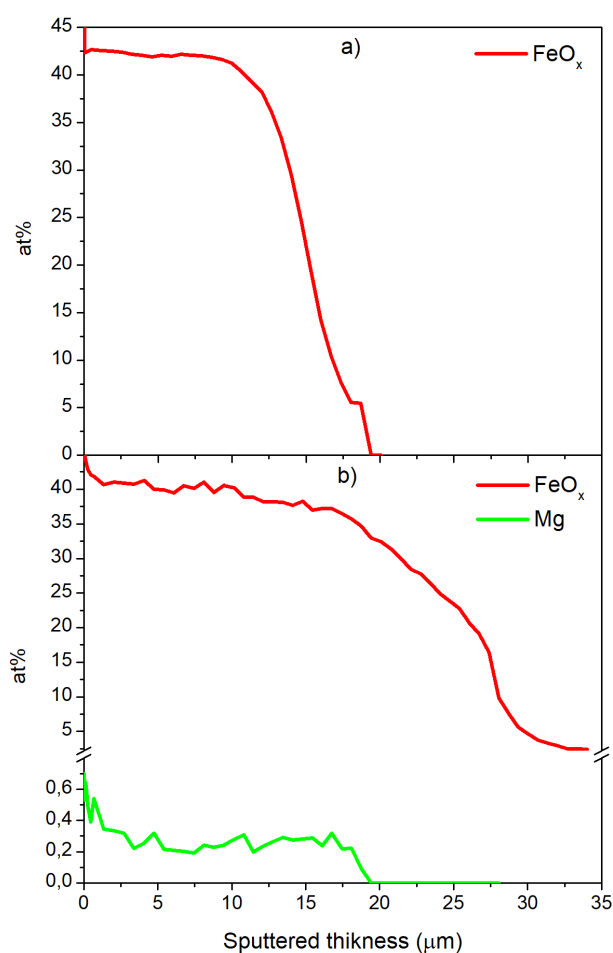
Figure 8.6. Atomic concentration of FeO_x and Mg versus the depth of the corrosion scale (sputtered thickness) obtained by XPS depth profiling.
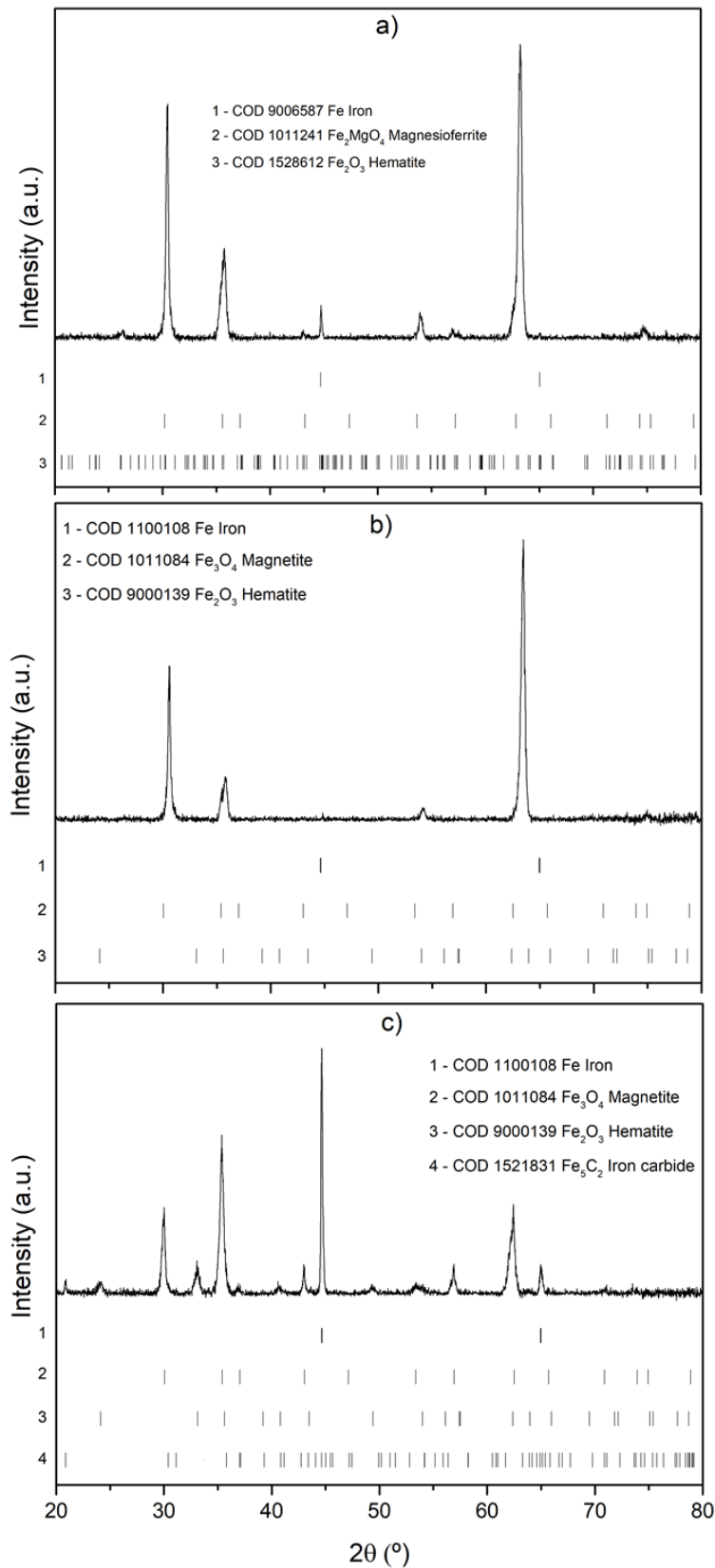
Figure 8.7. XRD patterns of the surfaces of carbon steel after 1500h corrosion tests at 390ºC. a) carbon steel + nitrate salt; b) graphitized carbon steel + nitrate salt; c) graphitized carbon steel + nitrate salt + 2%wt graphite.

Part 2. General Conclusions

Binary nitrate salt-based nanofluids were examined in terms of their corrosion aspects with carbon steel under air atmosphere. The following conclusions can be formulated:

- Doping the salt with alumina and silica nanoparticles considerably reduced the corrosion rates of carbon steel at 390ºC. After 1500 hours immersion tests, the corrosion layer was demonstrated to be about 3 times lower as compared to the base fluid (salt without nanoparticles), which was evident from the mass gain and statistical cross-section analysis. The lower oxidation rate for nanofluids was also evident from the XRD analysis. In addition, non-homogeneous oxidation with numerous defects was detected for nanoparticles-free nitrate salt by examination of the surfaces of carbon steel after the corrosion tests. On the contrary, the same analysis revealed homogeneous oxidation of carbon steel after the tests with nanofluids.

- Reduced corrosion rates of carbon steel may be due to the incorporation of nanoparticles into the corrosion layer, which was detected by EDX-SEM techniques for both cross-section and surface analysis.

- Two major counter corrosion aspects of nanofluids were identified: i) incorporation of nanoparticles into the oxide layer, which reduced the corrosion rates and ii) formation of microbubbles, which enhances the corrosion rate due to the increased amount of oxygen in the system.

- Experiments at 310ºC allowed to increase the effect of microbubbles due to their long-time entrapment in the molten salt (more than 3 days). Under these conditions, the corrosion layer for molten salts based nanofluids was about 2 times higher as compared to the base fluid.

- The dispersion of nanoparticles in the salt was examined before and after the corrosion tests. It was demonstrated that as-prepared salts contain agglomerates of nanoparticles of ~ 200 nm size. After the corrosion tests, nanoparticles tend to further agglomerate. In particular, agglomerates of ~ 2 μm were found after 1500h corrosion tests.

In the case of TiO_2 based nanofluid, the effect of titania nanoparticles on the corrosion rates of eutectic $NaNO_3$-KNO_3 molten salt was investigated for the first time. The following conclusions can be formulated:

- Addition of 1wt% of titania nanoparticles to molten binary nitrate salt reduced the corrosion rate of carbon steel tested at 390ºC by a factor of 3, which was demonstrated by mass gain, SEM cross-section, and XPS depth profiling analysis.

- The presence of titania nanoparticles in the salt resulted in homogeneous oxidation of the surface of carbon steel at 390ºC, which is in drastic contrast to the case of nanoparticles-free salt, where pronounced corrosion scale separation and peel-off were evident from SEM experiments.

- Formation of mixed iron-titanium oxide was demonstrated by XRD analysis and suggested to be responsible for the corrosion rates reduction and corrosion scale stabilization. By means of XRD, EDX and XPS it was shown that growth of surface iron-titanium oxide is competitive to the formation of iron-magnesium oxide - a chemical phase formed due to the presence of Mg impurity in the nitrate salt.

- By means of XPS depth profiling, it was demonstrated that such mixed oxide is located on the surface of corrosion scale on top of magnetite phase, hindering the diffusion of molten salt and further oxidation of carbon steel.

- The investigated molten salt-based nanofluid was found to have similar decomposition temperature and surface properties (contact angle on the carbon steel) as nanoparticles-free nitrate salt.

- All the salts were demonstrated to be stable during the corrosion tests and no modifications of melting temperature, enthalpy of melting, decomposition temperature and infrared spectra were detected.

Finally, the spray-graphitization was tested as an anticorrosion method for molten binary nitrate salt. It was demonstrated that corrosion rates of carbon steel at

390ºC were reduced almost twice when graphitization was applied. Moreover, it was shown that adding 2wt% of graphite into the salt reduces the corrosion rate more than 6 times compared to the non-graphitized carbon steel due to the formation of homogeneously distributed iron carbide crystals on the surface of carbon steel. Thus, the amount of sprayed graphite can be further optimized to obtain better protection. Finally, the molten salt-based nanofluids show the reduction of the corrosion rates, which will increase the lifetime of the storage tank.

In general, the newly developed protection and the addition of nanoparticles serve as a protection layer from the molten salt corrosivity. The obtained results have the potential to improve safety and to reduce the costs of construction materials for high-temperature molten salts applications like concentrated solar power plants. Furthermore, the obtained results provide important insights into the corrosion mechanisms of molten salts based nanofluids and allow to reconsider their feasibility for CSP applications due to the improved compatibility aspect.

Future Works

The development of nanofluids based on molten salt with anomalous enhanced thermophysical properties will lead to a further cost reduction in CSP plants. In the present thesis work, a big effort was made to understand the big discrepancy of the already reported in the literature which may due to several factors:

1. The initial state of the nanoparticle dispersion. The wet method followed in literature may be the responsible of the discrepancy of the results due to the partial dispersion states obtained by different groups for the same system, i.e. the same base fluid and nanoparticles, due to the complexity to disperse the nanoparticles in an aqueous medium. However, in this work, we present an optimized simple dry method for the preparation of nanofluids to obtain that allows us to obtain a homogeneous dispersion of nanoparticles within the molten salt. As future work, a cross verification of this new method by different research groups will be needed to validate it as an efficient way to obtain well-dispersed nanofluids.

2. The evolution of the dispersion stability with time. The long-term dispersion is very important not only to shed some light on understating the discrepancy of the results reported in the literature but also to maintain the anomalous enhancements of the thermophysical properties during the lifetime of the nanofluids. The investigation of this aspect was almost absent in literature despite its importance. In this work, we studied the evolutionary stability of the nanofluid by means of a visual stability test conducted in the furnace at high temperature. In the future, the development of a high-temperature dynamic light scattering (DLS) will help to perform in-situ analysis of the

dispersion state of nanofluids that will conduct to a better understanding of the mechanisms responsible for the agglomeration of the nanoparticles.

3. The nanoparticles size, shape and composition effect. In general, we demonstrate the effect of the shape, size and composition of the nanoparticles on the enhancement of the thermophysical properties and short-term dispersion stability of the nanofluids. In the future, systematic studies of the effect of the combination of those parameters, at least two, should be conducted aiming to maximize the enhancements of the thermophysical properties and to improve the long-term dispersion stability of the nanofluids.

4. The specific surface area of nanoparticles. It is very important to mention here that the surface area of the nanoparticles is playing a crucial factor for enhancing the thermophysical properties mainly the specific heat capacity and thermal conductivity. On the contrary, a high surface area of the nanoparticles plays a negative impact on increasing the viscosity of the investigated nanofluids. In the future, nanoparticles with big particle size and higher specific surface area, nanoporous materials, will be investigated looking for a better compromise between the enhancements of the thermophysical properties and limited impact on the viscosity.

5. The enhancement mechanisms of the thermophysical properties. The enhancement mechanisms of the thermophysical properties are still unknown, However, in order to investigate the interfacial phenomena between the molten salt and solid nanoparticle, more localized characterization techniques such as Small Angle Neutron Scattering (SANS), Small Angle X-ray Scattering (SAXS) and Small Angle Laser Scattering (SAXS) will be performed.

6. The compatibility of molten salt-based nanofluids was the storage tank materials. In this work, we demonstrated the positive effect of adding nanoparticles such as Al_2O_3, SiO_2 and TiO_2 on the corrosivity behaviour of molten salt. The corrosion tests were performed under static immersion conditions. In the future, it is very important to conduct these corrosion tests under dynamic mode aiming to investigate other effects as the erosion effect that may be caused by the addition of the nanoparticles that may depend on the shape of the nanoparticles.

Bibliography

[1] Global energy & CO_2 status report, (2018).

[2] D. Hales, Renewables 2018 global status report, 2018.

[3] Non-renewable energy [Online]:
https://www.nationalgeographic.org/encyclopedia/non-renewable-energy/

[4] Hannah Ritchie and Max Roser, CO_2 and other Greenhouse gas emissions, (2109) [online]: https://ourworldindata.org/co2-and-other-greenhouse-gas-emissions

[5] EPA, United States environmental protection agency, global greenhouse gas emission data [Online]: https://www.epa.gov/ghgemissions/global-greenhouse-gas-emissions-data

[6] L.E. Singer, D. Peterson, International energy outlook, 2016.

[7] G. Alva, Y. Lin, G. Fang, An overview of thermal energy storage systems, Energy. 144 (2018) 341–378. doi:10.1016/j.energy.2017.12.037.

[8] Energy education [Online]:
https://energyeducation.ca/encyclopedia/Photovoltaic_effect

[9] PV insights [Online]: http://pvinsights.com/Knowledge/Principle.php

[10] Photovoltaic [Online]: https://www.pinterest.com/pin/414401603183250304

[11] I. Sarbu and C. Sebarchievici, A comprehensive review of thermal energy storage, Sustainability 10 (2018) 191. doi:10.3390/su10010191.

[12] E. González-Roubaud, D. Pérez-Osorio, C. Prieto, Review of commercial thermal energy storage in concentrated solar power plants: Steam vs. molten salts, Renew. Sustain. Energy Rev. 80 (2017) 133–148. doi:10.1016/j.rser.2017.05.084.

[13] M. Liu, N.H.S. Tay, S. Bell, M. Belusko, R. Jacob, G. Will, W. Saman, F. Bruno, Review on concentrating solar power plants and new developments in high temperature thermal energy storage technologies, Renew. Sustain. Energy Rev. 53 (2016) 1411–1432. doi:10.1016/j.rser.2015.09.026.

[14] W. Fuqiang, C. Ziming, T. Jianyu, Y. Yuan, S. Yong, L. Linhua, Progress in concentrated solar power technology with parabolic trough collector system :

A comprehensive review, Renew. Sustain. Energy Rev. 79 (2017) 1314–1328. doi:10.1016/j.rser.2017.05.174.

[15] BIGDISHSOLAR [online]: https://bigdishsolar.com/the-csp-context/.

[16] I.E. Agency, technology roadmap, (2014).

[17] H.L. Zhang, J. Baeyens, J. Degreve, G. Caceres, Concentrated solar power plants : Review and design methodology, Renew. Sustain. Energy Rev 22 (2013) 466–481. doi:10.1016/j.rser.2013.01.032.

[18] Review of CSP technologies MENA assessment of the local manufacturing potential for concentrated solar power projects, (2011).

[19] SolarPACES, How CSP Works : Tower , Trough , Fresnel or Dish Power Tower Systems : Linear Fresnel Systems :, (2018) 2–3.

[20] D. Liu, L. Xin-Feng, L. Bo, Z. Si-quan, X. Yan, Progress in thermochemical energy storage for concentrated solar power : A review, Int J. Energy Res. (2018) 1–16. doi:10.1002/er.4183.

[21] G. Alva, L. Liu, X. Huang, G. Fang, Thermal energy storage materials and systems for solar energy applications, Renew. Sustain. Energy Rev. 68 (2017) 693–706. doi:10.1016/j.rser.2016.10.021.

[22] C.-C. Lai, W.-C. Chang, W.-L. Hu, Z.M. Wang, M.-C. Lu, Y.-L. Chueh, A solar-thermal energy harvesting scheme: enhanced heat capacity of molten HITEC salt mixed with Sn/SiOx core–shell nanoparticles, Nanoscale. 6 (2014) 4555. doi:10.1039/c3nr06810b.

[23] S.M.S. Murshed, K.C. Leong, C. Yang, Enhanced thermal conductivity of TiO_2-water based nanofluids, Int. J. Therm. Sci. 44 (2005) 367–373. doi:10.1016/j.ijthermalsci.2004.12.005.

[24] M. Gupta, V. Singh, R. Kumar, Z. Said, A review on thermophysical properties of nano fluids and heat transfer applications, Renew. Sustain. Energy Rev. 74 (2017) 638–670. doi:10.1016/j.rser.2017.02.073.

[25] E. B. Fox, A. E. Visser, N. J. Bridges, J. W. Amoroso, Thermophysical properties of nanoparticle-enhanced ionic liquids (NEILs) heat-transfer fluids, J. Mol. Liq. 188 (2013) 196–202. doi:http://dx.doi.org/10.1016/j.molliq.2013.09.031.

[26] W. Wang, Z. Wu, B. Li, B. Sunde, A review on molten-salt-based and ionic-liquid-based nanofluids for medium-to-high temperature heat transfer, Journal of Thermal Analysis and Calorimetry, 0123456789 (2018). doi:10.1007/s10973-018-7765-y.

[27] B. Jo, D. Banerjee, Enhanced specific heat capacity of molten salt-based nanomaterials : Effects of nanoparticle dispersion and solvent material, Acta Mater. 75 (2014) 80–91. doi:10.1016/j.actamat.2014.05.005.

[28] M. Lasfargues, A. Bell, Y. Ding, In situ production of titanium dioxide nanoparticles in molten salt phase for thermal energy storage and heat-transfer fluid applications, J. Nanoparticle Res. 18 (2016) 150. doi:10.1007/s11051-016-3460-8.

[29] M. Lasfargues, Q. Geng, H. Cao, Y. Ding, Mechanical dispersion of nanoparticles and its effect on the specific heat capacity of impure binary

nitrate salt mixtures, nanomaterials. 5 (2015) 1136–1146. doi:10.3390/nano5031136.

[30] M. Chieruzzi, G.F. Cerritelli, A. Miliozzi, J.M. Kenny, L. Torre, Heat capacity of nanofluids for solar energy storage produced by dispersing oxide nanoparticles in nitrate salt mixture directly at high temperature, Sol. Energy Mater. Sol. Cells. 167 (2017) 60–69. doi:10.1016/j.solmat.2017.04.011.

[31] V. Somani, Colloidal stability of magnetic nanoparticles in molten salts Thesis, (2010).

[32] D. Shin, D. Banerjee, Enhancement of specific heat capacity of high-temperature silica-nanofluids synthesized in alkali chloride salt eutectics for solar thermal-energy storage applications, International Journal of Heat and Mass Transfer 54 (2011) 1064–1070. doi:10.1016/j.ijheatmasstransfer.2010.11.017.

[33] R. Mondragón, J.E. Juliá, L. Cabedo, N. Navarrete, On the relationship between the specific heat enhancement of salt- based nanofluids and the ionic exchange capacity of nanoparticles, Scientific Reports 8 (2018) 7532. doi:10.1038/s41598-018-25945-0.

[34] M. Lu, C. Huang, Specific heat capacity of molten salt-based alumina nanofluid, Nanoscale Research Letters, 8 (2013) 292. doi.org/10.1186/1556-276X-8-292.

[35] M. Schuller, Q. Shao, T. Lalk, Experimental investigation of the specific heat of a nitrate-alumina nano fluid for solar thermal energy storage systems, Int. J. Therm. Sci. 91 (2015) 142–145. doi:10.1016/j.ijthermalsci.2015.01.012.

[36] M.R. Betts, The effects of nanoparticle augmentation of nitrate thermal storage materials for use in concentrating solar power applications, Thesis, (2011).

[37] S. Jung, Numerical and experimental investigation of inorganic nanomaterials for thermal energy storage (TES) and concentrated solar power (CSP) applications, Thesis, 2012.

[38] M. Chieruzzi, G.F. Cerritelli, A. Miliozzi, J.M. Kenny, Effect of nanoparticles on heat capacity of nanofluids based on molten salts as PCM for thermal energy storage, Nanoscale Res. Lett. 8 (2013) 1–9. doi:10.1186/1556-276X-8-448.

[39] Y. Hu, Y. He, Z. Zhang, D. Wen, Effect of Al_2O_3 nanoparticle dispersion on the specific heat capacity of a eutectic binary nitrate salt for solar power applications, Energy Convers. Manag. 142 (2017) 366–373. doi:10.1016/j.enconman.2017.03.062.

[40] B. Muñoz-sánchez, J. Nieto-maestre, I. Iparraguirre-torres, Silica and alumina nano-enhanced molten salts for thermal energy storage : A comparison 1850, 080018 (2017). doi:10.1063/1.4984439.

[41] M. Chieruzzi, G.F. Cerritelli, A. Miliozzi, J.M. Kenny, L. Torre, Heat capacity of nanofluids for solar energy storage produced by dispersing oxide nanoparticles in nitrate salt mixture directly at high temperature, Sol. Energy Mater. Sol. Cells. 167 (2017) 60–69. doi:10.1016/j.solmat.2017.04.011.

[42] H. Riazi, S. Mesgari, N.A. Ahmed, R.A. Taylor, The effect of nanoparticle

morphology on the specific heat of nanosalts, Int. J. Heat Mass Transf. 94 (2016) 254–261. doi:10.1016/j.ijheatmasstransfer.2015.11.064.

[43] Z. Jiang, A. Palacios, X. Lei, M.E. Navarro, G. Qiao, E. Mura, Novel key parameter for eutectic nitrates based nanofluids selection for concentrating solar power (CSP) system, Appl. Energy. 235 (2019) 529–542. doi:10.1016/j.apenergy.2018.10.114.

[44] B. Dudda, D. Shin, Effect of nanoparticle dispersion on specific heat capacity of a binary nitrate salt eutectic for concentrated solar power applications, Int. J. Therm. Sci. 69 (2013) 37–42. doi:10.1016/j.ijthermalsci.2013.02.003.

[45] P. Andreu-cabedo, R. Mondragon, L. Hernandez, R. Martinez-cuenca, L. Cabedo, J.E. Julia, Increment of specific heat capacity of solar salt with SiO_2 nanoparticles, 9 (2014) 1–11. doi:10.1186/1556-276X-9-582.

[46] Y. Hu, Y. He, Z. Zhang, D. Wen, Enhanced heat capacity of binary nitrate eutectic salt-silica nano fluid for solar energy storage, Sol. Energy Mater. Sol. Cells. 192 (2019) 94–102. doi:10.1016/j.solmat.2018.12.019.

[47] Q. Xie, Q. Zhu, Thermal storage properties of molten nitrate salt-based nanofluids with graphene nanoplatelets, nanoscale Res. Lett. 11 (2016) 306. doi:10.1186/s11671-016-1519-1.

[48] R. Prasher, P.E. Phelan, Convective-conductive model for the effective thermal conductivity of nanofluids, Journal of Heat Transfer. 128 (2013) 588–595. doi:10.1115/1.2188509.

[49] B. Ma, D. Banerjee, Experimental measurements of thermal conductivity of alumina nanofluid synthesized in salt melt, AIP Adv. 7 (2017). doi:10.1063/1.5007885.

[50] M. Belén Muñoz Sánchez, Nanofluids based on molten nitrates for thermal energy storage and heat transfer in concentrated solar power, Thesis, (2017).

[51] Y. Wu, J. Li, M. Wang, H. Wang, Y. Zhong, Y. Zhao, M. Wei, Y. Li, Solar salt doped by MWCNTs as a promising high thermal conductivity material for CSP, RSC Adv. 8 (2018) 19251–19260. doi:10.1039/c8ra03019g.

[52] X. Wei, Y. Yin, B. Qin, J. Ding, J. Lu, Thermal conductivity improvement of liquid nitrate and carbonate salts doped with MgO particles, Energy Procedia. 142 (2017) 407–412. doi:10.1016/j.egypro.2017.12.064.

[53] A. Awad, H. Navarro, Y. Ding, D. Wen, Thermal-physical properties of nanoparticle-seeded nitrate molten salts, Renew. Energy. 120 (2018) 275–288. doi:10.1016/j.renene.2017.12.026.

[54] B. Muñoz-sánchez, J. Nieto-maestre, E. Veca, S. Sau, H. Navarro, Y. Ding, N. Navarrete, J.E. Juliá, Á.G. Fernández, A. García-romero, S Rheology of Solar-Salt based nano fluids for concentrated solar power . Influence of the salt purity , nanoparticle concentration , temperature and rheometer geometry, Sol. Energy Mater. Sol. Cells. 176 (2018) 357–373. doi:10.1016/j.solmat.2017.10.022.

[55] X. Xiao, G. Zhang, Y. Ding, D. Wen, Rheological characteristics of molten salt seeded with Al_2O_3 nanopowder and graphene for concentrated solar power, Energies. 12 (2019) 467. doi:10.3390/en12030467.

[56] M. Lasfargues, H. Cao, Q. Geng, Y. Ding, Rheological analysis of binary eutectic mixture of sodium and potassium nitrate and the effect of low concentration CuO nanoparticle addition to its viscosity, Materials. 8 (2015) 5194–5204. doi:10.3390/ma8085194.

[57] S. Fotowat, S. Askar, M. Ismail, A. Fartaj, A study on corrosion effects of a water based nanofluid for enhanced thermal energy applications, Sustain. Energy Technol. Assessments. 24 (2017) 39-44. doi:10.1016/j.seta.2017.02.001.

[58] A. Rashidi, A. Amrollahi, R. Lotfi, H. Javaheryzadeh, H. Rahimi, A.R. Rahimi, A. Jorsaraei, An investigation of electrochemical behavior of nanofluids containing MWCNT on the corrosion rate of carbon steel, Mater. Res. Bull. 48 (2013) 4438–4443.
doi:https://doi.org/10.1016/j.materresbull.2013.07.042.

[59] A.M. Rashidi, M. Paknezhad, Erosion–corrosion synergism in an alumina/sea water nanofluid, Microfluid Nanofluid. (2013). doi:10.1007/s10404-013-1282-x.

[60] J.C. Gomez-vidal, Corrosion resistance of MCrAlX coatings in a molten chloride for thermal storage in concentrating solar power applications, Npj Mater. Degrad. 347 (2017) 1–8. doi:10.1038/s41529-017-0012-3.

[61] S. Qiu, L. Solomon, M. Fang, Study of material compatibility for a thermal energy storage system with phase change material, Energies. 11 (2018) 572. doi:10.3390/en11030572.

[62] Y. Song, G. Jiang, Y. Chen, P. Zhao, Y. Tian, Effects of chloride ions on corrosion of ductile iron and carbon steel in soil environments, Sci. Rep. 7 (2017) 1–13. doi:10.1038/s41598-017-07245-1.

[63] M.C. Trent, S.H. Goods, R.W. Bradshaw, Comparison of corrosion performance of grade 316 and grade 347H stainless steels in molten nitrate salt, AIP Conf. Proc. 1734, 160017 (2017). doi:10.1063/1.4949258.

[64] A.S. Dorcheh, R.N. Durham, M.C. Galetz, High temperature corrosion in molten solar salt : The role of chloride impurities, materials and corrosion (2017) 1–9. doi:10.1002/maco.201609300.

[65] S.H. Goods, R.W. Bradshaw, Corrosion of stainless steels and carbon steel by molten mixtures of mommercial nitrate salts, J. Mater. Eng. Perform. 13 (2004) 78–87. doi:10.1361/10599490417542.

[66] M.I. Lasanta, M.T. De Miguel, F.J. Pérez, Evaluation of corrosion resistance of A516 Steel in a molten nitrate salt mixture using a pilot plant facility for application in CSP plants, Sol. Energy Mater. Sol. Cells. 161 (2017) 226–231. doi:10.1016/j.solmat.2016.12.002.

[67] M. Cortes, E. Fuentealba, F.J. P, A.G. Fern, Corrosion properties of a ternary nitrate/nitrite molten salt in concentrated solar technology, Renewable Energy 80 (2015) 177-183. doi:10.1016/j.renene.2015.01.072.

[68] Y. Grosu, O. Bondarchuk, A. Faik, The effect of humidity , impurities and initial state on the corrosion of carbon and stainless steels in molten HitecXL salt for CSP application, Sol. Energy Mater. Sol. Cells. 174 (2018) 34–41. doi:10.1016/j.solmat.2017.08.026.

[69] Y. Yang, A. Kushima, W. Han, H. Xin, J. Li, Liquid-like, self-healing aluminum oxide during deformation at room temperature, Nano Lett. 18 (2018) 2492–2497. doi:10.1021/acs.nanolett.8b00068.

[70] D. Snihirova, S. V. Lamaka, M. Taryba, A.N. Salak, S. Kallip, M.L. Zheludkevich, M.G.S. Ferreira, M.F. Montemor, Hydroxyapatite microparticles as feedback-active reservoirs of corrosion inhibitors, ACS Appl. Mater. Interfaces. 2 (2010) 3011–3022. doi:10.1021/am1005942.

[71] D. Borisova, H. Möhwald, D. G. Shchukin, Mesoporous silica nanoparticles for active corrosion protection, ACS nano. 5, 3 (2011) 1939–1946.

[72] V. Encinas-sánchez, E. Batuecas, A. Macías-garcía, C. Mayo, R. Díaz, F.J. Pérez, Corrosion resistance of protective coatings against molten nitrate salts for thermal energy storage and their environmental impact in CSP technology, Sol. Energy. 176 (2018) 688–697. doi:10.1016/j.solener.2018.10.083.

[73] I. Santana, A. Pepe, E. Jimenez-pique, S. Pellice, I. Milo, S. Ceré, Corrosion protection of carbon steel by silica-based hybrid coatings containing cerium salts : Effect of silica nanoparticle content, Surface & Coatings Technology 265 (2015) 106–116. doi:10.1016/j.surfcoat.2015.01.050.

[74] Y. Grosu, N. Udayashankar, O. Bondarchuk, L. González-Fernández, A. Faik, Unexpected effect of nanoparticles doping on the corrosivity of molten nitrate salt for thermal energy storage, Sol. Energy Mater. Sol. Cells. 178 (2018) 91–97. doi:10.1016/j.solmat.2018.01.002.

[75] Y. Grosu, U. Nithiyanantham, A. Zaki, A. Faik, A simple method for the inhibition of the corrosion of carbon steel by molten nitrate salt for thermal storage in concentrating solar power applications, Npj Mater. Degrad. 4 (2018) 1–8. doi:10.1038/s41529-018-0055-0.

[76] B. Mu, A.G. Fern, A. García-romero, High temperature corrosion behavior on molten nitrate salt-based nano fluids for CSP plants, Renewable Energy 130 (2019) 902–909. doi:10.1016/j.renene.2018.07.018.

[77] M.-Y. Han, D. Wang, Z. Guo, Y. Han, J. Liang, Z. Teng, W. Yang, Z. Lu, Unraveling the growth mechanism of silica particles in the stöber method: in situ seeded growth model, Langmuir. 33 (2017) 5879–5890. doi:10.1021/acs.langmuir.7b01140.

[78] K. Ueno, M. Watanabe, From colloidal stability in ionic liquids to advanced soft materials using unique media, Langmuir. 27 (2011) 9105–9115. doi:10.1021/la103942f.

[79] B. Tang, J. Ge, L. Zhuo, G. Wang, J. Niu, Z. Shi, Y. Dong, A facile and controllable synthesis of γ-Al$_2$O$_3$ nanostructures without a surfactant, Eur. J. Inorg. Chem. 1 (2005) 4366–4369. doi:10.1002/ejic.200500159.

[80] K. Wefers, C. Misra, Oxides and hydroxides of aluminum, Technical paper no 19, 1987.

[81] J. Gangwar, K. Gupta, K. Tripathi, Phase dependent thermal and spectroscopic responses of Al$_2$O$_3$ nanostructures with different, Nanoscale 7 (2015) 13313–13344. doi:10.1039/c5nr02369f.

[82] F. E-Kabbany, Y. Badr, S. Taha, M. Tosson, A study of the phase transition in the system [Ag(1-x) Na)x]NO3 by infrared spectroscopy, Ann. Physik

Leipzig. 46 (1989) 5.

[83]　B. Barbés, R. Páramo, E. Blanco, M.J. Pastoriza-Gallego, M.M. Piñeiro, J.L. Legido, C. Casanova, Thermal conductivity and specific heat capacity measurements of Al_2O_3 nanofluids, J. Therm. Anal. Calorim. 111 (2013) 1615–1625. doi:10.1007/s10973-012-2534-9.

[84]　L. Xue, P. Keblinski, S.R. Phillpot, S.U.S. Choi, J.A. Eastman, Effect of liquid layering at the liquid-solid interface on thermal transport, Int. J. Heat Mass Transf. 47 (2004) 4277–4284. doi:10.1016/j.ijheatmasstransfer.2004.05.016.

[85]　B.-X. Wang, L.-P. Zhou, X.-F. Peng, Surface and size effects on the specific heat capacity of nanoparticles, Int. J. Thermophys. 27 (2006) 139–151. doi:10.1007/s10765-006-0022-9.

[86]　T. Bauer, D. Laing, R. Tamme, Overview of PCMs for concentrated solar power in the temperature range 200 to 350°C, Adv. Sci. Technol. 74 (2010) 272–277. doi:10.4028/www.scientific.net/AST.74.272.

[87]　D.A. Nlssen, Thermophysical properties of the equimolar mixture $NaNO_3$-KNO_3, from 300 to 600°C, J. Chem. Eng. Date. 27 (1982) 269–273. doi:10.1021/je00029e012.

[88]　X. Wang, X. Xu, S.U. S. Choi, Thermal conductivity of nanoparticle - fluid mixture, J. Thermophys. Heat Transf. 13 (1999) 474–480. doi:10.2514/2.6486.

[89]　R. L. Hamilton, O. K. Crosser, Thermal conductivity of heterogeneous two-component systems, Industrial and Engineering Chemistry Fundamentals. 1 (1962) 187–191. doi:10.1021/i160003a005.

[90]　L.G. Leal, On the effective conductivity of a dilute suspension of spherical drops in the limit of low particle peclet number of spherical drops in the limit of low particle peclet, Chemical Engineering Communications, 1 (2007) 37–41. doi.org/10.1080/00986447308960412

[91]　H. Xie, W. Yu, Y. Li, L. Chen, Influencing factors for thermal conductivity enhancement of nanofluids, ASME, 1 (2009) 591–598

[92]　R.W. Berg, D.H. Kerridge, The $NaNO_3/KNO_3$ system: the position of the solidus and sub- solidus, Dalton Trans. 1 (2004) 2224–2229.

[93]　S. Thomas, C. Balakrishna, P. Sobhan, A review of experimental investigations on thermal phenomena in nanofluids, Nanoscale Res. Lett. 6 (2011) 377. doi:10.1186/1556-276X-6-377.

[94]　B. Muñoz-Sánchez, J. Nieto-Maestre, E. Veca, R. Liberatore, S. Sau, H. Navarro, Y. Ding, N. Navarrete, J.E. Juliá, Á.G. Fernández, A. García-Romero, Rheology of Solar-salt based nanofluids for concentrated solar power. Influence of the salt purity, nanoparticle concentration, temperature and rheometer geometry, Sol. Energy Mater. Sol. Cells. 176 (2018) 357–373. doi:10.1016/j.solmat.2017.10.022.

[95]　S. Relloso, Y. Gutiérrez, SENER molten salt tower technology. Ouarzazate NOOR III Case. AIP Conf. Proc. 1850 (2017) 030041-1–030041-6. doi:10.1063/1.4984384.

[96]　Munasir, Z.A. Imam Supardi, Mashadi, Z. Nisa, D.H. Kusumawati, N.P. Putri, A. Taufiq, Sunaryono, N. Hidayat, Darminto, Phase transition of SiO_2

nanoparticles prepared from natural sand: The calcination temperature effect, J. Phys. Conf. Ser. 1093 (2018). doi:10.1088/1742-6596/1093/1/012025.

[97] J. Bautista-Ruiz, W. Aperador, A. Delgado, M. Díaz, − Lagos, Synthesis and characterization of anticorrosive coatings of SiO_2-TiO_2-ZrO_2 Obtained from Sol-Gel suspensions, Int. J. Electrochem. Sci. 9 (2014) 4144–4157. www.electrochemsci.org.

[98] V.H. Le, C. Nhan, H. Thuc, H.H. Thuc, Synthesis of silica nanoparticles from vietnamese rice husk by sol–gel method, Nanoscale Res. Lett. 8 (2013) 58–68. doi:10.1186/1556-276X-8-58.

[99] L. di Zhang, X. Chen, Y. ting Wu, Y. wei Lu, C. fang Ma, Lu-di Zhang , X. Chen, Yu-ting Wu, Yuan-wei Lu, Chong-fang Ma Effect of nanoparticle dispersion on enhancing the specific heat capacity of quaternary nitrate for solar thermal energy storage application, Sol. Energy Mater. Sol. Cells. 157 (2016) 808–813. doi:10.1016/j.solmat.2016.07.046.

[100] D. Shin, D. Banerjee, Enhanced thermal properties of SiO_2 nanocomposite for solar thermal energy storage applications, Int. J. Heat Mass Transf. 84 (2015) 898–902. doi:10.1016/j.ijheatmasstransfer.2015.01.100.

[101] B. Muñoz-Sánchez, J. Nieto-Maestre, I. Iparraguirre-Torres, J.E. Julià, A. García-Romero, Silica and alumina nano-enhanced molten salts for thermal energy storage: A comparison, AIP Conf. Proc. 1850 (2017). doi:10.1063/1.4984439.

[102] P.C. Mishra, S. Mukherjee, S.K. Nayak, A. Panda, A brief review on viscosity of nanofluids, Int. Nano Lett. 4 (2014) 109–120. doi:10.1007/s40089-014-0126-3.

[103] T. Aguilar, J. Navas, A. Sánchez-Coronilla, E.I. Martín, J.J. Gallardo, P. Martínez-Merino, R. Gómez-Villarejo, J.C. Piñero, R. Alcántara, C. Fernández-Lorenzo, Investigation of enhanced thermal properties in NiO-based nanofluids for concentrating solar power applications: A molecular dynamics and experimental analysis, Appl. Energy. 211 (2018) 677–688. doi:10.1016/j.apenergy.2017.11.069.

[104] J. Chevalier, O. Tillement, F. Ayela, Rheological properties of nanofluids flowing through microchannels, Appl. Phys. Lett. 91 (2007) 1–4. doi:10.1063/1.2821117.

[105] O. Arthur, M.A. Karim, An investigation into the thermophysical and rheological properties of nanofluids for solar thermal applications, Renew. Sustain. Energy Rev. 55 (2016) 739–755. doi:10.1016/j.rser.2015.10.065.

[106] R. Prasher, P.E. Phelan, P. Bhattacharya, Effect of aggregation kinetics on the thermal conductivity of nanoscale colloidal solutions (nanofluid), Nano Lett. 6 (2006) 1529–1534. doi:10.1021/nl060992s.

[107] S. Bhattacharjee, Review article DLS and zeta potential − What they are and what they are not ?, J. Control. Release. 235 (2016) 337–351. doi:10.1016/j.jconrel.2016.06.017.

[108] H. Jin, Z. Ji, Y. Li, M. Liu, J. Yuan, C. Xu, S. Hou, The preparation of a core/shell structure with alumina coated spherical silica powder, Colloids Surfaces A Physicochem. Eng. Asp. 441 (2014) 170–177.

doi:10.1016/j.colsurfa.2013.09.004.

[109] S.F. Wang, Y.F. Hsu, T.C.K. Yang, C.M. Chang, Y. Chen, C.Y. Huang, F.S. Yen, Silica coating on ultrafine α-alumina particles, Mater. Sci. Eng. A. 395 (2005) 148–152. doi:10.1016/j.msea.2004.12.007.

[110] A.H. Heuer, T. Nakagawa, M.Z. Azar, D.B. Hovis, J.L. Smialek, B. Gleeson, On the growth of Al_2O_3 scales, Acta Materialia 61 (2013) 6670-6683. doi:10.1016/j.actamat.2013.07.024

[111] A. Adamczyk, The structural studies of aluminosilicate gels and thin films synthesized by the sol-gel method using different Al_2O_3 and SiO_2 precursors, Mater. Sci. 33 (2015) 732–741. doi:10.1515/msp-2015-0109.

[112] D. Shin, D. Banerjee, Enhancement of specific heat capacity of high-temperature silica-nanofluids synthesized in alkali chloride salt eutectics for solar thermal-energy storage applications, Int. J. Heat Mass Transf. 54 (2011) 1064–1070. doi:10.1016/j.ijheatmasstransfer.2010.11.017.

[113] B. Muñoz-Sánchez, J. Nieto-Maestre, I. Iparraguirre-Torres, A. García-Romero, J.M. Sala-Lizarraga, Molten salt-based nanofluids as efficient heat transfer and storage materials at high temperatures. An overview of the literature, Renew. Sustain. Energy Rev. 82 (2018) 3924–3945. doi:10.1016/j.rser.2017.10.080.

[114] H. Riazi, S. Mesgari, N.A. Ahmed, R.A. Taylor, The effect of nanoparticle morphology on the specific heat of nanosalts, Int. J. Heat Mass Transf. 94 (2016) 254–261. doi:10.1016/j.ijheatmasstransfer.2015.11.064.

[115] K.Y. Leong, K.Z. Ku Ahmad, H.C. Ong, M.J. Ghazali, A. Baharum, Synthesis and thermal conductivity characteristic of hybrid nanofluids – A review, Renew. Sustain. Energy Rev. 75 (2017) 868–878. doi:10.1016/j.rser.2016.11.068.

[116] E. V. Timofeeva, J.L. Routbort, D. Singh, Particle shape effects on thermophysical properties of alumina nanofluids, J. Appl. Phys. 106 (2009). doi:10.1063/1.3155999.

[117] A.G. Fernández, M. Cortes, E. Fuentealba, F.J. Pérez, Corrosion properties of a ternary nitrate/nitrite molten salt in concentrated solar technology, Renew. Energy. 80 (2015) 177–183. doi:10.1016/j.renene.2015.01.072.

[118] J.C. Gomez-vidal, Corrosion resistance of MCrAlX coatings in a molten chloride for thermal storage in concentrating solar power applications, Npj Mater. Degrad. 347 (2017) 1–8. doi:10.1038/s41529-017-0012-3.

[119] M.P. Brady, J. Magee, Y. Yamamoto, D. Helmick, L. Wang, Co-optimization of wrought alumina-forming austenitic stainless steel composition ranges for high-temperature creep and oxidation/corrosion resistance , Mater. Sci. Eng. A. 590 (2014) 101–115. doi:10.1016/j.msea.2013.10.014.

[120] Y. Yamamoto, M. P. Brady, Z. P. Lu, P. J. Maziasz, C. T. Liu, B. A. Pint, K. L. More, H. M. Meyer, E. A. Payzant, Creep-resistant, Al_2O_3-forming austenitic stainless steels, SCIENCE 316 (2007) 433. doi:10.1126/science.1137711.

[121] Y. Yamamoto, M. P. Brady, G. Muralidharan, B.A. Pint, P.J. Maziasz, D. Shin, B. Shassere, S.S. Babuand, C.-H. Kuo, Development of creep-resistant,

alumina-forming ferrous alloys for high-temperature structural use, ASME 2018. doi:10.1115/ETAM2018-6727

[122] Y. Grosu, N. Udayashankar, O. Bondarchuk, L. González-fernández, A. Faik, Unexpected effect of nanoparticles doping on the corrosivity of molten nitrate salt for thermal energy storage, Sol. Energy Mater. Sol. Cells. 178 (2018) 91–97. doi:10.1016/j.solmat.2018.01.002.

[123] U. Zulfiqar, T. Subhani, S. Wilayat Husain, Synthesis of silica nanoparticles from sodium silicate under alkaline conditions, J. Sol-Gel Sci. Technol. 77 (2016) 753–758. doi:10.1007/s10971-015-3950-7.

[124] F.J. Ruiz-cabañas, C. Prieto, R. Osuna, V. Madina, A.I. Fernández, L.F. Cabeza, Corrosion testing device for in-situ corrosion characterization in operational molten salts storage tanks : A516 Gr70 carbon steel performance under molten salts exposure, Sol. Energy Mater. Sol. Cells. 157 (2016) 383–392. doi:10.1016/j.solmat.2016.06.005.

[125] A.G. Fernández, H. Galleguillos, E. Fuentealba, F.J. Pérez, Corrosion of stainless steels and low-Cr steel in molten $Ca(NO_3)_2$–$NaNO_3$–KNO_3 eutectic salt for direct energy storage in CSP plants, Sol. Energy Mater. Sol. Cells. 141 (2015) 7–13. doi:10.1016/j.solmat.2015.05.004.

[126] A. Padmanaban iyer, The effect of silica nanoparticles on corrosion of steel, Thesis, (2011).

[127] Z.H. Karadeniz, N. Garmendia, L. Hernández, The contact angle of nanofluids as thermophysical property, Journal of Colloid and Interface Science 547 (2019) 393-406.. doi:10.1016/j.jcis.2019.04.007.

Annex. Contributions to other papers in the field of this thesis that were not included in the previous sections.

Spray-graphitization as a protection method against corrosion by molten nitrate salts and molten salts based nanofluids for thermal energy storage applications

Julien Piquot, Udayashankar Nithiyanantham, Yaroslav Grosu[*], Abdessamad Faik[**]

CIC Energigune, Albert Einstein 48, Miñano, Álava, 01510, Spain

ARTICLE INFO

ABSTRACT

Nanoscale science rapidly enters nearly every field of technology providing perspectives of new advanced applications. In the area of thermal energy storage (TES) doping molten salts with small amounts of nanoparticles represents tremendous interest due to the perspective of pronounced enhancement of their thermophysical properties. This is particularly important for the concentrated solar power (CSP) technology where a considerable decrease of investment costs is required. However, the information about materials degradation in direct contact with molten salts based nanofluids is practically absent. In this work, the compatibility of carbon steel A516.Gr70 with $NaNO_3$-KNO_3-$Ca(NO_3)_2$ (15-43-42 wt%) molten salt known as HitecXL doped with SiO_2 nanoparticles was evaluated under thermal cycling conditions. We demonstrate that the presence of nanoparticles in the salt considerably increases the corrosion rates even for carbon steel protected by spray-graphitization method – the anti-corrosion method capable of reducing the corrosion rates for nanoparticles-free HitecXL under similar conditions.

1. Introduction

Concentrated solar power (CSP) is a renewable technology where electricity is produced from thermal energy obtained by means of solar irradiation concentration. Increasing interest in CSP technology [1–4] is explained by a relatively simple method of energy storage (thermal energy storage) that improves its dispatchability, which is considered as the bottle neck of every renewable technology.

However, apart from improved dispatchability the use of thermal energy storage (TES) at CSP increases the investment costs due to the construction of a large double- or single-tank system, as well as the need of a large amount of storage material (typically, thousands of tons). In these regards, storage material with enhanced energy capacity (heat capacity) is highly desirable. Today molten salts (nitrate salts in particular) are industrially preferred mature storage material for TES at CSP [1–4]. Many works are dedicated to the enhancement of thermophysical properties of molten salts by using small amounts of nanoparticles as dopants (normally, no more than 1 wt%) [5–10]. The enhancement of heat capacity was reported for nitrate salts (Solar salt and HitecXL) to reach 20–30% [5–9]. Also, first steps for the scale up of nanosalts production have been reported [10].

The aforementioned enhancement of heat capacity is certainly an attractive improvement for a storage material. However, the expected economic benefit can be completely suppressed by the enhanced corrosion. In these regards, understanding the effect of nanoparticles doping on the compatibility of molten salts is highly important. However, information on that topic is extremely limited. In our previous work, we demonstrated that the presence of nanoparticles in molten HitecXL nitrate salt noticeably enhances the corrosion of carbon steel and modifies its mechanism under isothermal (310 °C) conditions [11]. Whereas in Refs. [12,13], the authors claimed a decrease of corrosivity of binary carbonate salt doped with 1 wt% silica nanoparticles at 520 °C. Such contradicting results suggest that the effect of nanoparticles on the corrosion mechanism of molten salts is complex and it depends on the base salt and conditions of corrosion tests. To reveal the corrosion mechanism of molten salt based nanofluids a deeper understanding is required.

Despite the absence of sufficient studies on the effect of nanoparticles on the corrosivity of molten salts, the corrosion issues at CSP are well recognized and are under active investigation. Particularly, Fernandez et al. [14] explored the compatibility between HitecXL salt and stainless steels AISI 304 and 430, a low-Cr alloy steel (T22) and a

---

carbon steel (A1) at 390 °C. In this work it was shown that HitecXL salt is compatible with such materials and the presence of Cr in the steel composition decreases the corrosion rates, which were lower compared to Solar salt. In Ref. [15], Ruiz-Cabañas et al. investigated the corrosion behaviour of carbon steel A516.Gr70 in direct contact with Solar salt. The authors reported the incorporation of magnesium into the corrosion layer, which is in agreement with [14,16]. We recently studied the effect of humidity, impurities and initial state of material on the compatibility between HitecXL salt and carbon steel A516.Gr70, stainless steels AISI 304 and 316 at 310 °C [16]. We observed that the presence of humidity in the system severely increases the corrosion rate for carbon steel A516.Gr70 making it unacceptable choice under such conditions, while stainless steels AISI 304 and 316 at 310 °C demonstrated acceptable corrosion rates [16]. A long corrosion tests of 7000 h were performed in Solar Salt at 570 °C for stainless steels (SS-304 and SS-316) and at 316 °C for carbon steel (A36) [17]. The authors concluded that impurities such as NaCl, KClO₄ and Na₂SO₄ typically present in some commercial grades of alkalinitrates have relatively small effects on corrosion for the studied materials. Sandia National Laboratories reported the corrosion study for two iron-based alloys (SS-321 and SS-347) and two nickel-based alloys (In625 and HA230) in contact with Solar salt at temperatures of 400, 500 and 680 °C [18]. For all four materials, the corrosion rates were found to be very small at temperatures lower than 600 °C. However, at 680 °C a tremendous increase in corrosion rates was observed. It should be noted that decomposition temperature of Solar salt is around 600 °C, so such observation is rather important in case of abnormal overheating at the power plant. The negative role of chlorides on the compatibility of Solar salt was recently demonstrated [19].

Reaching higher efficiency for heat-to-electricity transformation cycle is possible by increasing the maximum operational temperature at CSP. In these regards, more corrosive salts able to operate at higher temperatures were explored in terms of corrosion [20,21]. In Refs. [20,21] authors explored the corrosion behaviour of Hastelloys C-276 and C-22 and stainless steel 304 with molten chloride salts at temperatures up to 800 °C. They found that corrosion rates decrease considerably if oxygen is absent in the atmosphere with better corrosion resistance of Hastelloys compared to stainless steel 304.

Application of anticorrosion coatings is known to be a proper solution to use cheaper materials. However, the stability of such coatings at high temperatures is a challenge. For example, slurry aluminizing was proposed for corrosion protection against molten nitrate salt at high temperature [22]. Particularly, ferritic–martensitic P91 (Cr9–Mo1) and stainless steel 304 were tested to demonstrate the improved compatibility. Inconel 738-LC was covered with a NiCrAlY bondcoat and with a nanostructured scandia (3.6 mol%) and (0.4 mol%) yttria co-stabilized zirconia (4SYSZ) topcoat by air plasma spraying (APS) [23]. Then, the material was tested for corrosion with 45 wt% Na₂SO₄ + 55 wt% V₂O₅ molten salt at 910 °C. The failure of such coating was reported due to the formation of mixed oxide [23]. TP347H coated with Hastelloy C22 (Ni–Cr–Mo) by means of laser cladding was tested for compatibility with chloride salts (KCl and NaCl) at temperatures up to 750 °C [24]. Such coating considerably improved the corrosion resistivity [24].

Both dynamic and static corrosion tests were performed for A516 carbon steel in contact with Solar salt at 500 °C. The oxide layer of ~23.3 μm for the static corrosion test and ~31 μm for the dynamic corrosion test after 100 h were reported by Lasanta et al. [25]. Corrosivity of molten LiNO₃–NaNO₃–KNO₃ salt was tested with SB450, T22, T5, T9 and X20 steels revealing (Fe, Cr)₃O₄ layer formation and positive effect of Cr in construction material composition [26]. Molten carbonate salt Li₂CO₃–Na₂CO₃–K₂CO₃ was studied with HR3C steel (25%Cr–20%Ni–53%Fe) in terms of corrosion [27]. A recent review on the corrosion monitoring and mitigation techniques on TES materials for CSP plants can be found in Ref. [28].

In the present work, for the first time we explore the effect of

nanoparticles on the corrosivity of molten HitecXL salt under thermal cycling. Additionally, the effect of such cycling on the spray-graphitization coating, previously proven to be effective against HitecXL corrosion [29], is explored for both nanoparticles-doped and nanoparticles-free HitecXL salts.

2. Materials and techniques

2.1. Materials

HitecXL salt was prepared by mixing 15%NaNO₃, 43%KNO₃ and 42%Ca(NO₃)₂ (weight concentrations). Commercial nitrates were used (KNO₃ and NaNO₃ from SQM and NitCal from YARA (NitCAl is a commercial mixture of calcium nitrate and potassium nitrate) [30]) with the detailed chemical composition presented elsewhere [11,16,29]. Nanoparticles-doped HitecXL salt was prepared using a dry method consisted of the following steps: a quantity of 2g of the mixture of HitecXL salt (99 wt%) and the nanoparticles (1 wt%) were introduced into a 50 ml aluminium bottle and subjected to a dynamic shaking by means of Spex Sample Prep 8000 Series Mixer\Mill during 15 min. The proper distribution of the nanoparticles was verified by SEM-EDX technique. The commercial SiO₂ nanoparticles delivered by Sigma-Aldrich with particle size of 12 nm were used to prepare the nanofluids. The salts with nanoparticles are referred as HitecXL + SiO₂ in the text.

The corrosion tests were carried out for the commonly used constructive material – carbon steel A516.Gr70 with the composition of 0.97%Mn, 0.36%Si, 0.31%C, 0.04%P and Fe for balance (weight concentrations).

2.2. Cycling corrosion tests protocol

For the corrosion experiments, the salts (around 10 g) were placed inside alumina crucibles and carbon steel pieces of 3 mm × 10 mm x 20 mm were immersed completely into the salt. The possibility of at least partial settling down or floating of nanoparticles was considered. For that reason, the coupons of carbon steel were positioned vertically in the crucible with molten salt during the corrosion test and the areas of 10 × 3 mm close to the top and bottom edges were excluded from the SEM-EDX analysis. Then, the crucibles were placed inside the furnace and kept under a cycling temperature from 300 to 500 °C with a heating/cooling ramp of 2 °C/min. Experiments with different duration of 24 h, 100 h and 500 h were performed. The salts were kept under air atmosphere during the corrosion test. At the end of the experiments, the coupons of carbon steel were washed in hot water.

2.3. Initial state of the materials

Two types of initial state were used in this work: pristine carbon steel and carbon steel coated with a thin layer of graphite following the procedure described elsewhere [29]. In brief, pristine carbon steel was successively washed in acetone, ethanol and water using an ultrasonic bath prior to the corrosion tests.

Graphitized carbon steel was prepared by spraying graphite over the clean surfaces of carbon steel pieces prior to the corrosion tests using Graphite 33 Spray from Kontakt Chimie. Comparison of the weights of the sample before and after the spraying revealed very small mass of deposited graphite. A quantity of approximately 3 mg was deposited, which is 0.05 wt% of the salt in the experiment and represents 5·10⁻³ mg/cm² of graphite per area of carbon steel. The samples coated with graphite are referred as "graphitized" in the text below.

2.4. Characterization techniques

2.4.1. Scanning electron microscopy - SEM

The surfaces of the samples of carbon steel were carefully washed

2

with hot water to remove salt stuck after the corrosion tests.

To examine the corrosion layer thickness and composition, the cross-sections of the samples were examined. A simplified scheme of such samples preparation for SEM analysis is described in detail elsewhere [11,16,29]. First, the mixture of KEM 90 Harz resin and KEM 90 Harter catalyst in 2:1 proportion was prepared. Next, the samples were completely immersed in the resin and left for 12 h. After solidification, the resin creates a proper holder for SEM imaging. Such holder helps to preserve all the corrosion products on the surface of the carbon steel, particularly, during the cross-section preparation. Then, the resin holder with the sample was cut in half and the cross-section was polished successively with SiC grinding discs of 240, 800, 1200 and 2500 roughness.

The prepared samples of carbon steel were imaged by means of a Quanta 200 FEG scanning electron microscope (SEM) operated in high vacuum mode at 30 kV and with a back scattered electron detector (BSED). In addition, energy-dispersive X-ray spectroscopy (EDX) analysis was carried out to obtain chemical composition. The thickness of corrosion layer was obtained from a statistical examination of the cross-sections of the carbon steel samples. The average and maximum values are presented. More than 200 values were used for averaging.

2.4.2. X-ray diffraction – XRD

A structural analysis of the materials before and after the corrosion tests was performed by XRD using a Bruker D8 Advance X-ray diffractometer equipped with a LYNXEYE detector using CuKα_1 radiation (λ = 1.5418 Å) and θ-2θ geometry. The data was collected at room temperature between 10° and 100° in 2θ with a step size of 0.02° and counting time of 8 s per step. The EVA software was used to identify the crystallographic phases present.

3. Results and discussion

3.1. Effect of nanoparticles

The summary of SEM micrographs of the carbon steel cross-sections after different corrosion tests is shown in Fig. 1. The corrosion layer is clearly seen on the surface of the material. As expected, such corrosion layer evolves with time for all the corrosion tests. Such observation is in agreement with the XRD analysis where it can be clearly seen that the peaks corresponding to the iron oxides (magnetite and hematite) increases with time on the normalized patterns (Fig. 2). The corrosion rate between 100 and 500 h time is 0.013 mm/year, which is about 20% higher compared to isothermal tests performed for similar system at 310 °C [16]. Such increase is most probably due to the higher temperature of the corrosion test and the cycling conditions.

A noticeable increase of thickness of the corrosion layer is observed in case silica nanoparticles were added to the salt (Fig. 1). Such observation is confirmed by the XRD analysis where the presence of iron oxides is more noticeable (Fig. 3). In our previous work it was shown that upon isothermal immersion tests the presence of nanoparticles affects the corrosivity of HitecXL salt due to two main mechanisms [11]: 1) the entrapped bubbles of air in the interparticle porosity increase the local concentration of oxygen and stimulates the oxidation of carbon steel; and 2) the reaction and incorporation of nanoparticles into the corrosion layer. It seems that similar mechanisms take place under thermal cycling. Particularly, EDX analysis of the cross section of the carbon steel after 500h corrosion test with HitecXL + SiO$_2$ nanoparticles reveals the presence of silicon in the corrosion layer (Fig. 4). In addition, the incorporation of calcium can be clearly seen, which is in agreement with our previous work [16].

The evolution of corrosion layer with time (number of cycles) clearly reveals the drastic effect of nanoparticles (Fig. 5). Not only the thickness is about two times higher when nanoparticles are added, but the variation of the corrosion rate has changed. In case of nanoparticles-free HitecXL the corrosion layer thickness demonstrates logarithmic
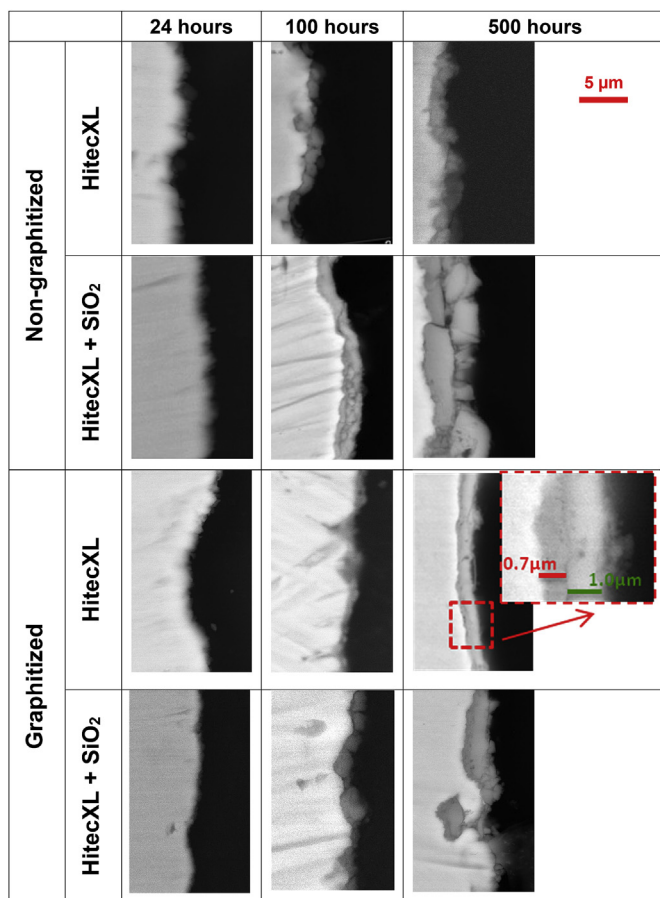
Fig. 1. SEM images of cross-sections of graphitized and non-graphitized carbon steels after corrosion tests with HitecXL and HitecXL + SiO$_2$ salts.
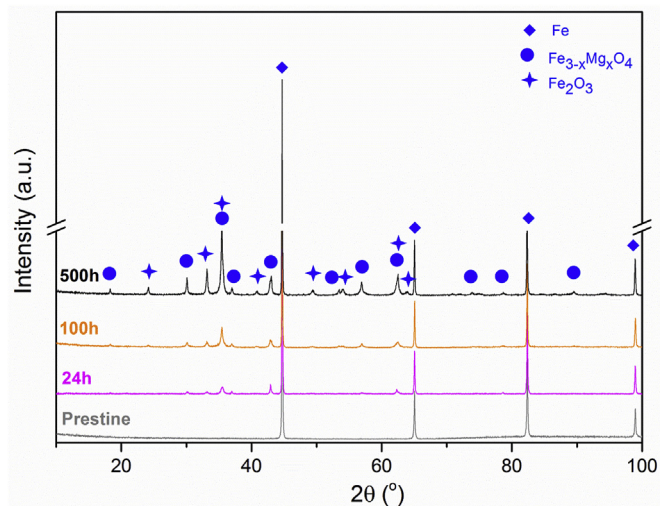
Fig. 2. XRD patterns of carbon steel after corrosion tests with HitecXL salt.

dependence on time and after 100 h the rate is strongly decreased. While in the case of nanoparticles-doped salt the dependence is parabolic and after 100 h the rate is 0.041 mm/year, which is more than 3 times higher compared to pure HitecXL.

Such change of corrosion rate was not observed for the isothermal corrosion tests [11], where adding nanoparticles increased the corrosion thickness, but the time dependence remained logarithmic. It appears, that thermal cycling is responsible for such differences. Under isothermal conditions after certain time the oxide layer is formed on the
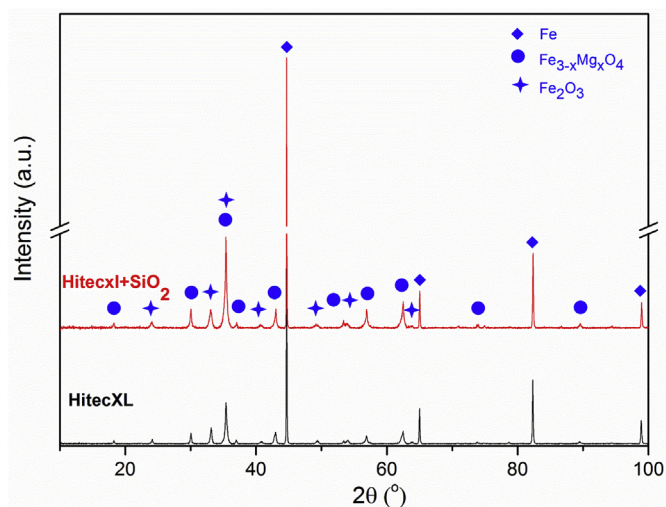
Fig. 3. XRD patterns of carbon steel after 500h corrosion tests with HitecXL and HitecXL + SiO₂ salts.

Fig. 5. Evolution of corrosion layer thickness of graphitized and non-graphitized carbon steels after corrosion tests with HitecXL and HitecXL + SiO₂ salts.

Fig. 6. Average and maximum values of corrosion layer of graphitized and non-graphitized carbon steels after corrosion tests with HitecXL and HitecXL + SiO₂ salts after 500 h corrosion tests.

surface of carbon steel, which decreases the further rate of oxidation due to limited diffusion of oxygen for both cases of nanoparticles-free and nanoparticles-doped salts. While under cycling conditions such effect takes place only for nanoparticles-free HitecXL. In case nanoparticles are added, the oxidation layer is less stable and breaks (detaches) from the surface of carbon steel (Fig. 1) due to thermal expansion, providing favorable conditions for further oxidation. Such observations suggest a strong interaction of carbons steel with nanoparticles during the corrosion test. It should be noted that in real CSP application such effect can be even more pronounced as the operation takes place under flow conditions.

It should be also noted that in the case of nanoparticles-doped HitecXL the corrosion layer is more irregular and additionally localized corrosion is observed. It can be seen that the maximum values of the corrosion layer increased nearly twice compared to nanoparticles-free HitecXL (Fig. 6).

3.2. Effect of nanoparticles doping on the spray-graphitization anti-corrosion coating

In our previous work, we demonstrated that graphite coating can serve as effective anti-corrosion protection for carbon steel against molten HitecXL salt due to the protective calcium carbonate layer formation [29]. In the present work, this method was tested under thermal cycling conditions and for nanoparticles-doped HitecXL salt.

In Fig. 1 pronounced differences can be seen when the graphite coating is used to protect the carbon steel. After 500 h test the formation of the uniform layer on the surface of carbon steel can be clearly seen. In our previous study we demonstrated in detail that such layer is formed by calcium carbonate CaCO₃ and acts as a protective layer [29]. Formation of such CaCO₃ layer is competitive with the oxidation
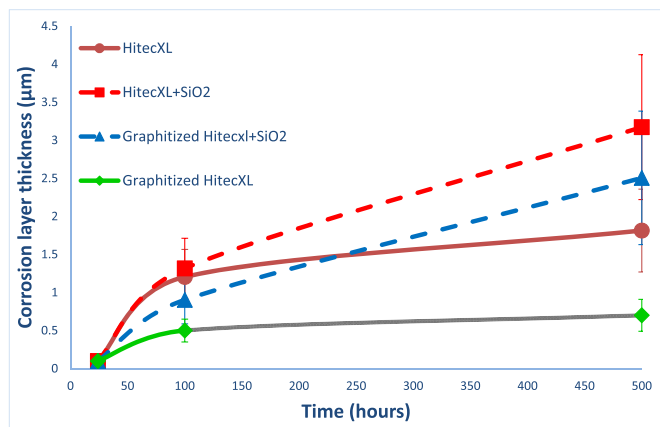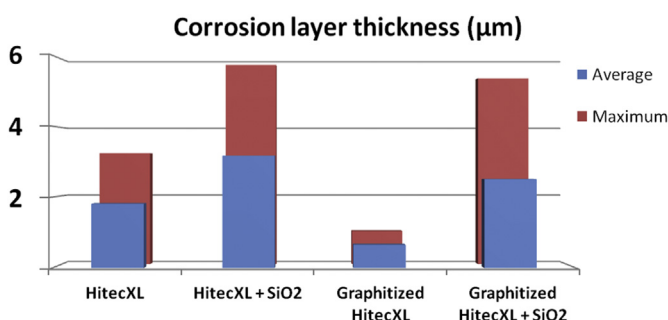
process, for that reason CaCO3 can form above oxidation layer, which is demonstrated in a zoom of Fig. 1. XRD analysis confirms such statement where the well crystallized CaCO₃ phase was clearly identified in the patterns (Fig. 7).

The graphitization considerably decreases the corrosion rate. At 500 h the average value of corrosion layer thickness is two times lower compared to non-graphitized carbon steel, while maximum value is more than 3 times lower (the formed layer is very uniform with the similar thickness all over the surface) – Fig. 6. Moreover, the corrosion layer evolution with time is logarithmic with the rate of 0.004 mm/year between 100 and 500 h, which is more than 3 times lower compared to non-coated carbon steel.

The situation is drastically different when nanoparticles are added into the salt. The formed protective layer is strongly non-homogeneous (Fig. 1) and CaCO₃ is hardly detectable by the XRD (Fig. 7). Additionally, CaCO₃ phase was detected on the surface of graphitized carbon steel after the corrosion tests with HitecXL (Fig. 7) and CaCO₃ crystals were rarely found in the salt (Fig. 8a). On the contrary, CaCO₃
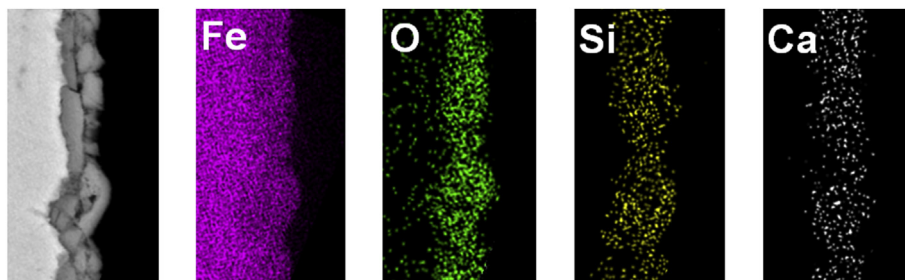
Fig. 4. SEM-EDX mapping of the cross-section of carbon steel after 500h corrosion test with HitecXL + SiO₂.
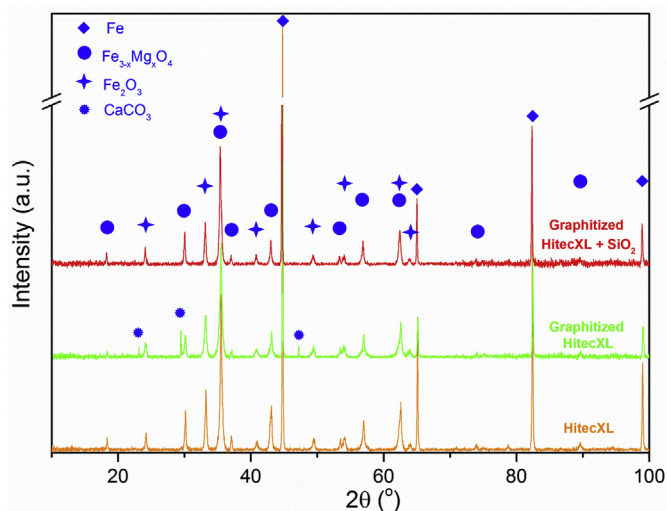
Fig. 7. XRD patterns of graphitized and non-graphitized carbon steel after 500h corrosion tests with HitecXL and HitecXL + SiO$_2$ salts.

Fig. 9. SEM image and EDX mapping of as-prepared HitecXL + SiO$_2$.

phase was not detected on the surface of graphitized carbon steel after the corrosion tests with HitecXL + SiO$_2$ (Fig. 7) and large number of CaCO$_3$ crystals was detected in the salt after the corrosion tests (Fig. 8b). These observations clearly indicate that nanoparticles prevent the CaCO$_3$ crystal growth on the surface of graphitized carbon steel. This can be due to chemical reaction of nanoparticles with the carbon steel, which was discussed in our previous work [11].

After 500h corrosion tests with HitecXL + SiO$_2$ the average corrosion layer thickness of graphitized carbon steel is slightly lower (~15%) compared to non-graphitized carbon steel (Fig. 6). However, the maximum values are similar within the statistical error (Fig. 6). The time dependence of the corrosion layer of graphitized carbon steel tested with HitecXL + SiO$_2$ is parabolic (Fig. 5) and corrosion rate is 0.035 mm/year. This corrosion rate is more than 2.5 times higher compared to non-graphitized carbons steel tested with HitecXL salt and almost 9 times higher compared to graphitized carbon steel tested with HitecXL salt. Such observations suggest that graphitization demonstrates excellent performance in the case of nanoparticles-free HitecXL under cycling conditions, while it is not effective against a corrosion attack of nanoparticles-doped HitecXL. This could be due to competitive reaction with silica nanoparticles, which inhibits the formation of proper protective layer of CaCO$_3$. Additionally, incorporation of nanoparticles into the corrosion layer may have negative effect on the stability of the protective layer and its detachment upon thermal cycling. The obtained results demonstrate strong effect of nanoparticles doping on the corrosivity of molten nitrate salt.

It is generally recognized that stability and homogeneous distribution of nanoparticles are essential for nanofluids properties and their corrosion aspects. In these regards, the distribution of the nanoparticles was examined for as-prepared and tested HitecXL + SiO$_2$ salts. Statistical examination of the as-prepared salt by the EDX technique revealed the concentration for Si of (1.1 ± 0.3) wt%, where 0.3 wt% is the maximum deviation from the average value of 1.1 wt%. This value was obtained by salt examination in 50 different areas 200 × 100 μm
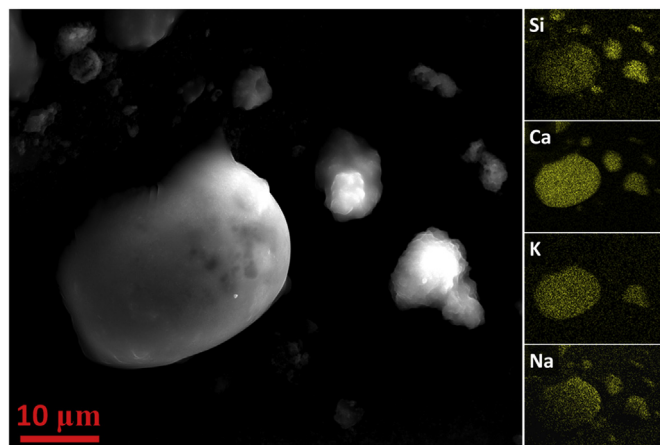
each. Following the same method, the average concentration of Si for the salt after 500 h corrosion test was found to be lower (0.7 ± 0.2) wt %, but the obtained value is within the maximum deviation. Such decrease may be due to the incorporation of some nanoparticles into the corrosion layer of the carbon steel (Fig. 4), as well as due to the partial settling down/floating of the nanoparticles during the 500 h corrosion tests. Fig. 9 demonstrates the typical SEM-EDX images for the salts.

After the corrosion tests nanoparticles formed agglomerates of around 1 μm, which were not detected for the as-prepared salt (Fig. 10). The obtained results suggest that even though during the corrosion test the local concentration of nanoparticles may be different from initial 1 wt%, the surface of carbon steel is constantly exposed to SiO$_2$ nanoparticles permitting chemical and physical interaction. On the other hand, the agglomeration of nanoparticles (Fig. 10) can have negative effect on the homogeneity of the protective layer.

4. Conclusions

In this work, the effect of nanoparticles-doping on the corrosivity of molten HitecXL nitrate salt was studied along with its effect on the efficiency of spray-graphitization anti-corrosion protection method. Thermal cycling conditions in the 300–500 °C temperature range were applied for corrosion tests. The following can be concluded:

- Presence of nanoparticles has strong effect on the carbon steel under cycling conditions, increasing the corrosion rate more than three times.
- Spray-graphitization of carbon steel provides effective anti-corrosion protection against nanoparticles-free HitecXL corrosion attack, decreasing the corrosion rate more than 3 times compared to non-coated carbon steel.
- Nanoparticles doping has strong effect on the spray-graphitization method, decreasing its efficiency.

Obtained results suggest that additional costs related to corrosion must be taken into account when evaluating the feasibility of molten salts doped with nanoparticles.
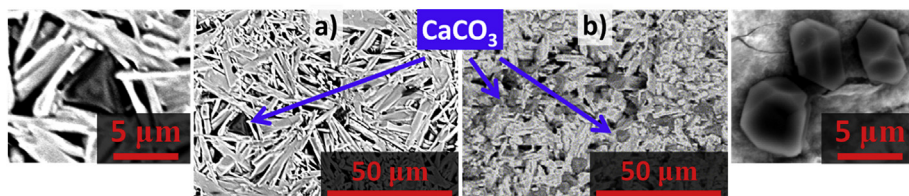
Fig. 8. SEM images of a) HitecXL and b) HitecXL + SiO$_2$ after 500 h corrosion test with graphitized carbon steel.
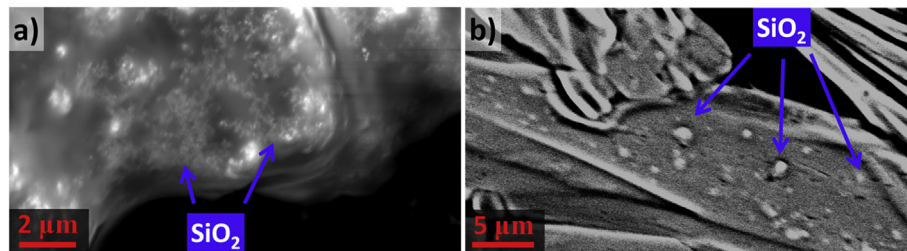
Fig. 10. SEM images a) of as-prepared HitecXL + SiO$_2$ and b) HitecXL + SiO$_2$ after 500 h corrosion test.

Appendix A. Supplementary data

Supplementary data to this article can be found online at https://doi.org/10.1016/j.solmat.2019.110024.

References

[1] H. Zhang, J. Baeyens, G. Cáceres, J. Degrève, Y. Lv, Thermal energy storage: recent developments and practical aspects, Prog. Energy Combust. Sci. 53 (2016) 1–40.

[2] M. Liu, N.S. Tay, S. Bell, M. Belusko, R. Jacob, G. Will, W. Saman, F. Bruno, Review on concentrating solar power plants and new developments in high temperature thermal energy storage technologies, Renew. Sustain. Energy Rev. 53 (2016) 1411–1432.

[3] T.M.I. Mahlia, T.J. Saktisahdan, A. Jannifar, M.H. Hasan, H.S.C. Matseelar, A review of available methods and development on energy storage; technology update, Renew. Sustain. Energy Rev. 33 (2014) 532–545.

[4] S. Kuravi, J. Trahan, D.Y. Goswami, M.M. Rahman, E.K. Stefanakos, Thermal energy storage technologies and systems for concentrating solar power plants, Prog. Energ. Combust. 39 (2013) 285–319.

[5] I.M. Shahrul, I.M. Mahbubul, S.S. Khaleduzzaman, R. Saidur, M.F. Sabri, A comparative review on the specific heat of nanofluids for energy perspective, Renew. Sustain. Energy Rev. 38 (2014) 88–98.

[6] O. Arthur, M.A. Karim, An investigation into the thermophysical and rheological eproperties of nanofluids for solar thermal applications, Renew. Sustain. Energy Rev. 55 (2016) 739–755.

[7] H. Riazi, S. Mesgari, N.A. Ahmed, R.A. Taylor, The effect of nanoparticle morphology on the specific heat of nanosalts, Int. J. Heat Mass Transf. 94 (2016) 254–261.

[8] S.F. Ahmed, M. Khalid, W. Rashmi, A. Chan, K. Shahbaz, Recent progress in solar thermal energy storage using nanomaterials, Renew. Sustain. Energy Rev. 67 (2017) 450–460.

[9] H. Riazi, T. Murphy, G.B. Webber, R. Atkin, S.S.M. Tehrani, R.A. Taylor, Specific heat control of nanofluids: a critical review, Int. J. Therm. Sci. 107 (2016) 25–38.

[10] M. Chieruzzi, G.F. Cerritelli, A. Miliozzi, J.M. Kenny, L. Torre, Heat capacity of nanofluids for solar energy storage produced by dispersing oxide nanoparticles in nitrate salt mixture directly at high temperature, Sol. Energy Mater. Sol. Cells 167 (2017) 60–69.

[11] Y. Grosu, N. Udayashankar, O. Bondarchuk, L. González-Fernández, A. Faik, Unexpected effect of nanoparticles doping on the corrosivity of molten nitrate salt for thermal energy storage, Sol. Energy Mater. Sol. Cells 178 (2018) 91–97.

[12] M. Schuller, F. Little, D. Malik, M. Betts, Q. Shao, J. Luo, W. Zhong, S. Shankar, Molten Salt-Carbon Nanotube Thermal Energy Storage for Concentrating Solar Power Systems, (2012), https://doi.org/10.1007/s13398-014-0173-7.2.

[13] A. Padmanaban, The Effect of Silica Nanoparticles on Corrosion of Steel by Molten Carbonate Eutectics, Master thesis (2011).

[14] A.G. Fernández, H. Galleguillos, E. Fuentealba, F.J. Pérez, Corrosion of stainless steels and low-Cr steel in molten Ca (NO3)2–NaNO3–KNO3 eutectic salt for direct energy storage in CSP plants, Sol. Energy Mater. Sol. Cells 141 (2015) 7–13.

[15] F.J. Ruiz-Cabañas, C. Prieto, R. Osuna, V. Madina, A.I. Fernández, L.F. Cabeza, Corrosion testing device for in-situ corrosion characterization in operational molten salts storage tanks: a516 Gr70 carbon steel performance under molten salts exposure, Sol. Energy Mater. Sol. Cells 157 (2016) 383–392.

[16] Y. Grosu, O. Bondarchuk, A. Faik, The effect of humidity, impurities and initial state on the corrosion of carbon and stainless steels in molten HitecXL salt for CSP application, Sol. Energy Mater. Sol. Cells 174 (2018) 34–41.

[17] S. Goods, R. Bradshaw, Corrosion of stainless steels and carbon steel by molten mixtures of commercial nitrate salts, J. Mater. Eng. Perform. 13 (2004) 78–87.

[18] Corrosion of High Temperature Alloys in Solar Salt at 400, 500 and 680 C. Sandia Report 2013. Sand 2013-8256.

[19] A.S. Dorcheh, R.N. Durham, M.C. Galetz, High temperature corrosion in molten solar salt: the role of chloride impurities, Mater. Corros. 68 (2017) 943–951.

[20] K. Vignarooban, X. Xu, K. Wang, E.E. Molina, P. Li, D. Gervasio, A.M. Kannan, Vapor pressure and corrosivity of ternary metal-chloride molten-salt based heat transfer fluids for use in concentrating solar power systems, Appl. Energy 159 (2015) 206–213.

[21] K. Vignarooban, P. Pugazhendhi, C. Tucker, D. Gervasio, A.M. Kannan, Corrosion resistance of Hastelloys in molten metal-chloride heat-transfer fluids for concentrating solar power applications, Sol. Energy 103 (2014) 62–69.

[22] A.S. Dorcheh, M.C. Galetz, Slurry aluminizing: a solution for molten nitrate salt corrosion in concentrated solar power plants, Sol. Energy Mat. Sol. Cells 146 (2016) 8–15.

[23] M.R. Loghman-Estarki, M. Nejati, H. Edris, R.S. Razavi, H. Jamali, A.H. Pakseresht, Evaluation of hot corrosion behavior of plasma sprayed scandia and yttria co-stabilized nanostructured thermal barrier coatings in the presence of molten sulfate and vanadate salt, J. Eur. Ceram. Soc. 35 (2015) 693–702.

[24] S. Liu, Z. Liu, Y. Wang, J. Tang, A comparative study on the high temperature corrosion of TP347H stainless steel, C22 alloy and laser-cladding C22 coating in molten chloride salts, Corros. Sci. 83 (2014) 396–408.

[25] M.I. Lasanta, M.T. De Miguel, F.J. Pérez, Evaluation of corrosion resistance of A516 Steel in a molten nitrate salt mixture using a pilot plant facility for application in CSP plants, Sol. Energy Mater. Sol. Cells 161 (2017) 226–231.

[26] W.J. Cheng, C. Ding-Jhih, W. Chaur-Jeng, High-temperature corrosion of Cr–Mo steel in molten LiNO3–NaNO3–KNO3 eutectic salt for thermal energy storage, Sol. Energy Mater. Sol. Cells 132 (2015) 563–569.

[27] M.T. de Miguel, V. Encinas-Sánchez, M.I. Lasanta, G. García-Martín, F.J. Pérez, Corrosion resistance of HR3C to a carbonate molten salt for energy storage applications in CSP plants, Sol. Energy Mater. Sol. Cells 157 (2016) 966–972.

[28] A.G. Fernández, L.F. Cabeza, Corrosion monitoring and mitigation techniques on advanced thermal energy storage materials for CSP plants, Sol. Energy Mater. Sol. Cells 192 (2019) 179–187.

[29] Y. Grosu, U. Nithiyanantham, A. Zaki, A. Faik, A simple method for the inhibition of the corrosion of carbon steel by molten nitrate salt for thermal storage in concentrating solar power applications, npj Mater. Degrad. 2 (2018) 34.

[30] http://www.yara.us/images/NitCal-TDS-industrial_tcm399-66077.pdf.

ARTICLE   OPEN

A simple method for the inhibition of the corrosion of carbon steel by molten nitrate salt for thermal storage in concentrating solar power applications

Yaroslav Grosu [1], Udayashankar Nithiyanantham[1], Abdelali Zaki[1] and Abdessamad Faik[1]

Corrosion is an important issue in high-temperature applications such as Concentrated Solar Power (CSP) technology, playing a crucial role in the long-term use of storage tanks, heat exchanger and piping materials which account for a considerable component of the investment costs. While there are many studies regarding the corrosion rates of container materials under the conditions of CSP, there is little progress in the field of their degradation prevention by anticorrosion methods. This work presents an analysis of the corrosion mechanisms between the most economical construction material—carbon steel—and molten nitrate salt. A method to protect the carbon steel against corrosion by molten salt at high temperature was proposed, involving the formation of a calcium carbonate layer on the carbon steel surface. The stability of the layer was tested under isothermal and temperature cycling conditions up to 500 °C, in both inert and air atmospheres in the presence or absence of humidity. The protection method proposed has potential to reduce investment costs for CSP technology.

INTRODUCTION

The durability of materials is particularly important for high-temperature applications like Concentrated Solar Power (CSP) technology.[1,2] CSP is a renewable energy technology, which aims to utilize thermal energy for electricity production by concentrating solar irradiation on a working body.[3–6] The absorbed heat is then used for electricity production using classical power cycles. One of the most important competitive advantages of CSP is its dispatchability (ability to produce electricity on demand) thanks to the relatively simple storage technology—Thermal Energy Storage (TES).[1,2] This can be achieved by heating a large amount of storage material held in a storage tanks. Typically, thousands of tons of molten salts are used. For example, the mass of salts at GEMASOLAR CSP plant is 8500 tons (ref. [7]), at Andasol-1 CSP plant it is 28500 tons (ref. [8]) and at Solana CSP plant it is 125000 tons (http://www.abengoasolar.com, ref. [9]). The heat stored in the molten salt is transferred, when needed, to the power block by a heat exchanger. In some CSP plants, the same molten salt is used as the heat transfer fluid in the solar field.[7,10] Currently, the investment costs for CSP are high due to the cost of construction materials for storage tanks, heat exchanger, pipes and receiver. The initial investment costs are a large contribution to the final price of produced electricity. This affects the competitiveness of this renewable technology in the market. In this context, numerous studies have explored the corrosion behaviour of potential construction materials with different storage media or heat transfer fluids.[11–30]

Molten nitrate salt, known as Solar Salt, is the most technologically mature solution for CSP. It consists of 60 wt% $NaNO_3$–40 wt%KNO_3. Corrosion studies of solar salt go back to 1985 where Slusser et al. tested several nickel- and iron-based

alloys.[13] In this work, immersion tests were done at 510 °C and 705 °C followed by weight loss analysis. Slusser et al. found that the chromium content positively influenced the resistance of the alloys to corrosion. Particularly, the alloys with a chromium content of 15–20 wt% behaved better compared with iron alloys with lower chromium content, especially at higher temperatures. The study showed a drastic increase in corrosion damage at temperatures above 650 °C for all the investigated alloys, which may be attributed to the decomposition of nitrate salt at higher temperature. More recent studies have been dedicated to the corrosion aspects of other nitrate salts like Hitec (53 wt% KNO_3–40 wt% $NaNO_2$–7 wt% $NaNO_3$) and HitecXL (42 wt% Ca $(NO_3)_2$–15 wt% $NaNO_3$–43 wt% KNO_3). Stainless steels such as AISI 304 and 430, a low-Cr alloy steel known as T22 and a carbon steel A1 were tested by Fernandez et al.[14] The authors concluded that HitecXL salt is less corrosive compared with solar salt, demonstrating the positive effect of $Ca(NO_3)_2$ in a nitrate salt. Ruiz-Cabañas et al.[15] investigated the corrosion behaviour of solar salt by means of in situ tests with carbon steel A516.Gr70. In this study,[15] homogenous oxidation was recorded after immersion corrosion tests. In both studies,[14,15] magnesium was present as an impurity in the salt and was incorporated into the corrosion layer. Hitec and solar salts were examined by Federsel et al. with several types of steel (1.4541 and 2.4816 steels with Hitec; 1.4541 and 1.4571 steels with solar salt) demonstrating that chlorides increase the corrosion rates.[16] It was also shown in this work[16] that an addition of a small amount of Na_2O has increased the corrosion rates. A molten ternary salt composed of $LiNO_3$–$NaNO_3$–KNO_3 was tested with five different steels (SB450, T22, T5, T9 and X20) revealing that corrosion resistance improves with increasing Cr content since it creates a protective layer of $(Fe,Cr)_3O_4$ (ref. [17]). It was found that Li absorbed into the corrosion scales due to the presence of

[1]CIC Energigune, Albert Einstein 48, Miñano (Álava) 01510, Spain
Correspondence: Yaroslav Grosu (ygrosu@cicenergigune.com) or Abdessamad Faik (afaik@cicenergigune.com)

npj

simple method for the inhibition of the corrosion…
Y Grosu et al.

2

LiNO₃ in the molten salt.[17] Goods and Bradshaw investigated the compatibility of stainless steels SS-304 and SS-316 at 570 °C as well as carbon steel A36 at 316 °C with several nitrate salts mixtures.[18] In long immersion tests of about 7000 h, the authors reported acceptable corrosion rates even in the presence of some impurities in the salt.[18] A corrosion investigation for molten solar salt with SS-321 and SS-347 iron-based alloys and In625 (22% Cr–8%Mo–61%Ni –5%Fe–3%Nb) and HA230 (22%Cr–1%Mo–60% Ni–1%Fe–14%W) alloys was conducted by Sandia National Laboratories at different temperatures.[19] In the aforementioned study, an increase of the corrosion rate was observed for all materials when the temperature was increased to 680 °C.[19] Moreover, in this work,[19] it was demonstrated that the corrosion mechanism changes with rising temperatures and the dissolution of Cr, Mo and W in the molten salt take place above 600 °C. This resulted in a decreased corrosion rate for iron-based alloys when compared with nickel-based alloys at temperatures above 600 °C, while nickel-based alloys performed better at lower temperatures. In a recent study, the effect of humidity, the initial state of the material and impurities in the salt were investigated for carbon steel and two stainless steels of 304 and 316 types in contact with molten HitecXL salt.[20] The rates of corrosion increased for carbon steel with the presence of moisture in the salt, while corrosion rates for stainless steels were not considerably affected by the presence of moisture.[20] Alumina and silica nanoparticle doping was demonstrated to increase the corrosion rates of molten HitecXL salt due to the excess of oxygen in the system from the air entrapped in the interparticle porosity[12]

The need to improve the efficiency of thermal to electrical energy transformation requires operating CSP technology at higher temperatures. In this regard, storage materials and heat transfer fluids with higher stability like carbonate or chloride salts are also considered as candidates. The ternary salt Li₂CO₃–Na₂CO₃–K₂CO₃ was investigated for compatibility with HR3C steel (25%Cr–20%Ni–53%Fe), demonstrating that oxidation is the main corrosion mechanism.[21] Hastelloy C-276 and C-22 and stainless steel 304 with chloride salts were studied at temperatures up to 900 °C in the presence[22,23] and absence[23] of air. The authors concluded that the corrosion rates decrease with the absence of oxygen in the atmosphere. Different hastelloys have demonstrated a better corrosion resistance compared with stainless steel 304. In ref. [24] a new sensible TES material (a by-product from potash industry) was tested for compatibility with A316 stainless steel. The by-products composition was predominately NaCl. The corrosion rate was found to be around two times greater when compared with solar salt. These results are in-agreement with other studies which show the negative effect of chlorides on the compatibility of construction materials, including the case of Solar salt.[25] Stainless steel 316 was examined by Sarvghad et al. for compatibility with mixtures of (NaCl–Na₂CO₃) and (NaCl–Na₂SO₄) at 700 °C and (Li₂CO₃–K₂CO₃–Na₂CO₃) at 450 °C (ref. [31]). Their analysis showed that intergranular attack of the steel occurred in case of (NaCl–Na₂CO₃) salt, while homogeneous oxidation of the stainless steel was reported when ternary carbonate salt was used.

The corrosion studies of some thermochemical (TCM) and Phase Change Materials (PCMs) with different construction materials can be found in ref. [26–30]. It can be generally noticed that stainless steels SS316 and SS304 are resistant to the corrosion by low-temperature PCMs/TCMs, including Zinc nitrate hexahydrate,[26] hydrogen phosphate dodecahydrate,[26] Na₂S/H₂O (ref. [30]) and others.[27–29] While aluminium is often being corroded by those materials,[26] demonstrating resistance to some commercial PCMs like Na₂SO₄ + H₂O and MgSO₄·7H₂O (ref. [27]). Copper often demonstrates poor corrosion behaviour, particularly with Na₂S/ H₂O (ref. [30]), CaCL₂, Na₂S, Ca(OH)₂, MgCl₂ and MgSO₄ (ref. [29]).

A review of the heat-transfer fluids which are used in CSP is found in ref. [1] This includes liquids such as oils, molten salts and

molten metals as well as their corrosion aspects with other materials used for containers.

According to the literature, it is evident that the most economically attractive material, namely carbon steel, cannot nominally sustain the harsh conditions of molten salt at high temperature. Such incompatibility is an obstacle in decreasing the levelized cost of electricity (LCOE) produced by CSP if such technology requires the use of costly or specialised construction materials.

Application of coatings is one of the most effective solutions to lower the cost of construction materials,[32–36] however, the stability of these coatings at high temperatures is an issue. Some solutions which have been applied to water boilers, where the temperature can rise up to 550 °C, include thermal spraying, pad welding and cold spraying with corrosion resistive materials like Al, high Cr-content alloys with Ni or Fe matrix, ZrO₂, ZrO₂ + Y₂O₃, Al₂O₃.[32,33] In ref. [34] an aluminized slurry was proposed to protect against corrosion by molten nitrate salt at high temperature. Particularly, ferritic–martensitic P91 (Cr9–Mo1) and stainless steel 304 were tested to demonstrate the improved compatibility.[34] In ref. [35], the Inconel 738-LC was tested for corrosion with 45 wt% Na₂SO₄ + 55 wt% V₂O₅ molten salt at 910 °C. This coating was reported to have failed due to the formation of a mixed-oxide layer even though the material was sprayed with a NiCrAlY bond coat, a nanostructured scandia (3.6 mol%), yttria (0.4 mol%) and co-stabilized zirconia (4SYSZ) topcoat by air plasma spraying (APS). TP347H coated with Hastelloy C22 (Ni–Cr–Mo) using a laser cladding technique was tested for compatibility with chloride salts (KCl and NaCl) at temperatures up to 750 °C.[36] This coating considerably improved the corrosion resistance.[36] An Al slurry coating was recently proposed and demonstrated to be effective against molten nitrate and carbonate salts corrosion at 580 °C and 650 °C, respectively.[37]

From the literature review, it can be deduced that the main mechanism for construction materials degradation is oxidation, if the maximum temperature is below the molten salt decomposition. The two main strategies to improve the compatibility of construction materials with molten salts are: (i) The use of metal alloys with high content of Cr and/or Ni; and (ii) the use of stable anticorrosion coatings. Considering that investment costs for CSP technology play a critical role, new reliable methods for anticorrosion protection are specific targets.

In this work, we propose a new simple spray-coating method for improving the corrosion resistance of carbon steel against molten nitrate salt attack, expanding its lifetime and operational temperature range, particularly for CSP technology.

RESULTS AND DISCUSSION

Isothermal corrosion tests

Isothermal corrosion tests for carbon steel A516.Gr70, unexposed to the graphite layer (non-graphitized), with hydrated HitecXL·H₂O salt produced a corrosion layer, which was observed by SEM cross-section analysis (Fig. 1a, b). XRD analysis of the samples surface showed that the layer is composed of iron oxides in the magnetite and haematite phases (Figure S3). On the other hand, the SEM analysis shows the formation of a protective layer on the surface of the carbon steel, which is an iron carbonate layer as discussed in our previous work.[20] These layer is expected to be protective.[38–41]

When the carbonate layer separates from the carbon steel, the oxidation thickness is observed to be around 1.0 μm (Fig. 1a). However, when the carbonate layer remains attached, the oxidation thickness is around 0.6 μm (Fig. 1b). Hence the presence of a carbonate layer reduces the amount of oxidation by nearly twofold. Though, the case shown in Fig. 1b was rarely detected while statistically examining the carbon steel samples after the
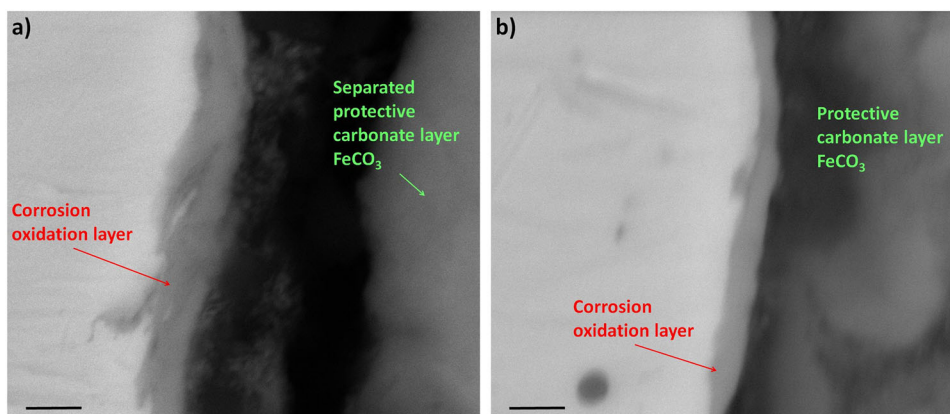
simple method for the inhibition of the corrosion...
Y Grosu et al.

npj

3

Fig. 1 SEM images of cross-sections of carbon steel after 1500 h corrosion test with HitecXL·H_2O. The cases of **a** separated and **b** attached protective $FeCO_3$ layer. Scale bars are 1 μm
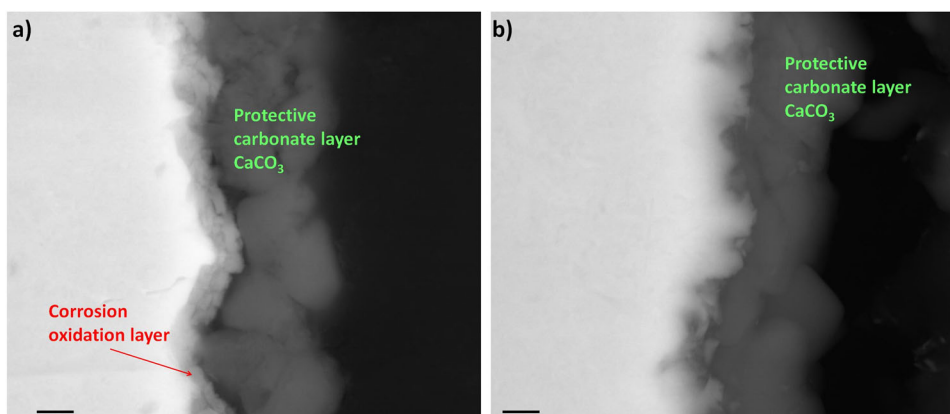
Fig. 2 SEM images of cross-sections of carbon steel after 1500 h corrosion test with HitecXL·H_2O + 2 wt% Graphite. The cases of **a** presence and **b** absence of oxidation layer under $CaCO_3$ carbonate layer. Scale bars are 1 μm

corrosion tests, and it was estimated that less than 1% of the surface was covered with $FeCO_3$.

While being inspired by the protective properties of this carbonate layer, we decided to increase its formation during the corrosion test. In particular, the carbon concentration in the system was increased. To achieve this, graphite was added up to a total mass of 2 wt% into the salt prior to the corrosion tests (see section 'Salts preparation' for details). The isothermal corrosion tests revealed an unexpected and intriguing result. A dense firmly attached layer of calcium carbonate was formed on the surface of carbon steel (Fig. 2a, b). The formation of calcium carbonate was confirmed using XRD analysis with the spectra presented in Figure S3. The layer demonstrates the desired protective behaviour, by completely inhibiting the formation of the oxide layer (Fig. 2b). Only in a few rare zones, the corrosion layer was found on the steel surface. However, the thickness of the corrosion layer was reduced (Fig. 2a) when compared with the carbon steel without the graphite exposure (Fig. 1a). The same observations were seen on the surface of the carbon steel after the corrosion tests by SEM-EDX (Fig. 3). In this case, the surface of carbon steel is covered by the cubic crystals of calcium carbonate in contrast to carbon steel which was not exposed to graphite. There are some spots on the carbon steel surface, which present a much lower concentration of carbon and a higher concentration of oxygen, suggesting the presence of oxides. XRD analysis confirmed the presence of a mixture of $CaCO_3$ and iron oxide phases (Figure S3).

The obtained results illustrate the possibility of increasing the compatibility between carbon steel and molten HitecXL salt by raising the carbon concentration in the system. However, direct addition of graphite into the salt can cause a problem with the thermal decomposition of the unconsumed graphite at a higher temperature. The last point is demonstrated in Figure S5, where HitecXL·H_2O salt with 2 wt% graphite shows a behaviour like pure HitecXL only until 450 °C. Nevertheless, the further increase of the temperature drives the decomposition process resulting with a pronounced mass loss at ~450 °C.

These experiments provide important information on the corrosion process of carbon steel in molten nitrate salts and build a strong basis for the improvement of corrosion resistance method. The accumulated knowledge was used to develop more application-suitable anticorrosion methods. In particular, a simple method of spraying the carbon steel surface with a very thin layer of graphite was tested (see section 'Carbon steel samples preparation' for more details on sample preparation). In this case, the mass of graphite in the system is very low—~$5 \cdot 10^{-3}$ g·cm^{-2} of graphite per area of carbon steel. This corresponds to about 0.08 wt% of graphite in the salt.

The results of the corrosion test for the graphite-treated (graphitized) carbon steel are summarized in Fig. 4. It was found that almost 99.9% of the surface is completely covered by the crystals of calcium carbonate. Only few spots exhibit lower concentration of crystals (Fig. 4b). The complete coverage of the carbon steel surface by the protective layer is mostly due to the

npj

simple method for the inhibition of the corrosion…
Y Grosu et al.

4
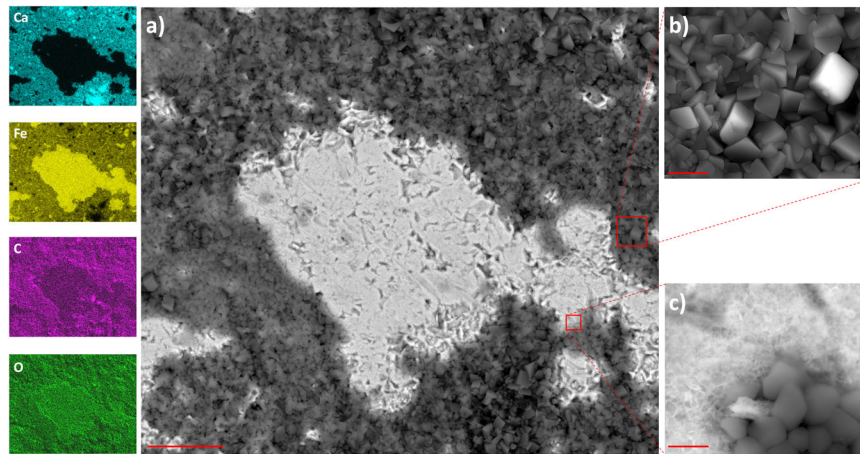
Fig. 3 SEM images and EDX mapping of the surface of carbon steel after 1500 h corrosion test with HitecXL·H_2O + 2 wt% graphite under different magnifications. Scale bar is **a** 25 μm, **b** 5 μm and **c** 2 μm
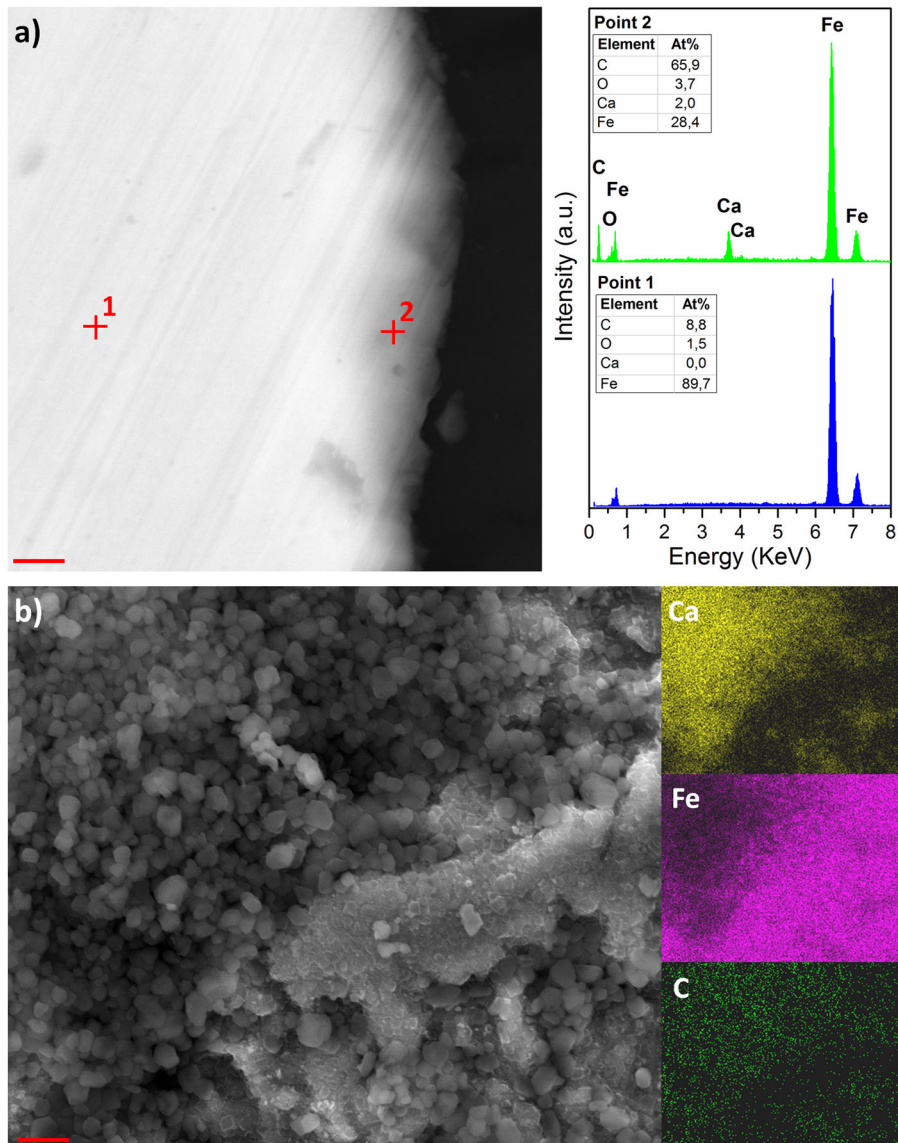
Fig. 4 SEM images and EDX mapping of **a** cross-section (scale bar is 1 μm) and **b** surface of graphitized carbon steel after 1500 h corrosion test with HitecXL·H_2O (scale bar is 2 μm)

simple method for the inhibition of the corrosion…
Y Grosu et al.

npj

5

Table 1. Corrosion rates of carbon steel under different conditions

Conditions	System	Corrosion rate, μm/year
Isothermal, 310 °C, Argon, 1500 h	Carbon steel + HitecXL·H$_2$O	8.8 ± 0.6
	Carbon steel + HitecXL·H$_2$O + 2 wt% Graphite	3.2 ± 0.5
	Graphitized carbon steel + HitecXL·H$_2$O	Not detected
Cycling, 300–500 °C, air, 125 cycles	Carbon steel + HitecXL	31.5 ± 1.6
	Graphitized carbon steel + HitecXL	11.4 ± 1.2
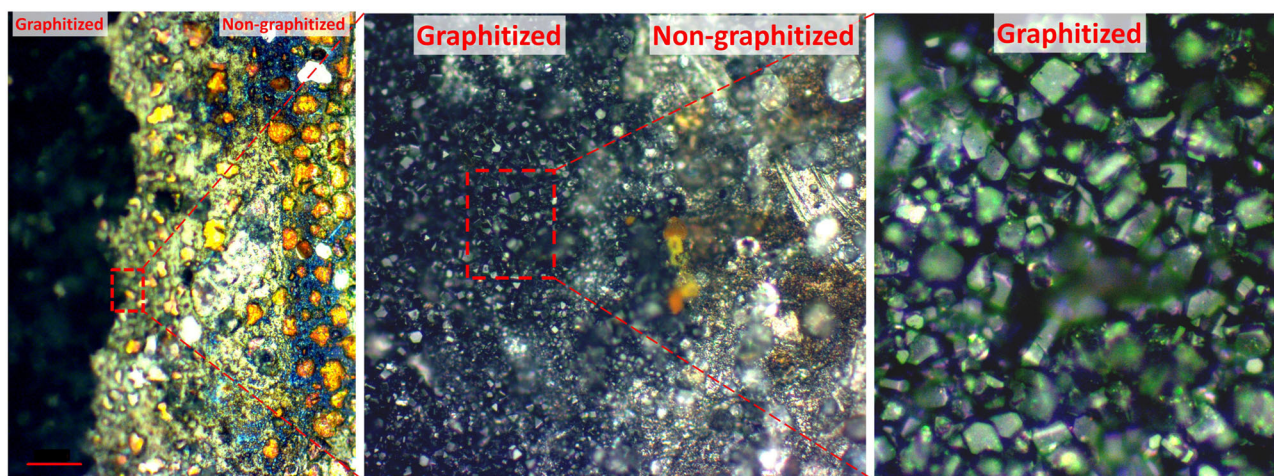
Fig. 5 Optical microscope images of the surface of partially graphitized carbon steel after 24 h corrosion test with HitecXL. Scale bar is 50 μm

initial homogenous distribution of graphite (Figure S11). The analysis of the cross-section revealed the absence of detectable corrosion layer and a very thin layer of CaCO$_3$ on the surface, which is confirmed by EDX (Fig. 4a) and XRD (Figure S3) analyses. This result confirms the protective activity of CaCO$_3$. The thermogravimetric curve of the salt after the corrosion test with graphitized carbon steel showed a decomposition temperature like the pure HitecXL (Figure S5). XRD analysis of these samples could barely detect the residual amount of iron oxides (much lower when compared with 2 wt% graphite case) and showed a clear peak of CaCO$_3$ (Figure S3). The corrosion rates obtained for the experiments presented above are summarized in Table 1.

Other methods for creating the carbonate layer were tested in this work: (1) graphite doping of the salt to a concentration of 1 wt %; (2) ethanol-deposition of graphite onto the surface of carbon steel; (3) temperature pre-treatment under CO$_2$ atmosphere and (4) MgCO$_3$ doping of the salt. Details on the results of these experiments are presented in the Supplementary information (Figures S6–S10). For all the methods except for MgCO$_3$ doping, the formation of CaCO$_3$ protective layer was observed, however, complete coverage of the surface of carbon steel was not achieved.

Effect of oxygen and thermal cycling

Reactions which form the carbonate surface layer and the oxidation reactions on the carbon steel are competitive reactions.[38–41] Thus additional corrosion test for the proposed method was performed under an air atmosphere to observe the formation of carbonate layer under more challenging conditions.

First, for demonstration purposes, half of the piece of carbon steel was sprayed with graphite, while the other half was not treated. After a 24 h corrosion test with HitecXL at 310 °C under an air atmosphere, crystals of CaCO$_3$ appeared and were observed under an optical microscope (Fig. 5). The line of separation

between graphitized and non-graphitized surfaces is very clear (Fig. 5): while the graphitized part is well protected by CaCO$_3$, the non-graphitized one exhibits clear signs of oxidation. XRD and SEM-EDX analyses further confirmed the formation of crystal CaCO$_3$.

Given the excellent results under an air atmosphere, we decided to try more challenging conditions by performing thermal cycling in the range of 300–500 °C with exposure to air, which is the typical condition for a CSP plant. The experiment consisted of 125 consecutive cycles over a 500 h period, the results of these tests are seen in Fig. 6. In the case of non-graphitized carbon steel, the corrosion layer thickness is high and layer detachment is observed (Fig. 6a). While the increased rate of oxidation can be attributed to a higher maximum temperature in the cycling test compared with isothermal at 310 °C, the layering of the material is probably due to thermal cycling and is caused by different dilatation of oxide layer and carbon steel. On the other hand, graphitized samples clearly demonstrate the formation of a layer of CaCO$_3$ crystal over the entire surface (Fig. 6b), with little evidence of the oxidation. XRD analysis reveals the presence of CaCO$_3$ phase and two iron oxides—magnetite and haematite (Figure S4). This suggests that some oxides form during the corrosion test, however, the corrosion rate decrease about three times compared with non-graphitized carbon steel (Table 1).

The results demonstrate the potential of a simple graphitization method to improve the corrosion resistance of carbon steel against molten nitrate salts. The final evaluation, however, requires further corrosion tests by using experimental conditions close to real conditions. In particular, it is necessary to verify the stability of the formed carbonate layer under flow conditions. It must be noted that the presence of graphite on the surface of carbon steel is also beneficial in terms of lowering the surface energy of the carbon steel, which is observed from the contact angle images of the molten salt (Figure S12). This property is beneficial for molten salt pumping under harsh conditions. It

npj

simple method for the inhibition of the corrosion…
Y Grosu et al.

6
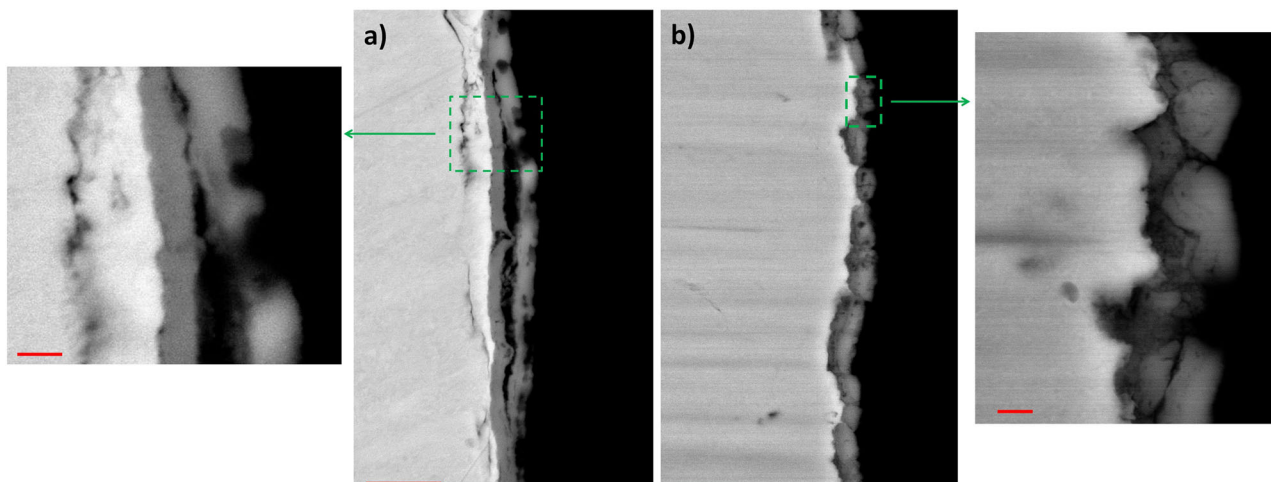
Fig. 6 SEM images of cross-sections of **a** carbon steel and **b** graphitized carbon steel after 125 heating-cooling cycles in the 300–500 °C temperature range. Scale bars in the main Figures are 5 μm. Scale bars in the insets are 1 μm

reduces the frictional dissipation associated with laminar flow near the walls while reducing the stress on the carbonate layer increasing its lifetime. More dynamic tests are required to further confirm this method.

Molten salt and carbonate layer chemistry analysis

In this section, we present how the proposed method of graphitization affects the molten salt and its interaction with the $CaCO_3$ protective layer. Especially, the solubility of $CaCO_3$ in the molten nitrate salt is a concern. In general, it is known that carbonates are soluble in molten salts. To explore this phenomenon, which directly affects the stability of this protective layer for long-term use, several tests were performed.

Firstly, the thermophysical properties (heat capacity, enthalpy of melting and melting temperature) of the salts, both before and after corrosion tests with carbon steel and graphitized carbon steel, were compared and found to be similar within the precision of equipment (Figure S13). These observations suggest that there is no significant change in the composition of the salt.

Additionally, FTIR spectra of the HitecXL salts after the corrosion tests with carbon steel and graphitized carbon steel are shown in Figure S14. It was observed that there are no changes related to the main nitrate peaks, however, the presence of traces of $CaCO_3$ is evident in the HitecXL salt after the test with graphitized carbon steel. This observation is in favour of the limited dissolution of $CaCO_3$ into the molten salt during the corrosion test. It should be also noted that no detectable traces of iron were present in the salts after the corrosion tests.

Finally, to further explore the stability of $CaCO_3$ in the molten HitecXL salt under the same conditions of the corrosion test, a controlled solubility experiment was carried out. Pellets of pure $CaCO_3$ were immersed into the molten HitecXL salt and kept at 310 °C for 1 month. A small concentration of $CaCO_3$ was used (0.05 wt%). Next, the mixture was quenched by immersing in liquid nitrogen. In this way, the crystals of $CaCO_3$ are easily distinguished from glassy HitecXL by SEM. The $CaCO_3$ crystals remained in the crystalline form is the indication of their limited solubility in HitecXL. This approach was used by Su et al. to study the solubility in molten salts.[42] The observation of the stability of $CaCO_3$ micropellets in a quenched salt, (Figure S15a and S15b) as well as $CaCO_3$ crystals (Figure S15c) are considered as an evidence of its insolubility (or very limited solubility) in the molten HitecXL salt under the test conditions. Figures S15a and S15b show the cross-section of the $CaCO_3$ pellet in the quenched HitecXL. It is clearly observed that the pellet retains its sharp edges and does

not show signs of dissolution. Separated crystals of $CaCO_3$ have been also found in the salt and support the limited solubility in molten HitecXL salt (Figure S15c).

We consider the above-presented observations (Figures S13–S15) combined with the well-formed $CaCO_3$ layer on the surface of carbon steel (Figs. 2–6) as a good sign of the stability of $CaCO_3$ protective layer in the molten nitrate salts. However, longer tests are required for further confirmation of the proposed method. It must be noted that limited solubility of $CaCO_3$ can be eliminated by including minor additions of $CaCO_3$ up to the saturation concentration i.e. Le Chatelier principle.

In this work, the mechanism of corrosion for carbon steel A516. Gr70 in molten HitecXL nitrate salt was investigated and reported. It was shown that upon direct contact of carbon steel and molten nitrate salts, two competitive reactions take place, namely oxidation (corrosion) and carbonization (protection). This finding has allowed the proposal of a simple method to improve the resistance of carbon steel to corrosion by spray graphitization. The proposed method improves the corrosion resistance of the carbon steel to molten nitrate salt under both air and inert atmospheres, in presence of humidity and under the stress of thermal cycling up to 500 °C. In particular, corrosion was not detected for graphitized carbon steel after 1500 h isothermal immersion tests at 310 °C under Ar in the presence of humidity, while non-graphitized carbon steel demonstrated the corrosion rate of 8.8 ± 0.6 μm/year under similar conditions. After the cycling immersion tests in the 300–500 °C temperature range under air atmosphere, the corrosion rate of graphitized carbon steel was found to be almost three times lower than non-graphitized one (11.4 ± 1.2 against 31.5 ± 1.6 μm/year). Further corrosion tests under dynamic (flow) conditions are required to confirm the proposed method for practical use or to set points for its improvement. Particularly the complete coverage of the protected surface is a factor to be considered to avoid localized corrosion.

METHODS

Materials preparation

Salts preparation. HitecXL was composed of the following mixture of nitrate salts: 15 wt% of $NaNO_3$, 43 wt% of KNO_3 and 42 wt% of $Ca(NO_3)_2$. The chemical composition of the individual components can be found in Table S1. NitCal was purchased from YARA (http://www.yara.us/images/NitCal-TDS-industrial_tcm399-66077.pdf). KNO_3 and $NaNO_3$ were purchased from SQM. From these chemicals two different HitecXL samples were prepared. The first sample, which is referred to as HitecXL·H_2O is a salt which has not been dried and thus maintaining the calcium nitrate

simple method for the inhibition of the corrosion…
Y Grosu et al.

npj

7

tetrahydrate $Ca(NO_3)_2 \cdot 4H_2O$. This sample was used for experiments with an argon atmosphere. The second sample, which is referred to as HitecXL is a dry sample. This salt mixture (HitecXL) is melted and dried at a temperature of 200 °C for 12 h. This sample was used for experiments exposed to atmospheric air.

Carbon steel samples preparation. Carbon steel A516.Gr70 used in this work consisted mostly of Fe with small amounts of C (0.31 wt%), Mn (0.97 wt%), Si (0.36 wt%) and P (0.04 wt%). The coupons of carbon steel were cut to the size of (20 mm × 10 mm × 3 mm) then successively washed in acetone, ethanol and water using an ultrasonic bath prior to the corrosion tests. The initial state of the carbon steel surface has a strong effect on its corrosion behaviour.[20] Therefore, the samples were not polished before the corrosion tests. Polishing removes the naturally occurring oxide layer including the carbon-rich layer. This initial state would not be comparable to the real industrial conditions.

In this work, several methods of preparing the protective carbonate layer were explored:

1. Graphite in the form of powder (from Sigma-Aldrich) was added to the salt upon its preparation. Two concentrations of 1 wt% and 2 wt% were investigated.
2. Graphite was sprayed, by using graphite 33 spray from Kontakt Chemie, over the clean surfaces of carbon steel pieces prior to the corrosion tests. The weights of the sample before and after the spraying were compared to calculate the mass of graphite deposited on the carbon steel.
3. The deposition of graphite using a graphite–ethanol solution, which was poured on the surface of carbon steel, followed by the evaporation of ethanol.
4. Samples of carbon steel were pre-treated under a CO_2 atmosphere in the presence of humidity at 90 °C for 12 h aiming to form an iron carbonate layer on the surface of the material. For that method, samples of carbon steel were placed into an alumina crucible along with 0.5 g of water to intensify the reaction of iron carbonate formation. Later, the crucible was placed inside a hermetic high-pressure reactor (BR-300, Berghof) controlling the temperature and pressure. The reactor was purged with CO_2 for 1 h, pressurised to 2 bar and then hermetically sealed by high-pressure valves. The temperature was increased to 90 °C and held for 12 h.

Corrosion tests protocol

Isothermal corrosion tests. The scheme for the preparation of the isothermal corrosion tests is presented in Figure S1. All the samples were prepared in a glove box under an argon atmosphere to avoid the presence of oxygen in the reactor. A coupon of carbon steel was completely immersed in 6 g of HitecXL salt. The alumina crucible containing the salt and the carbon steel was covered with an alumina lid and introduced into the stainless-steel reactor. The reactor was hermetically sealed using a flexible copper ring. Then the reactor was kept inside the furnace for 1500 h at 310 °C. The proper sealing of the reactors was verified by comparing their weights before and after the tests.

Cycling corrosion tests. To investigate the effect of thermal cycling on the corrosion behaviour of the studied carbon steel, tests were conducted between 300–500 °C with heating/cooling rates of 2 °C/min. For these tests, the samples of carbon steel were completely immersed into the salt which is placed inside an alumina crucible. Then, the alumina crucible was placed inside the furnace and kept under an air atmosphere during the corrosion test. The formation of carbonates and oxidation of the metal surface are known to be competitive reactions,[38–41] therefore, the presence of oxygen drives the oxidation of carbon steel and provides a more challenging condition for corrosion tests when compared to an inert atmosphere. Each experiment was conducted 3 times to confirm the results.

Techniques

Scanning electron microscopy (SEM). The surface as well as cross-sections of carbon steel samples after the corrosion tests were scanned with a Quanta 200 FEG scanning electron microscope (SEM) using a back-scattered electron detector (BSED). Energy-dispersive X-ray spectroscopy (EDX) analysis was also performed. A simplified scheme of the cross-section samples preparation for SEM analysis is shown in Figure S2, which has been described and verified elsewhere.[12,20] The values of corrosion

layer were calculated by averaging about 200 measurements along the perimeter of the cross-section using ImageJ software.

X-ray diffraction (XRD). The phase composition of the carbon steel before and after the corrosion tests was identified by XRD analysis using a Bruker D8 Advance X-ray diffractometer with CuKα$_1$ radiation ($\lambda = 1.5418$ Å) and θ–2θ geometry and the EVA program from Bruker.

Optical microscope. Carl Zeiss Axio optical microscope was used to scan the surface of the samples after the corrosion tests.

Thermogravimetric analysis. Thermogravimetric analysis of each of the different salts was performed using a NETZSCH STA 449 F3 Jupiter. The measurements were conducted with constant air flow of 60 ml/min to study the thermal stability of the sample from room temperature up to 700 °C with a heating rate of 10 °C/min.

Differential scanning calorimetry (DSC). The specific heat capacity (C_p), specific enthalpy of melting and melting temperature of the salts before and after corrosion tests were measured by DSC technique (TA instruments Q2500). A heating rate of 10 °C/min was chosen. The instrument was calibrated using sapphire as a standard material. Masses of ~10 mg of salt were placed inside a high-conductive aluminium holder sample which then was hermetically closed. The experimental error of this technique is below 3%.

Fourier transform infrared spectroscopy (FTIR). To identify any degradation or contamination of the salt after the corrosion tests, the FTIR measurements were performed. Bruker Vertex 70 spectrometer equipped with diamond ATR and DLaTGS detector was used. The spectra were collected in the range of 4000–450 cm^{-1} in transmission mode.

CaCO$_3$ solubility test

Solubility tests were performed to determine the stability of the protective $CaCO_3$ layer in molten HitecXL salt. First, pellets of as-received pure $CaCO_3$ powder were prepared by using the hydraulic press and 10 mm die with a maximum load of 1 ton. Then, the indicated pellets were immersed in molten HitecXL salt and the temperature was raised to 310 °C and held for 1 month. Then, the mixture was quenched by immersion in liquid nitrogen. Quenching produced a glassy form of HitecXL and with possible dissolved $CaCO_3$, while undissolved $CaCO_3$ remains in a crystalline form. The stability of $CaCO_3$ pellets was examined by SEM. The concentration of $CaCO_3$ was 0.05 wt%.

DATA AVAILABILITY

The datasets generated during and/or analysed during the current study are available from the corresponding author on reasonable request.

AUTHOR CONTRIBUTIONS

Y.G. and A.F. designed research; Y.G., U.N. and A.Z. performed research; all authors analysed data. Y.G. wrote the paper. All authors contributed to writing the paper.

ADDITIONAL INFORMATION

Supplementary information accompanies the paper on the *npj Materials Degradation* website (https://doi.org/10.1038/s41529-018-0055-0).

Competing interests: The authors declare no competing interests.

Publisher's note: Springer Nature remains neutral with regard to jurisdictional claims in published maps and institutional affiliations.
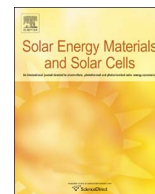
npj

simple method for the inhibition of the corrosion...
Y Grosu et al.

8

REFERENCES

1. Vignarooban, K., Xu, X., Arvay, A., Hsu, K. & Kannan, A. M. Heat transfer fluids for concentrating solar power systems – a review. *Appl. Energy* **146**, 383–396 (2015).

2. Gil, A. et al. State of the art on high temperature thermal energy storage for power generation. Part 1—Concepts, materials and modellization. *Renew. Sustain. Energy Rev.* **14**, 31–55 (2010).

3. Zhang, H., Baeyens, J., Cáceres, G., Degrève, J. & Lv, Y. Thermal energy storage: recent developments and practical aspects. *Prog. Energy Combust. Sci.* **53**, 1–40 (2016).

4. Liu, M. et al. Review on concentrating solar power plants and new developments in high temperature thermal energy storage technologies. *Renew. Sustain. Energy Rev.* **53**, 1411–1432 (2016).

5. Mahlia, T. M. I., Saktisahdan, T. J., Jannifar, A., Hasan, M. H. & Matseelar, H. S. C. A review of available methods and development on energy storage; technology update. *Renew. Sustain. Energy Rev.* **33**, 532–545 (2014).

6. Kuravi, S., Trahan, J., Goswami, D. Y., Rahman, M. M. & Stefanakos, E. K. Thermal energy storage technologies and systems for concentrating solar power plants. *Prog. Energ. Combust.* **39**, 285–319 (2013).

7. Burgaleta, J. I., Arias, S. & Ramirez, D. Gemasolar, the first tower thermosolar commercial plant with molten salt storage. *SolarPACES* **2011**, 20–23 (2011).

8. Relloso, S. & Delgado E. B. Experience with molten salt thermal storage in a commercial parabolic trough plant. Andasol-1 commissioning and operation. *In Proc. 15th SolarPACES Symposium.* 14-18 (2009).

9. Bonk, A., Sau, S., Uranga, N., Hernaiz, M. & Bauer, T. Advanced heat transfer fluids for direct molten salt line-focusing CSPplants. *Prog. Energ. Combust.* **67**, 69–87 (2018).

10. Maccari, A. et al. Archimede solar energy molten salt parabolic trough demo plant: a step ahead towards the new frontiers of CSP. *Energy Procedia* **69**, 1643–1651 (2015).

11. Gomez-Vidal, J. C. Corrosion resistance of MCrAlX coatings in a molten chloride for thermal storage in concentrating solar power applications. *npj Mater. Degrad.* **1**, 7 (2017).

12. Grosu, Y., Udayashankar, N., Bondarchuk, O., González-Fernández, L. & Faik, A. Unexpected effect of nanoparticles doping on the corrosivity of molten nitrate salt for thermal energy storage. *Sol. Energy Mater. Sol. Cells* **178**, 91–97 (2018).

13. Slusser, J., Titcomb, J., Heffelfinger, M. & Dunbobbin, B. Corrosion in molten nitrate–nitrite salts. *JOM* **37**, 24–27 (1985).

14. Fernández, A. G., Galleguillos, H., Fuentealba, E. & Pérez, F. J. Corrosion of stainless steels and low-Cr steel in molten Ca (NO3)2–NaNO3–KNO3 eutectic salt for direct energy storage in CSP plants. *Sol. Energy Mater. Sol. Cells* **141**, 7–13 (2015).

15. Ruiz-Cabañas, F. J. et al. Corrosion testing device for in-situ corrosion characterization in operational molten salts storage tanks: A516 Gr70 carbon steel performance under molten salts exposure. *Sol. Energy Mater. Sol. Cells* **157**, 383–392 (2016).

16. Federsel, K., Wortmann, J. & Ladenberger, M. High-temperature and corrosion behavior of nitrate nitrite molten salt mixtures regarding their application in concentrating solar power plants. *Energy Procedia* **69**, 618–625 (2015).

17. Cheng, W. J., Ding-Jhih, C. & Chaur-Jeng, W. High-temperature corrosion of Cr–Mo steel in molten LiNO3–NaNO3–KNO3 eutectic salt for thermal energy storage. *Sol. Energy Mater. Sol. Cells* **132**, 563–569 (2015).

18. Goods, S. & Bradshaw, R. Corrosion of stainless steels and carbon steel by molten mixtures of commercial nitrate salts. *J. Mater. Eng. Perform.* **13**, 78–87 (2004).

19. Kruizenga, A. M., Gill, D. D., Laford, M., McConohy, G. Corrosion of high temperature alloys in solar salt at 400, 500 and 680 C. *SANDIA National Laboratories report.* Sand 2013-8256 (2013).

20. Grosu, Y., Bondarchuk, O. & Faik, A. The effect of humidity, impurities and initial state on the corrosion of carbon and stainless steels in molten HitecXL salt for CSP application. *Sol. Energy Mater. Sol. Cells* **174**, 34–41 (2018).

21. de Miguel, M. T., Encinas-Sánchez, V., Lasanta, M. I., García-Martín, G. & Pérez, F. J. Corrosion resistance of HR3C to a carbonate molten salt for energy storage applications in CSPplants. *Sol. Energy Mater. Sol. Cells* **157**, 966–972 (2016).

22. Vignarooban, K., Pugazhendhi, P., Tucker, C., Gervasio, D. & Kannan, A. M. Corrosion resistance of Hastelloys in molten metal-chloride heat-transfer fluids for concentrating solar power applications. *Sol. Energy* **103**, 62–69 (2014).

23. Vignarooban, K. et al. Vapor pressure and corrosivity of ternary metal-chloride molten-salt based heat transfer fluids for use in concentrating solar power systems. *Appl. Energy* **159**, 206–213 (2015).

24. Miró, L. et al. Experimental characterization of a solid industrial by-product as material for high temperature sensible thermal energy storage (TES). *Appl. Energy* **113**, 1261–1268 (2014).

25. Dorcheh, A. S., Durham, R. N. & Galetz, M. C. High temperature corrosion in molten solar salt: The role of chloride impurities. *Mater. Corros.* **9**, 943–951 (2017).

26. Cabeza, L. F. et al. Immersion corrosion tests on metal-salt hydrate pairs used for latent heat storage in the 32 to 36 °C temperature range. *Mater. Corros.* **52**, 140–146 (2001).

27. Moreno, P. et al. Corrosion of metal and metal alloy containers in contact with phase change materials (PCM) for potential heating and cooling applications. *Appl. Energy* **125**, 238–245 (2014).

28. Ferrer, G., Solé, A., Barreneche, C., Martorell, I. & Cabeza, L. F. Corrosion of metal containers for use in PCM energy storage. *Renew. Energy* **76**, 465–469 (2015).

29. Solé, A., Miró, L., Barreneche, C., Martorell, I. & Cabeza, L. F. Corrosion of metals and salt hydrates used for thermochemical energy storage. *Renew. Energy* **75**, 519–523 (2015).

30. Sole, A., Barreneche, C., Martorell, I. & Cabeza, L. F. Corrosion evaluation and prevention of reactor materials to contain thermochemical material for thermal energy storage. *Appl. Therm. Eng.* **94**, 355–363 (2016).

31. Sarvghad, M., Steinberg, T. A., & Will, G. Corrosion of stainless steel 316 in eutectic molten salts for thermal energy storage. *Solar Energy.* In Press, 2018. https://doi.org/10.1016/j.solener.2018.03.053

32. Szymański, K., Hernas, A., Moskal, G. & Myalska, H. Thermally sprayed coatings resistant to erosion and corrosion for power plant boilers-a review. *Surf. Coat. Tech.* **268**, 153–164 (2015).

33. Hassani-Gangaraj, S. M., Moridi, A. & Guagliano, M. Critical review of corrosion protection by cold spray coatings. *Surf. Eng.* **31**, 803–815 (2015).

34. Dorcheh, A. S. & Galetz, M. C. Slurry aluminizing: a solution for molten nitrate salt corrosion in concentrated solar power plants. *Sol. Energy Mater. Sol. Cells* **146**, 8–15 (2016).

35. Loghman-Estarki, M. R. et al. Evaluation of hot corrosion behavior of plasma sprayed scandia and yttria co-stabilized nanostructured thermal barrier coatings in the presence of molten sulfate and vanadate salt. *J. Eur. Ceram. Soc.* **35**, 693–702 (2015).

36. Liu, S., Liu, Z., Wang, Y. & Tang, J. A comparative study on the high temperature corrosion of TP347H stainless steel, C22 alloy and laser-cladding C22 coating in molten chloride salts. *Corros. Sci.* **83**, 396–408 (2014).

37. Agüero, A., Audigié, P., Rodríguez, S. & Encinas-Sánchez, V. Protective coatings for high temperature molten salt heat storage systems. in solar concentration powerplants. *SOLARPACES 2017.* 1-8 (2017).

38. Dugstad., A. Fundamental aspects of CO2 metal loss corrosion, part 1: mechanism. *NACECorrosion* **2006**. 1-18 (2006).

39. Dugstad, A., Hemmer, H. & Seiersten, M. Effect of steel microstructure on corrosion rate and protective iron carbonate film formation. *Corrosion* **57**, 369–378 (2001).

40. Choi, Y. S., Nesic, S. & Young, D. Effect of impurities on the corrosion behavior of CO_2 transmission pipeline steel in supercritical CO2−water environments. *Environ. Sci. Technol.* **44**, 9233–9238 (2010).

41. Kermani, M. B. & Morshed, A. Carbon dioxide corrosion in oil and gas production-A compendium. *Corrosion* **59**, 659–683 (2003).

42. Su, S., Villalon, T., Pal, U., Powell, A. Techniques for measuring solubility and electrical conductivity in molten salts. *Advances in Molten Slags, Fluxes, and Salts: Proceedings of the 10th International Conference on Molten Slags, Fluxes and Salts.* 465–475, (2016).

Contents lists available at ScienceDirect

Solar Energy Materials and Solar Cells

journal homepage: www.elsevier.com/locate/solmat

Unexpected effect of nanoparticles doping on the corrosivity of molten nitrate salt for thermal energy storage

Yaroslav Grosu*, Nithiyanantham Udayashankar, Oleksandr Bondarchuk, Luis González-Fernández, Abdessamad Faik

CIC Energigune, Albert Einstein 48, Miñano, Álava 01510, Spain

ABSTRACT

Molten nitrate salts are currently the most common mature solution for thermal energy storage at the concentrated solar power (CSP) plants. Enhancing heat capacity and thermal conductivity of molten salts via doping by inorganic nanoparticles has attracted an explosively increasing interest due to the possibility of a considerable decrease of the investment costs for CSP technology. However, to the best of our knowledge there is almost no information on the effect of such doping on the corrosivity of the molten salts. In this work we demonstrate that adding small amounts of nanoparticles into the molten nitrate HitecXL salt considerably increases its corrosivity and modifies the corrosion mechanisms. A set of advanced techniques such as SEM-EDX, XPS and XRD are applied to get insights into the effect of inorganic nano-additives on the corrosion phenomenon.

1. Introduction

Thermal energy storage (TES) represents an important route for increasing the dispatchability of the concentrated solar power (CSP) technology [1–4]. Currently, molten salts (nitrate salts in particular) are frequently used as storage media as well as heat transfer fluids. Corrosive degradation of the construction materials due to the contact with molten salts can lead to a power plant failure and negative environmental impact. Understanding the corrosion mechanism as well as effect of different factors on the corrosion rates allows to improve the safety, while decreasing the investment costs.

With these regards, compatibility of different molten salts with potential construction and storage [7] materials is often addressed in scientific literature. In particular, Fernández et al. [5] performed a corrosion study between the HitecXL salt and several stainless and carbon steels. They have shown acceptable compatibility and corrosion rate dependence on the steel composition. Moreover, they have found out that the HitecXL salt is less corrosive compared to the commonly used solar salt [5]. Additionally, they detected the incorporation of the magnesium atoms (impurity in the salt) into the carbon steel corrosion layer. In [6], the authors presented a corrosion testing device and used it for solar salt with carbon steel A516Gr70 system. They demonstrated that the corrosion rates are acceptable for practical use and they also confirmed the incorporation of magnesium into the corrosion layer. In [8] the corrosion resistance of the Hastelloys in molten metal-chloride

heat-transfer fluids was studied showing dependence of the corrosion rates on steel composition. Federsel et al. [17] conducted a compatibility study between the Hitec salt and several types of steel revealing a negative effect of chlorides on the corrosion behaviour. Cheng et al. [25] performed a corrosion study between molten $LiNO_3$-$NaNO_3$-KNO_3 salt and several steels. The corrosion resistivity was found to be proportional to the Cr concentration in the steel and that the main mechanisms of corrosion are oxidation and lithiumization. Miguel et al. [26] investigated the compatibility between HR3C steel and Li_2CO_3–Na_2CO_3–K_2CO_3 carbonate salt demonstrating multi-layer formation of different oxides as corrosion products. García-Martín et al. [9] presented a device for dynamic corrosion studies demonstrating that the dynamic conditions increase the corrosion rates compared to static ones. The stability and corrosion aspects of molten salts doped with carbon based nanomaterials were addressed in [27,28]. For the recent review on the corrosion of some PCM materials the interested reader can refer elsewhere [29].

On the other hand, there is a growing interest in molten salt based nanofluids development, due to their enhanced thermophysical properties (thermal conductivity and heat capacity) [30–33]. However, there are almost no studies demonstrating how such doping with nanoparticles affects the corrosion behaviour of molten salts. Some information can be found in [13,24]. In these studies, adding 1%wt of silica nanoparticles into 42.7%Li_2CO_3–K_2CO_3 eutectic salt at 520 °C was claimed to considerably reduce the corrosion rates compared to that of

---

the pure salt. Formation of a protective layer of silica nanoparticles during the immersion corrosion tests was put forward in [13,24] as an explanation of the improvement mentioned above. However, the authors arrived to this conclusion solely based on mass variation of the samples of SS304 in the corrosion tests, while refereeing to the work of Suegama et al. [23], where bis-[trimethoxysilylpropyl]amine anti-corrosion coating filled with silica nanoparticles was developed. Further investigations are needed to support this explanation.

The effect of nanoparticles on the corrosion and erosion in water and in ethylene glycol based nanofluids was studied in more details in [18–22]. Particularly, Celata et al. studied erosion and corrosion of the metal surfaces by water based nanofluids containing TiO_2, Al_2O_3, SiC, ZrO_2 nanoparticles under dynamic conditions [18]. They have concluded that these nanofluids had no effect on the erosion of the stainless steel pipe, while the aluminium pipe had demonstrated increased erosion [18]. Rashmi et al. studied water and ethylene glycol based nanofluids containing carbon nanotubes [19] and they have found that, regardless of the fluid used, the corrosion rate of the tested materials increases in the order: aluminium, stainless steel, copper. The corrosion rate was increasing with temperature (27–90 °C) for all the materials [19]. In another work of the same authors, an increase of erosion and corrosion for nanofluid formed by alumina nanoparticles and sea water was demonstrated [20]. Bubbico et al. [22] investigated the corrosion and erosion of stainless steel 316, copper and aluminium by nanofluids based on different aqueous solutions and have found that the pH played an important role in the corrosion process. Among the investigated construction materials, only the aluminium was affected. Recently, Fotowat et al. [21] have studied the impact of pH on the corrosivity of water + Al_2O_3 nanofluid with the same materials (aluminium, copper and stainless steel). Among the three investigated construction materials, copper was found to be the most corroded one while the stainless steel 316 was the most corrosion resistant [21]. However, to the best of our knowledge there are no studies focused on the effect of nanoparticles on the corrosion behaviour of molten inorganic salts.

In this work, we studied the effect of adding the inorganic nanoparticles on the corrosivity of the molten salts. In particular, the corrosion tests were carried out for nanofluids based on the commercial HitecXL salt in direct contact with carbon steel. It was demonstrated that the presence of nanoparticles in this nitrate salt affects the corrosion rate noticeably. This finding can have far reaching implications for the practical use of nanodoped molten salts.

2. Materials and techniques

2.1. Materials and preparation

In this work, carbon steel A516. Gr70 with the following chemical composition was used: 98.68% Fe, 0.97% Mn, 0.31% C and 0.04% P (weight concentrations). Small pieces of the material were successively washed in acetone, ethanol and water in ultrasonic bath prior to the corrosion tests. As was demonstrated in our previous work [11], the initial state of the material has strong effect on the corrosion behaviour. For that reason, the samples were not polished before the corrosion tests as such treatment activates the surface, removing the oxide and carbon-rich layers, providing the initial state of the material far from the one corresponding to the application.

The above indicated material was tested with HitecXL salt consisted of 15% of $NaNO_3$, 43% of KNO_3 and 42% of $Ca(NO_3)_2$ (weight concentrations), which was prepared using commercial compounds (NitCal from YARA [14], KNO_3 and $NaNO_3$ from SQM) with the chemical composition presented in Table 1S. All the components were completely dried at 200 °C over 24 h prior to weighing under controlled conditions inside the glove box.

Two types of commercial nanoparticles were used to prepare the nanofluids. The Al_2O_3 nanoparticles produced by Aeroxide® with particle size of 13 nm and the SiO_2 nanoparticles delivered by Sigma-

aldrich with particle size of 12 nm.

To prepare the nanofluids a dry method was used. A quantity of 2 g of the mixture of HitecXL salt (99%wt) and the nanoparticles (1%wt) were introduced into a 50 ml aluminium bottle and subjected to dynamic shaking by means of ball milling machine during 15 min. The proper distribution of the nanoparticles was verified by different techniques and is a topic of a separate paper.

2.2. Corrosion tests protocol

For the corrosion experiments, around 6 g of salt were placed inside an alumina crucible and then a piece of 3 mm x 10 mm x 20 mm of carbon steel was immersed completely into the salt. Then, the alumina crucible was placed inside the furnace and kept at a constant temperature of 310 °C under air atmosphere for exposure times of 500, 1000 and 1500 h. The test temperature was selected in view of the operation conditions of the pilot CSP plant developed within ORC-Plus project [10], where the HitecXL salt is considered as one of storage material candidates to be used in the thermocline storage system, where, no controlled atmosphere on the top of TES tank is envisaged.

After the corrosion tests, the carbon steel samples were removed from the salt and carefully washed with hot water in order to remove the salt residues stuck at the surface.

2.3. Characterization techniques

2.3.1. Scanning Electron Microscopy - SEM

The surface and a cross section of the samples were imaged by means of a scanning electron microscope Quanta 200 FEG operated in high vacuum mode at 30 kV featured with a back scattered electron detector (BSED). In addition, energy-dispersive X-ray spectroscopy (EDX) analyses were carried out for elemental mapping. The images of the oxidation/corrosion layers were recorded along the whole perimeter of the samples' cross sections and average values are presented.

The cross sections of the samples were obtained following the simplified scheme shown in Fig. 1S. The carbon steel piece was immersed in rubber prepared by mixing KEM 90 Harz resin and KEM 90 Harter catalyst in 2:1 proportion, which upon solidification creates a proper holder for SEM imaging and helps to avoid possible removal of the corrosion and/or oxidation layers during the cutting and polishing of the cross section of the sample. A comparison of the SEM results of samples with and without the resin holder confirms that such holder does not bring any detrimental information, but helps to keep the separated corrosion/oxidation layer close to the surface of the material.

2.3.2. Fourier Transform Infrared spectroscopy – FTIR

The FTIR was used to identify any degradation or contamination of the salt upon testing with the carbon steel. The FTIR measurements were performed with a Bruker Vertex 70 spectrometer equipped with diamond ATR and DLaTGS detector. The FTIR spectra of the salts before and after the corrosion tests were recorded at room temperature in the range of 4000 – 450 cm^{-1} in transmission mode.

2.3.3. X-ray photoelectron spectroscopy characterization – XPS

XPS characterization was performed in an ultra high vacuum system described elsewhere [15] to follow composition changes in the surface layer of carbon steel. The XPS spectra were acquired by means of a hemispherical electron energy analyzer PHOIBOS 150 (SPECS). A twin Al/Mg anode X-ray source XR50 (SPECS) operated at 12 keV and 100W power was used to excite the photoelectron spectra. The XPS spectra were acquired in the fixed analyzer transmission mode with pass energies of 20 eV and 100 eV for detecting elemental spectral lines with high resolution and survey spectra, respectively. The XPS spectra were peak-fitted using CasaXPS data processing software. The quantification has been done using sensitivity factors provided by the elemental library of the CasaXPS software [16].
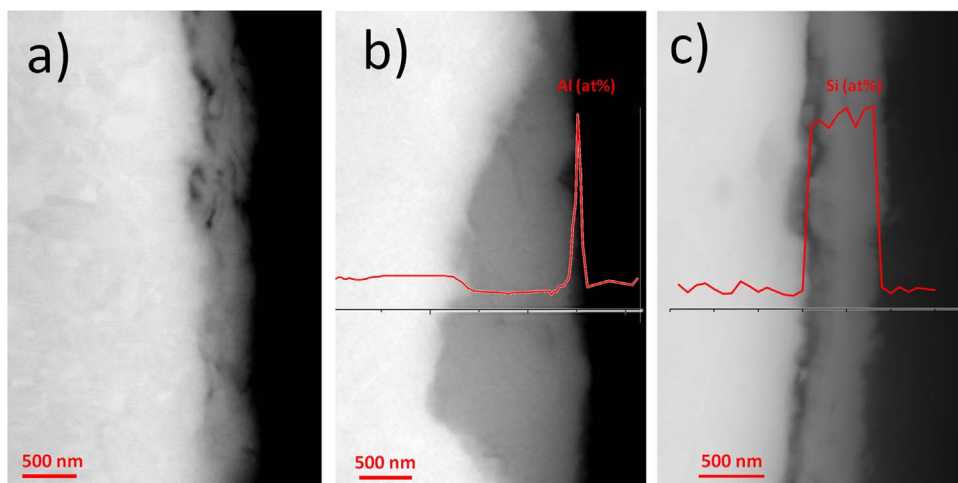
Fig. 1. SEM images and EDX analyses of the cross sections of carbon steel after 1500 h corrosion tests with a) HitecXL; b) HitecXL + Al₂O₃ nanoparticles and c) HitecXL + SiO₂ nanoparticles.

The XPS depth profiling was performed by means of a sputter gun IQ12 (SPECS) operated in scanning mode with Argon ion beam with kinetic energy of 5 keV. The estimated sputter rate was ~ 1–3 nm min⁻¹.

2.3.4. X-ray diffraction – XRD

A structural analysis of the materials before and after the corrosion tests was performed by XRD using a Bruker D8 Advance X-ray diffractometer equipped with a LYNXEYE detector using CuKα1 radiation ($\lambda = 1.5418$ Å) and θ-2θ geometry. The data were collected at room temperature between 5° and 110° in 2θ with a step size of 0.02° and counting time of 8 s per step. The EVA program was used to determine the phase composition of the material.

3. Results

3.1. Scanning electron microscopy

Fig. 1 shows SEM micrographs of the corrosion layers formed on the surface of the carbon steel tested with HitecXL, HitecXL + 1%Al₂O₃ and HitecXL + 1%SiO₂ nanoparticles.

The corrosion layer evolves with time of corrosion test. The time dependence of the corrosion layer thickness is depicted in Fig. 2. As can be observed, the Al₂O₃ and SiO₂ nanoparticles, although considered to be chemically inert, surprisingly lead to thicker corrosion layer when compared to the non-doped HitecXL salt. Moreover, the EDX analysis demonstrates the incorporation of these nanoparticles in the corrosion layer (Fig. 1b and c). It is also interesting to note, that in the case of
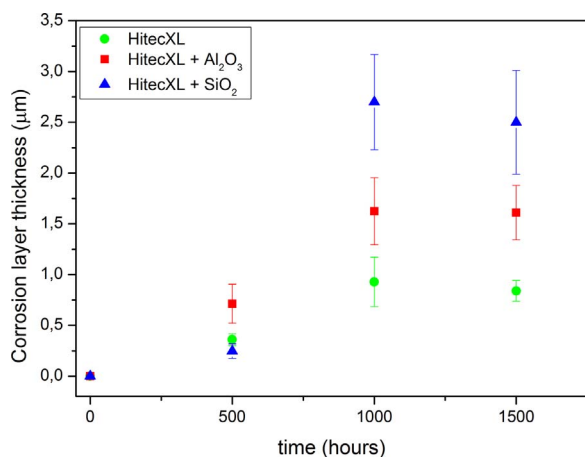

Fig. 2. Evolution of corrosion layer thickness for carbon steel in molten salts: HitecXL, HitecXL + Al₂O₃ nanoparticles and HitecXL + SiO₂ nanoparticles.

HitecXL + Al₂O₃ the Al penetration depth into the corrosion layer is limited (sharp peak of Al concentration in Fig. 1b). While in the case of HitecXL + SiO₂ the whole corrosion layer contains Si (Fig. 1c).

Noteworthy, that in the case of pure HitecXL salt the corrosion layer thickness is uniform over the cross section perimeter, while in the case of nanoparticles doped salts the corrosion layers are not uniform with different propagation depths. This is the reason for the higher statistical deviations in the measured corrosion thickness for the salts with nano-additives (Fig. 2).

From several works dedicated to the corrosion between nitrate salts and different construction materials [5,6], one can note that magnesium (common impurity of such salts) incorporates into the steel after the tests. Indeed, the SEM-EDX analysis of the carbon steel surface tested in pure HitecXL evidences a substantial amount of Mg distributed over all the surface (Fig. 3b). While in the case of HitecXL salt doped with nanoparticles no Mg was detected in the corrosion layers (Fig. 3c and d).

From Fig. 3a it can be also seen that the initial raw carbon steel has two types of surface states, similar in terms of the chemical composition, but different in term of roughness. From the EDX analysis it is evident that such different regions have different concentration of oxygen before and after the corrosion tests (Fig. 3). This may suggest that these two regions are formed by different iron oxides - Magnetite (Fe₃O₄) and Hematite (Fe₂O₃). To support this hypothesis the XPS and XRD results will be discussed in the next sections. Elemental analyses of the samples tested with salts are shown in Fig. 3b,c,d revealing non-homogeneous distribution of Mg, C, Al and Si over the carbon steel surfaces. Mg rich regions of up to ~100 µm (Fig. 3b) in size were detected only in the case of nanoparticles-free salt. In the cases of salts with alumina/silica nanoparticles two types of regions were detected: regions rich with silicon/aluminium and the ones rich with carbon (Fig. 3c and d).

3.2. X-ray photoelectron spectroscopy characterization

The XPS measurements were performed to assess the elemental composition and chemical state of the components of the corrosion layers. By performing XPS depth profiling we estimated the thickness of the iron oxide layer for all the samples. Results obtained with XPS demonstrate that strong decrease of iron oxide's signature takes place after sputtering away approximately 1 µm for nanoparticles-free HitecXL. The thickness of the sputtered layer was estimated based on the sputtering time needed to sputter away the top oxide layer.

Blue and black curves in Fig. 4a present Fe2p XPS spectra after removing ~0.1 µm and ~1 µm of top layers, respectively. The shape of the spectral lines and positions of the peaks in the blue spectra are characteristic of iron oxide. The black spectrum in Fig. 4a contains
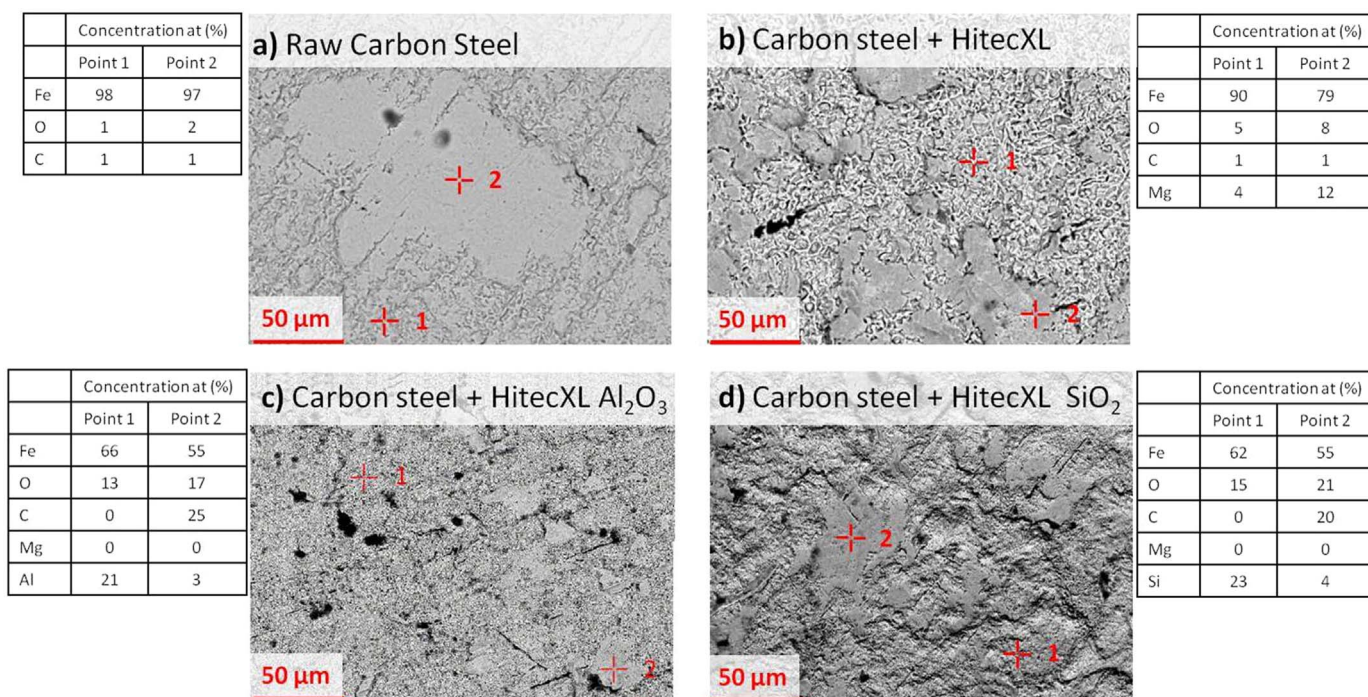
	Concentration at (%)	
	Point 1	Point 2
Fe	98	97
O	1	2
C	1	1

	Concentration at (%)	
	Point 1	Point 2
Fe	90	79
O	5	8
C	1	1
Mg	4	12

	Concentration at (%)	
	Point 1	Point 2
Fe	66	55
O	13	17
C	0	25
Mg	0	0
Al	21	3

	Concentration at (%)	
	Point 1	Point 2
Fe	62	55
O	15	21
C	0	20
Mg	0	0
Si	23	4

Fig. 3. SEM and EDX analyses of the surface of a) raw carbon steel; and carbon steels after 1500 h corrosion tests with b) HitecXL; c) HitecXL + Al_2O_3 nanoparticles; d) HitecXL + SiO_2 nanoparticles.

peaks shifted towards lower binding energies with respect to those in the blue curve. The main peak at ~707 eV corresponds to $Fe2p_{3/2}$ line in metallic iron. Correspondent intensity of the O1s signal (not shown here) after removing ~1 µm dropped virtually to negligible level thus confirming removal of the top oxide layer.

In the case of nanoparticles doped salts it took much longer sputtering time to completely remove the iron oxide layer: Fe2p spectrum (black curve in Fig. 4b) exhibit a strong shoulder at ~710 eV which indicates presence of the iron oxide after removing top layer of ~1 µm. The latter observation is in accord with the SEM data presented in Fig. 1b,c thus supporting the conclusion on the heavily non-uniform thickness of the corrosion layers when the nano-additives to the salts were used.

Fig. 5 shows wide range XP spectra of the carbon steel surface acquired after testing in nanoparticles-free HitecXL (Fig. 5, black curve) and in HitecXL doped with SiO_2 nanoparticles (Fig. 5, red curve).

The spectrum for the test with SiO_2 doped HitecXL indicates the

presence of Si and Ca, while spectrum for nanoparticles-free HitecXL (Fig. 5, black curve) reveals strong Auger signal from magnesium (peak at 305 eV) which was not observed for the pristine carbon steel. By performing depth profiling, we have found that the thickness of the magnesium enriched layer is around 1 µm thus it is close to that of the iron oxide layer thickness. Interestingly, the magnesium was not detected on the surface of the sample tested with nanoparticles doped salts (Fig. 5, red curve), which is in agreement with EDX data (Fig. 3).

From Fig. 5 it is also evident that the SiO_2 nanoparticles are incorporating into the corrosion layer, which is in agreement with EDX analysis (Fig. 1c and Fig. 3d). Moreover, in this case the calcium was found to be incorporated in the corrosion layer of the carbon steel (Fig. 5, red curve).

3.3. X-ray diffraction

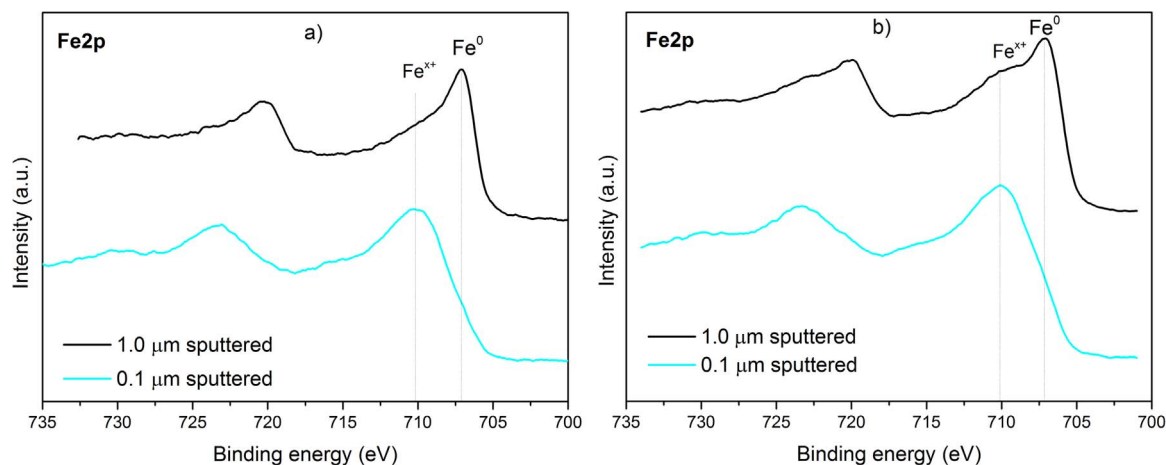The structure of the carbon steel samples after the corrosion tests

Fig. 4. XPS depth profiling for carbon steel after 1500 h corrosion tests with a) HitecXL and b) Hitec XL + SiO_2 nanoparticles. Blue and black curves are Fe2p XPS spectra after removing of ~0.1 µm and ~1 µm top layers by Ar-ion sputtering respectively.
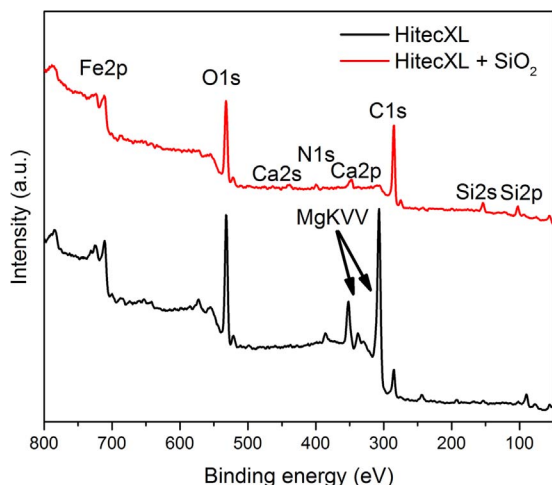
Fig. 5. XP spectra of carbon steel after 1500 h corrosion tests with HitecXL (black curve) and HitecXL + SiO$_2$ nanoparticles (red curve).
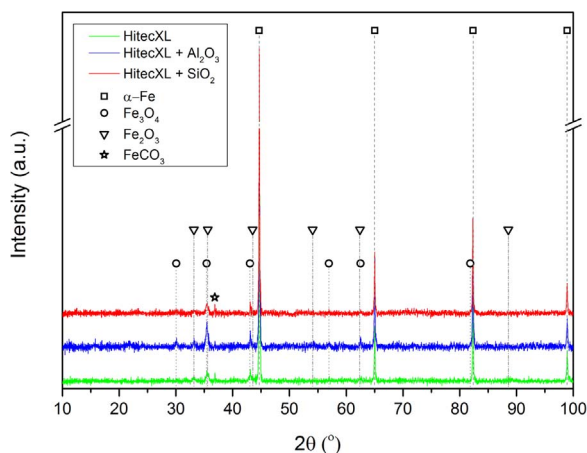

Fig. 6. XRD diffractograms of carbon steel after the corrosion tests with HitecXL, HitecXL + Al$_2$O$_3$ and HitecXL + SiO$_2$ nanoparticles.

was analyzed by the XRD. The XRD diffractograms shown in Fig. 6 indicate presence of the iron oxides magnetite (Fe$_3$O$_4$) and hematite (Fe$_2$O$_3$) and also a small amount of iron carbonate (FeCO$_3$). As expected, no phases containing Al or Si elements were identified due to their low concentrations.

In our previous work [11], it was shown that iron carbonate layer acts as protective layer in case that it is firmly attached to the surface of material and evenly distributed over the surface. Iron carbonate is formed during the corrosion test due to the presence of amorphous carbon-rich layer on the surface of pristine carbon steel as a result of a long-time exposure to the atmosphere. In this work, the identified iron carbonate layer is distributed non-homogenously occupying only small area of the carbon steel surface (Fig. 3). Moreover, when such carbonate layer is found, it is poorly attached to the surface of carbon steel and does not provide corrosion protection. Example of preservation of such layer is demonstrate in Fig. 2S. It is interesting that in case of similar corrosion tests performed under inert atmosphere, the formation of such protective carbonate layer is much more favorable and it is observed along almost all the surface of the carbon steel [11]. Such result is logical considering that the oxidation and carbonization reactions on the surface of steel are known to be competitive reactions [12], hence the air atmosphere results in higher level of oxidation and as a result inhibition of carbonization.

3.4. Stability of the salt

It is worth mentioning, that we didn't observe any effect of adding nanoparticles on the stability of the salt. The temperature as well as the enthalpy of melting of the tested salts were not modified. Moreover, no changes were observed in the FTIR spectra of tested salts as can be clearly observed in Fig. 3S.

4. Discussion

The above described corrosion tests combined with the characterization of the corrosion layer by means of SEM-EDX imaging (Figs. 1–3) and XPS depth profiling (Figs. 4 and 5) indicate that the compatibility between nitrate salt and carbon steel can be substantially modified/compromised by adding into the salt small amounts of SiO$_2$ or Al$_2$O$_3$ nanoparticles.

Taking into account that the main mechanism of carbon steel corrosion is oxidation, one may consider that additional oxygen could be supplied from the air entrapped in the interparticles pores. In other words, the nanoparticles, having high specific surface area, effectively provide additional source of oxygen. To verify this idea, small droplets of salts (15 mg) were deposited on the glassy carbon surface for observation under corrosion test conditions (310°C, air). The glassy carbon surface was chosen as chemically inert and smooth surface.

Light images at the bottom of Fig. 7 display large number of bubbles nested in the droplets of the salt doped with nanoparticles. It is obvious from the light images in Fig. 7 (bottom) that the amount of trapped air is considerably higher when nanoparticles are present. The evolution of the droplets mass in course of time is presented by the graphs in Fig. 7 (right top). During the first 30 min the mass vs time dependence levels out for all the tested materials, while, it takes about 4 days to completely remove all the bubbles. Given the fact that the mass variation for all the three samples is the same within the measurement error we conclude that the observed bubbles are bubbles of trapped/dissolved air. Releasing of the trapped bubbles from the droplets proceeds in parallel with decreasing of the contact angle. The apparent concentration of bubbles is higher for the SiO$_2$ doped salt as compared to the Al$_2$O$_3$ doped salt one. This could be explained by the higher volumetric concentration of SiO$_2$ nanoparticles compared to that of the Al$_2$O$_3$ nanoparticles (due to lower density of SiO$_2$).

The above observations correlate well with the finding that the corrosion layer is thicker for SiO$_2$ doped salt than for Al$_2$O$_3$ doped salt (Fig. 2). On account of the above observations, it appears reasonable to assign the increased corrosion of carbon steel to the air entrapped in the interparticle porosity.

Apart from the increased thickness of the corrosion layer, it is clear that the corrosion mechanism has been also changed. Pariculary, we found that magnesium incorporation did not occur when salt was doped with silica or alumina nanoparticles (Figs. 3–5).

It is important to note that while the corrosion layer in the case of pure HitecXL has uniform thickness, for nanoparticles-doped HitecXL case regions with considerably thicker corrosion layer are present, which is evident from SEM analysis (Fig. 1 and Fig. 2) and XPS depth profiling (Fig. 4). The difference in the corrosion layers' morphologies may be due to several reasons: 1) The bubbles observed in Fig. 7 are non-homogeneously distributed and hence result in non-homogeneous oxidation of the carbon steel. This is particularly evident for the case of alumina nanoparticles (Fig. 1b), where the bubbles are larger (Fig. 7) and hence are distributed even more non-homogeneously compared to the silica case. It should be also noted that the size of the bubbles is most probably due to different agglomeration states of the nanoparticles (interparticle porosity). 2) The nanoparticles tend to agglomerate forming some regions with higher concetrations. 3) The initial state of the carbon steel seems to have noticeable effect on the incorporation of the nanoparticles during the corrosion test, which is evident from the SEM-EDX analysis of the surface of carbon steel
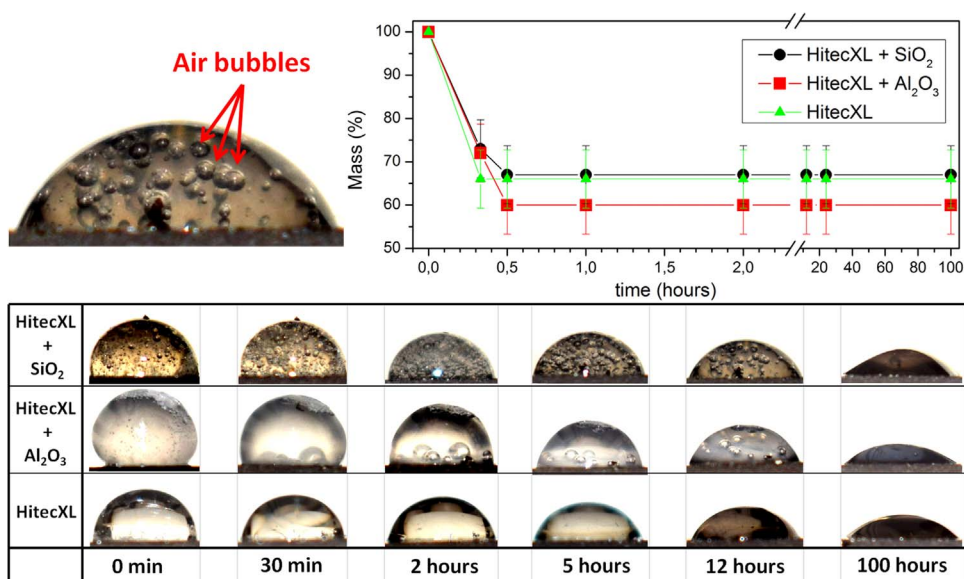
(Fig. 3) and is explained in more details below.

From the Fig. 3a it can be seen that the pristine carbon steel has two different states of the surface, which have similar chemical composition, but are different in terms of roughness and oxygen content. The corrosion tests exposed the different behaviour/properties of the regions. In the case of pure HitecXL (Fig. 3b) the regions with pronounced roughness and lower concentration of oxygen contain substantially less magnesium, compared to the smoother regions, which have higher amount of oxygen. Combining this observation with the XRD analysis (Fig. 6) one can argue that such regions represent different iron oxides - Magnetite (Fe_3O_4) and Hematite (Fe_2O_3). In this view, incorporation of Magnesium is more likely to occur into the Hematite regions. For the experiments with nanoparticles-doped salts one can see that there is no Magnesium incorporated into the carbon steel (Fig. 3c and d). Magnesium free corrosion layers in the cases of salt doped with silica or alumina could be thought of as an evidence of magnesium substitution by the dopants with higher electronegativity. Indeed, the electronegativity of the involved elements is increasing in the following order: Mg, Al, Si. Hence, in case if more than one of these elements are present, the one having higher electronegativity should react first with carbon steel. This explains the absence of Mg in case alumina or silica nanoparticles are added.

At the same time the smoother regions - initially Hematite - contain smaller amount of nanoparticles compared to the rough regions - initially Magnetite (Fig. 3c and d). It is logical since nanoparticles are expected to participate in oxidation process and Magnetite tends to oxidize to Hematite during the corrosion test, while Hematite is the final oxidation state of iron. This can result in a non-homogeneous thickness of corrosion layer as well.

To summarize, we have shown that the air bubbles accumulation and their distribution within the salt, the affinity of the elements forming nanoparticles-doped salt as well as the initial state of the construction material have pronounced effects on the corrosion behaviour of carbon steel. The chart in Fig. 8 compares corrosion rates of the carbon steel when contacting molten HitecXL salt under different conditions at temperature of 310°C.

It can be seen that the corrosion rate of carbon steel being in direct contact with molten HitecXL salt depends on the atmosphere. In case of inert (argon) atmosphere the corrosion rate is higher than that under ambient conditions. We believe this is due to formation of more corrosive nitrites under oxygen free atmosphere. The negative effect of inert atmosphere on the corrosion behaviour of stainless steels was recently demonstrated by DLR [34]. It was shown that drastic increase
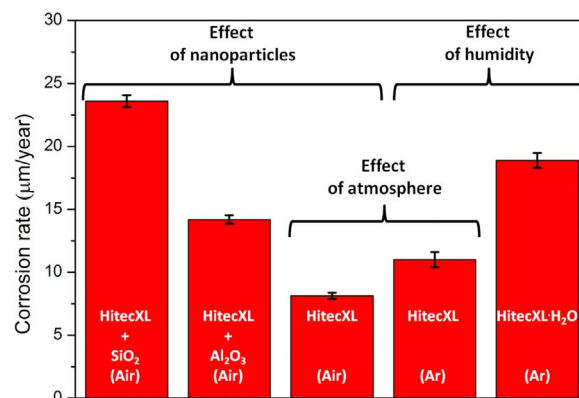

Fig. 8. Comparison of corrosion rates of carbon steel in direct contact with molten HitecXL salt under different conditions at 310°C. The values for experiments performed under argon atmosphere are taken from [11].

of nitrites as well as oxides formation was detected for Solar Salt in case air atmosphere is replaced by nitrogen gas. Importantly, the corrosive effect of atmosphere is noticeably lower compared to that of nanoparticle doping of the salt, where corrosion rate increased nearly 3 times in case of SiO₂ dopant. The effect of adding nanoparticles is comparable with the effect of humidity in the system (Fig. 8), which was in detail discussed in our previous work [11].

5. Conclusions

The effect of silica and alumina nanoparticle doping on the corrosivity of molten nitrate HitecXL salt was investigated. The following can be concluded based on the performed experiments:

1. The doping of the salt with nanoparticles considerably increases salt's corrosivity. The corrosion layer thickness in the cases of SiO₂ and Al₂O₃ nanoparticles doped salts is 3 times and ~2 times of that for the nanoparticles-free salts, respectively. Moreover, the presence of nanoparticles increases the non-homogeneity of the corrosion layer thickness.
2. The entrapped air in the interparticle porosity could be responsible for the increased oxidation (corrosion) rates of carbon steel, while non-homogeneous distribution of bubbles results in non-homogeneous thickness of the corrosion layer.
3. The presence of nanoparticles affects the mechanism of corrosion

layer formation. Particularly, magnesium, which is known to incorporate into the corrosion layer of carbon steel, has not been detected in the case of salts doped with nanoparticles. Al and Si were detected instead. This might be due to the different electronegativity of the elements involved.

4. The initial state of the material (oxide phases, roughness) has strong effect on the corrosivity of the investigated molten nitrate salt, particularly in the case when nanoparticles are added.

From the obtained results it is evident that the corrosion aspect must be strongly considered in case nanoparticles-doped salts with enhanced thermophysical properties are used under the conditions of thermal energy storage at concentrated solar power plant.

Further experiments with nanoparticles-doped molten salts under dynamic conditions and different atmospheres would be useful for general understanding of the problem.

Acknowledgement

Appendix A. Supporting information

Supplementary data associated with this article can be found in the online version at http://dx.doi.org/10.1016/j.solmat.2018.01.002.

References

[1] H. Zhang, J. Baeyens, G. Cáceres, J. Degrève, Y. Lv, Thermal energy storage: recent developments and practical aspects, Prog. Energy Combust. Sci. 53 (2016) 1–40.

[2] M. Liu, N.S. Tay, S. Bell, M. Belusko, R. Jacob, G. Will, W. Saman, F. Bruno, Review on concentrating solar power plants and new developments in high temperature thermal energy storage technologies, Renew. Sustain. Energy Rev. 53 (2016) 1411–1432.

[3] T.M.I. Mahlia, T.J. Saktisahdan, A. Jannifar, M.H. Hasan, H.S.C. Matseelar, A review of available methods and development on energy storage; technology update, Renew. Sustain. Energy Rev. 33 (2014) 532–545.

[4] S. Kuravi, J. Trahan, D.Y. Goswami, M.M. Rahman, E.K. Stefanakos, Thermal energy storage technologies and systems for concentrating solar power plants, Prog. Energ. Combust. 39 (2013) 285–319.

[5] A.G. Fernández, H. Galleguillos, E. Fuentealba, F.J. Pérez, Corrosion of stainless steels and low-Cr steel in molten Ca (NO3)2–NaNO3–KNO3 eutectic salt for direct energy storage in CSP plants, Sol. Energy Mater. Sol. Cells 141 (2015) 7–13.

[6] F.J. Ruiz-Cabañas, C. Prieto, R. Osuna, V. Madina, A.I. Fernández, L.F. Cabeza, Corrosion testing device for in-situ corrosion characterization in operational molten salts storage tanks: A516 Gr70 carbon steel performance under molten salts exposure, Sol. Energy Mater. Sol. Cells 157 (2016) 383–392.

[7] S. Guillot, A. Faik, A. Rakhmatullin, J. Lambert, E. Veron, P. Echegut, C. Bessada, N. Calvet, X. Py, Corrosion effects between molten salts and thermal storage material for concentrated solar power plants, Appl. Energy 94 (2012) 174–181.

[8] K. Vignarooban, P. Pugazhendhi, C. Tucker, D. Gervasio, A.M. Kannan, Corrosion resistance of Hastelloys in molten metal-chloride heat-transfer fluids for concentrating solar power applications, Sol. Energy 103 (2014) 62–69.

[9] G. García-Martín, M.I. Lasanta, V. Encinas-Sánchez, M.T. de Miguel, F.J. Pérez,

[10] ⟨http://www.orc-plus.eu/⟩.

[11] Y. Grosu, O. Bondarchuk, A. Faik, The effect of humidity, impurities and initial state on the corrosion of carbon and stainless steels in molten HitecXL salt for CSP application, Sol. Energy Mater. Sol. Cells 174 (2018) 34–41.

[12] A. Ikeda, S. Mukai, M. Ueda Prevention of CO2 Corrosion of Line Pipe and Oil Country Tubular Goods. CORROSION/84, paper no. 289 (Houston, TX: NACE, 1984).

[13] M. Schuller, F. Little, D. Malik, M. Betts, Q. Shao, J. Luo, W. Zhong, S.A.P. Shankar, Molten Salt-Carbon Nanotube Thermal Energy Storage for Concentrating Solar Power Systems. doi:10.1007/s13398-014-0173-7.2, 2012.

[14] ⟨http://www.yara.us/images/NitCal-TDS-industrial_tcm399-66077.pdf⟩.

[15] O. Bondarchuk, A. Morel, D. Bélanger, E. Goikolea, T. Brousse, R. Mysyk, Thin films of pure vanadium nitride: evidence for anomalous non-faradaic capacitance, J. Power Sources 324 (2016) 439–446.

[16] N. Fairley, @Casa Software ltd, Copyright (C) 1999–2010, 2010.

[17] K. Federsel, J. Wortmann, M. Ladenberger, High-temperature and corrosion behaviour of nitrate nitrite molten salt mixtures regarding their application in concentrating solar power plants, Energy Procedia 69 (2015) 618–625.

[18] G.P. Celata, F.D. Annibale, A. Mariani, Nanofluid flow effects on metal surfaces, Energ. Ambient. e Innov. 4–5 (2011) 94–98.

[19] W. Rashmi, A.F. Ismail, M. Khalid, A. Anuar, T. Yusaf, Investigating corrosion effects and heat transfer enhancement in smaller size radiators using CNT-nanofluids, J. Mater. Sci. 49 (2014) 4544–4551.

[20] A.M. Rashidi, M. Packnezhad, M. Moshrefi-Torbati, F.C. Walsh, Erosion–corrosion synergism in an alumina/sea water nanofluid, Microfluid. nanofluidics 17 (2014) 225–232.

[21] S. Fotowat, S. Askar, M. Ismail, A. Fartaj A study on corrosion effects of a water based nanofluid for enhanced thermal energy applications. Sustainable Energy Technologies and Assessments2017; Just accepted. doi: http://dx.doi.org/10.1016/j.seta.2017.02.001.

[22] R. Bubbico, G.P. Celata, F. D'Annibale, B. Mazzarotta, C. Menale, Experimental analysis of corrosion and erosion phenomena on metal surfaces by nanofluids, Chem. Eng. Res Des. 104 (2015) 605–614.

[23] P.H. Suegama, Corrosion behavior of carbon steel protected with single and bi-layer of silane films filled with silica nanoparticles, Surf. Coat. Technol. 202 (2008) 2850–2858.

[24] A. Padmanaban, The Effect of Silica Nanoparticles on Corrosion of Steel by Molten Carbonate Eutectics. Master thesis, 2011.

[25] W.J. Cheng, D.J. Chen, C.J. Wang, High-temperature corrosion of Cr–Mo steel in molten LiNO 3–NaNO 3–KNO 3 eutectic salt for thermal energy storage, Sol. Energy Mater. Sol. Cells 132 (2015) 563–569.

[26] M.T. de Miguel, V. Encinas-Sánchez, M.I. Lasanta, G. García-Martín, F.J. Pérez, Corrosion resistance of HR3C to a carbonate molten salt for energy storage applications in CSP plants, Sol. Energy Mater. Sol. Cells 157 (2016) 966–972.

[27] J. Sure, A.R. Shankar, S. Ramya, C. Mallika, U.K. Mudali, Corrosion behaviour of carbon materials exposed to molten lithium chloride-potassium chloride salt, Carbon 67 (2014) 643–655.

[28] Y.H. Wang, J.H. Zhang, J.B. Zang, E.B. Ge, H. Huang, Etching and cutting of multiwalled carbon nanotubes in molten nitrate, Corros. Sci. 53 (2011) 3764–3770.

[29] A. Vasu, F.Y. Hagos, M.M. Noor, R. Mamat, W.H. Azmi, A.A. Abdullah, T.K. Ibrahim, Corrosion effect of phase change materials in solar thermal energy storage application, Renew. Sustain. Energy Rev. 76 (2017) 19–33.

[30] I.M. Shahrul, I.M. Mahbubul, S.S. Khaleduzzaman, R. Saidur, M.F. Sabri, A comparative review on the specific heat of nanofluids for energy perspective, Renew. Sustain. Energy Rev. 38 (2014) 88–98.

[31] O. Arthur, M.A. Karim, An investigation into the thermophysical and rheological properties of nanofluids for solar thermal applications, Renew. Sustain. Energy Rev. 55 (2016) 739–755.

[32] H. Riazi, S. Mesgari, N.A. Ahmed, R.A. Taylor, The effect of nanoparticle morphology on the specific heat of nanosalts, Int J. Heat. Mass Transf. 94 (2016) 254–261.

[33] S.F. Ahmed, M. Khalid, W. Rashmi, A. Chan, K. Shahbaz, Recent progress in solar thermal energy storage using nanomaterials, Renew. Sustain. Energy Rev. 67 (2017) 450–460.

[34] A. Bonk, M. Braun, A. Hanke, J. Forstner, D. Rückle, S. Kaesche, V.A. Sötz, T. Bauer Influence of Different Atmospheres on Molten Salt Chemistry and its Effect on Steel Corrosion. SolarPaces2017, Santiago de Chile, Chile, 26-29 September 2017.

Investigation of new nanofluids based on molten salts and their corrosion mechanisms for thermal energy storage applications

Thermal energy storage (TES) is considered as a vital component for concentrated solar power (CSP) technology, which leads to cost-effective dispatchable electricity production. The commercial TES technology in CSP plants is based on a two-tank solution of molten nitrate salts. The binary inorganic salt which consists of a mixture of 60 wt% of $NaNO_3$ and 40 wt% of KNO_3, so-called "Solar salt", is used due to its suitable operating temperature range, high density, low vapor pressure, and relatively high heat capacity. While its poor thermal conductivity is considered as the main drawback that requires a complicated heat exchanger design for a better heat transfer efficiency during the charge and discharge processes. Thus, it contributes to the increment of the levelized cost of electricity (LCOE) in CSP plants. However, for further reduction of the CSP costs, the efficiency of the whole system can be improved by enhancing the thermophysical properties of the molten salt as the specific heat capacity and thermal conductivity. Recently, the development of nanofluids based on molten salt with anomalous enhancements of those properties was identified as a promising approach. Even some enhancements were already reported in the literature, a big discrepancy of the results was observed due to several factors such as the enhancement mechanisms are still unknown, the complexity of the nanofluid preparation method, the determination of those properties, the initial state of the nanoparticles dispersion and its evolution with time. In this work, we present an optimized simple dry method for the preparation of nanofluids to obtain a homogeneous dispersion of nanoparticles within the molten salt. In addition, to reveal the mechanisms of thermophysical properties and improve the dispersion stability, different types of nanoparticles with different sizes, compositions, and shapes were used. For that purpose, monodispersed SiO_2 and $SiO_2@Al_2O_3$ core-shell nanoparticles were developed for the first time to prepare the molten salt-based nanofluids with improved stability compared to the commercial nanoparticles based nanofluids. Finally, the effect of adding nanoparticles in the molten salt on its corrosivity with the tank material is still needed to be explored. In the present work, we discovered new corrosion mechanisms related to the addition of the nanoparticles in the molten salts. In addition, a simple graphitization method was proposed as an anticorrosion method for molten binary nitrate salt with carbon steel.